WRF Meteorological Modeling In Support Of Regional Air Quality Modeling for the 2011 Base Year

David Brown
Iowa Department of Natural Resources

June 4, 2014

[This page was intentionally left blank.]

Table of Contents

1. INTRODUCTION 1

1.1. Background 1
1.2. Objectives 1

2. MODEL SELECTION AND DESCRIPTION 2

2.1. Selection Background 2
2.2. Description 2
2.2.1. Model Features 2
2.2.2. Modeling System Components 4

3. NUDGING SENSITIVITY ANALYSIS 6

4. INPUT DATA ACQUISITION AND PROCESSING 31

4.1. Initial and Boundary Conditions 31
4.2. Static Terrestrial Data 32
4.3. 3D Analysis Nudging 33

5. MODEL CONFIGURATION 35

5.1. Time Period 35
5.2. Modeling Domain 36
5.2.1. Horizontal Grid 36
5.2.2. Vertical Levels 37
5.3. Physics Parameterizations 39
5.4. Dynamics Options 41

6. PERFORMANCE EVALUATION 43

6.1. Methodology 43
6.2. Results 46
6.2.1. Near-Surface Statistics 46
6.2.2. Upper-Air Statistics 49
6.2.3. Precipitation 50

7. CONCLUSIONS 51

8. REFERENCES 53

APPENDIX A: WRF NAMELIST FILES 55

APPENDIX B: NEAR-SURFACE EVALUATION PLOTS 62

APPENDIX C: UPPER AIR EVALUATION PLOTS 101

APPENDIX D: MONTHLY ACCUMULATED PRECIPITATION PLOTS 107

1. INTRODUCTION

1.1. Background

The Iowa Department of Natural Resources (DNR), in collaboration with the Lake Michigan Air Directors Consortium and the Wisconsin Department of Natural Resources, has completed an annual meteorological model simulation using the Weather Research and Forecasting (WRF) model. This simulation serves as the initial component of an air quality modeling platform for the 2011 calendar year. Meteorological output fields are required to drive both emissions and photochemical transport modeling. Air quality simulations are then used to address current and anticipated air quality issues focused on the Central and Eastern U.S., including State Implementation Plan (SIP) development, non-attainment of the National Ambient Air Quality Standards (NAAQS), and interstate transport related to ozone, fine particles, and visibility impairment.

1.2. Objectives

The purpose of this technical support document is twofold. The first is to serve as the protocol which communicates the steps and decisions required to complete the meteorological modeling project, which include:

- Selection and description of the modeling system;
- Spatial extent and resolution of the modeling domain;
- Temporal modeling period;
- Appropriate and necessary model configuration sensitivity analyses;
- Final model configuration of the meteorological model;
- Performance evaluation methodology;
- Delivery of the meteorological model outputs for subsequent use in air quality modeling;
- Documentation of the meteorological modeling study findings.

The second objective of this report is to document the methodology and results of the statistical performance evaluation of the meteorological dataset conducted by the Iowa DNR. The error statistics generated by this analysis put into a historical context the accuracy and reliability of the simulated meteorological fields. A strong understanding of these error quantities is important, because these uncertainties will be input into the photochemical transport model and comprise a component of the errors in predicted ambient pollution concentrations. This section of the document focuses upon model performance over the states belonging to the CenSARA and LADCO organizations.

The ultimate goal of this project is to create a scientifically sound simulation of atmospheric dynamics observed over the Central and Eastern United States as part of a one-atmosphere air quality modeling platform. A cohesive modeling system which uses a consistent meteorological basis is valuable as meteorological data affects emissions, atmospheric chemical transformations, and the transport of pollutants such as fine particles, ozone, and those affecting visibility impairment (regional haze).

This project is the second iteration of a meteorological study using WRF and builds upon experience and knowledge gained from the initial deployment of the WRF model (Brown et al., 2012). An annual WRF simulation for the calendar year 2007 was produced through collaboration with several regulatory agencies within the Central and Eastern U.S. The optimal configuration established from this study reflects a consensus among the parties involved.

2. MODEL SELECTION AND DESCRIPTION

2.1. Selection Background

Over the past decade, the increase in affordable computing power combined with advances in parallel computing methods have opened the door to more sophisticated meteorological and air quality studies. Mesoscale model simulations with horizontal domains covering the entire continental U.S. and spanning an entire calendar year are now common.

The meteorological model is a critical component of air quality simulations. High quality meteorological inputs are necessary for accurate representations of transport and dispersion, cloud properties, radiative fluxes, temperature and humidity fields, boundary layer evolution, and surface fluxes of both meteorological quantities (heat, moisture, and momentum) and chemical species (dry deposition) (Gilliam et al., 2009).

The Weather Research and Forecasting (WRF) model was selected for this study due to its status as the state-of-the-science meteorological model and acceptance in the air quality community. Several meteorological modeling projects have utilized WRF over the past few years (Environ, 2012; McNally and Loomis, 2012; Baker et al., 2013; EPA, 2013). WRF is a common choice for air quality studies because the model is:

- Generally considered the most technically advanced public-domain prognostic model available for operational use in preparing inputs to urban- and regional-scale photochemical air quality models.
- Suitable for a broad spectrum of applications across scales ranging from meters to thousands of kilometers.
- Flexible and efficient computationally, while offering the advances in physics, numerics, and data assimilation contributed by the research community.

2.2. Description

2.2.1. Model Features

The WRF version 3.5 mesoscale meteorological model is a fully compressible, non-hydrostatic model with an Eulerian mass dynamical core (Skamarock et al., 2008). Two dynamical cores are available: the Advanced Research WRF (ARW) core, developed and supported by NCAR, and the Non-hydrostatic Mesoscale Model (NMM) core, whose development is centered at NCEP's Environmental Modeling Center (EMC) and support is provided by NCAR's Development Testbed Center (DTC). The ARW core is preferred by air quality modelers, due to its flexibility in physics options and its four-dimensional data assimilation (FDDA) capabilities. Hereinafter references to WRF will refer to the ARW core. It is available for public download at http://www2.mmm.ucar.edu/wrf/users/download/get_source.html.

The ARW core contains several major features. The prognostic equations are fully compressible and non-hydrostatic and are written in flux form to conserve mass, momentum, entropy, and scalars. Second- to 6th-order advection options in the horizontal and vertical are available for spatial discretization. WRF performs time-split integration using a 2nd- or 3rd-order Runge-Kutta scheme with a smaller time step for acoustic and gravity wave modes. A variable time step capability, known as Adaptive Time Step, is available. This method optimizes the computational efficiency of the simulation, while maintaining numerical stability.

The ARW equations are formulated using a terrain-following, hydrostatic-pressure coordinate

$$\eta = \frac{p_h - p_{ht}}{\mu}, \mu = p_{hs} - p_{ht} \tag{1}$$

where p_h is the hydrostatic component of the pressure at the vertical model level, and p_{hs} and p_{ht} are the hydrostatic pressures at the surface and top boundaries, respectively. The top boundary of the model is a constant pressure surface. The grid structure follows the Arakawa C staggering, shown in Figure 2-1.

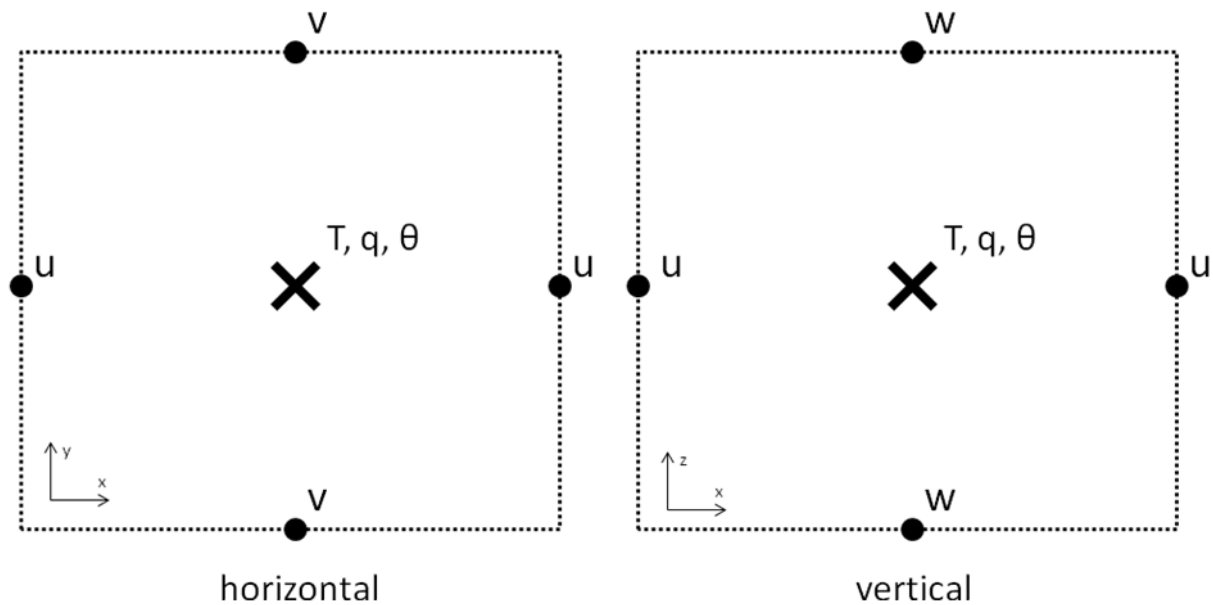

Figure 2-1. An example of the Arakawa C grid staggering used by WRF.

Multiple nested grids with multiple integer ratios are permitted. The interactions between nested grids and their parent grids may be one-way concurrent, one-way consecutive, or two-way.

WRF contains the option of FDDA to nudge modeled fields towards observations. Gridded analysis and observational nudging capabilities are available. This allows air quality modelers the ability to incorporate observations in retrospect in an attempt to reduce model error.

A full suite of physics options are available to represent sub-grid scale processes related to atmospheric radiation, surface and boundary layers, convection, and cloud and precipitation processes. For each of these sub-grid schemes, WRF offers three to nine different parameterizations from which a user may select. To make these choices, the modeler must consider not only the individual merits of each parameterization but also how it interacts with the other physics parameterization options. Figure 2-2 illustrates the interaction of the WRF physics modules.

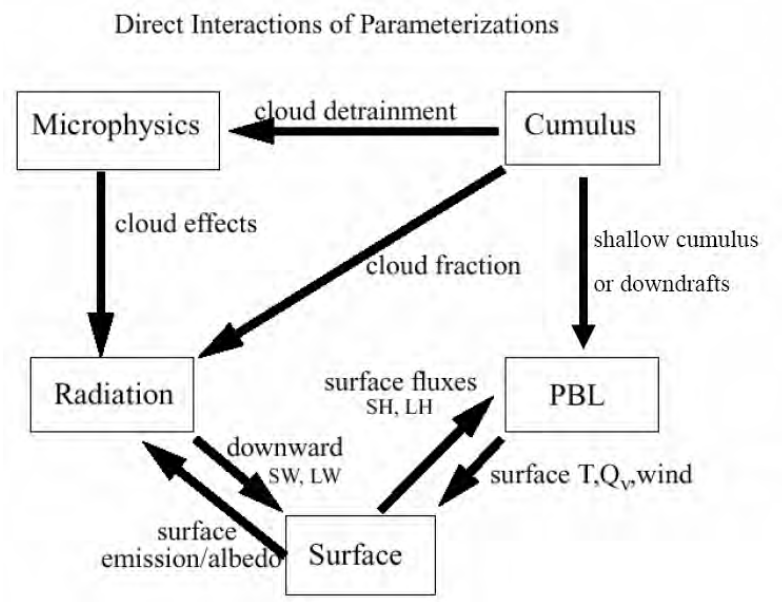

Figure 2-2. The direct interaction between the various parameterizations of sub-grid processes in WRF (source unknown).

2.2.2. Modeling System Components

The WRF modeling system consists of several processors to complete the various simulation tasks, from ingesting the input fields required to generate initial and boundary conditions, to generating the surface nudging fields, to running the dynamical core. The WRF components are illustrated in Figure 2-3. The modeling system is divided into two three main groups: the WRF Pre-processing System (WPS), the WRF model, and the post-processing and visualization tools.

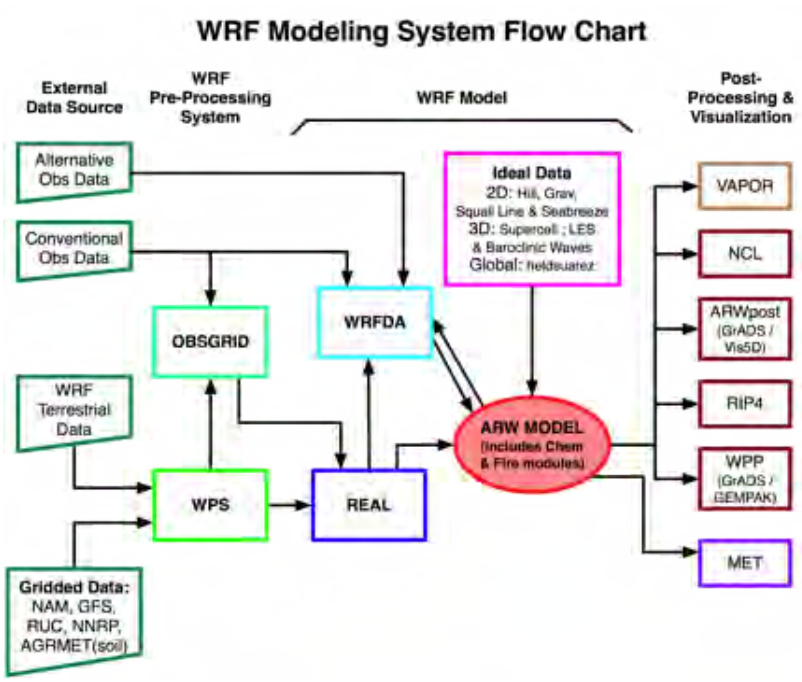

Figure 2-3. Illustration of the various components of the WRF modeling system (from WRF User's Guide).

WPS consists of three pre-processors: ungrib, geogrid, and metgrid. Ungrib reads gridded analysis files, extracts the necessary variables, and outputs them into an intermediate format. Geogrid operates independently from ungrib to define the modeling domain, extract terrestrial data, interpolate them to the model grid, and output the data to netCDF format. The metgrid program reads the output from geogrid and ungrib and combines the terrestrial and analysis data into a single netCDF file. The analysis data are interpolated to the horizontal domain, while the vertical structure of the original data is preserved for the time being. The program obsgrid may be considered a part of WPS; however it is obtained and compiled separately from the other WPS pre-processors. The purpose of this routine is to read observational data in little_r format and the gridded output of metgrid (which is considered the first-guess field) and perform an objective analysis. Obsgrid then outputs a surface analysis to be used by the FDDA routine and a 3D analysis to be input by the WRF model.

The modeling component consists of two processors: real and the ARW core itself. Real is responsible for reading the analysis fields output by WPS and interpolating them to the model's vertical layers. Real generates the initial and boundary conditions required by the ARW core to integrate the model equations. Real also outputs the 3D gridded analysis nudging files used by the FDDA scheme.

Several packages are available to post-process and visualize the output of a WRF simulation. More detail on each package may be found in the WRF-ARW V3 Modeling System User's Guide (http://www.mmm.ucar.edu/wrf/users/docs/user_guide_V3/ARWUsersGuideV3.pdf). The Iowa DNR used the Read Interpolate Plot version 4 (RIP4) plotting software (Stoelinga, 2006). RIP4 invokes NCAR Graphics routines to visualize output from MM5, WRF, and potentially, any mesoscale model.

The most currently available version of WRF at the time of this project was version 3.5, released on April 18th, 2013. This version represents the fourth major update to WRF since version 3.1.1, which was used for the 2007 annual simulation.

3. NUDGING SENSITIVITY ANALYSIS

The majority of the physics and dynamics options for WRF were selected based on a comprehensive sensitivity analysis conducted prior to the 2007 annual simulation. However, as major updates to the WRF modeling system introduced new features and settings, further sensitivity testing was warranted. Evaluation of the previous simulation revealed weaknesses in model performance which may potentially be improved through refinement of model settings. Therefore, a number of small sensitivity analyses were performed prior to the 2011 annual simulation in an effort to fine-tune and improve the WRF configuration. Most tests results in minimal changes to model results. The most notable sensitivity study was the test of the 3D and surface analysis nudging configuration and is the only test discussed in this chapter.

A significant weakness of the 2007 annual simulation was the persistent underprediction of 10-m wind speed during the daytime hours. Figure 3-1 shows an example timeseries plot of observed and modeled wind speed during June 2007 for the CENRAPN evaluation region, which included Iowa, Minnesota, Missouri, Nebraska, and Kansas. The daily peaks in wind speed were consistently underpredicted by roughly 1 m/s.

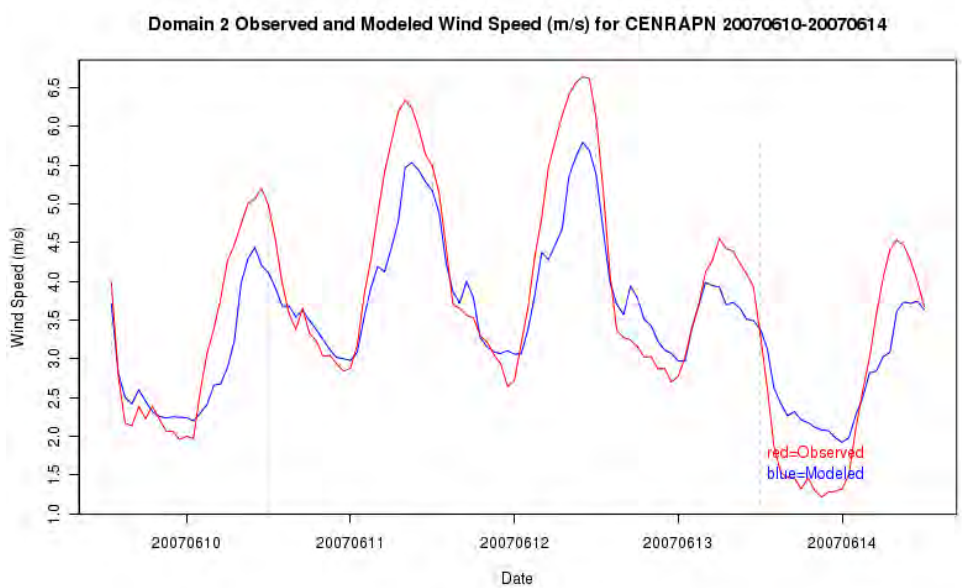

Figure 3-1. Time series of observed and modeled 10-m wind speed averaged over the CENRAPN region from the 2007 annual simulation.

The Environmental Protection Agency (EPA) recently revisited the nudging scheme used in their meteorological modeling in an effort to reduce uncertainties in modeled wind speed within the planetary boundary layer (PBL), especially those associated with low-level nocturnal jets (Gilliam et al., 2012). That study showed improvements in modeled wind speed may be achieved through the elimination of wind vector nudging within the PBL and incorporation of additional observations from wind profilers and Doppler radar.

The Iowa DNR gridded analysis nudging configuration is based on EPA's configuration described by Gilliam and Pleim (2010). Therefore, it was advantageous to attempt a similar sensitivity study to determine if similar improvements in modeled wind speeds would be achieved. First, a baseline simulation was conducted for an abbreviated time period in 2011. The WRF model was run for the

months of June and December to sample both summer and winter meteorological conditions. The WRF configuration from the 2007 annual simulation was adopted for this test. Figure 3-2 shows a time-height plot of average observed wind speeds measured by the UHF profilers located within the 12 km domain used for the 2007 annual simulation, which covers the Central and Eastern U.S., for the month of June. Figure 3-3 shows a time-height plot of wind speed bias calculated from the UHF profiler data paired with modeled wind speed for the same time period. A low-level nocturnal jet feature is evident and well resolved by WRF. Bias values were acceptable at less than 0.5 m/s at the center of the low-level jet. Unfortunately, WRF did a poor job simulating the wind speed within the daytime PBL. Wind speeds were underpredicted by as much as 1.6 m/s. Figure 3-4 shows a time-height plot of average observed wind speed for the month of December, while Figure 3-5 shows a time-height plot of modeled wind speed bias. At any given height, observed wind speeds were fairly consistent across the day. A much shallower layer of vertical mixing was observed during the day and WRF significantly underpredicted wind speed in this region. These findings are consistent with the underprediction in modeled wind speed shown for the 2007 annual simulation. The purpose of this sensitivity study was to find a configuration which would alleviate these errors.

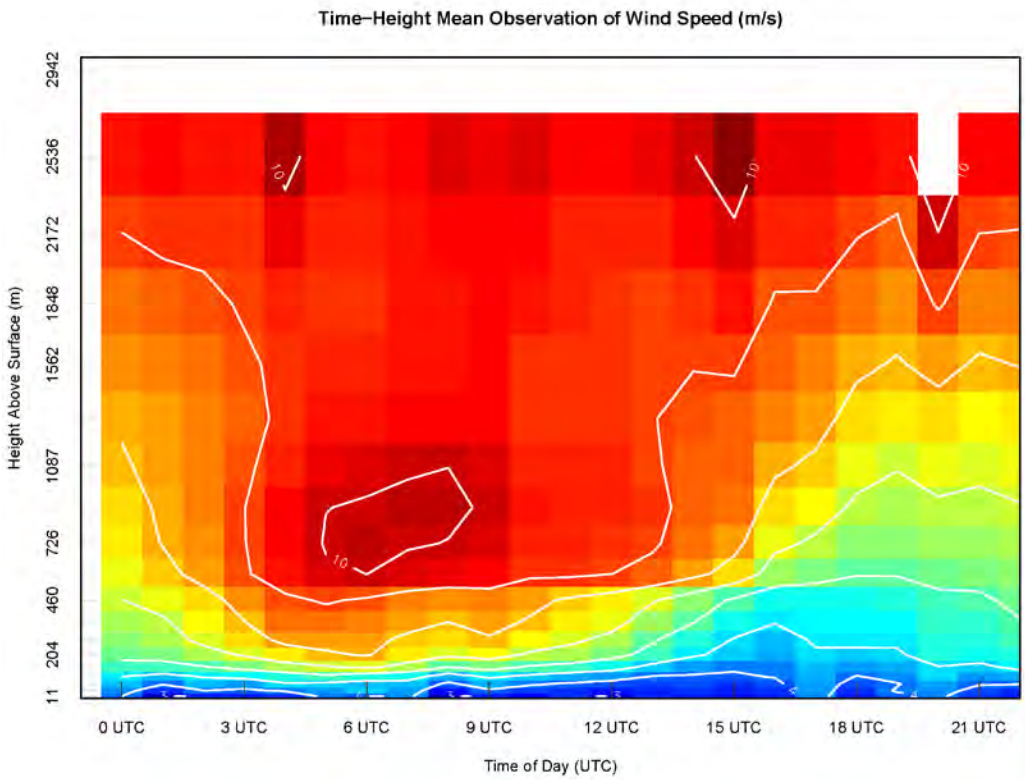

Figure 3-2. Time-height plot of average observed wind speed measured by UHF profilers within the 12 km domain during the month of June.

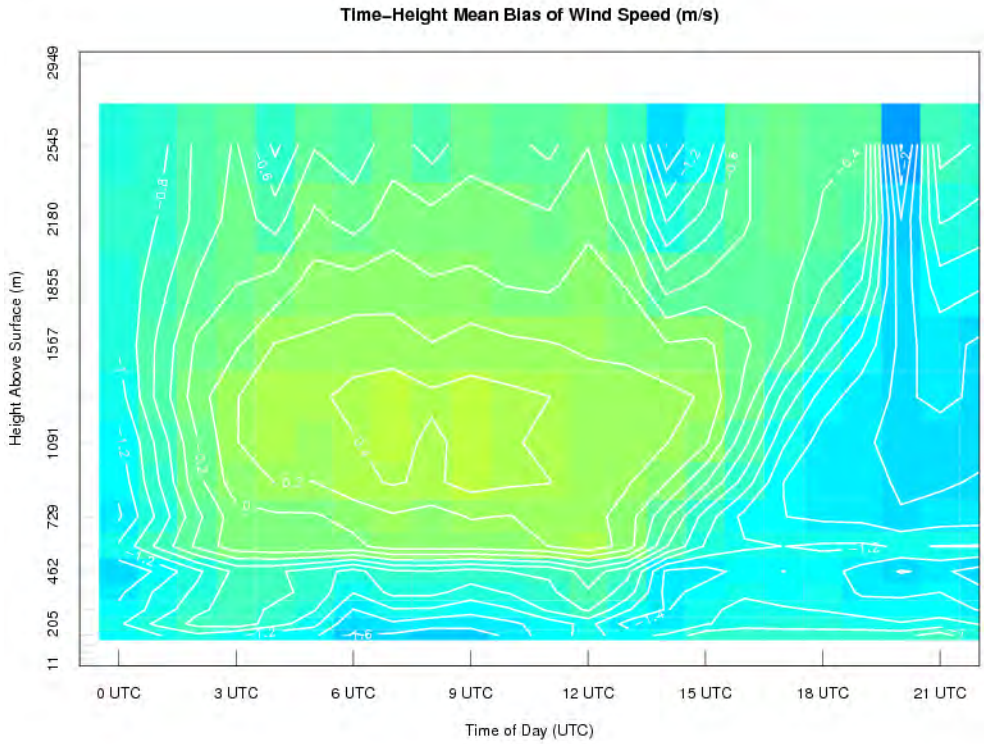

Figure 3-3. Time-height plot of wind speed bias for the 2011 12 km baseline test for the month of June.

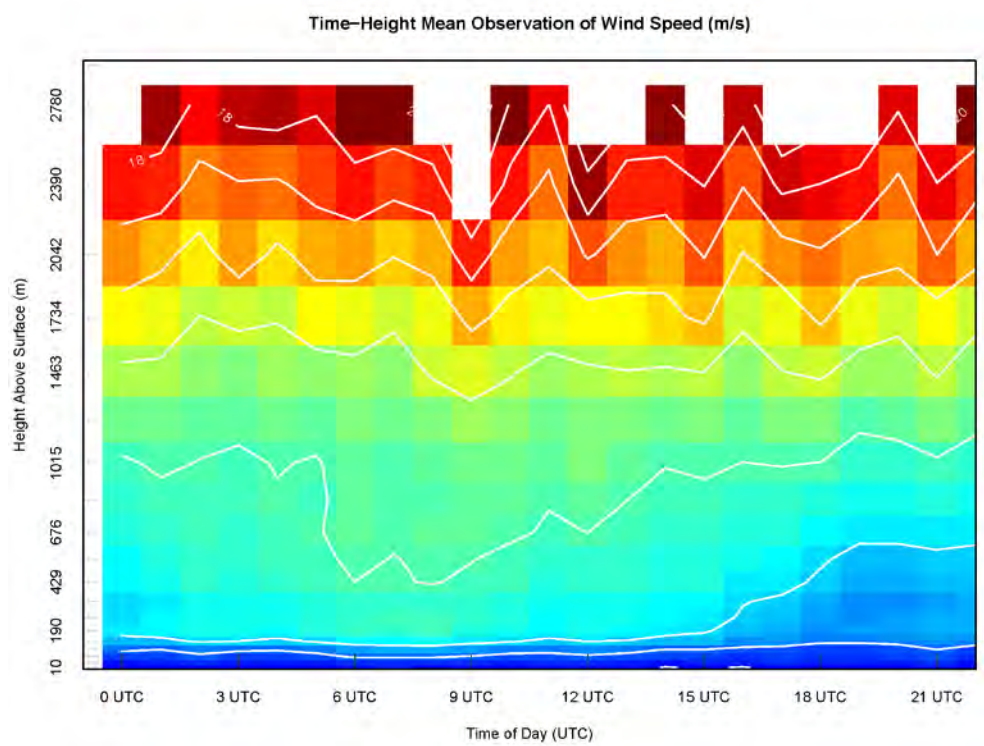

Figure 3-4. Time-height plot of average observed wind speed measured by UHF profilers within the 12 km domain during the month of December.

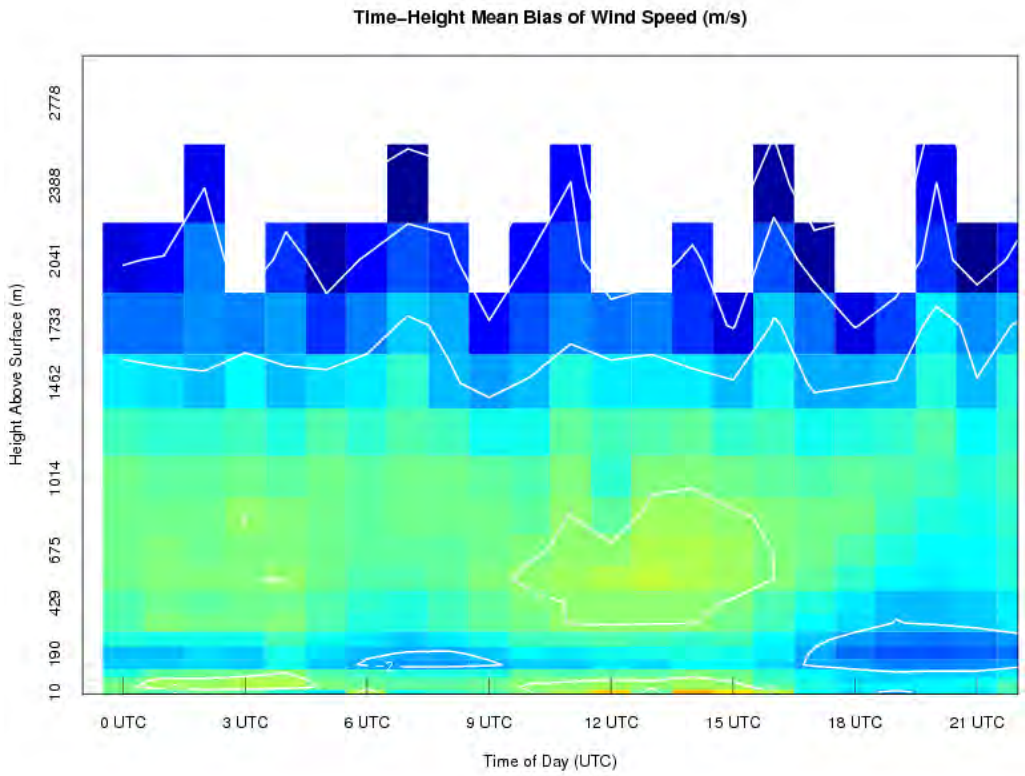

Figure 3-5. Time-height plot of wind speed bias for the 2011 12 km baseline test for the month of December.

Three sensitivity simulations were selected to test the nudging settings in WRF and are shown in Table 3-1. The baseline settings represent the current nudging configuration. Temperature, humidity, and wind vectors were nudged above the PBL, while only wind vectors were nudged within the PBL and near the surface. The first sensitivity (ns01) tested weakening of the nudging strengths for all fields. For the second sensitivity (ns02), nudging was turned off for all fields throughout the entire atmospheric column. This was done as a reference; it was not anticipated to be a viable option in future meteorological modeling. The third sensitivity (ns03) tested turning off nudging of the wind vectors within the PBL and also at the surface.

The modeled results were compared to UHF profilers, as well as twice-daily radiosonde soundings and conventional near-surface observations from the National Weather Service Automated Surface Observing System (ASOS) stations. For comparison to UHF profilers wind speed bias was calculated and visualized as a function of height and hour of day. The upper air evaluation consists of the calculation of wind speed bias at the mandatory reporting levels of the radiosonde platform for select locations over the Midwest. The near-surface evaluation consists of the calculation of bias, root mean square error, and correlation coefficient of 10-m wind speed, 2-m temperature, 2-m mixing ratio. The near-surface statistics were calculated for three geographic regions shown in Figure 3-6. The performance statistics are described in detail in Chapter 6.

Table 3-1. Nudging flags and coefficients for the baseline and three sensitivity simulations.

Sensitivity	Nudging Above PBL		Nudging Within PBL		Surface Nudging		gt	gq	guv	guv_sfc
	T, Q	Wind	T, Q	Wind	T, Q	Wind				
BASE	Y	Y	N	Y	N	Y	3.0E-04	1.0E-05	3.0E-04	3.0E-04
ns01	Y	Y	N	Y	N	Y	5.0E-05	1.0E-05	5.0E-05	5.0E-05
ns02	N	N	N	N	N	N	N/A	N/A	N/A	N/A
ns03	Y	Y	N	N	N	N	3.0E-04	1.0E-05	3.0E-04	N/A

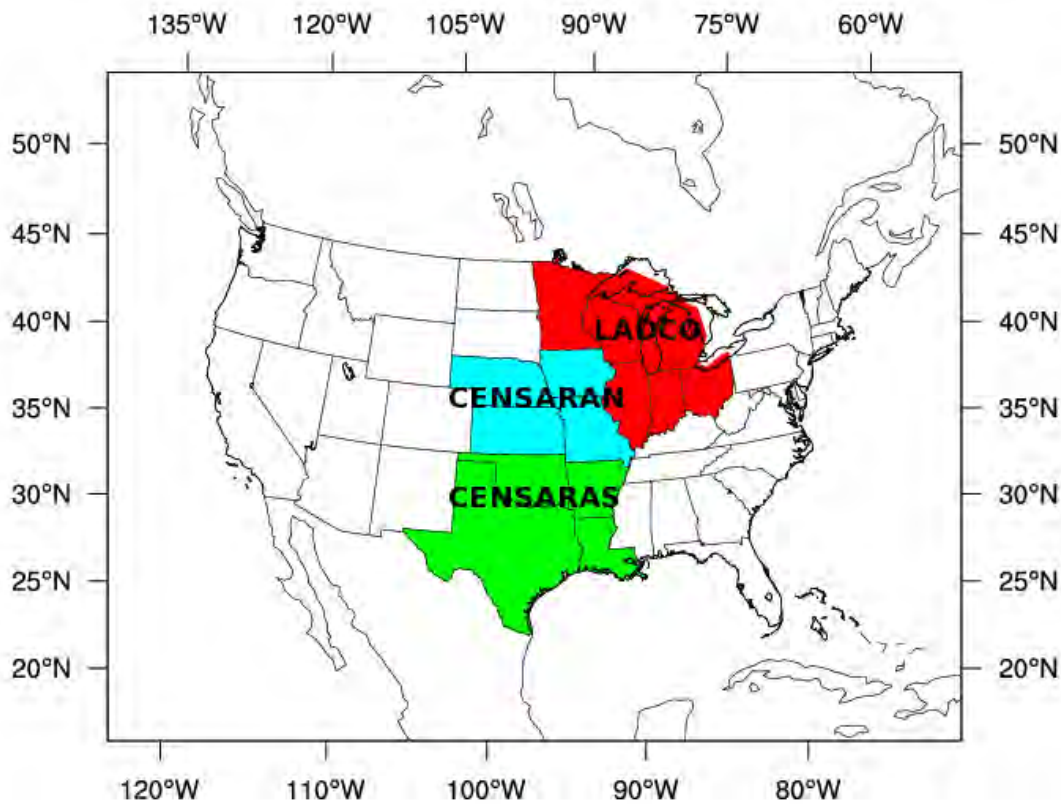

Figure 3-6. Geographical regions used to group the model-observed data pairs for evaluating the 2011 WRF simulation.

Figure 3-7 shows a timeseries of observed and modeled near-surface meteorological fields from the baseline and nudging sensitivity runs for the CENSARAN region and summer time period. The different nudging flags and strengths result in large variations among the sensitivity runs in wind speed, and modest variations in temperature and mixing ratio. The persistent underprediction in wind speed is evident in the 2007 annual simulation is again apparent in the 2011 baseline run. Completely turning off nudging, as shown with the ns02 sensitivity, results in a dramatic increase in wind speed to the point of producing significant overpredictions. The ns01 and ns03 sensitivities properly correct the baseline underprediction and wind speeds from these sensitivities more closely resemble observed wind speed. Figure 3-8 shows a timeseries of observed and modeled near-surface meteorological fields from the baseline and nudging sensitivity runs for the CENSARAS region and summer time period. Large variations among the sensitivity runs in wind speed and mixing ratio, and modest variations in

temperature were evident. Like in the CENSARAN region, the baseline run underpredicted wind speed. The ns02 sensitivity resulted in overprediction of only temperature and mixing ratio. Again, the ns01 and ns03 best reproduced observed wind speeds. Figure 3-9 shows a timeseries of observed and modeled near-surface meteorological fields from the baseline and nudging sensitivity runs for the LADCO region and summer time period. Large variations in among the sensitivity runs were evident for all three meteorological fields. Again, the persistent underprediction in wind speed was apparent in the baseline run. The ns02 sensitivity resulted in a severe overprediction of wind speed. The ns01 and ns03 sensitivities properly corrected the baseline underprediction and wind speeds from these sensitivities more closely resembled observed wind speed.

Figure 3-10 compares daily bias, root mean square error, and correlation coefficient (from top to bottom) for wind speed from the sensitivity runs for the CENSARAN region and for the summer time period. Wind speeds from the ns01 and ns03 sensitivities showed a clear improvement from the baseline and were nearly unbiased. Figure 3-11 shows the same daily statistics for wind speed for the CENSARAS region and for the summer time period. The ns01 sensitivity showed bias values near zero, while the ns03 sensitivity very slightly overpredicted wind speed. Figure 3-12 shows the same daily statistics for wind speed for the LADCO region and for the summer time period. Again, wind speeds from the ns01 and ns03 sensitivities showed a significant improvement from the baseline, with bias values near zero.

Figure 3-13 through Figure 3-15 show hourly wind speed statistics arranged by hour of the day for the month of June and for the CENSARAN, CENSARAS, and LADCO regions, respectively. The improvement in wind speed is evident for all hours of the day. Figure 3-16 through Figure 3-18 show time-height profiles of wind speed from the three sensitivities compared to observed wind speed measured by UHF profilers in the 2007 12 km domain for the month of June. These plots show modeled performance through the depth of the PBL and the results are consistent with the results near the surface. Wind speeds for ns01 and ns03 during the day were increased in the PBL relative to the baseline run (the desired effect) and bias value approach zero. Modeled winds were overpredicted for ns02, significantly so near the surface. Figure 3-19 and Figure 3-20 show wind speed performance for the sensitivity runs throughout the entire depth of the model domain at 00Z and 12Z, respectively, in the month of June. Modeled wind speeds were compared to twice-daily radiosonde measurements at select stations in the Midwest. At 00Z, the ns01 and ns03 showed a dramatic improvement in wind speed bias within the PBL. The underprediction of winds in the baseline run is more than 1.5 m/s below 700 mb, while wind speed bias for ns03 is between -0.5 and 0.0 m/s.

Figure 3-21 shows a timeseries of observed and modeled near-surface meteorological fields from the baseline and nudging sensitivity runs for the CENSARAN region and winter time period. The only significant variation in results for the sensitivity runs was for wind speed. Like in the summer period, wind speeds in the baseline simulation were persistently underpredicted, while wind speeds for the ns02 sensitivity were frequently overpredicted. Wind speeds from the ns01 and ns03 sensitivities more closely follow observations. Figure 3-22 shows a timeseries of observed and modeled near-surface meteorological fields from the baseline and nudging sensitivity runs for the CENSARAS region and winter time period. Modeled mixing ratio from the ns02 sensitivity run deviated from the remaining runs and significant variations in wind speed existed for all sensitivity runs. Like in the CENSARAN region, the baseline simulation underpredicted wind speeds, while the ns02 run frequently overpredicted wind speeds. The ns01 and ns03 sensitivities more closely matched observations. Figure 3-23 shows a timeseries of observed and modeled near-surface meteorological fields from the baseline and nudging sensitivity runs for the LADCO region and winter time period. The only significant variation in results for the sensitivity runs was for wind speed. Like in the other regions, wind speeds in the baseline simulation

were persistently underpredicted, while wind speeds for the ns02 sensitivity were frequently overpredicted. Wind speeds from the ns01 and ns03 sensitivities more closely follow observations.

Figure 3-24 through Figure 3-26 compare daily statistics for wind speed for the winter time period and for the CENSARAN, CENSARAS, and LADCO regions, respectively. Similar to in the summer, ns01 and ns03 showed a major improvement in wind speed bias compared to the baseline run. Figure 3-27 through Figure 3-29 show hourly wind speed statistics by hour of the day for December 2011. The improvement in wind speed bias was evident for all hours of the day.

Figure 3-30 through Figure 3-32 show time-height profiles of wind speed from the three sensitivities compared to observed wind speed measured by UHF profilers for December. Like in the summer period, wind speeds for ns01 and ns03 were increased throughout the depth in the PBL and bias values were much closer to zero compared to the base case. Figure 3-33 and Figure 3-34 show wind speed performance for all sensitivity runs throughout the depth of the model domain at 00Z and 12Z, respectively, for December. At 00Z, wind speeds were generally underpredicted by all sensitivities above the PBL. Within the PBL, however, wind speed bias for ns01 and ns03 approached zero. The ns03 sensitivity showed the best performance overall. At 12Z, ns02 showed the best performance, while the remaining sensitivities significantly underpredict winds throughout the depth of the troposphere. The ns01 sensitivity exhibited the worst performance.

Overall, the ns03 configuration, in which nudging of winds only occurs above the PBL similar to temperature and moisture, improved the performance of winds compared to the nudging configuration used in previous WRF modeling. The improvements were primarily found within the PBL during the daytime hours in the summer. The ns03 configuration is the optimum choice for retrospective meteorological analysis. Gilliam et al. (2012) also found elimination of nudging of winds in the PBL to greatly improve performance in their study. This nudging strategy was incorporated into the Iowa DNR modeling configuration and was implemented in the 2011 annual simulation.

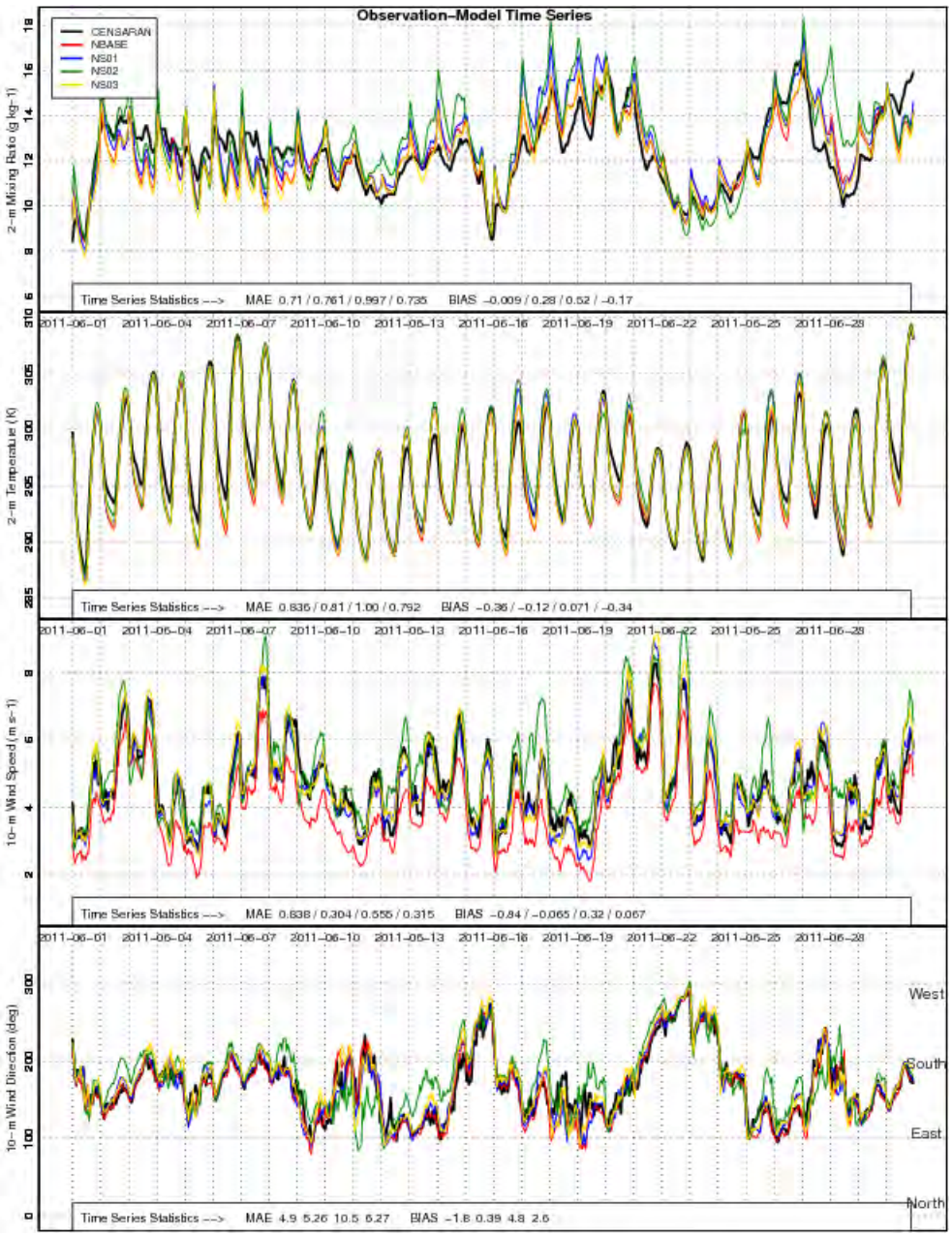

Figure 3-7. Timeseries of observed and modeled 2-m mixing ratio, 2-m temperature, and 10-m wind speed and direction averaged over the CENSARAN region for June 2011.

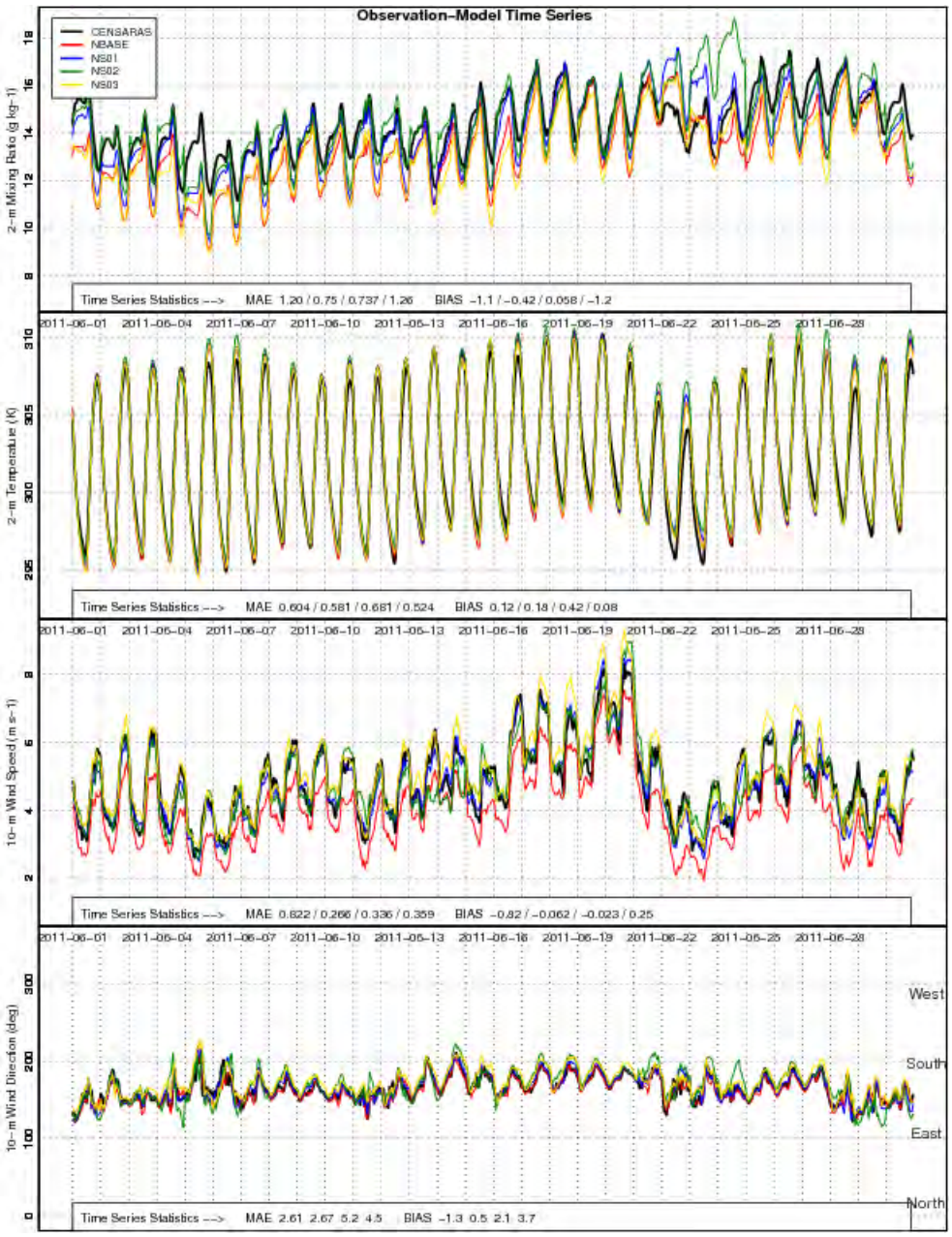

Figure 3-8. Timeseries of observed and modeled 2-m mixing ratio, 2-m temperature, and 10-m wind speed and direction averaged over the CENSARAS region for June 2011.

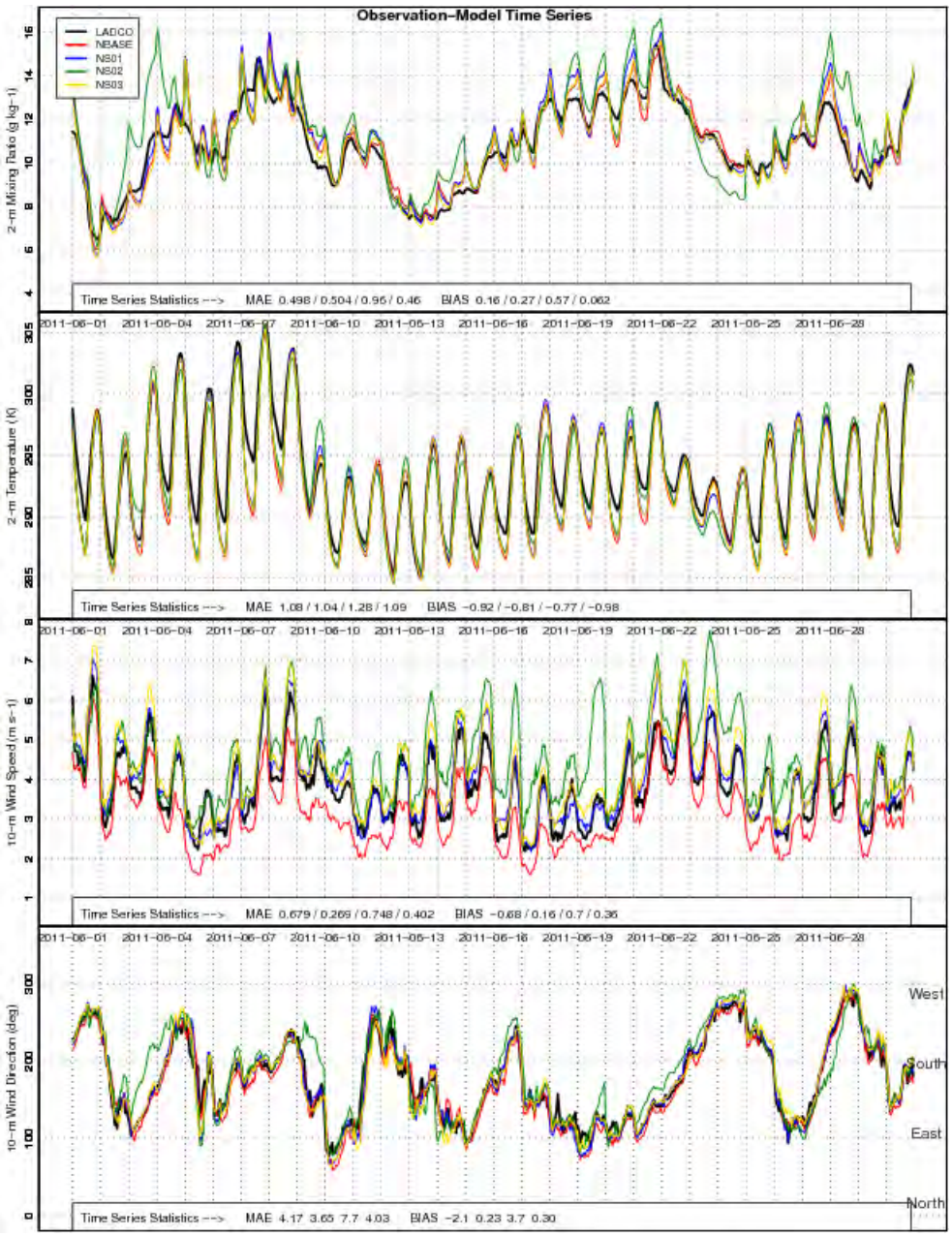

Figure 3-9. Timeseries of observed and modeled 2-m mixing ratio, 2-m temperature, and 10-m wind speed and direction averaged over the LADCO region for June 2011.

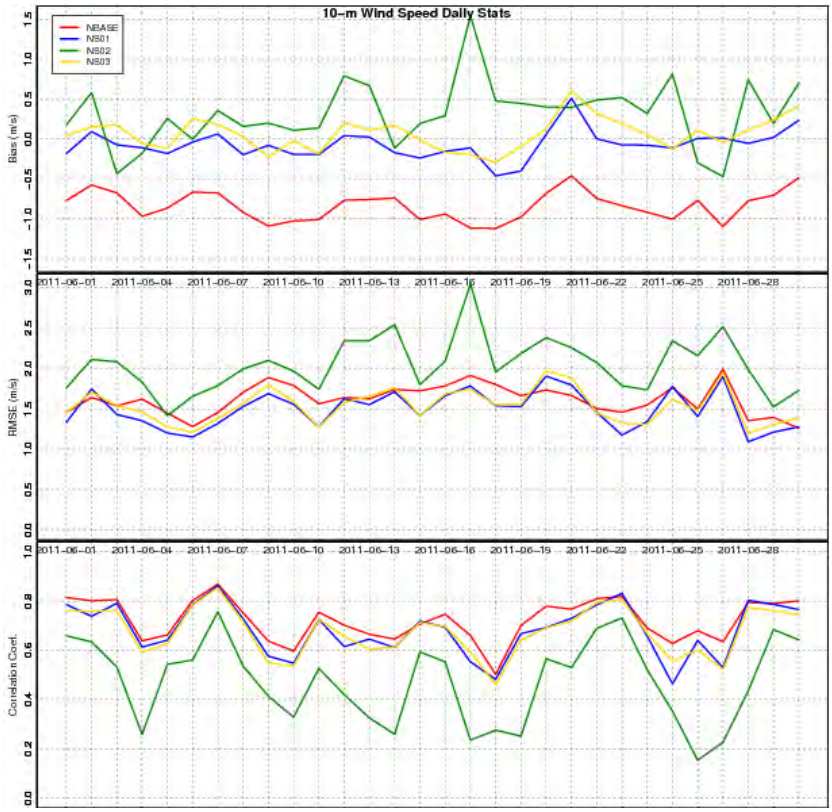

Figure 3-10. Timeseries of daily statistics for 10-m wind speed for the CENSARAN region for June 2011.

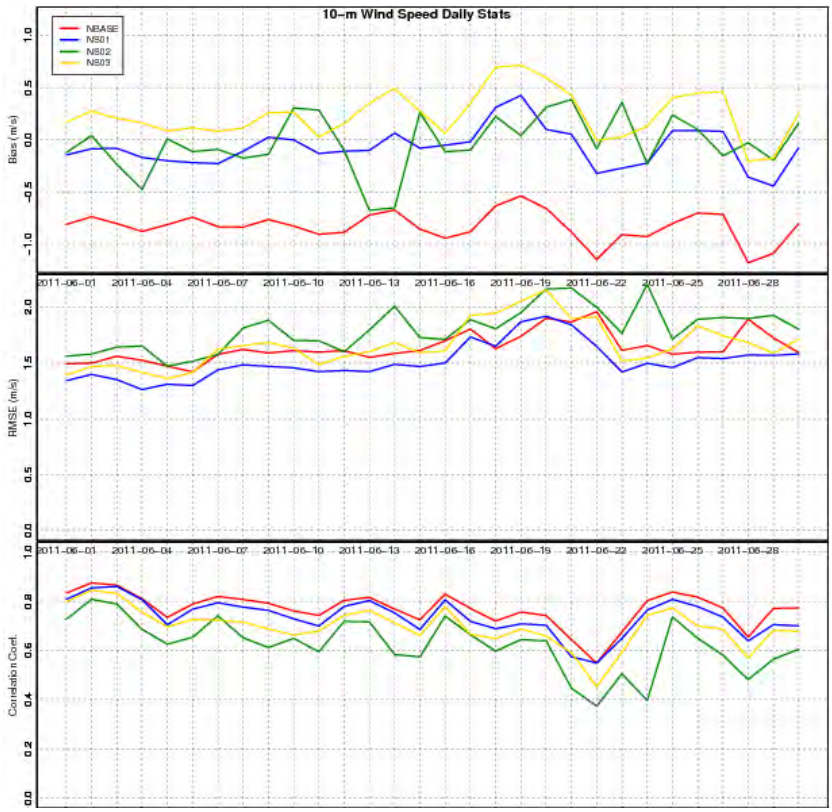

Figure 3-11. Timeseries of daily statistics for 10-m wind speed for the CENSARAS region for June 2011.

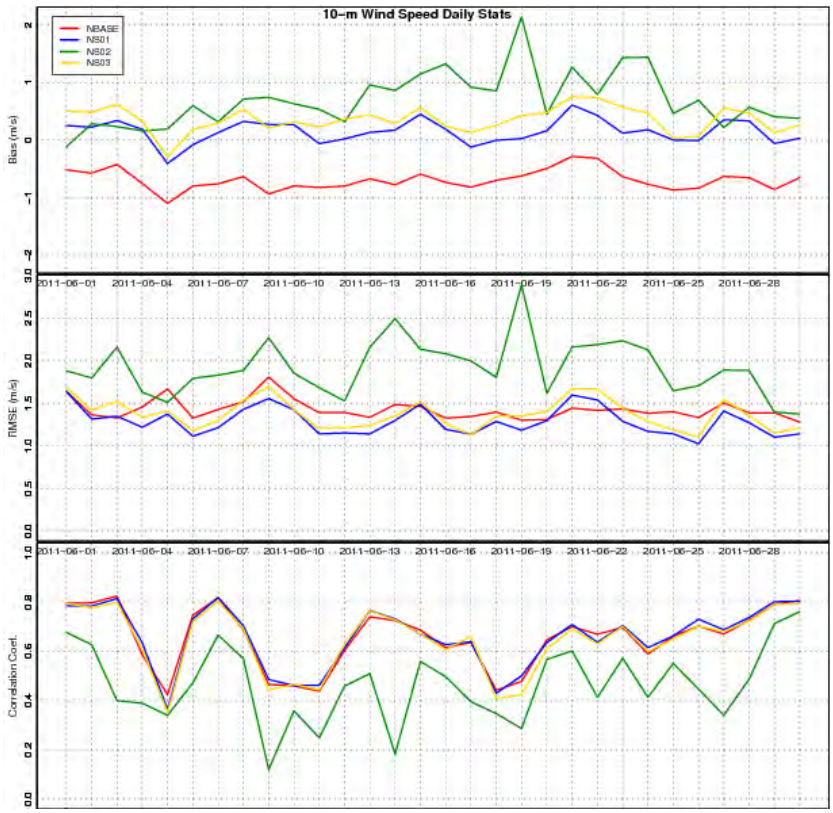

Figure 3-12. Timeseries of daily statistics for 10-m wind speed for the LADCO region for June 2011.

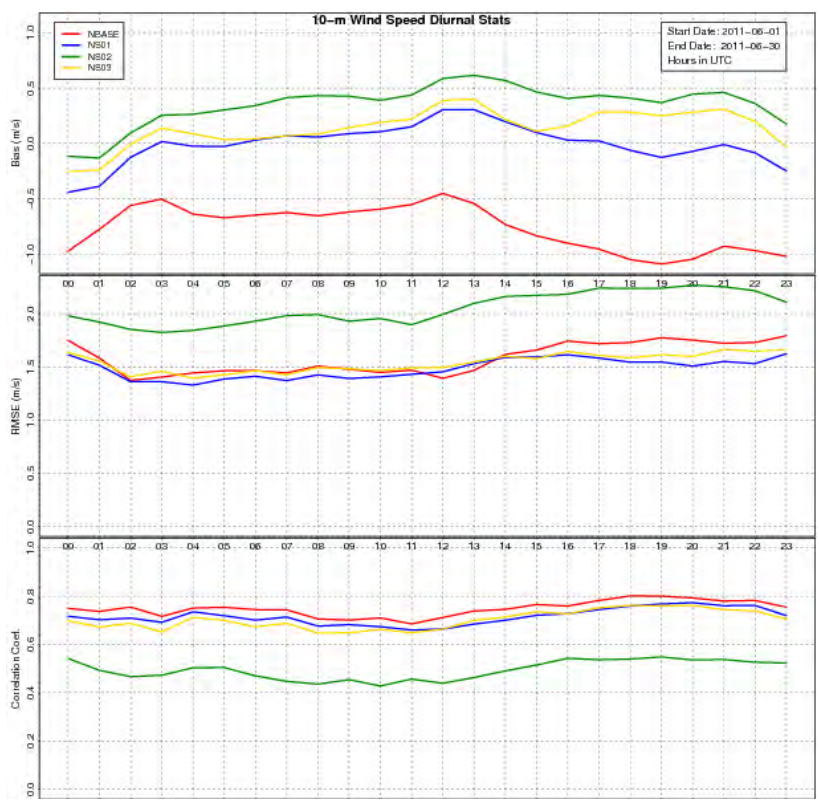

Figure 3-13. Diurnal profiles of hourly statistics for 10-m wind speed for the CENSARAN region for June 2011.

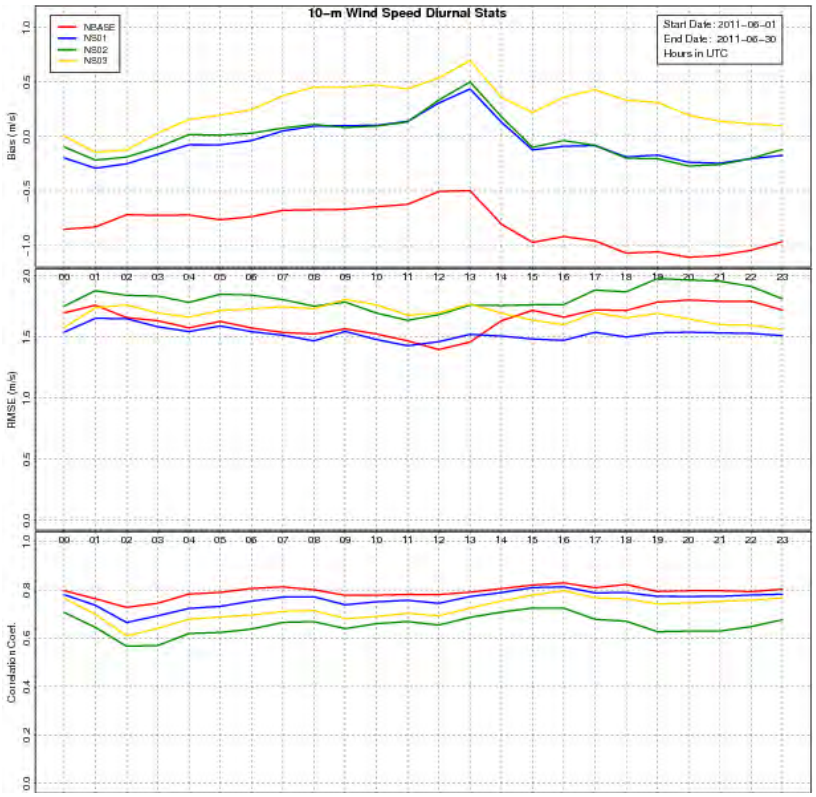

Figure 3-14. Diurnal profiles of hourly statistics for 10-m wind speed for the CENSARAS region for June 2011.

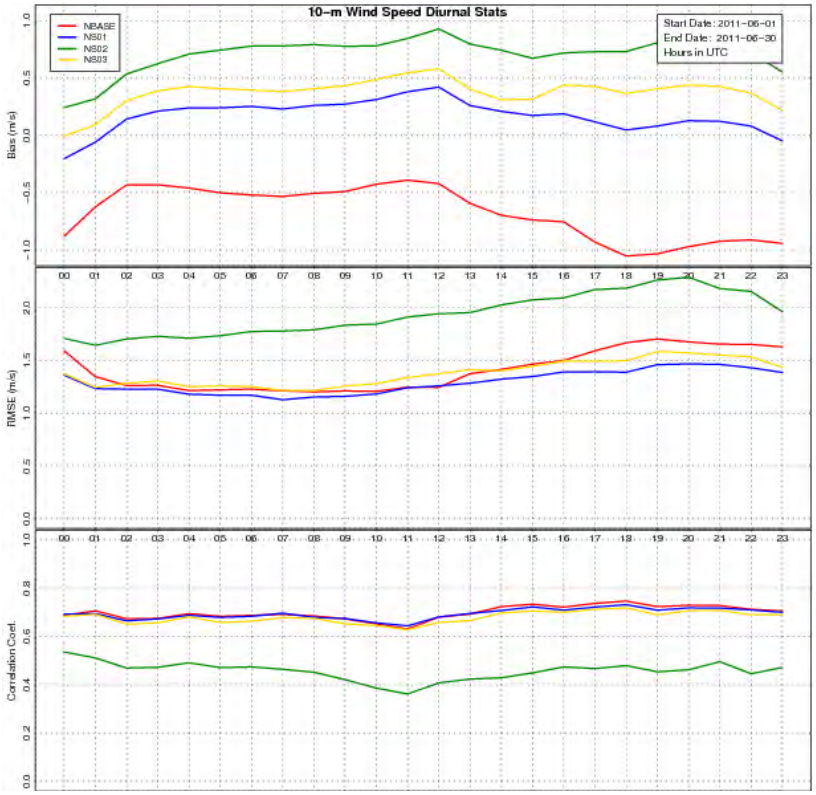

Figure 3-15. Diurnal profiles of hourly statistics for 10-m wind speed for the LADCO region for June 2011.

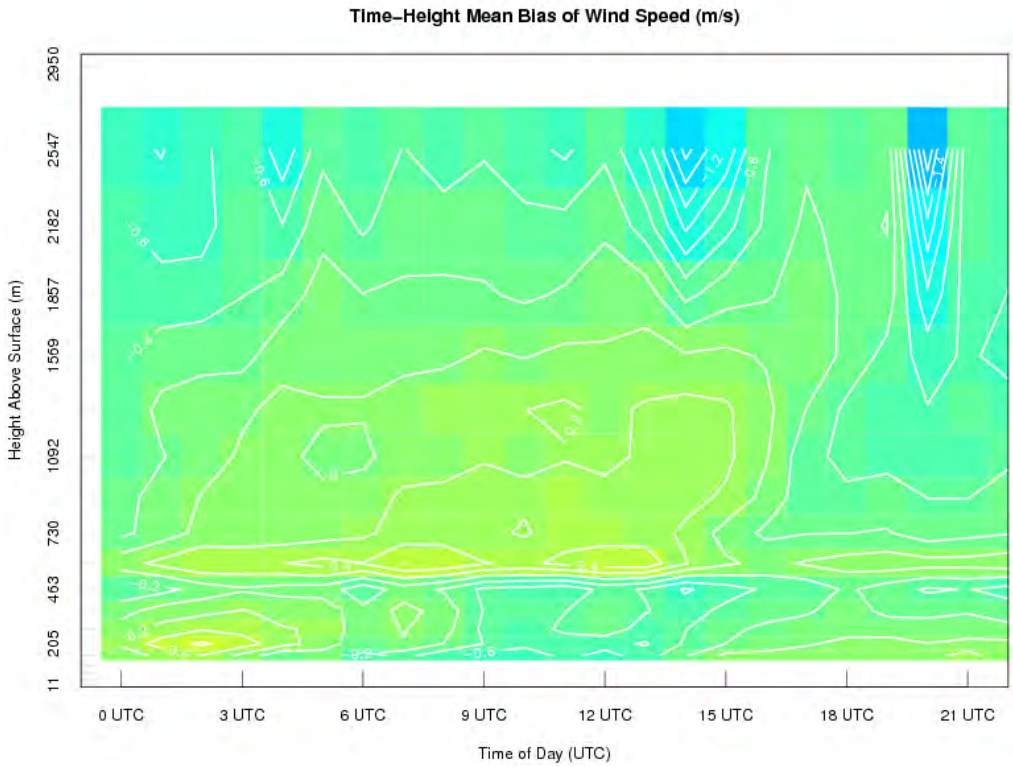

Figure 3-16. Time-height plot of wind speed bias for the ns01 sensitivity for June 2011.

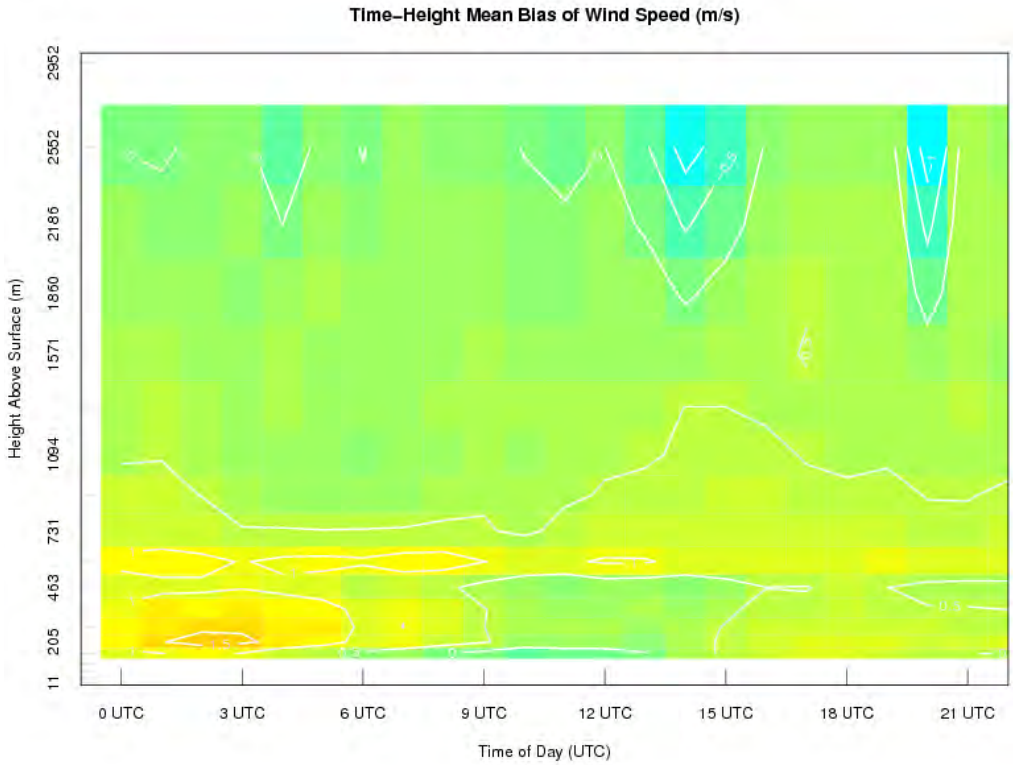

Figure 3-17. Time-height plot of wind speed bias for the ns02 sensitivity for June 2011.

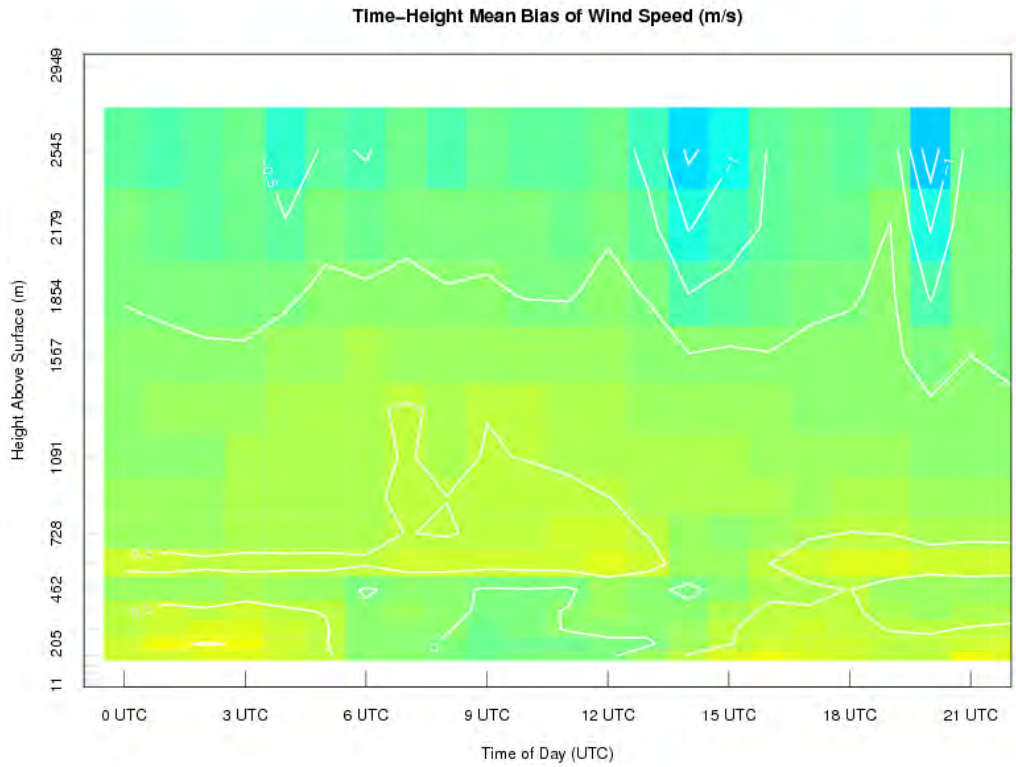

Figure 3-18. Time-height plot of wind speed bias for the ns03 sensitivity for June 2011.

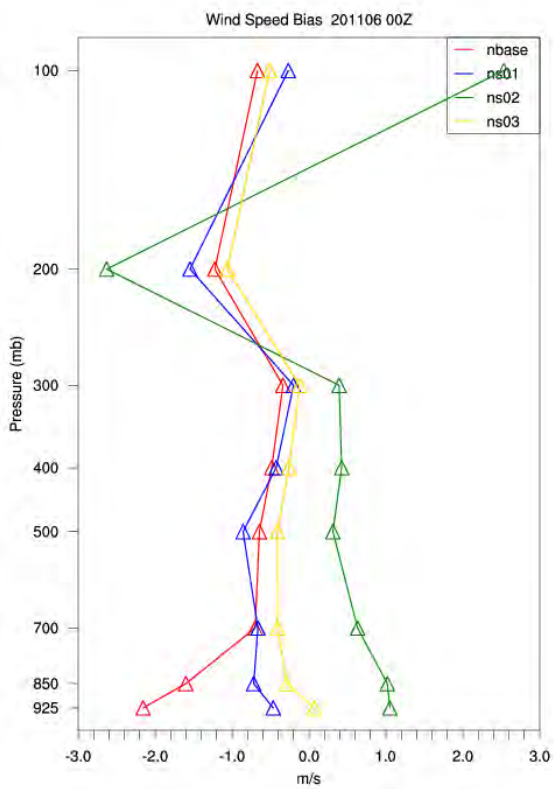

Figure 3-19. Vertical profile of wind speed bias relative to all 00Z radiosonde soundings for June 2011.

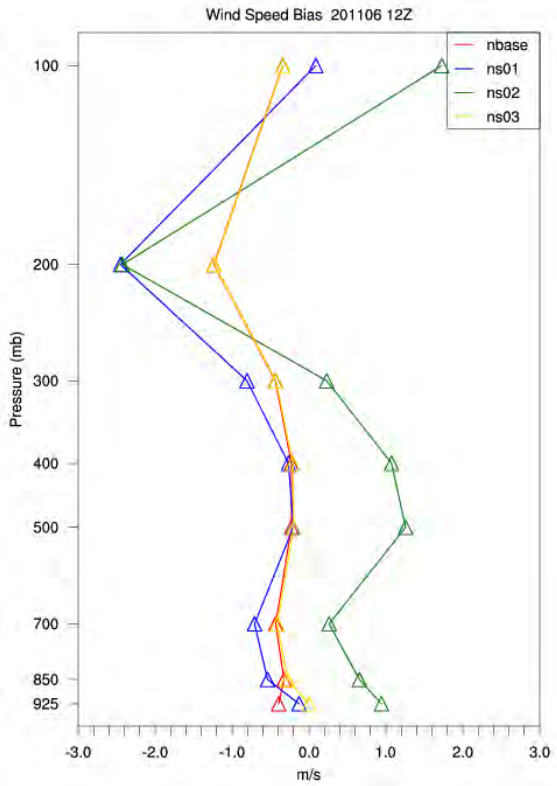

Figure 3-20. Vertical profile of wind speed bias relative to all 12Z radiosonde soundings for June 2011.

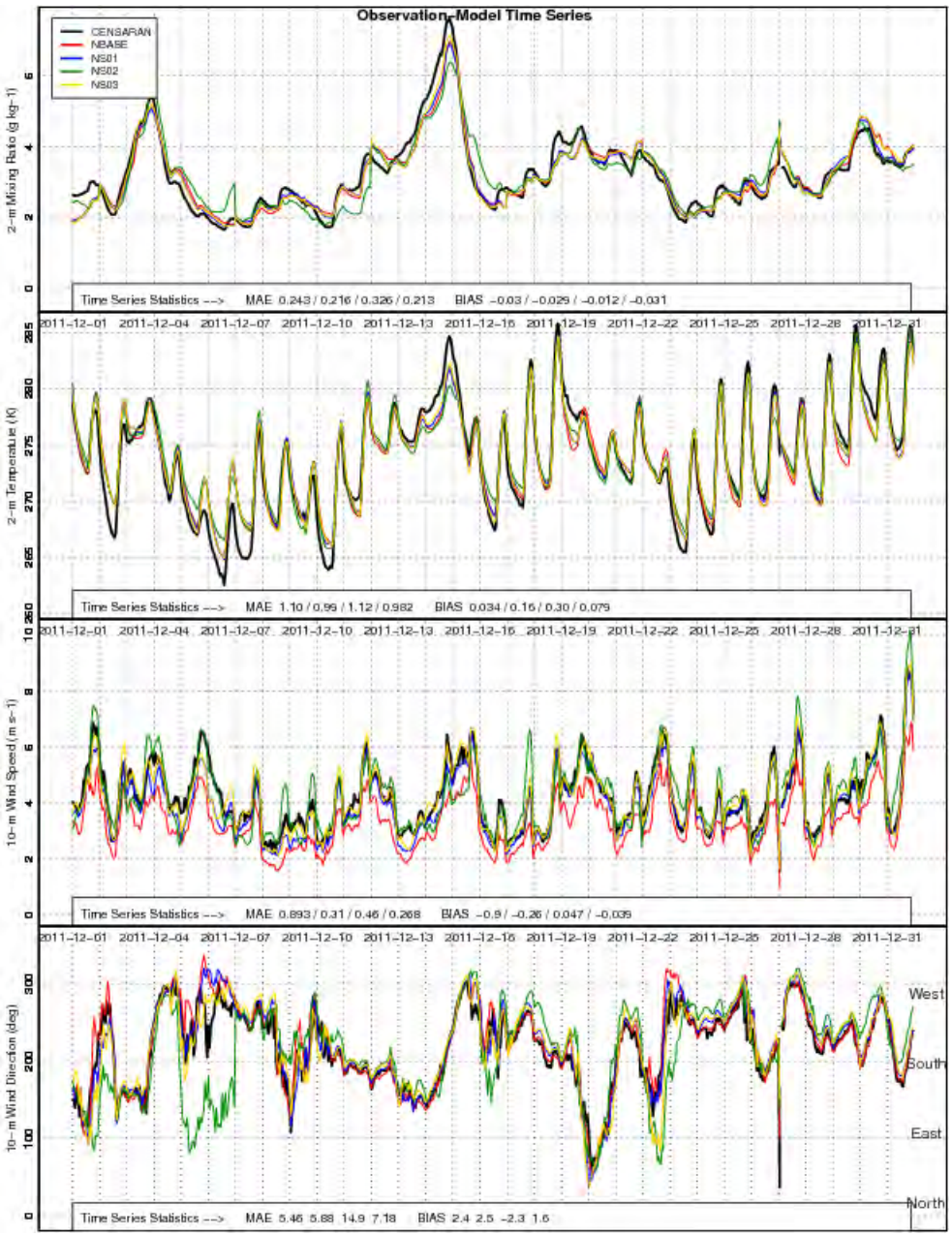

Figure 3-21. Timeseries of observed and modeled 2-m mixing ratio, 2-m temperature, and 10-m wind speed and direction averaged over the CENSARAN region for December 2011.

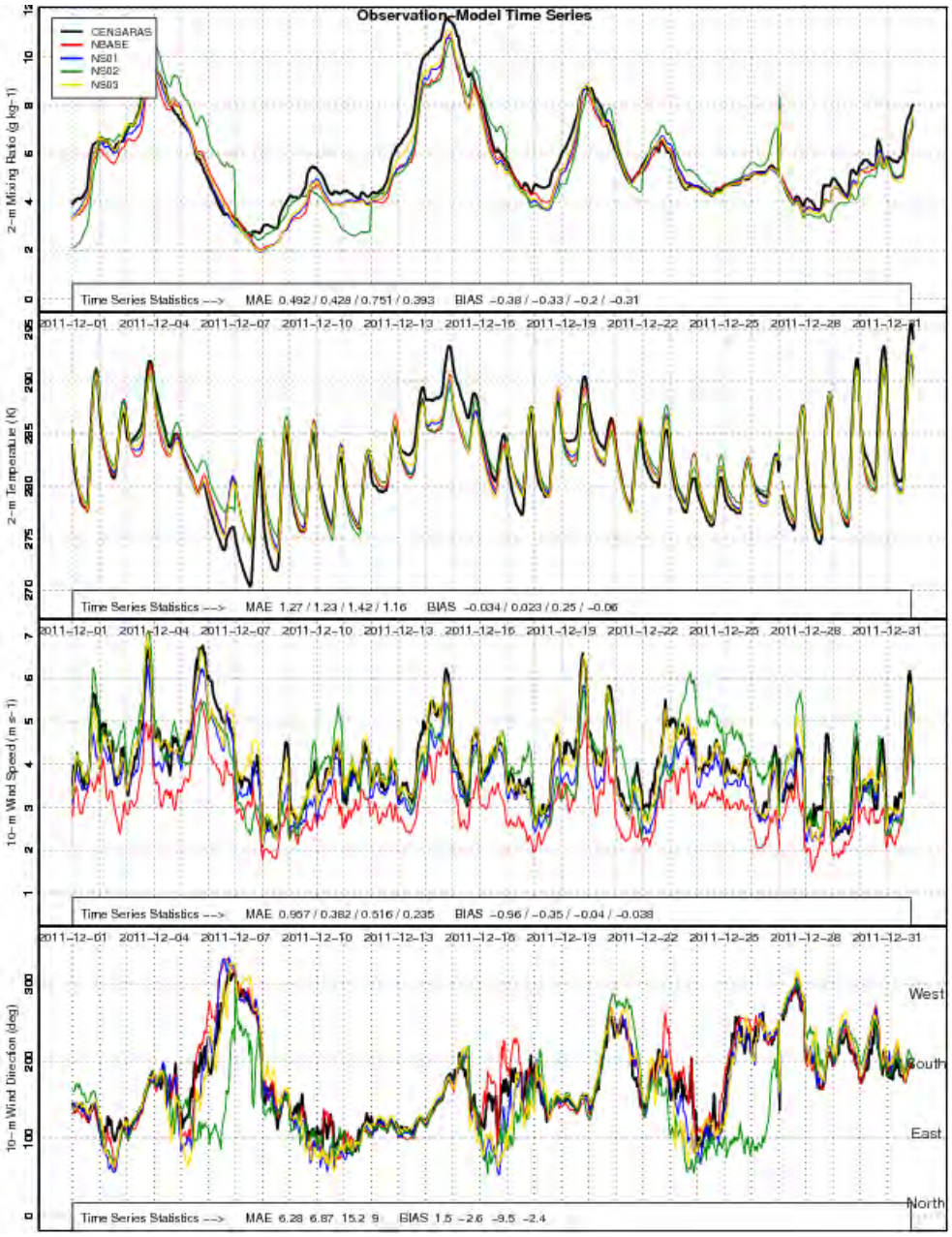

Figure 3-22. Timeseries of observed and modeled 2-m mixing ratio, 2-m temperature, and 10-m wind speed and direction averaged over the CENSARAS region for December 2011.

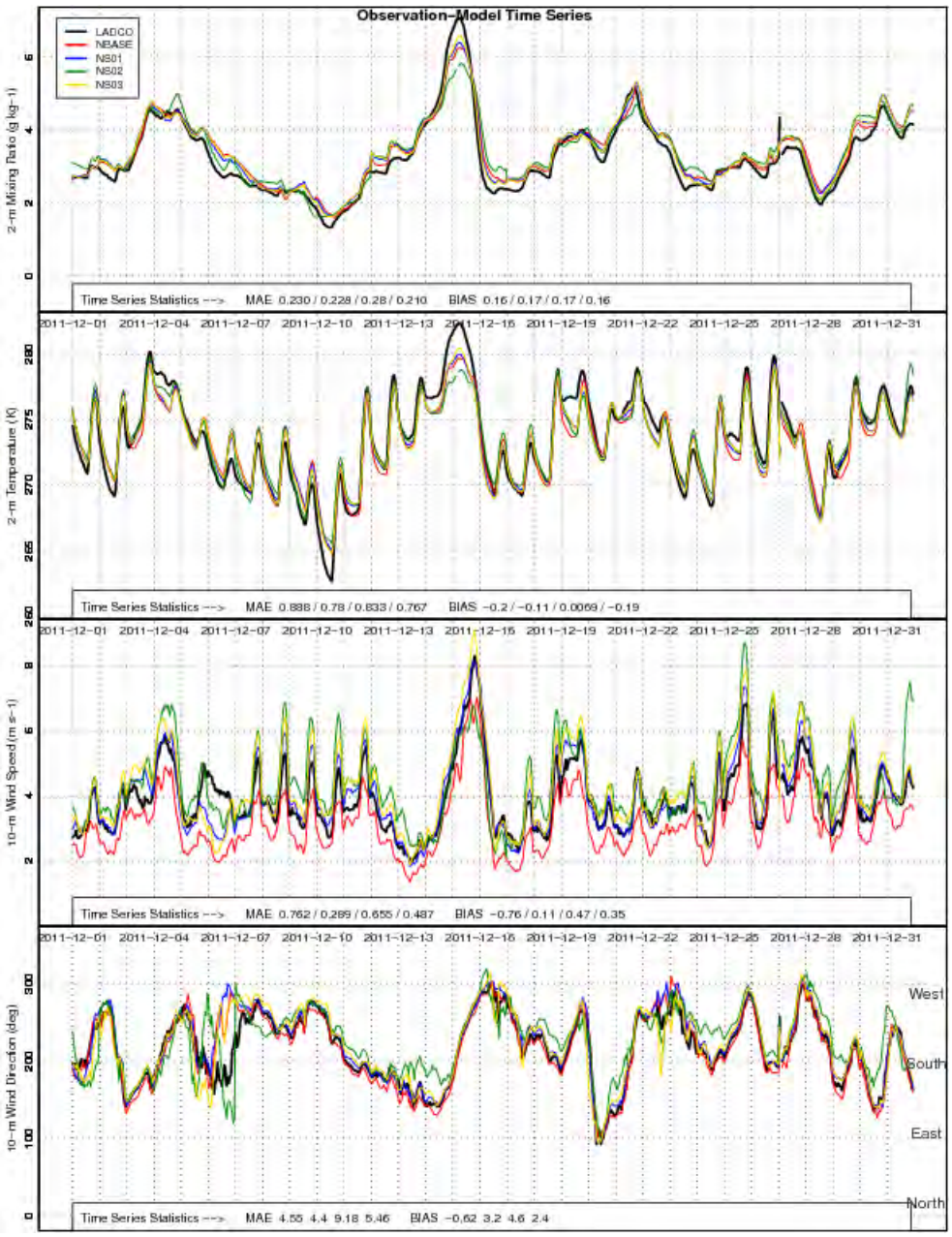

Figure 3-23. Timeseries of observed and modeled 2-m mixing ratio, 2-m temperature, and 10-m wind speed and direction averaged over the LADCO region for December 2011.

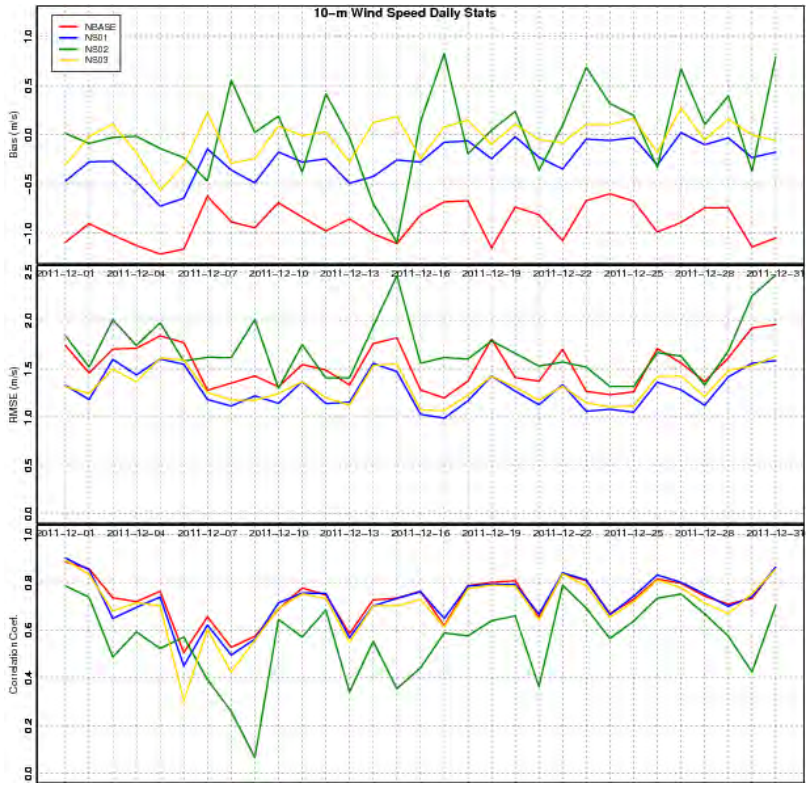

Figure 3-24. Timeseries of daily statistics for 10-m wind speed for the CENSARAN region for December 2011.

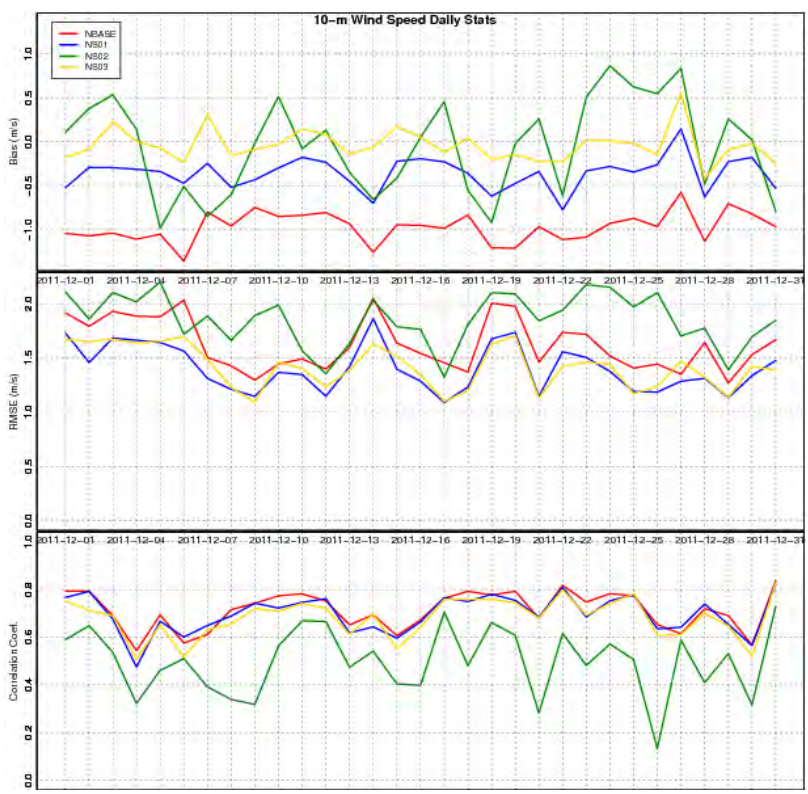

Figure 3-25. Timeseries of daily statistics for 10-m wind speed for the CENSARAS region for December 2011.

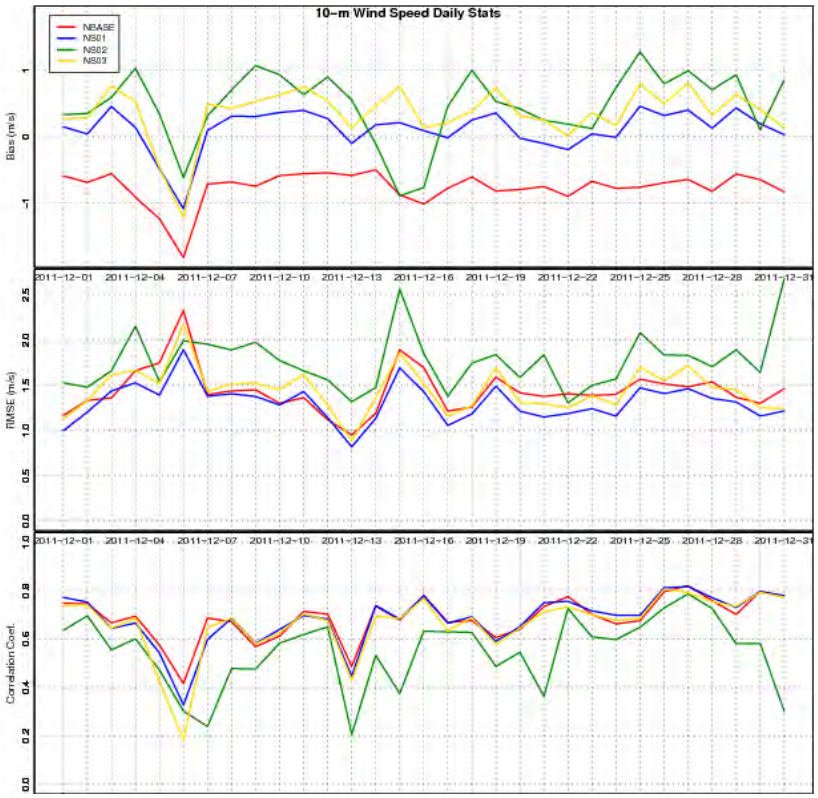

Figure 3-26. Timeseries of daily statistics for 10-m wind speed for the LADCO region for December 2011.

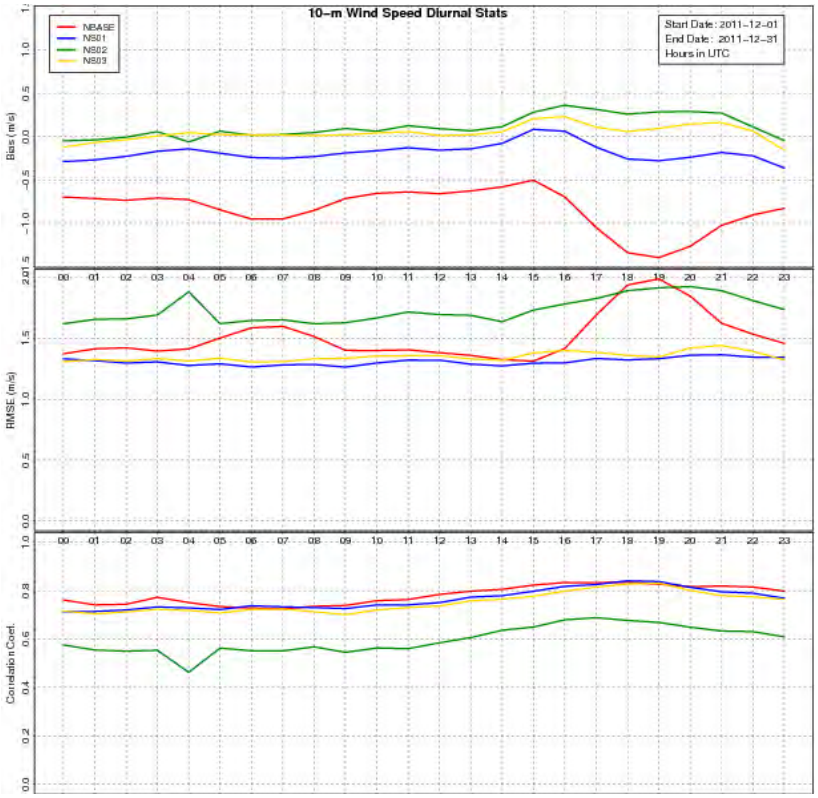

Figure 3-27. Diurnal profiles of hourly statistics for 10-m wind speed for the CENSARAN region for December 2011.

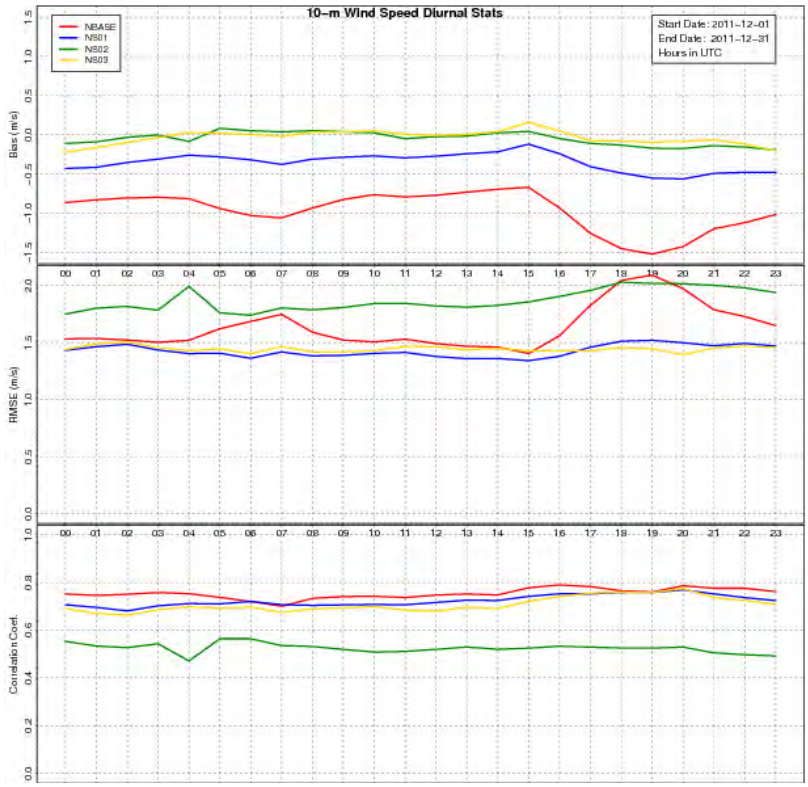

Figure 3-28. Diurnal profiles of hourly statistics for 10-m wind speed for the CENSARAS region for December 2011.

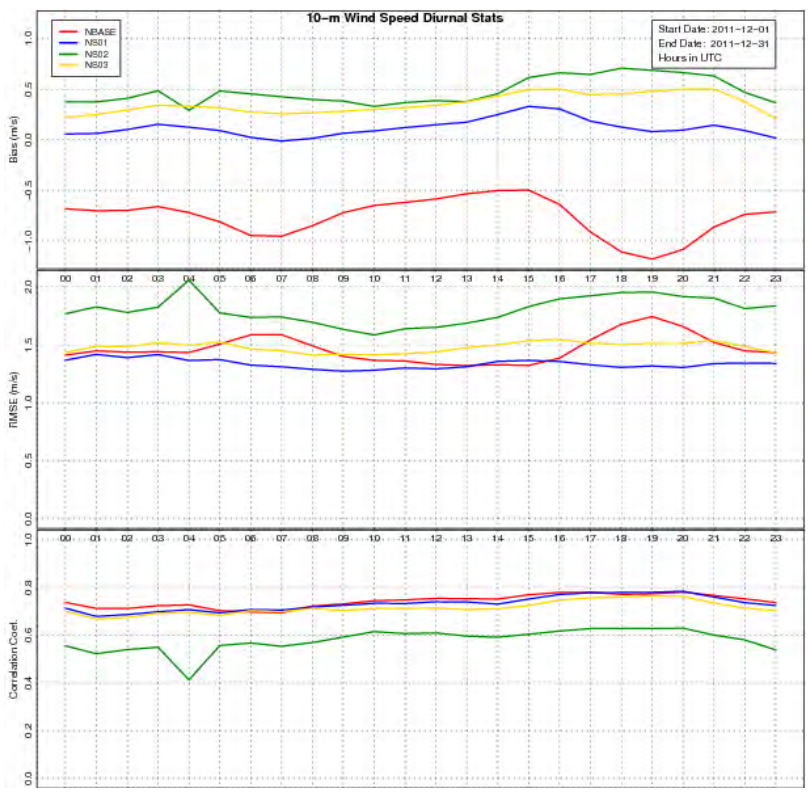

Figure 3-29. Diurnal profiles of hourly statistics for 10-m wind speed for the LADCO region for December 2011.

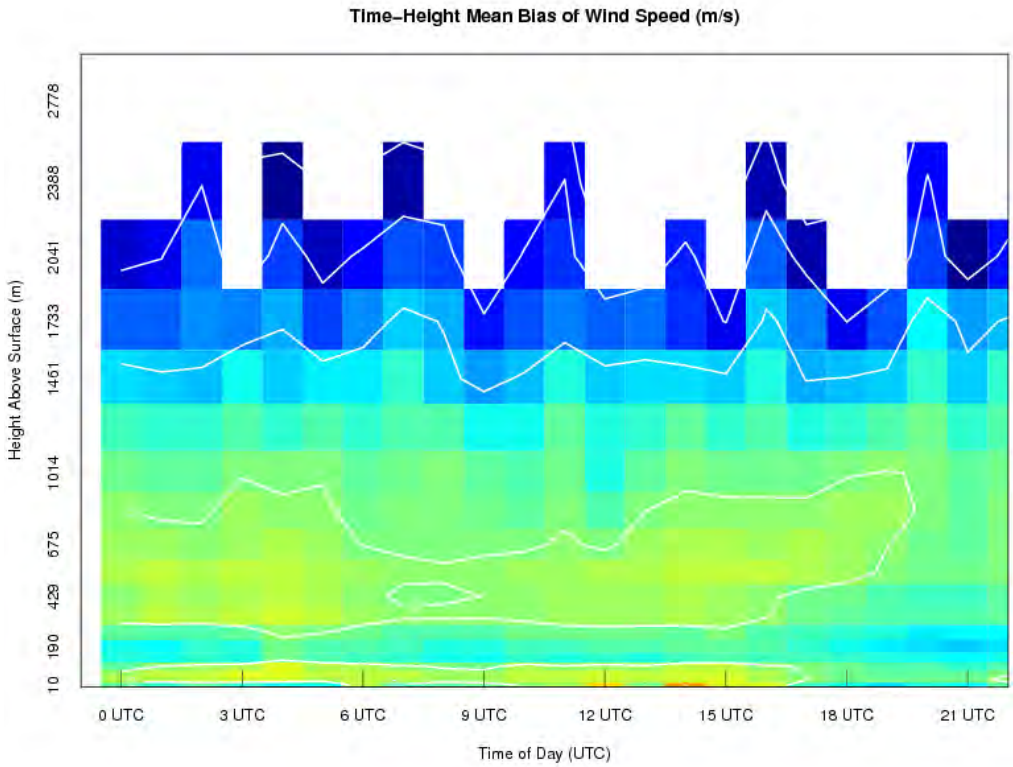

Figure 3-30. Time-height plot of wind speed bias for the ns01 sensitivity for December 2011.

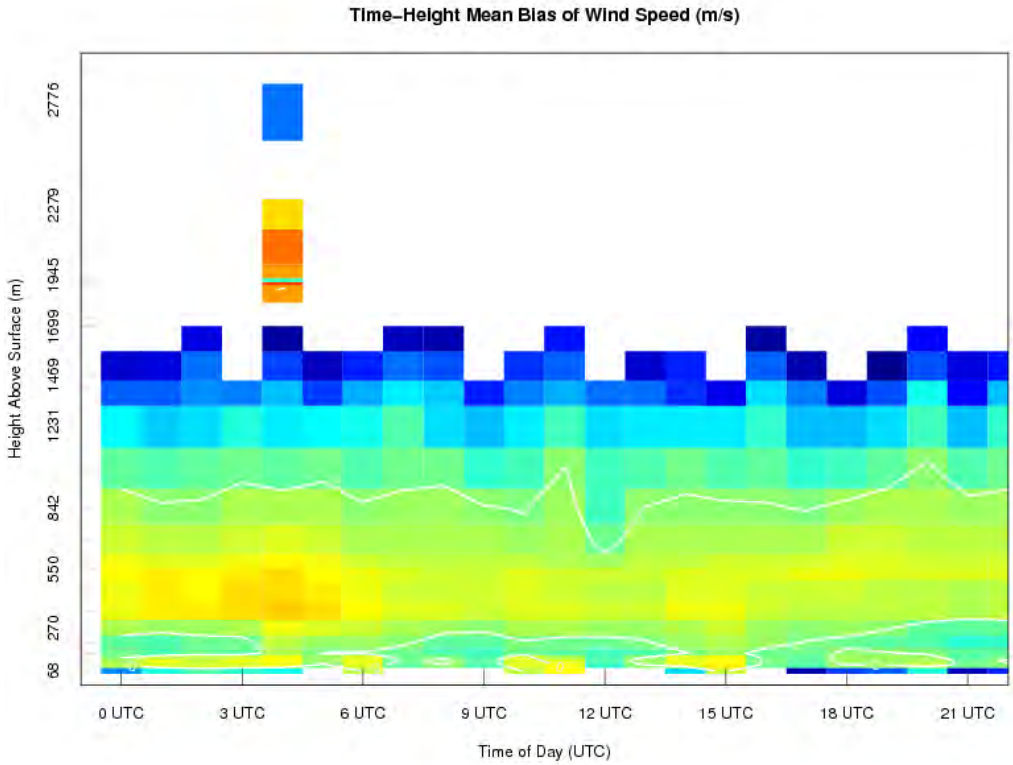

Figure 3-31. Time-height plot of wind speed bias for the ns02 sensitivity for December 2011.

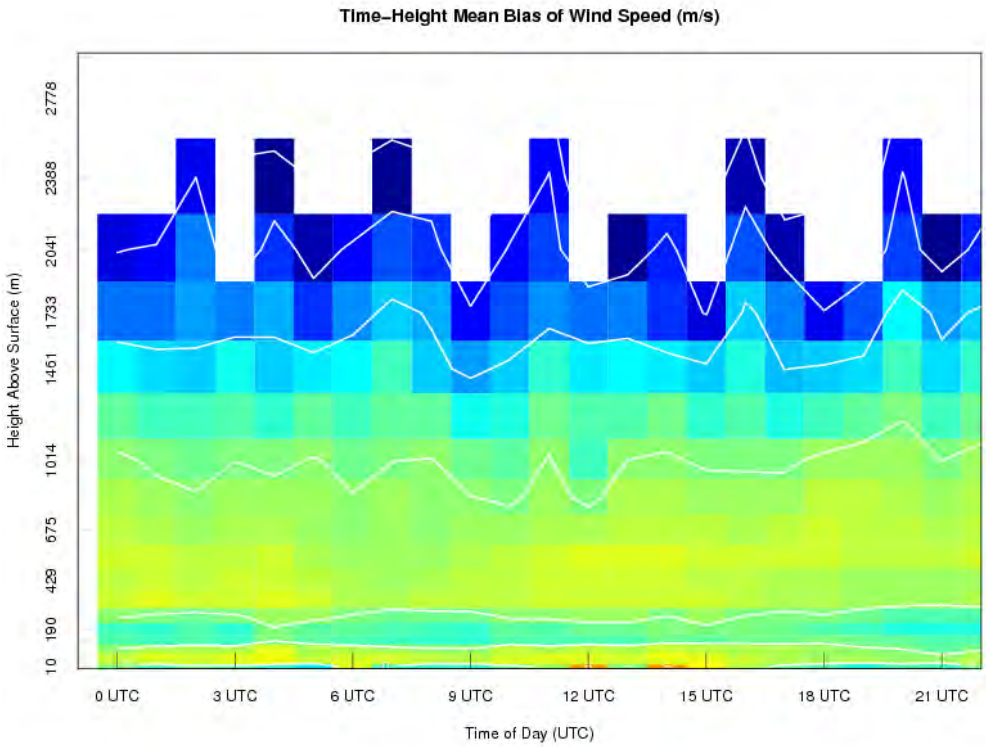

Figure 3-32. Time-height plot of wind speed bias for the ns03 sensitivity for December 2011.

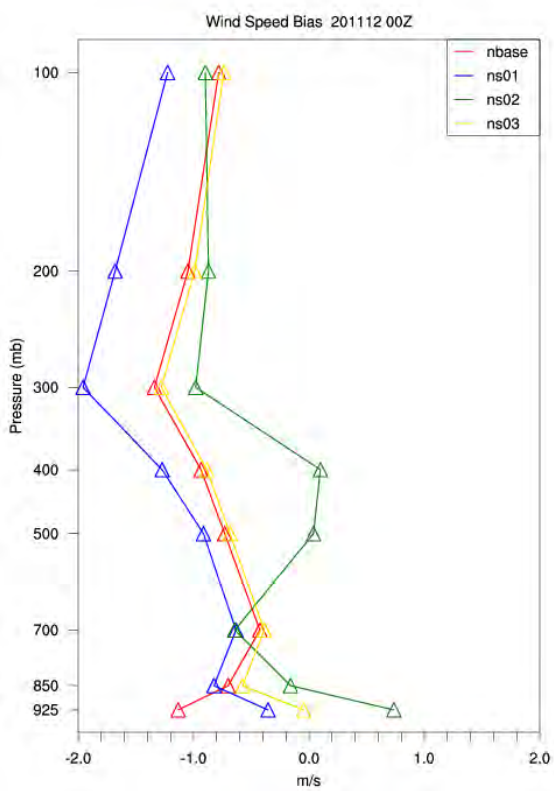

Figure 3-33. Vertical profile of wind speed bias relative to all 00Z radiosonde soundings for December 2011.

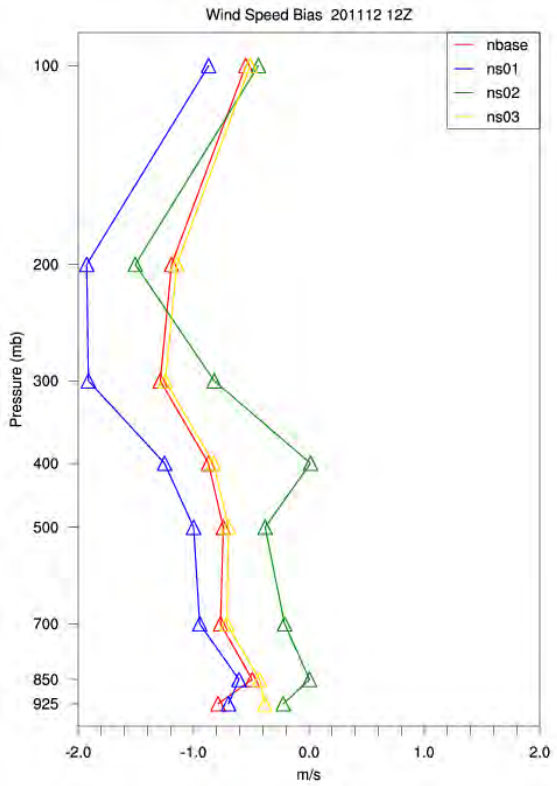

Figure 3-34. Vertical profile of wind speed bias relative to all 12Z radiosonde soundings for December 2011.

4. INPUT DATA ACQUISITION AND PROCESSING

The WRF model requires input of initial and boundary conditions, land-use and topography data, as well as conventional observations for objective analysis. As shown in Figure 2-3, gridded atmospheric fields, typically the output of another model or assimilation system, are processed by WPS. Static terrestrial fields are also read and processed by WPS. When objective analysis is required to generate surface and 3D nudging fields, conventional observations in little_r format are required by obsgrid.

4.1. Initial and Boundary Conditions

The initial and boundary conditions for the WRF model have historically been generated by the Iowa DNR using output from the Eta Data Analysis System (EDAS). EDAS generates pre-forecast surface and 3D analyses at 3-hourly intervals. These fields are output on the NCEP 212 grid, a modeling grid on a Lambert conformal projection with 40 km resolution covering the continental U.S. and most of Canada and Mexico. However, an initial version of the 2011 annual simulation revealed model performance was very poor for the last three months of the year. The EPA 2011 simulation, which used output from the North American Mesoscale Forecast System (NAM) (http://www.emc.ncep.noaa.gov/index.php?branch=NAM) for the initial and boundary conditions, did not exhibit the same poor performance. The EPA WRF configuration is very similar to Iowa DNR's. Also, several blocks during these months were initialized using NAM output due to periods of missing EDAS data. Model performance for these blocks were much better than the overall performance during the final three months. Based on these two factors, it was concluded that EDAS data was no longer acceptable for use to generate initial and boundary conditions for WRF modeling. The NAM analysis and forecast data were obtained for 2011 and processed to generate initial and boundary conditions.

The NAM model is run operationally by the Environmental Modeling Center (EMC) of the National Center for Environmental Prediction (NCEP) and is one of the primary sources of mesoscale modeling guidance for public and private sector meteorologists. The output grid, shown in Figure 4-1, has 12 km spatial resolution and is similar to the EDAS output grid. It is run four times daily at 00Z, 06Z, 12Z, and 18Z. The NAM data assimilation system used to generate the initial analyses utilize the following observational platforms:

- Rawinsonde;
- Pilot balloon (PIBAL);
- Dropwindsondes;
- UHF vertical profilers;
- Surface land;
- Surface marine;
- Aircraft;
- Satellite cloud-drift winds; and
- GPS-integrated water retrievals.

The analyses generated at the initialization time, as well as the 3-hour forecast fields at 03Z, 09Z, 15Z, and 21Z, are used to generate the 3-hourly boundary conditions.

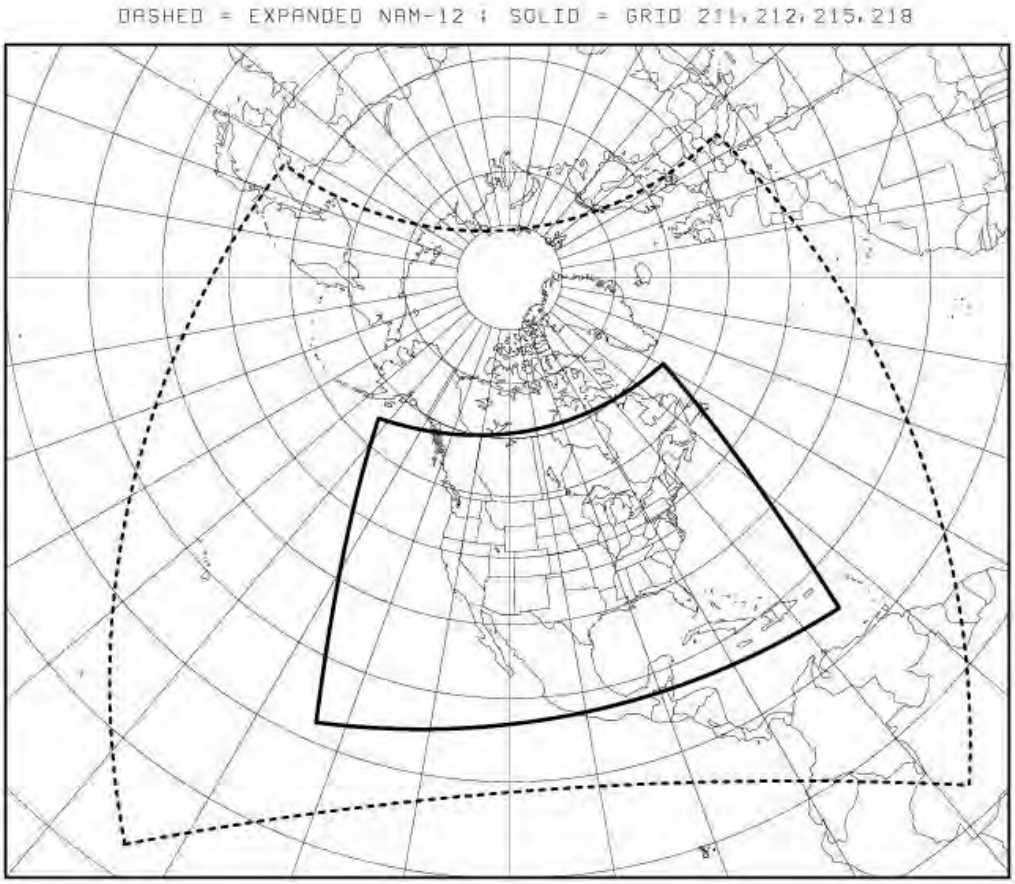

Figure 4-1. The output domain (solid black line) of the NAM analysis and forecast fields used to generate the initial and boundary conditions for the 2011 WRF annual simulation.

4.2. Static Terrestrial Data

WRF requires static terrestrial fields to describe surface and soil characteristics which influence atmospheric processes. These data include albedo, terrain elevation, vegetation/land-use type, land/water mask, soil texture category, soil temperature, and vegetation greenness fraction and are provided with the WRF model code. Beginning with version 3.1, WRF includes a gravity wave drag parameterization option (Shin et al., 2009), and the input data for this scheme must be provided whether the option is enabled or not. There are 16 soil categories, shown in Table 4-1. For the previous WRF simulation land cover data was provided by the 24-category USGS land cover dataset. For this simulation land cover data was obtained from the 2006 National Land Cover Database (NLCD) (Fry et al., 2011). The NLCD is a 16-category, 30-m resolution dataset that represents the most up-to-date representation of land cover across the continental U.S. The WRF-compatible version is available at 30 second resolution and is supplemented with the MODIS 20-category land cover dataset for geographical regions outside the continental U.S.

Table 4-2 shows the NLCD/MODIS land cover categories available for WRF. Since the resolution of the land use data is much higher than the model grid cells a grid-cell average interpolation method is employed to interpolate land-use fractions to the model grid cells. The method takes a simple average of the values of all data points that are nearer to the center of grid cell than to the center of any other.

Table 4-1. Soil texture categories used to initialize the soil layers.

Code	Soil Category
1	Sand
2	Loamy sand
3	Sandy loam
4	Silt loam
5	Silt
6	Loam
7	Sandy clay loam
8	Silty clay loam
9	Clay loam
10	Sandy clay
11	Silty clay
12	Clay loam
13	Organic matter
14	Water
15	Bedrock
16	Other

Table 4-2. Land use categories in the WRF NLCD/MODIS land cover dataset.

MODIS		NLCD	
Number	**Category Name**	**Number**	**Category Name**
1	Evergreen Needleleaf Forest	22	Perennial Ice/Snow
2	Evergreen Broadleaf Forest	23	Developed Open Space
3	Deciduous Needleleaf Forest	24	Developed Low Intensity
4	Deciduous Broadleaf Forest	25	Developed Medium Intensity
5	Mixed Forests	26	Developed High Intensity
6	Closed Shrublands	27	Barren Land (Rock/Sand/Clay)
7	Open Shrublands	28	Deciduous Forest
8	Woody Savannas	29	Evergreen Forest
9	Savannas	30	Mixed Forest
10	Grasslands	32	Shrub/Scrub
11	Permanent Wetlands	33	Grassland/Herbaceous
12	Croplands	37	Pasture/Hay
13	Urban And Built Up	38	Cultivated Crops
14	Cropland/Natural Vegetation Mosaic	39	Woody Wetlands
15	Permanent Snow and Ice	40	Emergent Herbaceous Wetlands
16	Barren or Sparsely Vegetated		
17	IGBP Water		

4.3. 3D Analysis Nudging

The FDDA scheme used in WRF for retrospective simulations requires gridded fields of analyzed atmospheric variables. These fields are generated by the program, obsgrid, which performs an objective analysis using a first-guess field and conventional observations. The first-guess field originates from the

same input data provided for the initial and boundary conditions, as explained in Section 4.1. In fact, these fields are processed through obsgrid before initial and boundary conditions are generated. During this step, the surface and nudging fields are generated. The input fields for 00Z, 06Z, 12Z, and 18Z are not true first-guess fields, as they already constitute an objectively analyzed field produced by the NAM Data Assimilation System. The objective analysis performed by obsgrid is a second pass analysis, and is required in order to generate the surface and 3D nudging fields. This is not an issue though, as the additional objective analysis has been shown to improve the initial analysis fields (Pleim and Gilliam, 2009). Even though surface nudging is no longer implemented the surface nudging fields generated by obsgrid are still required for the soil nudging scheme in the Pleim-Xiu land surface model.

The conventional observations used in the objective analysis are obtained from the Meteorological Assimilation Data Ingest System (MADIS) operated by the Earth System Research Laboratory (ESRL) Global Systems Division (GSD) of NOAA. The datasets from MADIS include observations from most North American networks. Land-based surface observations originate from standard METARs (ASOS, AWOS, non-automated stations), SAOs (Canadian stations), the UrbaNet mesonet, and the Integrated mesonet, comprised of observations from local, state, and federal agencies and private mesonets. Maritime reports are also available, including the Coastal Marine Automated Network (C-MAN), fixed and drifting buoys, and ship reports. Upper air observations include radiosondes, wind profilers, automated aircraft reports and airport profiles, and satellite derived wind fields. These observations are archived in netCDF format and must be converted to little_r format by an external utility in order to be ingested by obsgrid.

5. MODEL CONFIGURATION

5.1. Time Period

The selection of the time period for which the meteorological fields are generated is an important decision for air quality modelers. The length of the modeling study is typically a compromise between the sample size of air quality episodes and computational resources available. The availability of meteorological observations and other air quality related data such as emissions inventories should also be considered. The goal of meteorological modeling for air quality applications is to reproduce meteorology responsible for elevated concentrations of pollutants such as $PM_{2.5}$ and ozone. Since secondary formation of $PM_{2.5}$ occurs throughout the year, with a seasonal dependence on the exact chemical composition of fine particles, a minimum of a full calendar year of meteorology is desirable. Three full years, the length of time required for design value calculation of ambient pollutants, may not be feasible due to computational and time requirements. A simulation length of one year satisfies the aforementioned criteria, without being computationally burdensome.

The calendar year to model should be recent enough to reflect the most up to date development of emissions inventories. The year 2011 was the most recent reporting year for the National Emissions Inventory (NEI). The simulated year of meteorology should also capture conditions conducive to both high ozone and $PM_{2.5}$ concentration episodes. The modeled year should be representative of recent climatology and thus should not contain any climatological anomalies. It has been accepted amongst the air quality modeling community that 2011 fits these criteria and, therefore, was selected as the modeling base year.

The beginning of the WRF simulation was selected to be 15 days prior to the start of the year to allow adequate spin-up time for the photochemical transport model. The simulation should also continue beyond the end of the calendar year long enough to account for time zone differences between U.S. time zones and UTC when the photochemical transport model is run using local standard time.

In order to minimize the growth of errors as the forecast hour increases during the simulation, the WRF simulation was split into many short runs with the model being re-initialized for each new simulation. Each simulation is fundamentally independent of each other, and integrated for 132 hours (5.5 days) with 12 hours of overlap between consecutive runs to allow for spin-up time. The first 12 hours of each run were discarded. The runs were then stitched together to provide a continuous meteorological dataset to the photochemical transport model. Table 5-1 shows the initialization dates for the 77 runs that comprise the annual simulation.

Table 5-1. Initialization dates for the 77 simulation blocks that make up the 2011 WRF annual simulation. All runs are initialized at 12Z.

2010-12-16	2011-03-06	2011-05-25	2011-08-13	2011-11-01
2010-12-21	2011-03-11	2011-05-30	2011-08-18	2011-11-06
2010-12-26	2011-03-16	2011-06-04	2011-08-23	2011-11-11
2010-12-31	2011-03-21	2011-06-09	2011-08-28	2011-11-16
2011-01-05	2011-03-26	2011-06-14	2011-09-02	2011-11-21
2011-01-10	2011-03-31	2011-06-19	2011-09-07	2011-11-26
2011-01-15	2011-04-05	2011-06-24	2011-09-12	2011-12-01
2011-01-20	2011-04-10	2011-06-29	2011-09-17	2011-12-06
2011-01-25	2011-04-15	2011-07-04	2011-09-22	2011-12-11
2011-01-30	2011-04-20	2011-07-09	2011-09-27	2011-12-16
2011-02-04	2011-04-25	2011-07-14	2011-10-02	2011-12-21
2011-02-09	2011-04-30	2011-07-19	2011-10-07	2011-12-26
2011-02-14	2011-05-05	2011-07-24	2011-10-12	2011-12-31
2011-02-19	2011-05-10	2011-07-29	2011-10-17	
2011-02-24	2011-05-15	2011-08-03	2011-10-22	
2011-03-01	2011-05-20	2011-08-08	2011-10-27	

5.2. Modeling Domain

5.2.1. Horizontal Grid

The computational domain for this simulation consists of a coarse and nested grid (Figure 5-1) with horizontal resolutions of 36 and 12km, respectively. The domains reside on a Lambert conic conformal projection with specifications used in previous modeling projects, with true latitudes of 33 and 45° N. The coarse grid is centered at 40° N and 97° W, and consists of an array of 165 staggered grid points (164 grid cells) in the west-east direction and 129 staggered grid points (128 grid cells) in the south-north direction. As indicated previously, the grid spacing is 36 km in both directions. This domain was initially designed to maximize the usage of the Eta model 212 analysis domain. A nested domain was implemented to resolve finer scale meteorological features. The nested domain was expanded from the previous WRF simulation to suit a larger photochemical modeling grid planned by LADCO, and is a 286 by 268 array of staggered grid points (285 by 267 grid cells) with a grid spacing of 12 km. This domain begins at grid coordinate (55, 17) of the course domain. A summary of the horizontal structure of the modeling domain is given in Table 5-2. The namelist settings used by WPS to create the model domain are provided in Appendix A.

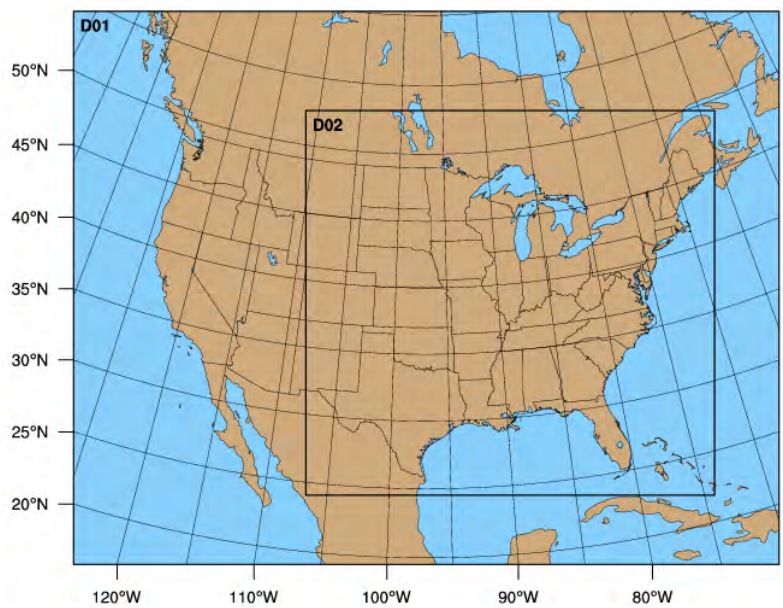

Figure 5-1. Coarse (36 km) and fine (12 km) grids utilized in the Iowa DNR 2011 WRF simulation.

Table 5-2. Grid parameters for the course and nested WRF domains.

Domains	Course (1)	Nested (2)
Resolution (km)	36	12
Starting Location (i,j)	1,1	55,17
nx (E-W)	165	286
ny (N-S)	129	268
SW Coordinate (km)	-2952, -2304	-1008, -1728
NE Coordinate (km)	2952, 2304	2412, 1476

5.2.2. Vertical Levels

The vertical grid structure consists of 35 full sigma levels (34 layers) beginning at the surface and extending to the model top (50 millibars). Figure 5-2 shows the thickness (in sigma coordinates) of each layer increases with height until the 26th model layer, then decreases until the top of the model. The purpose of this design was to provide increased resolution near atmospheric layer interfaces. The planetary boundary layer near the surface is the location of many important atmospheric processes, and thus warrants increased resolution. Near the top of the model the tropopause is another layer interface where increased resolution was desired. The second full sigma level was placed at approximately 20 meters so the midpoint of the first layer is located at 10 meters and corresponds to the standard National Weather Service (NWS) anemometer height. The top of the model is fixed at 50 millibars. Table 5-3 summarizes the vertical structure of the modeling domain.

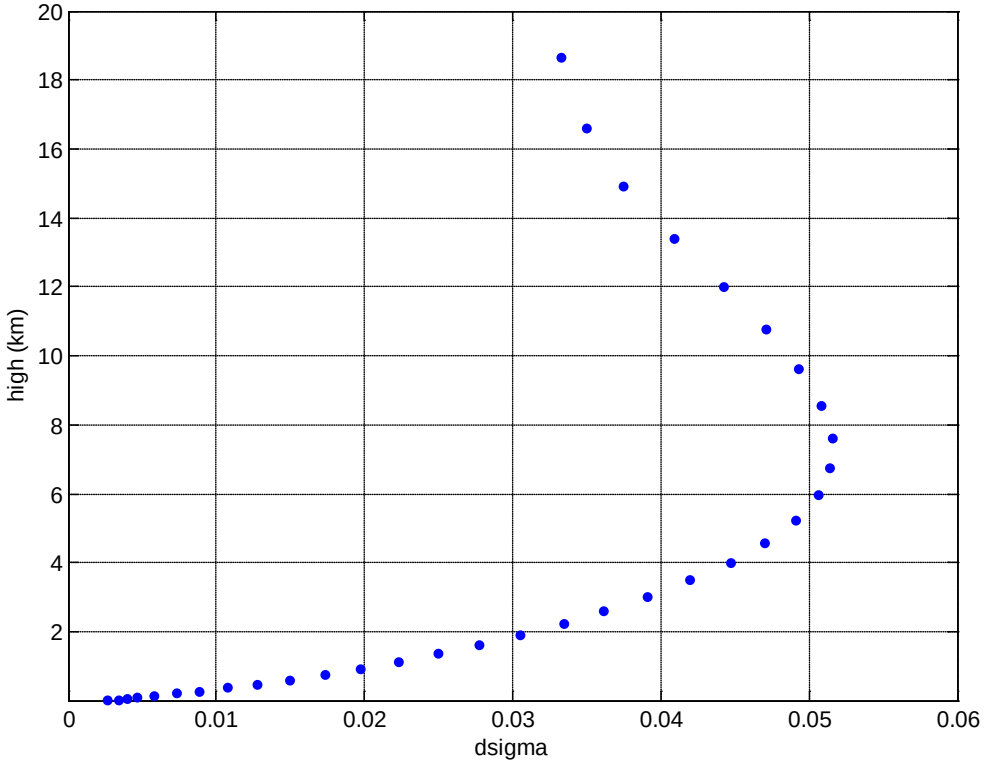

Figure 5-2. The vertical structure of the 2011 WRF modeling domain.

Table 5-3. Detailed statistics of the vertical structure of the 2011 WRF modeling domain.

Level	Sigma	Height (m)	Pressure (mb)	Depth (m)
35	0.0000	18663	50	2034
34	0.0332	16629	82	1715
33	0.0682	14914	115	1515
32	0.1056	13399	150	1375
31	0.1465	12024	189	1255
30	0.1907	10769	231	1145
29	0.2378	9624	276	1045
28	0.2871	8579	323	955
27	0.3379	7624	371	870
26	0.3895	6754	420	790
25	0.4409	5964	469	715
24	0.4915	5249	517	645
23	0.5406	4604	564	580
22	0.5876	4024	608	520
21	0.6323	3504	651	465
20	0.6742	3039	690	415
19	0.7133	2624	728	370
18	0.7494	2254	762	330
17	0.7828	1924	794	293
16	0.8133	1631	823	259
15	0.8410	1372	849	228
14	0.8659	1144	873	200
13	0.8882	944	894	174
12	0.9079	770	913	150
11	0.9252	620	929	128
10	0.9401	492	943	108
9	0.9528	384	955	90
8	0.9635	294	965	74
7	0.9723	220	974	60
6	0.9796	160	981	48
5	0.9854	112	986	38
4	0.9900	74	991	30
3	0.9940	44	994	24
2	0.9974	20	998	20
1	1.0000	0	1000	0

5.3. Physics Parameterizations

Table 5-4 lists the physics parameterizations selected for the 2011 WRF annual simulation. They were chosen based upon a sensitivity study conducted in support of the Iowa DNR 2007 annual simulation. The Asymmetric Convective Model version 2 was selected as the planetary boundary layer (PBL) scheme, which includes the nonlocal scheme of the original ACM combined with an eddy diffusion scheme (Pleim, 2007). Thus, the ACM2 is able to represent both the supergrid- and subgrid-scale components of turbulent vertical transport in the convective boundary layer (Pleim, 2007). The top of the PBL is diagnosed from the critical bulk Richardson number. The PBL scheme is responsible for

representing vertical sub-grid fluxes of heat, momentum, and moisture in the whole atmospheric column, but primarily in a shallow layer near the Earth's surface.

Table 5-4. Physics options selected for the 2011 WRF annual simulation.

Physics Scheme	Option Selected
Planetary Boundary Layer	Asymmetric Convective Model 2
Surface Layer	Pleim-Xiu
Land Surface Model	Pleim-Xiu w/ IPXWRF
Microphysics	Morrison et al.
Radiation (Shortwave)	Rapid Radiative Transfer Model for GCMs
Radiation (Longwave)	Rapid Radiative Transfer Model for GCMs
Cumulus	Kain-Fritsch

The land-surface parameterization uses atmospheric information from other parameterizations along with internal information on the land's state variables and land-surface properties to provide heat and moisture fluxes over land and sea-ice points. These fluxes provide a lower boundary condition for the vertical transport calculated by the PBL scheme. The Pleim-Xiu (PX) land surface model (LSM) (Xiu and Pleim, 2001) was chosen as the land surface parameterization due to its compatibility with the ACM2 PBL scheme. It is a two layer force-restore soil temperature and moisture model. The two layers include a 1 cm surface layer and 1 m root zone layer. The PXLM features three pathways for moisture fluxes: evapotranspiration, soil evaporation, and evaporation from wet canopies. Evapotranspiration is controlled by bulk stomatal and aerodynamics resistance that is dependent on root zone soil moisture, photosynthetically active radiation, air temperature, and the relative humidity at the leaf surface (Xiu and Pleim, 2001). It requires snow cover data to be input from another numerical model or analysis.

The Intermediate processor for Pleim-Xiu for WRF (IPXWRF) was used for this simulation. This utility served two purposes. First, it replaced the initial deep soil temperature field at the start of the spin-up period (2010 December 16) with a 5-day average 2-m temperature field from the NAM input data to initialize the first WRF run. In accordance, deep soil moisture was set based on soil moisture availability and soil type. For all subsequent runs, IPXWRF was used to carry over soil temperature and moisture fields from both layers to the next run. This technique was developed and is implemented by the EPA and the sensitivity study in Chapter 3 showed using IPXWRF improves 2-m temperature, mainly by correcting the underprediction at night.

The surface layer scheme calculates friction velocities and exchange coefficients required for the calculation of surface heat and moisture fluxes by the land-surface models and surface stress in the planetary boundary layer scheme. The Pleim-Xiu surface layer scheme (Pleim, 2006) was chosen as this scheme was developed as part of the PX LSM. This parameterization is a simple scheme for analytical estimation of the surface-layer similarity functions from state variables. It determines vertical eddy diffusivity based on boundary layer scaling similarity theory. This eddy diffusion component is critical for realistic gradients in the surface layer. It is different from other surface layer schemes in that it includes parameterizations of a viscous sub-layer in the form of a quasi-laminar boundary layer resistance. This accounts for differences in the diffusivity of heat, water vapor, and trace chemical species. For very stable surface layers, it uses a reduced slope to avoid decoupling from the surface (Pleim, 2006).

The microphysics scheme includes explicitly resolved water vapor, cloud, and precipitation processes and their associated heat and moisture tendencies. The Morrison Double-Moment parameterization

(Morrison et al., 2009) was selected. This scheme generates both mixing ratios and number concentration of cloud ice, rain, snow, and graupel/hail and mixing ratios of cloud droplets and water vapor. The simulation of two moments allows for a more robust treatment of the particle size distribution.

The cumulus parameterization is responsible for the sub-grid effect of convective and/or shallow clouds. The schemes are designed to estimate vertical fluxes due to unresolved updrafts and downdrafts and compensating motion outside the clouds. The modified version of the Kain-Fritsch scheme was selected. This scheme is based on Kain and Fritsch (1990) and Kain and Fritsch (1993), with modifications made based on testing within the Eta model. The scheme uses a simple cloud model with moist updrafts and downdrafts and includes the effects of detrainment, entrainment, and relatively simple microphysics. The scheme includes a minimum entrainment rate imposed to suppress widespread convection in marginally unstable, yet relatively dry environments. The entrainment rate is allowed to vary as a function of low-level convergence. The convective available potential energy (CAPE) removal time scale is used for closure (Kain and Fritsch, 1993). A moisture-advection trigger option based on Ma and Tan (2009) was enabled.

The radiation parameterization is responsible for simulating the interaction between shortwave and longwave radiation with atmospheric gases and particles and the Earth's surface. For shortwave radiation, these processes include absorption, reflection, and scattering in the atmosphere and at surfaces and heating at the surface due to downwelling radiation. For longwave radiation, processes include infrared and thermal radiation absorbed and emitted by gases and surfaces and heating due to radiative flux divergence and downwelling radiation at the surface. The Rapid Radiative Transfer Model for GCMs (RRTMG) (Iacono et al., 2008) was chosen to estimate both shortwave and longwave processes. It is a sophisticated radiative transfer model that utilizes a correlated-k approach to calculate fluxes and heating rates efficiently and accurately. More information on the key features of RRTMG along with the differences from the original RRTM is available at http://rtweb.aer.com/rrtm_frame.html.

5.4. Dynamics Options

The WRF model was run in non-hydrostatic mode. The simple diffusion option was used for horizontal diffusion. The horizontal eddy viscosity was calculated from the 2D deformation field. The vertical eddy viscosity was assumed to be estimated by the PBL scheme. An implicit gravity wave damping layer was selected to control reflection from the upper boundary. Vertical velocity damping was enabled to prevent the model from becoming unstable with locally large vertical velocities. An explicit, 6th-order diffusion scheme (Kneivel et al., 2007) was enabled that preserves the high effective resolution of WRF and uses a flux limiter to ensure monotonicity. The scheme is effective in removing the high frequency numerical noise that is worst when grid-relative wind speeds are low and stratification is nearly neutral or unstable (Kneivel et al., 2007). Monotonic advection was enabled for moisture and scalars.

A model time step of 90 seconds was used for the annual simulation. A larger time step of 120 seconds was used in the 2007 simulation, however for the version of WRF used for this study this time step resulted in model crashes. The 90 second time step applies to integration on the course (36 km) domain. For the nested (12 km) domain, the time step is divided by the grid ratio of 3. The planetary boundary layer, surface layer, land-surface, and microphysics parameterizations are called every integration time step. The radiation scheme is called every 30 minutes on the course domain and every 15 minutes on the nest. The cumulus parameterization is called every 5 minutes on both domains.

The course and nested domains were run in a concurrent 1-way nesting mode. Both domains were simulated during the same WRF run. The course grid output provides lateral boundary conditions to the nested grid. The course grid integrates one time step, and then the nested grid integrates up to the same time. Feedback of the nested grid output to the course grid cells containing the nested domain was disabled. In this manner the exchange of information during the simulation was only in one direction.

Specified lateral boundary conditions are used for the course domain's boundary. A relaxation zone five grid cells in width was used to nudge or relax the model towards the boundary values.

6. PERFORMANCE EVALUATION

6.1. Methodology

A comprehensive performance evaluation was conducted to assess the adequacy and suitability of the 2011 WRF dataset for use in regional air quality modeling. This study implements the operational evaluation component of the evaluation philosophy described by Tesche (1994). Statistical performance metrics were applied to modeled 3D fields of temperature, wind speed and direction, and humidity by pairing these data with observations in space and time. Performance statistics were calculated separately for near-surface and upper air fields.

Near-surface variables 2 meter temperature, 10 meter wind speed and direction, and 2 meter mixing ratio were paired hourly with observations via bilinear interpolation to observation locations. Model-observed pairs were grouped by geographical region and select time periods such as by hour, day, and month to produce an adequate sample needed to calculate error statistics. The conventional statistical metrics, shown in Table 6-1, were used for the evaluation. Bias error, hereinafter bias, is the degree of correspondence between the mean prediction and the mean observation. An unbiased set of model predictions will have a bias value of zero. Model predictions with a bias greater than zero indicate a general tendency for over-prediction of a variable, while conversely a bias less than zero implies a tendency for under-prediction. Root mean square error (RMSE) is a useful overall measure of model performance. It is defined as the square root of the mean of the squared differences between modeled and observed values. Values of RMSE range from zero, for a perfect model simulation to large positive values, as the accuracy of the simulation degrades. Since large errors are weighted heavily (due to squaring), large errors in a small sub-region may produce a large RMSE even though the majority of errors may be small and quite acceptable elsewhere. RMSE is calculated in tandem with bias because desirable bias values near zero may be the result of the cancellation of positive and negative differences between modeled and observed values.

Table 6-1. Performance metrics calculated to evaluate the 2011 WRF run.

Metric	Equation
Bias	$B = \frac{1}{IJ}\sum_{j=1}^{J}\sum_{i=1}^{I}\left(P_j^i - O_j^i\right)$
Mean Absolute Error (MAE)	$MAE = \frac{1}{IJ}\sum_{j=1}^{J}\sum_{i=1}^{I}\left\lvert P_j^i - O_j^i\right\rvert$
Root Mean Square Error (RMSE)	$RMSE = \sqrt{\frac{1}{IJ}\sum_{j=1}^{J}\sum_{i=1}^{I}\left(P_j^i - O_j^i\right)^2}$
Correlation Coefficient	$r = \frac{\sum_{i=1}^{n}\left(\left(O_i - \overline{O}\right)\left(P_i - \overline{P}\right)\right)}{\sqrt{\sum_{i=1}^{n}\left(O_i - \overline{O}\right)^2\sum_{i=1}^{n}\left(P_i - \overline{P}\right)^2}}$

In order to assess the performance of the simulation, the daily statistics are compared to a set of benchmark values (Emery et al., 2001). The purpose of these benchmarks is not to determine whether the simulation is either sufficient or unusable, but rather to put the errors in the context of the performance of past simulations. The benchmark values are shown in Table 6-2.

Table 6-2. Benchmark values for the performance metrics used to evaluate the WRF simulation.

Variable	Statistic	Benchmark
Wind Speed	Bias	≤ ± 0.5 m/s
	RMSE	≤ 2 m/s
Wind Direction	Bias	≤ ± 10 deg
	MAE	≤ 30 deg
Temperature	Bias	≤± 0.5 °C
	MAE	≤ 2 °C
Mixing Ratio	Bias	≤± 1 g/kg
	MAE	≤ 2 g/kg

When evaluating modeled wind speeds the presence of observed calm wind speeds must be addressed. The NWS ASOS network historically used cup and vane anemometers to measure wind speed and direction. The instruments possess a minimum measurement threshold, due to the mechanical friction of the instrument, of 2 knots (NOAA, 1998). Due to truncation of the reported decimal places all wind speeds below 3 knots are reported as calm, or 0 knots. Therefore, light winds may be reported as zero. Meteorological models never produce a truly zero wind speed. Thus, this measurement artifact introduces an artificial positive bias in the wind speed evaluation. This bias becomes most pronounced in areas such as the southeastern U.S. at night and during the summer when the synoptic scale pattern over the region is dominated by high pressure and calm winds are routinely produced (Olerud and Sim, 2004).

From 2002 to 2010 the NWS ASOS anemometers were upgraded to sonic anemometers to eliminate the measurement issues related to instrument icing. These instruments possess measurement thresholds approaching 0 knots. However, this threshold is still applied during post-processing of these data and therefore, the calm wind artifact still exists in 2011 ASOS data.

The simplest approaches to this issue are to exclude all model-observed pairs in which the observed winds are 0 knots or to include all wind speeds. The drawback to the first approach is it may greatly reduce the sample size of model-observed pairs used in the calculation of the performance metrics when numerous calm winds are measured. The second approach is to treat calms winds the same as any measurement. There is also no way to distinguish between winds less than 3 knots that are reported as calm (0 knots) and winds that are actually near 0 knots. The drawback to the second approach, obviously, is the introduction of the artificial positive bias. Olerud and Sims (2004) approached this problem by setting all calm wind speeds equal to 1.5 knots, halfway between 0 knots and the measurement threshold. For this study, the first approach of ignoring model-observation pairs with a measured wind speed of 0 knots was used.

Although performance metrics are valuable, it's still important to consider that observations also contain uncertainties (although they're not quantified in this study). Other issues in evaluation model data also exist. Model fields at the mass grid coordinates represent grid cell averages, not values at finite locations. Model values output at the top of the hour must be compared to observations generally collected eight minutes prior to the top of the hour. Observed values are frequently truncated to the nearest whole number, while model values maintain a large amount of precision. At least some component of model error will be attributable to these factors.

Figure 6-1 shows the geographical regions used to calculate performance statistics. The multi-jurisdictional organization (MJO) boundaries were used to group modeled-observed pairs. Each region has associated statistics by hour, day, and month. The LADCO and CENSARA MJOs were the only two regions for which statistics were generated. Statistical evaluation of the WRF output for other regions of the country is beyond the scope of this document. Due to spatial extent of the CENSARA MJO, it was split into two performance regions.

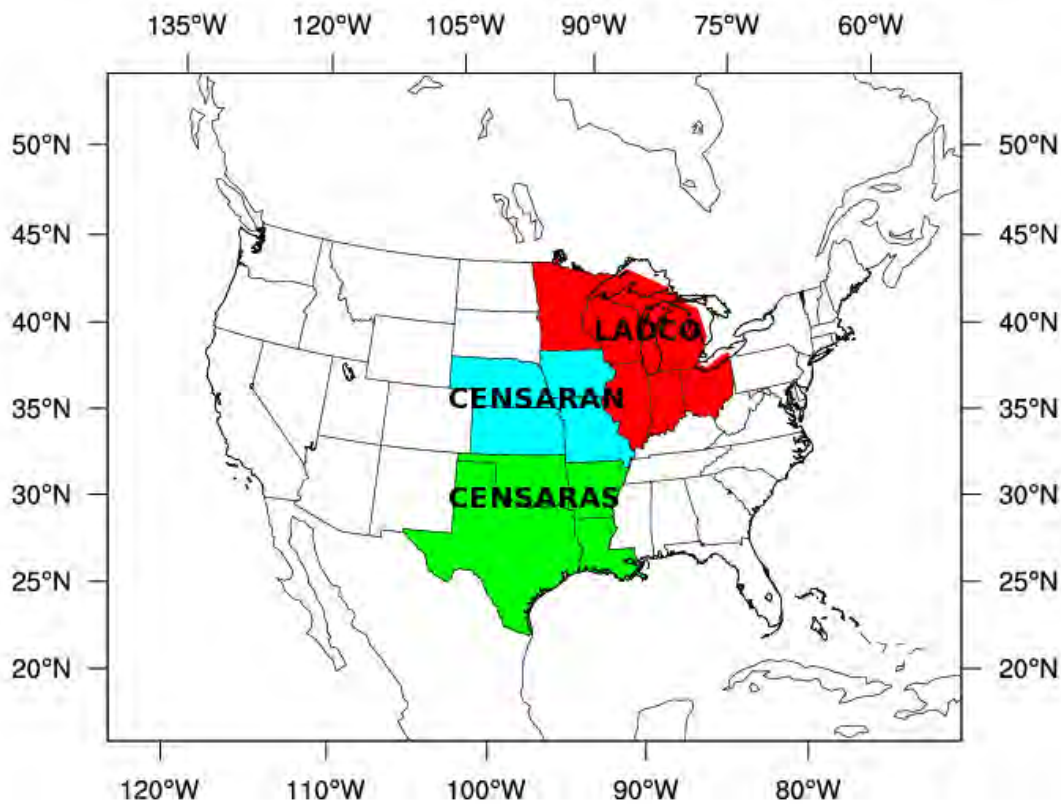

Figure 6-1. Geographical regions used to group the model-observed data pairs for evaluating the 2011 WRF simulation.

Performance statistics were also calculated for upper air fields of temperature, wind speed, and moisture at the mandatory reporting levels for the radiosonde measurement platform: 925, 850, 700, 500, 400, 300, 200, and 100 mb. Similar to the procedure for calculating near-surface statistics, model data were interpolated to observation locations. Model fields were paired with observations at 00Z and 12Z, with statistics calculated separately for each time for each month. Model output for both domains was evaluated against all radiosondes within a rectangular area (shown in Figure 6-2) over the Midwest referred to as UA_EASTUS. While no benchmarks exist for upper air evaluations, it is still insightful to quantify the uncertainty of model output above the surface.

Two software packages were used to calculate near-surface and upper air statistics. Version 3.0.1 of the Model Evaluation Tools (MET) (http://www.dtcenter.org/met/users/) was used to calculate performance statistics for both near-surface and upper air fields. The software uses the PrepBUFR observational dataset (http://dss.ucar.edu/datasets/ds337.0/) to evaluate the modeled output. Version 1.1 of the Atmospheric Model Evaluation Tool (AMET) (http://www.cmascenter.org) was also used to

calculate and visualize near-surface performance statistics. This tool uses observations archived by the Meteorological Assimilation Data Ingest System (MADIS) (http://madis.noaa.gov).

A qualitative assessment of modeled precipitation fields was also conducted by comparing modeled accumulated precipitation with analyzed fields. For each month of the year, accumulated model precipitation were compared against the NCEP Stage IV gridded precipitation analysis (Lin and Mitchell, 2005) to assess the magnitude and spatial extent of model fields.

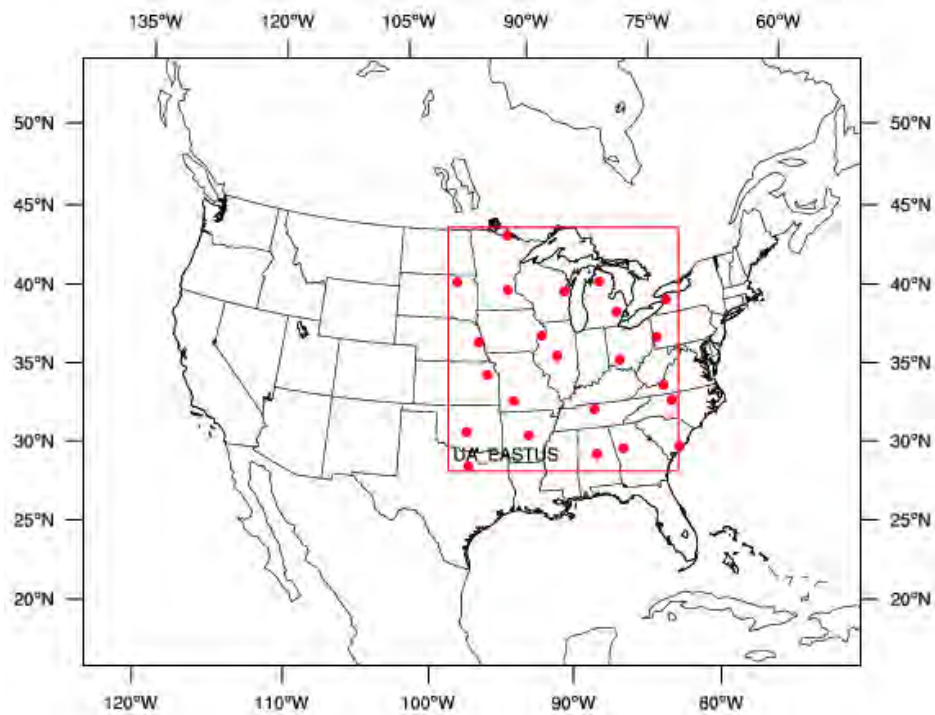

Figure 6-2. The radiosonde observation stations used to evaluate upper air WRF output for both the course and nested domains for the 2011 annual simulation. The bounded area is referred to as the "UA_EASTUS" region.

6.2. Results

Due to the vast number of statistics and plots generated, this document focuses solely on the results of the nested 12 km domain. All plots shown and discussed for the 12 km domain have been generated for the 36 km domain and are available upon request. A brief comparison of select plots for the 36 and 12 km domains showed similar performance characteristics.

6.2.1. Near-Surface Statistics

The plots generated as part of the statistical evaluation of near-surface meteorological variables simulated by WRF are presented in Appendix B. Figures B-1 through B-3 show monthly error statistics for the entire 2011 calendar year for wind speed, temperature, and mixing ratio over the CENSARAN region. Wind speed was underpredicted slightly during the winter and spring, while being slightly overpredicted in the fall. Bias values ranged from -0.2 to 0.2 m/s. Root mean square error values ranged from 1.3 to 1.8 m/s, with the lowest values occurring in the winter and highest values in the late spring and early summer. Temperature was slightly overpredicted in every month except April, November, and December. Bias values ranged from -0.2 to 0.3 °C. Mean absolute errors ranged from

1.4 to 2.2 °C. Temperature errors were highest in late winter and lowest during the summer. Mixing ratio bias was generally low except during the summer in fall. Mixing ratio was overpredicted in June and August, and underpredicted in autumn. Values ranged from -0.3 to 0.4 g/kg. Mean absolute errors ranged from 0.3 to 1.5 g/kg, with larger values occurring during warmer months. Mixing ratio performance appears to improve in the cooler months but this is likely just an artifact of a colder climate holding less moisture.

Figures B-4 through B-6 show monthly error statistics for the entire 2011 calendar year for wind speed, temperature, and mixing ratio over the CENSARAS region. Wind speed was generally underpredicted throughout the year, except in the fall. Bias values ranged from -0.3 to 0.0 m/s. Root mean square error ranged from 1.5 to 2.1 m/s. Error values were highest during the late spring, but were otherwise consistent across the year. Temperature bias was very near zero in every month except February, September, and October. Values ranged from -0.2 to 0.2 °C. Mean absolute error values ranged from 1.3 to 2.2 °C. The largest errors occurred during the winter, while the lowest occurred in the summer. Mixing ratio bias was near zero, except during winter. Values ranged from -0.3 to 0.0 g/kg. Mean absolute error was lowest during the winter at 0.6 g/kg, and highest during the summer with a maximum of 1.7 g/kg.

Figures B-7 through B-9 show monthly error statistics for the entire 2011 calendar year for wind speed, temperature, and mixing ratio over the LADCO region. Wind speed was overpredicted during the whole year, with the largest bias values in the fall. Values ranged from 0.1 to 0.4 m/s. Root mean square error ranged from 1.3 to 1.7 m/s. The seasonal pattern was similar to those in the other two regions, however not as drastic. Temperature was underpredicted during the spring and late fall/early winter months and over predicted in August and February. Values ranged from -0.5 to 0.2 °C. Mean absolute error was consistent across the year and ranged from 1.3 to 1.7 °C. Mixing ratio was generally overpredicted throughout the year, except during the autumn months. Values ranged from 0.0 to 0.5 g/kg. Mean absolute error ranged from 0.3 to 1.3 g/kg. Again, winter time mixing ratio performance shows an apparent improvement due to colder climatological conditions in the north-central U.S.

Figures B-10 through B-15 show daily error statistics in the form of boxplots for each month of 2011 for wind speed, temperature, and mixing ratio over the CENSARAN region. The boxplots show the median daily statistics, along with the interquartile range (middle 50% of values) and minimum and maximum values for each month. The benchmark values for each statistic are also shown for reference. These plots are useful for showing the percentage of daily statistics in each month which fall within their respective benchmarks. Greater than 75% of daily bias and root mean square error values for wind speed were within their respective benchmarks each month (except for June RMSE). Daily temperature bias values were highly variable in all months except July and August. Many daily values were outside of the temperature bias benchmark. At least 75% of mean absolute error values were within the benchmark for all months except January, February, March, and October. Nearly all bias and mean absolute error values for mixing ratio were within their respective benchmarks.

Figures B-16 through B-21 show daily error statistics in the form of boxplots for each month of 2011 for wind speed, temperature, and mixing ratio over the CENSARAS region. All of daily bias values for wind speed with the exception of a few outliers were within the benchmark. At least 75% of root mean square error values for wind speed were within the benchmark in all months except April and May. Like in the CENSARAN region, daily temperature bias was highly variable in all months except June, July, and August. A large percentage of mean absolute error values met the benchmark in all months except February and November. Nearly all bias and mean absolute error values for mixing ratio were within their respective benchmarks.

Figures B-22 through B-27 show daily error statistics in the form of boxplots for each month of 2011 for wind speed, temperature, and mixing ratio over the LADCO region. Nearly all daily wind speed bias values were within the benchmark in every month except September, October, and November where between 50 and 75% of values met the benchmark. Nearly all daily wind speed root mean square error values were within the benchmark. Daily temperature bias values were not as variable as in the other two regions. Between 50 and 75% of values were within the benchmark during the summer, while slightly less than half were within the benchmark the remaining months. Greater than 75% of daily temperature mean absolute error values were within the benchmark. Nearly all bias and mean absolute error values for mixing ratio were within their respective benchmarks.

Figures B-28 through B-33 show bakergrams of daily error statistics for wind speed, temperature, and mixing ratio for the CENSARAN region during 2011. Unlike the previous boxplots, these plots display the temporal structure (on a sub-monthly basis) of the daily statistics. Daily wind speed bias was near zero or slightly negative in the winter and spring, but slightly positive during the late summer and early fall. Wind speed RMSE was highest during the spring and summer, otherwise consistently below 2.0 m/s during the year. There was no discernable seasonal pattern in temperature bias. Values routinely alternated between periods of large overprediction and large underprediction. Bias was noticeably better in July and August than the remainder of the year. Temperature MAE was high at times in the winter and fall. In the spring and summer values were generally acceptable. A slight positive bias in daily mixing ratio was evident during the summer, while a small portion of days during the fall showed a slight underprediction. Otherwise, mixing ratio was usually unbiased. Mixing ratio MAE was low throughout the year.

Figures B-34 through B-39 show bakergrams of daily error statistics for wind speed, temperature, and mixing ratio for the CENSARAS region during 2011. Daily wind speed bias was generally slightly negative in the winter and spring, but often unbiased the rest of the year. Wind speed RMSE was highest in April and May, with a number of daily values exceeding 2.0 m/s. During the remaining months wind speed RMSE is very satisfactory. Temperature bias was similar to bias in the CENSARAN region. Bias values were acceptable in the summer, otherwise they were large and highly variable. Temperature MAE was frequently large in November and February, but was otherwise generally acceptable. Mixing ratio bias and mean absolute error were generally satisfactory.

Figures B-40 through B-45 show bakergrams of daily error statistics for wind speed, temperature, and mixing ratio for the CENSARAS region during 2011. Daily wind speed bias was generally slightly positive throughout the year. Overpredictions were largest during the fall. Wind speed RMSE was generally satisfactory. Temperature bias patterns were similar to those in the other regions, however, bias was variable during all seasons. Temperature MAE was still generally acceptable. A slight positive bias in daily mixing ratio was evident during the spring and summer, but was otherwise near zero. Mean absolute error values were generally satisfactory.

Figures B-46 through B-57 show hourly timeseries of mean observed and modeled mixing ratio, temperature, wind speed and direction for the CENSARAN region in each month of the year. These plots are useful for showing how well modeled values matched observed values and patterns, especially diurnal variations. Modeled wind speed and direction generally closely followed observations throughout the year. During the winter observed daytime peaks in wind speed were occasionally underpredicted. During spring, summer, and fall observed daytime peaks in wind speed were occasionally overpredicted. Throughout the simulation there were frequent occurrences of temperature over- and under-predictions of the daily minima and maxima (respectively) that persisted for several days. Alternatively, during the spring there were occasional occurrences of both over- and

under-prediction of daytime maximums and underprediction of nighttime minimum temperatures. Modeled temperatures more closely matched observations during the summer and fall. However, there existed many occurrences of overpredicted nighttime temperatures. During the winter, spring, and fall modeled and observed mixing ratio were very similar, however, this result is not particularly informative as the observed values were also small during this time of year. During the summer a stronger diurnal pattern develops in observed mixing ratio. Modeled daytime peaks around 0Z were much too large and pronounced compared to observations.

Figures B-58 through B-69 show hourly timeseries of mean observed and modeled wind speed and direction, temperature, and mixing ratio for the CENSARAS region in each month of the year. Modeled wind speed and direction closely matched observations, however occasionally modeled daytime peaks in wind speed were underpredicted. This occurred most often during the summer. Modeled temperature during the winter and spring showed similar diurnal variations to observations, however there were frequent periods of persistent over- and under-prediction. During the summer and partially in the fall, temperatures more closely followed observations, however most often daytime maximums were underpredicted and nighttime minimums were overpredicted. During the winter and spring mixing ratio closely followed observations, however these values were generally low. During the summer mixing ratio most often agreed with observed values, however there were occasional under-predictions. During the fall modeled mixing ratio agreed very well with observations.

Figures B-70 through B-81 show hourly timeseries of mean observed and modeled wind speed and direction, temperature, and mixing ratio for the LADCO region in each month of the year. Modeled wind speed and direction closely matched observations throughout the year; however daytime maximums in wind speed were frequently overpredicted. During the late summer and fall nighttime minimums were also frequently overpredicted. During the winter the correspondence between modeled and observed temperatures was fair. There were periods of persistent over- and under-predictions. During the spring, and early summer temperatures more closely followed observations, with the notable exception that during the summer there were frequent overpredictions of nighttime minimums. Modeled mixing ratio generally followed observations closely, but over-exaggerate diurnal variations in the winter. During the spring a slight but persistent overprediction in mixing ratio existed. During the summer daytime maximums were overpredicted. Modeled and observed mixing ratio were very similar during the fall.

6.2.2. Upper-Air Statistics

The plots generated as part of the statistical evaluation of upper air meteorological variables simulated by WRF are presented in Appendix C. All statistics were calculated for the UA_EASTUS evaluation region. Figures C-1 through C-6 show vertical profiles of monthly statistics for wind speed, temperature, and specific humidity at 12 Z each day and at various pressure levels throughout the lower atmosphere. While wind speeds near the surface were nearly unbiased winds above 925 mb were slightly underpredicted. Root mean square error values were larger in the upper troposphere than near the surface and increased with decreasing pressure. Wind speed performance was generally better during the warmer months. Temperature bias was consistently just slightly positive from near the surface up to 400 mb, but increased above that level. Root mean square errors from 700 to 300 mb were lower than near the surface, but increased above 300 mb. There did not appear to be a seasonal dependence for temperature performance in the upper atmosphere. Specific humidity was underpredicted near the surface for the warmest months of the year, but was otherwise nearly unbiased near the surface and in the upper troposphere. Bias values were slightly positive at 500 mb. Root mean square errors were largest during the summer months. Values decrease with height due to decreasing moisture contents of the upper troposphere.

Figures C-7 through C-12 show vertical profiles of monthly statistics for wind speed, temperature, and specific humidity at 0 Z each day and at various pressure levels throughout the troposphere. Wind speed was underpredicted throughout the depth of the troposphere, similar to wind speed at 12Z. However, at 925 mb wind speed bias ranged from near zero during the warmer months to positively biased during the colder months. Wind speed RMSE at 0 Z was similar to 12Z. Temperature was nearly unbiased from 925 to 400 mb and was slightly positive above 400 mb. Temperature RMSE was lowest between 700 and 300 mb and highest at 925 mb and above 300 mb. Specific humidity bias was slightly positive throughout the troposphere. Specific humidity RMSE was highest near the surface and decreased with height. Error values were highest during the warmer months of the year.

6.2.3. Precipitation

The plots generated as part of the basic precipitation analysis are presented in Appendix D. For each month three plots were generated. The first was a plot of monthly accumulated observed precipitation, the second was of monthly accumulated modeled precipitation, and the third of the difference between observed and modeled precipitation. Figures D-1 through D-6 show plots for January and February. Figures D-34 through D-36 show plots for the other winter month, December. Precipitation was observed mainly over the southeast, Midwest, and northeast U.S. WRF reproduced the spatial patterns and extent well, however the magnitude was generally underpredicted.

Figures D-7 through D-15 show plots for March, April, and May. Most precipitation was observed over the same areas as during the winter months, however, more was measured. Again, WRF adequately reproduced the spatial patterns and extent of the precipitation well, while it underpredicted the magnitude. Precipitation was also observed over the northern plains, while WRF adequately reproduced both the spatial extent and magnitude. Precipitation was measured over the front range of the Rockies at the western edge of the modeling domain. WRF overpredicted the precipitation in this area.

Figures D-16 through D-24 show plots for June, July, and August. WRF adequately reproduced the spatial patterns and extent of observed precipitation fields across the majority of the domain. WRF generally underpredicted precipitation over the Northern Plains and Midwest, while overpredicted precipitation over the Southeast. Heavy precipitation was observed over the Northeast in August, which was adequately represented by WRF.

Figures D-25 through D-33 show plots for September, October, and November. WRF adequately reproduced the spatial patterns and extent of observed precipitation fields across the domain. Precipitation was more often underpredicted in September and November, but otherwise the magnitude of precipitation was well represented by WRF during the autumn months.

7. CONCLUSIONS

An annual meteorological simulation using the WRF model was generated for the year 2011 for the purpose of supporting regional scale air quality modeling over the Central and Eastern U.S. WRF has been established as an appropriate state-of-the-science model for generating meteorological fields to drive photochemical transport modeling and is widely used by the air quality modeling community. This simulation uses a configuration and settings established by previous sensitivity studies. The analysis nudging implementation has been refined based on recent sensitivity analyses which showed turning off nudging of winds within the lowest layer of the atmosphere where the PBL resides improves wind performance near the surface.

The statistical evaluation showed generally a slight negative bias in wind speed for the CENSARAN and CENSARAS regions, but a slight positive bias for the LADCO region across the year. A slight warm bias was shown for the CENSARAN region in the summer and fall, while a cold bias was shown during spring for the LADCO region. Otherwise, temperature was generally unbiased. Mixing ratio was overpredicted across the year for the LADCO region and during the summer for the CENSARAN region, but was otherwise unbiased. Wind speed errors were generally highest during the spring and lowest during the winter for all regions. Temperature errors were highest during the winter and lowest during the summer. Mixing ratio errors were highest during the summer and lowest during the winter. However, mixing ratio performance was highly dependent on the amount of moisture in the atmosphere. Errors were lower during the winter mainly because less moisture was available.

Most wind speed daily bias and error values were within their respective benchmarks. A majority of temperature bias and error values were within their respective benchmarks, however temperature bias during the winter was highly variable and many values were outside the benchmarks. Nearly all mixing ratio bias and error values were within the benchmarks. It should be noted, however, the mixing ratio benchmarks were developed based on modeling of summer environments. These benchmarks are not necessarily valuable for assessing modeled moisture fields during the winter in colder climates.

The precipitation evaluation showed WRF generally adequately reproduced the spatial extent and patterns in accumulated precipitation across the Central and Eastern U.S. However, the magnitude of precipitation was typically underpredicted with the exception of summer convective precipitation over the Southeast.

Several meteorological simulations using the WRF model have been conducted over the past few years. Comparing the 2011 Iowa DNR WRF simulation to other simulations with 12 km domains over the Central and/or Eastern U.S. to is another helpful method for assessing the suitability for air quality studies. McNally and Loomis (2012) conducted a WRF modeling study with a 12 km domain of similar size and location for the year 2007. Monthly statistics shown in Appendix B are very similar to the monthly performance statistics for this study. The EPA conducted a 12 km simulation covering the continental U.S. for the year 2011 (EPA, 2013). Near-surface error statistics appear to be similar between the Iowa DNR and EPA WRF runs. However, the statistics presented for the EPA simulation were calculated on an hourly basis and apply to the entire 12 km domain. A more detailed and direct comparison between the two simulations comparing statistics calculated for the same time scale and geographic region is beyond the scope of this document. An updated version of the EPA WRF simulation, which incorporates the GHRSST dataset (https://www.ghrsst.org/), has recently been completed and documentation of the performance of this run will be available at a future date.

Monthly statistics for temperature, wind speed, and mixing ratio for the 2011 Iowa DNR WRF simulation are very similar to those from the 2007 WRF simulation. Daytime wind speeds show significant improvement due to the improved analysis nudging implementation. A comparison to the performance evaluation of the 2007 WRF simulation done by AER, Inc (http://sesarm.aer.com) shows wind speeds have gone from being frequently underpredicted during the daytime to being just slightly overpredicted.

Based on the configuration and implementation of the WRF model, the evaluation of the statistical performance metrics, and comparison to other WRF simulations, the 2011 annual simulations should be considered acceptable for use in photochemical transport modeling. Daily error statistics for temperature, humidity, and wind speed were within their respective benchmarks for a significant portion of the year. No major deficiencies were discovered during the performance evaluation.

8. REFERENCES

Baker, K., C. Misenis, M. D. Obland, R. A. Ferrare, A. J. Scarino, and J. T. Kelly, 2013: Evaluation of surface and upper air fine scale WRF meteorological modeling of the May and June 2010 CalNex period in California. *Atmospheric Environment*, **80**, 299-309.

Brown, D., D. Baker, T. Downs, M. Ku, W. Hao, G. Sistla, M. Kiss, N. Witcraft, M. Johnson, and D.-L. Zhang, 2012: WRF Meteorological Modeling in Support of SIP Regional Air Quality Modeling for Base Year 2007. http://www.iowadnr.gov/portals/idnr/uploads/air/insidednr/regmodel/wrf_tsd_2007.pdf

Emery, C.A., E. Tai, G. Yarwood, 2001: Enhanced Meteorological Modeling and Performance Evaluation for Two Texas Ozone Episodes. Prepared for the Texas Natural Resource Conservation Commission, by ENVIRON International Corp, Novato, CA.

Environ, 2012: Western Regional Air Partnership (WRAP) West-wide Jump Start Air Quality Modeling Study (WestJumpAQMS): WRF Application/Evaluation. Prepared for the Western Regional Air Partnership, by ENVIRON International Corp, Novato, CA.

Environmental Protection Agency, 2013: Meteorological Model Performance for Annual 2011 Simulation WRF v3.4.

Fry, J., Xian, G., Jin, S., Dewitz, J., Homer, C., Yang, L., Barnes, C., Herold, N., and Wickham, J., 2011: Completion of the 2006 National Land Cover Database for the Conterminous United States, *Photogrammetric Engineering and Remote Sensing*, **77**, 858-864.

Gilliam, R. C., J. M. Godowitch, and S. T. Rao, 2012: Improving the horizontal transport in the lower troposphere with four dimensional data assimilation. *Atmospheric Environment*, **53**, 186-201.

Gilliam, R. C. and J. E. Pleim, 2010: Performance assessment of new land surface and planetary boundary layer physics in the WRF-ARW. *J. Appl. Meteor. Climatol.*, **49**, 760-774.

Gilliam, R. C., J. E. Pleim, and T. L. Otte, 2009: Multiscale meteorological modeling for air quality applications, EPA Atmospheric and Modeling Analysis Division Peer Review Conference, January 27-29, Research Triangle Park, NC.

Iacono, M., J. Delamares, E. Mlawer, M. Shepard, S. Clough, and W. Collins, 2008: Radiative forcing by long-lived gases: Calculations with AER radiative transfer models, *J. Geophys. Res.*, **113**, D13103, doi:10.1029/2008JD00994

Kain, J. S. and J. M. Fritsch, 1990: A one-dimensional entraining/detraining plume model and its application in convective parameterization. *J. Atmos. Sci.*, **47**, 2784-2802.

Kain, J. S. and J. M. Fritsch, 1993: Convective parameterization for mesoscale models: The Kain-Fritsch scheme, *The representation of cumulus convection in numerical models*, K. A. Emanuel and D.J. Raymond, Eds., Amer. Meteor. Soc., 246 pp.

Knievel, J., G. Bryan, and J. Hacker, 2007: Explicit numerical diffusion in the WRF model. *Mon. Wea. Rev.*, **135**, 3808-3824.

Lin, Y., and K. E. Mitchell, 2005: The NCEP Stage II/IV hourly precipitation analyses: development and applications. Preprints, 19th Conf. on Hydrology, American Meteorological Society, San Diego, CA, 9-13 January 2005, Paper 1.2.

Ma, L.-M. and Z.-M. Tan, 2009: Improving the behavior of the cumulus parameterization for tropical cyclone prediction: Convection trigger. *Atmospheric Research*, **92**, 190-211.

McNally, D. and Loomis, C. Application and Evaluation of WRF for Calendar Year 2007. Prepared by Alpine Geophysics, LLC, Arvada, CO. Prepared for Anthony Sadar, Allegheny County Health Department, Pittsburgh, PA; 2012.

Morrison, H., G. Thompson, and V. Tatarskii, 2009: Impact of cloud microphysics on the development of trailing stratiform precipitation in a simulated squall line: Comparison of one- and two-moment schemes. *Mon. Wea. Rev.*, **137**, 991-1007.

National Oceanic and Atmospheric Administration, 1998: Automated Surface Observing System User's Guide. http://www.nws.noaa.gov/asos/pdfs/aum-toc.pdf

Olerud, D., and A. Sims, 2004: MM5 2002 modeling in support of VISTAS (Visibility Improvement – State and Tribal Association) (DRAFT). Prepared for Mr. Mike Abraczinskas, VISTAS Technical Analysis Workgroup.

Pleim, J. E., 2006: A simple, efficient solution of flux-profile relationships in the atmospheric surface layer. *J. Appl. Meteor. And Clim.*, **45**, 341-347.

Pleim, J. E., 2007: A combined local and nonlocal closure model for the atmospheric boundary layer. Part I: Model description and testing. *J. Appl. Meteor. Clim.*, **46**, 1383–1395.

Pleim, J. E. and R. Gilliam, 2009: An indirect data assimilation scheme for deep soil temperature in the Pleim-Xiu land surface model. *J. Appl. Meteor. Clim.,* **48**, 1362-1376.

Shin, H. H., S.-Y. Hong, and J. Dudhia, 2009: Orographically-induced Gravity Wave Drag (GWDO) parameterization in the WRF model. http://www.mmm.ucar.edu/wrf/users/workshops/WS2009/abstracts/P2B-01.pdf

Skamarock, W., J. Klemp, J. Dudhia, D. Gill, D. Barker, M. Duda, X.-Y. Huang, W. Wang, and J. Powers, 2008: A description of the Advanced Research WRF version 3, NCAR Tech. Note, NCAR TN-475+STR, 113 pp.

Stoelinga, M. T., 2006: A users' guide to RIP version 4: A program for visualizing mesoscale model output. http://www.mmm.ucar.edu/mm5/documents/ripug_V4.html

Tesche, T. W., 1994: Evaluation Procedures for Regional Emissions, Meteorological, and Photochemical Models. Presented at the 86th Annual Meeting of the Air and Waste Management Association, 14-18 June, Denver, CO.

Xiu, A. and J. E. Pleim, 2001: Development of a land surface model. Part I: Application in a mesoscale meteorology model. *J. Appl. Meteor.*, **40**, 192-209.

APPENDIX A: WRF NAMELIST FILES

WPS Namelist

```
&share
 wrf_core = 'ARW',
 max_dom = 2,
 start_date = '2010-12-31_00:00:00','2010-12-31_00:00:00',
 end_date   = '2010-12-31_21:00:00','2010-12-31_21:00:00',
 interval_seconds = 10800,
 io_form_geogrid = 2,
 opt_output_from_geogrid_path = './',
 debug_level = 200
/

&geogrid
 parent_id         =   1,   1,
 parent_grid_ratio =   1,   3,
 i_parent_start    =   1,  55,
 j_parent_start    =   1,  17,
 e_we              =  165, 286,
 e_sn              =  129, 268,
 geog_data_res     = '10m','5m',
 dx = 36000,
 dy = 36000,
 map_proj = 'lambert',
 ref_lat   =  40.0,
 ref_lon   = -97.0,
 truelat1  =  33.0,
 truelat2  =  45.0,
 stand_lon = -97.0,
 geog_data_path = '/j1/WRF/geog',
 opt_geogrid_tbl_path = './'
/

&ungrib
 out_format = 'WPS',
 prefix = '/j2/2011wrfv35/ungrib/2010-12/NAM'
/

&metgrid
 fg_name = '/j2/2011wrfv35/ungrib/2010-12/NAM',
 constants_name = '/j2/2011wrfv35/ungrib/2010-12/SST:2010-12-31_00',
 opt_metgrid_tbl_path  = './',
 io_form_metgrid = 2,
/
```

OBSGRID Namelist

```
&record1
 start_year              =  2010
 start_month             =    12
 start_day               =    16
 start_hour              =    12
 end_year                =  2010
 end_month               =    12
 end_day                 =    22
 end_hour                =    00
 interval                = 10800/

&record2
 grid_id                 = 2
 obs_filename            = "/j2/madis/little_r_obs/obs/obs"
 trim_domain             = .FALSE.
 trim_value              = 5
 remove_unverified_data      = .TRUE.
 remove_data_above_qc_flag   = 32768
/

&record3
 max_number_of_obs          = 120000
 fatal_if_exceed_max_obs     = .TRUE./

&record4
 qc_test_error_max          = .TRUE.
 qc_test_buddy              = .TRUE.
 qc_test_vert_consistency    = .TRUE.
 qc_test_convective_adj      = .TRUE.
 max_error_t                = 5
 max_error_uv               = 5
 max_error_z                = 8
 max_error_rh               = 20
 max_error_p                = 600
 max_buddy_t                = 8
 max_buddy_uv               = 8
 max_buddy_z                = 8
 max_buddy_rh               = 40
 max_buddy_p                = 800
 buddy_weight               = 1.0
 max_p_extend_t             = 1300
 max_p_extend_w             = 1300/

&record5
 print_obs_files            = .TRUE.
 print_found_obs            = .FALSE.
```

```
 print_header              = .FALSE.
 print_analysis            = .FALSE.
 print_qc_vert             = .FALSE.
 print_qc_dry              = .FALSE.
 print_error_max           = .FALSE.
 print_buddy               = .FALSE.
 print_oa                  = .TRUE./

&record7
 use_first_guess           = .TRUE.
 f4d                       = .TRUE.
 intf4d                    =  10800
 lagtem                    = .FALSE. /

&record8
 smooth_type               =  1
 smooth_sfc_wind           =  0
 smooth_sfc_temp           =  0
 smooth_sfc_rh             =  0
 smooth_sfc_slp            =  0
 smooth_upper_wind         =  0
 smooth_upper_temp         =  0
 smooth_upper_rh           =  0/

&record9
 oa_type                   = 'Cressman'
 mqd_minimum_num_obs       = 30
 mqd_maximum_num_obs       = 1000
 radius_influence          = 25,24,23,22,
 oa_min_switch             = .TRUE.
 oa_max_switch             = .TRUE./


&plot_sounding
 file_type                 = 'raw'
 read_metoa                = .TRUE.
 grid_id                   = 1
/
 file_type                 = 'qc'
 file_type                 = 'results'
 file_type                 = 'discard'

&plot_level
 file_type                 = '3D'
 grid_id                   = 1
/
 file_type                 = 'sfc_fdda'
```

WRF Namelist

```
&time_control
 run_days                    = 0,
 run_hours                   = 132,
 run_minutes                 = 0,
 run_seconds                 = 0,
 start_year                  = 2010,   2010, 2000,
 start_month                 = 12,   12,   01,
 start_day                   = 16,   16,   24,
 start_hour                  = 12,   12,   12,
 start_minute                = 00,   00,   00,
 start_second                = 00,   00,   00,
 end_year                    = 2010,   2010, 2000,
 end_month                   = 12,   12, 01,
 end_day                     = 22,   22, 25,
 end_hour                    = 00,   00, 12,
 end_minute                  = 00,   00,   00,
 end_second                  = 00,   00,   00,
 interval_seconds            = 10800
 input_from_file             = .true.,.true.,.true.,
 history_interval            = 60,  60,   60,
 frames_per_outfile          = 1,   1,    1000,
 restart                     = .false.,
 restart_interval            = 1440,
 auxinput1_inname            = "metoa_em.d<domain>.<date>"
 io_form_history             = 2
 io_form_restart             = 2
 io_form_input               = 2
 io_form_boundary            = 2
 auxinput4_inname            = "wrflowinp_d<domain>",
 auxinput4_interval          = 720, 720
 io_form_auxinput4           = 2,
 debug_level                 = 200
/

&domains
 time_step                   = 90,
 time_step_fract_num         = 0,
 time_step_fract_den         = 1,
 max_dom                     = 2,
 e_we                        = 165,   286,    94,
 e_sn                        = 129,   268,    91,
 e_vert                      = 35,    35,     28,
 p_top_requested             = 5000,
 num_metgrid_levels          = 40,
 num_metgrid_soil_levels     = 4,
 eta_levels                  = 1.0000, 0.9974, 0.9940, 0.9900,
```

```
                    0.9854, 0.9796, 0.9723, 0.9635,
                    0.9528, 0.9401, 0.9252, 0.9079,
                    0.8882, 0.8659, 0.8410, 0.8133,
                    0.7828, 0.7494, 0.7133, 0.6742,
                    0.6323, 0.5878, 0.5406, 0.4915,
                    0.4409, 0.3895, 0.3379, 0.2871,
                    0.2378, 0.1907, 0.1465, 0.1056,
                    0.0682, 0.0332, 0.0000
dx                  = 36000, 12000,  3333.33,
dy                  = 36000, 12000,  3333.33,
grid_id             = 1,     2,     3,
parent_id           = 0,     1,     2,
i_parent_start      = 1,     55,    30,
j_parent_start      = 1,     17,    30,
parent_grid_ratio   = 1,     3,     3,
parent_time_step_ratio = 1,     3,     3,
feedback            = 0,
smooth_option       = 0
/

&physics
mp_physics          = 10,    10,    3,
ra_lw_physics       = 4,     4,     1,
ra_sw_physics       = 4,     4,     1,
radt                = 30,    15,    30,
sf_sfclay_physics   = 7,     7,     1,
sf_surface_physics  = 7,     7,     2,
bl_pbl_physics      = 7,     7,     1,
bldt                = 0,     0,     0,
cu_physics          = 1,     1,     0,
cudt                = 5,     5,     5,
kfeta_trigger       = 2,
isfflx              = 1,
ifsnow              = 1,
icloud              = 1,
surface_input_source = 1,
num_soil_layers     = 2,
pxlsm_smois_init    = 1, 1
sf_urban_physics    = 0,
num_land_cat        = 40,
maxiens             = 1,
maxens              = 3,
maxens2             = 3,
maxens3             = 16,
ensdim              = 144,
slope_rad           = 1,
topo_shading        = 1,
shadlen             = 25000.,
```

```
sst_update                          = 1,
prec_acc_dt                         = 60, 60,
mp_zero_out                         = 2
mp_zero_out_thresh                  = 1.0E-8
/

&fdda
grid_fdda                           = 1,  1
gfdda_inname                        = "wrffdda_d<domain>",
GFDDA_END_H                         = 1310, 1310,
gfdda_interval_m                    = 180, 180,
fgdt                                = 0,
if_no_pbl_nudging_uv                = 1, 1,
if_no_pbl_nudging_t                 = 1, 1,
if_no_pbl_nudging_q                 = 1, 1,
if_zfac_uv                          = 0,
k_zfac_uv                           = 0,
if_zfac_t                           = 0,
k_zfac_t                            = 0,
if_zfac_q                           = 0,
k_zfac_q                            = 0,
guv                                 = 5.0E-4,3.0E-4,
gt                                  = 5.0E-4,3.0E-4,
gq                                  = 1.E-5,1.E-5,
if_ramping                          = 0,
dtramp_min                          = 60.0,
io_form_gfdda                       = 2,
grid_sfdda                          = 1, 1
sgfdda_inname                       = "wrfsfdda_d<domain>",
sgfdda_interval_m                   = 180, 180,
sgfdda_end_h                        = 1310, 1310,
io_form_sgfdda                      = 2,
guv_sfc                             = 0, 0,
gt_sfc                              = 0, 0,
gq_sfc                              = 0, 0,
pxlsm_soil_nudge                    = 1, 1,
rinblw                              = 250
/

&dynamics
w_damping                           = 1,
diff_opt                            = 1,
km_opt                              = 4,
diff_6th_opt                        = 2,      2,      0,
diff_6th_factor                     = 0.12,   0.12,   0.12,
base_temp                           = 290.
damp_opt                            = 3,
zdamp                               = 5000.,  5000.,  5000.,
```

```
dampcoef                    = 0.2,   0.2,   0.2
khdif                       = 0,      0,      0,
kvdif                       = 0,      0,      0,
non_hydrostatic             = .true., .true., .true.,
moist_adv_opt               = 2,      2,      1,
scalar_adv_opt              = 2,      2,      1,
/

&bdy_control
spec_bdy_width              = 5,
spec_zone                   = 1,
relax_zone                  = 4,
specified                   = .true., .false.,.false.,
nested                      = .false., .true., .true.,
/

&grib2
/

&namelist_quilt
nio_tasks_per_group = 0,
nio_groups = 1,
/
```

APPENDIX B: NEAR-SURFACE EVALUATION PLOTS

Monthly Statistics – CENSARAN

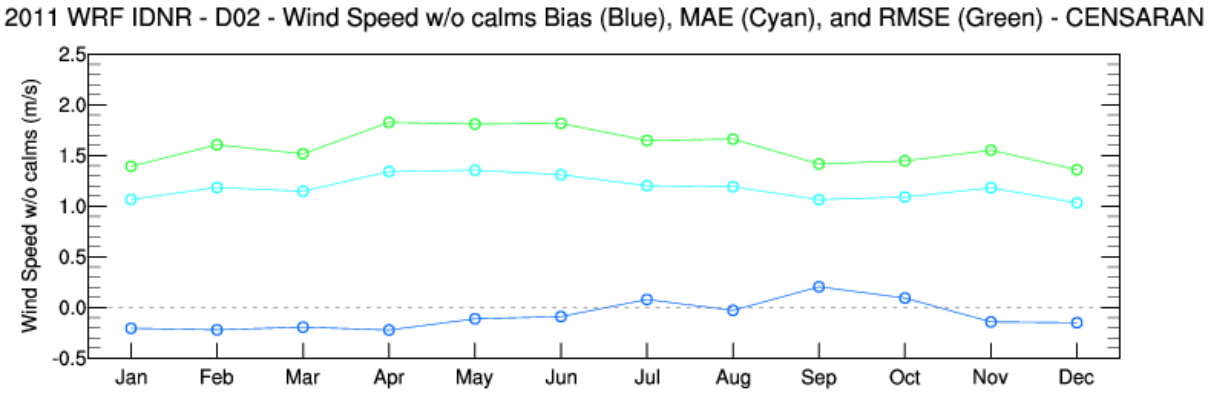

Figure B-1. Monthly bias, mean absolute error, and root mean square error for 10-m wind speed (w/o calms included) for the nested domain for the CENSARAN region.

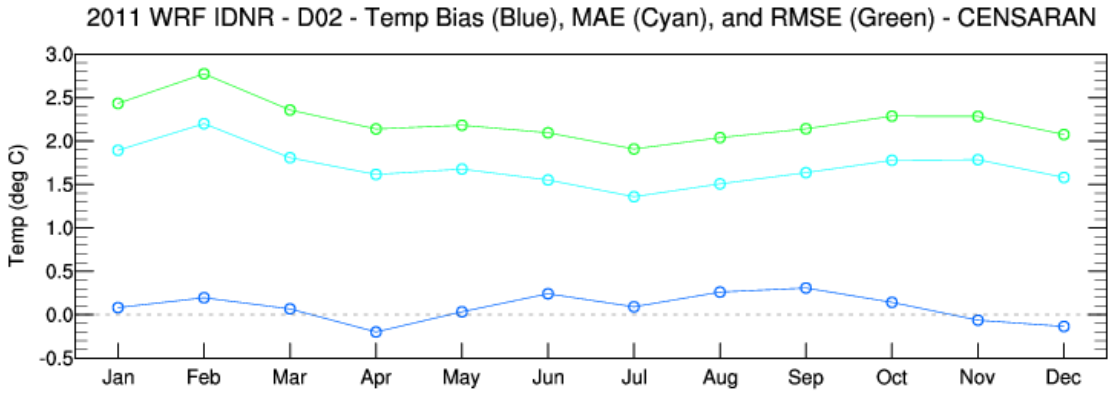

Figure B-2. Monthly bias, mean absolute error, and root mean square error for 2-m temperature for the nested domain for the CENSARAN region.

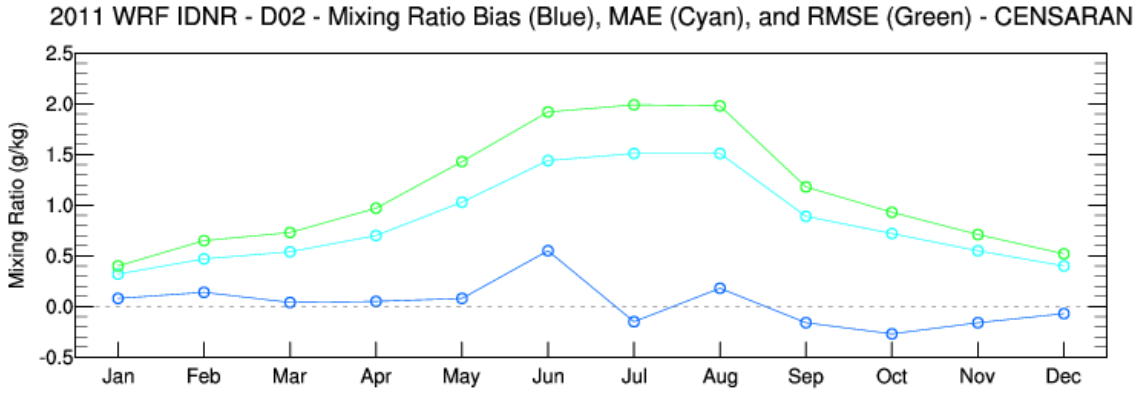

Figure B-3. Monthly bias, mean absolute error, and root mean square error for 2-m mixing ratio for the nested domain for the CENSARAN region.

Monthly Statistics – CENSARAS

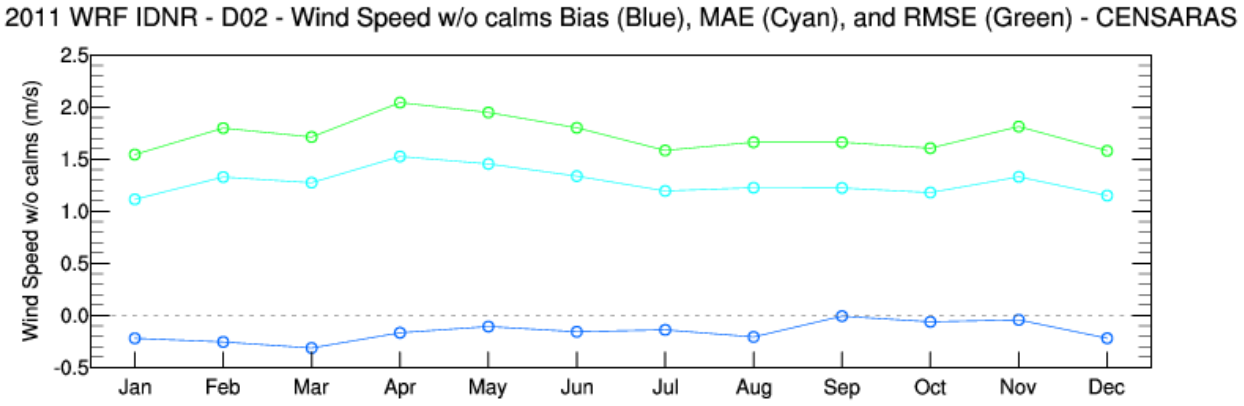

Figure B-4. Monthly bias, mean absolute error, and root mean square error for 10-m wind speed (w/o calms included) for the nested domain for the CENSARAS region.

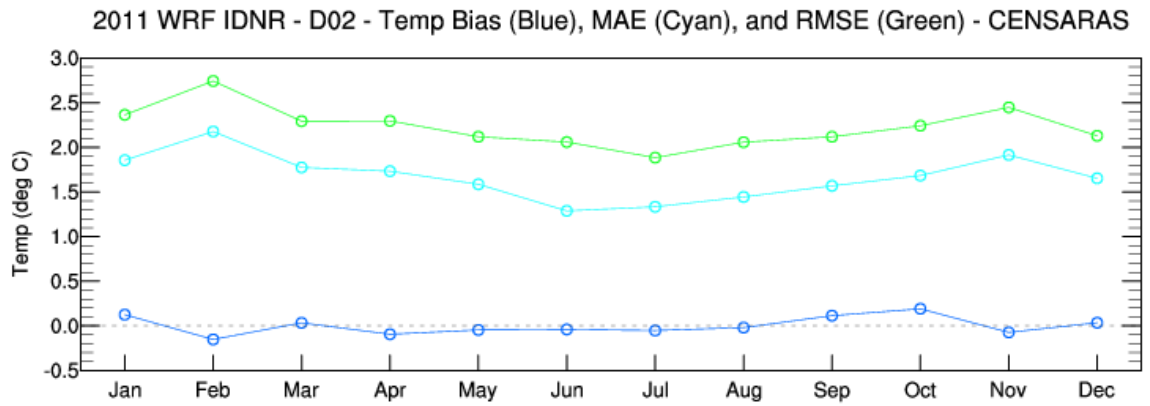

Figure B-5. Monthly bias, mean absolute error, and root mean square error for 2-m temperature for the nested domain for the CENSARAS region.

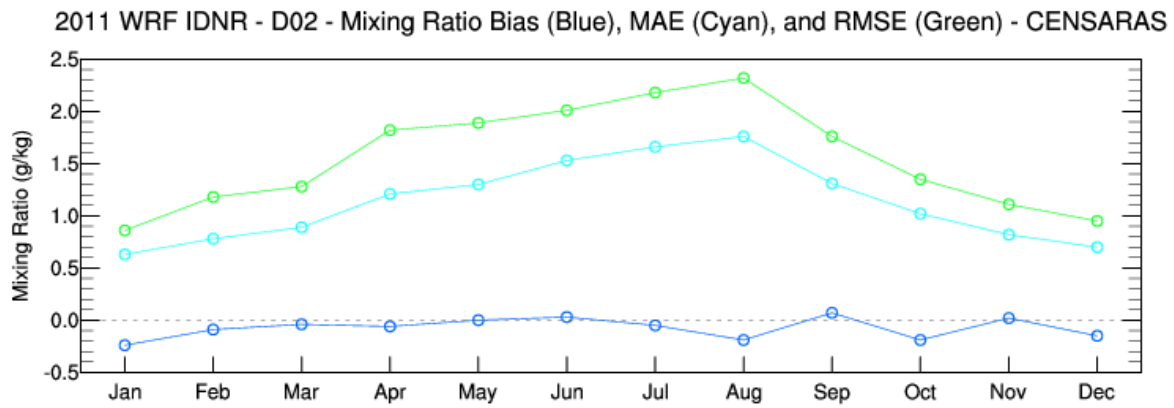

Figure B-6. Monthly bias, mean absolute error, and root mean square error for 2-m mixing ratio for the nested domain for the CENSARAS region.

Monthly Statistics – LADCO

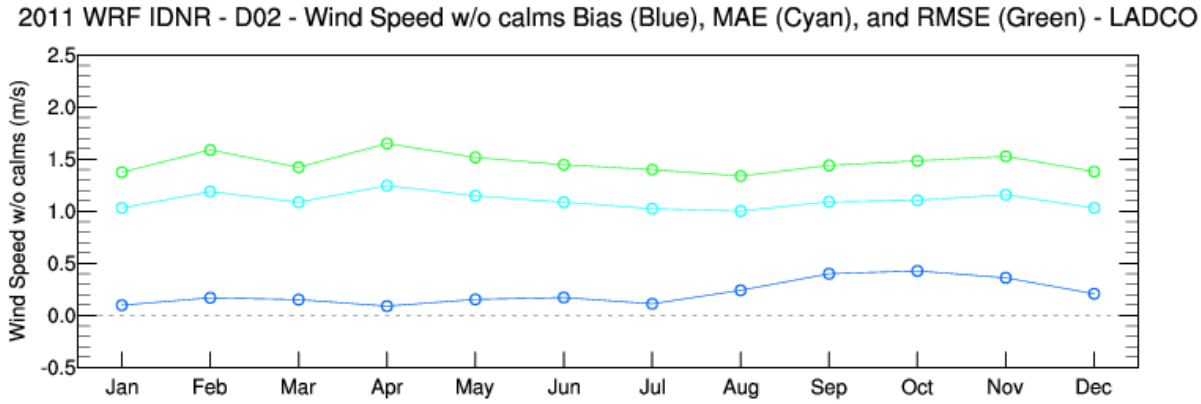

Figure B-7. Monthly bias, mean absolute error, and root mean square error for 10-m wind speed (w/o calm winds included) for the nested domain for the LADCO region.

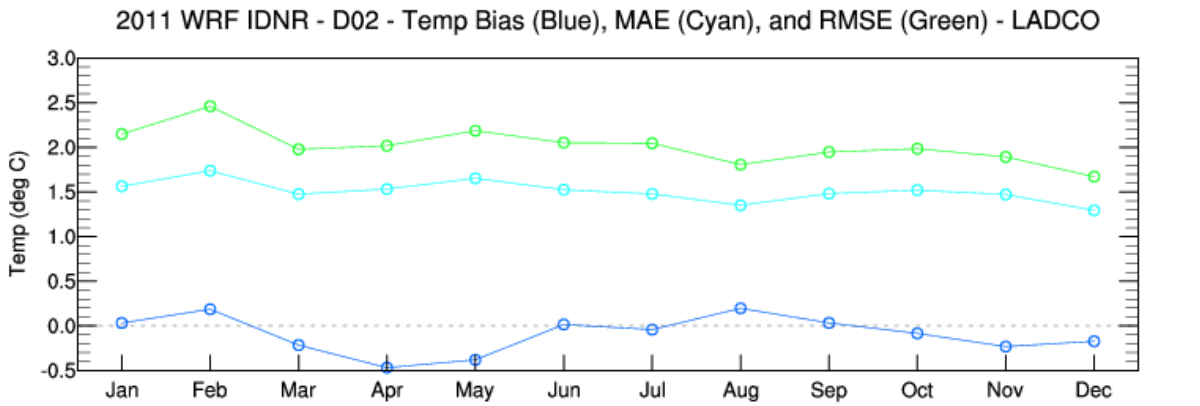

Figure B-8. Monthly bias, mean absolute error, and root mean square error for 2-m temperature for the nested domain for the LADCO region.

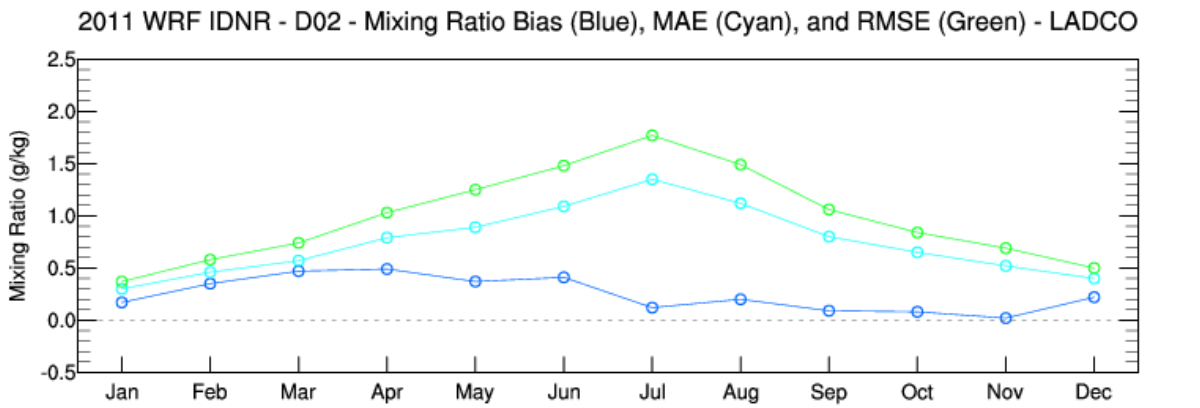

Figure B-9. Monthly bias, mean absolute error, and root mean square error for 2-m mixing ratio for the nested domain for the LADCO region.

Daily Statistics Boxplots – CENSARAN

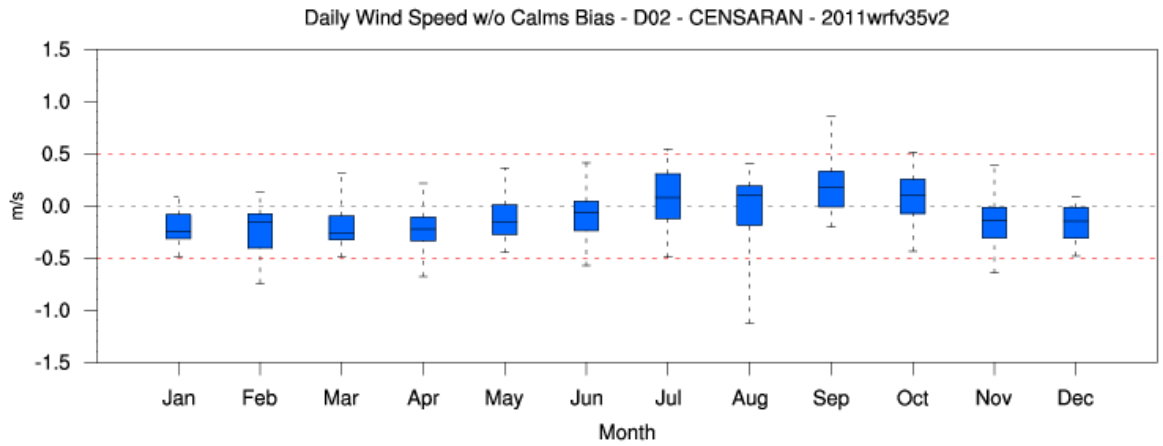

Figure B-10. Monthly boxplots of daily bias for 10-m wind speed (w/o calms included) for the nested domain for the CENSARAN region.

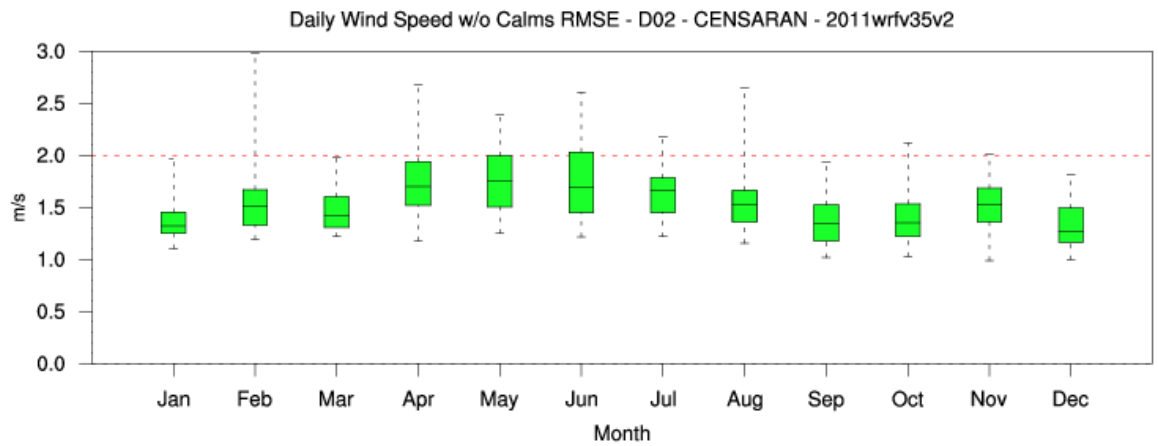

Figure B-11. Monthly boxplots of daily root mean square error for 10-m wind speed (w/o calms included) for the nested domain for the CENSARAN region.

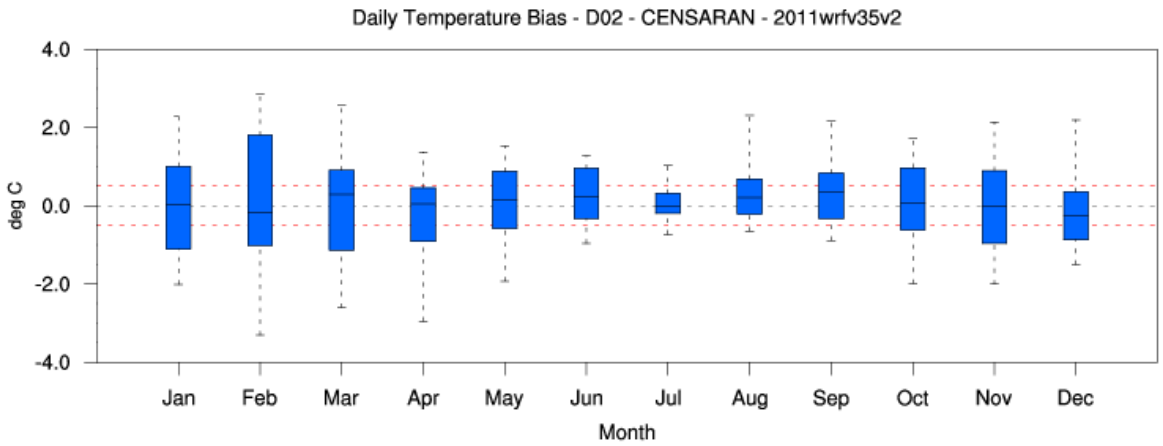

Figure B-12. Monthly boxplots of daily bias for 2-m temperature for the nested domain for the CENSARAN region.

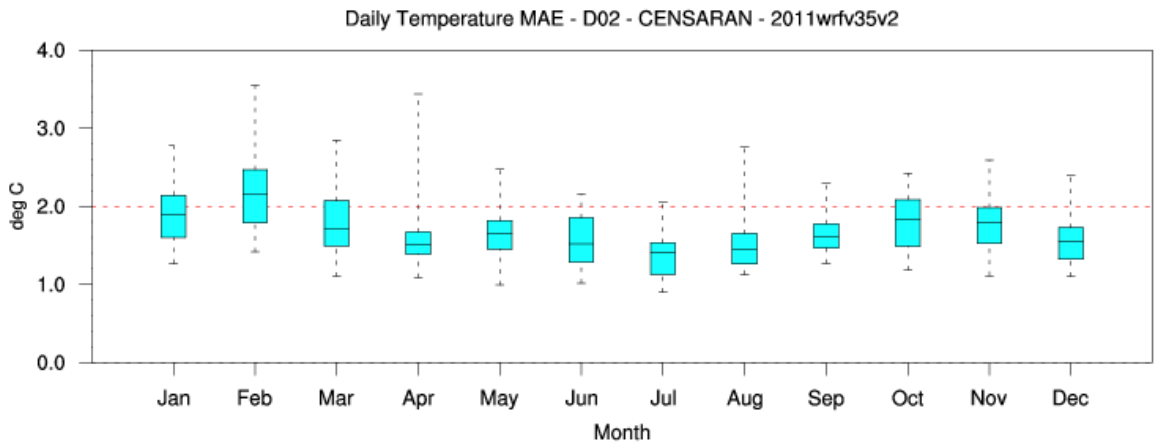

Figure B-13. Monthly boxplots of daily mean absolute error for 2-m temperature for the nested domain for the CENSARAN region.

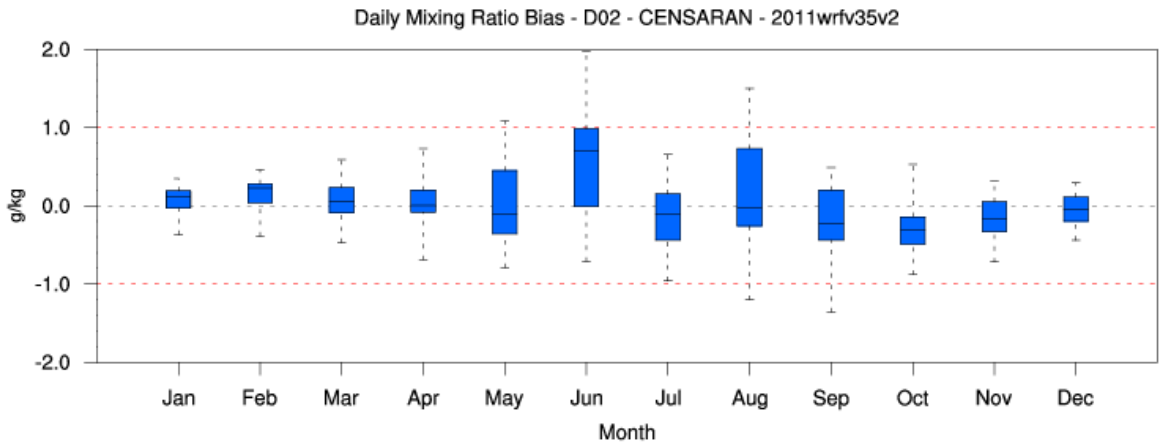

Figure B-14. Monthly boxplots of daily bias for 2-m mixing ratio for the nested domain for the CENSARAN region.

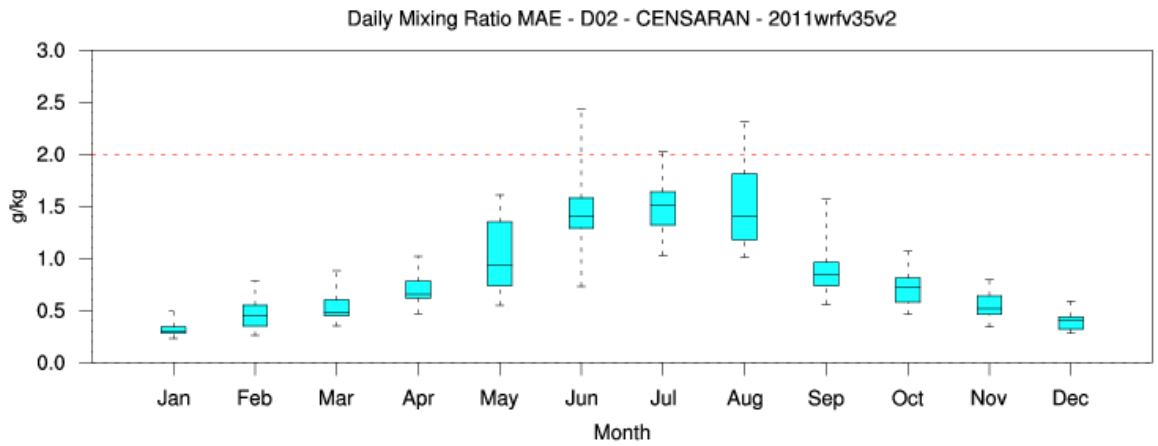

Figure B-15. Monthly boxplots of daily mean absolute error for 2-m mixing ratio for the nested domain for the CENSARAN region.

Daily Statistics Boxplots – CENSARAS

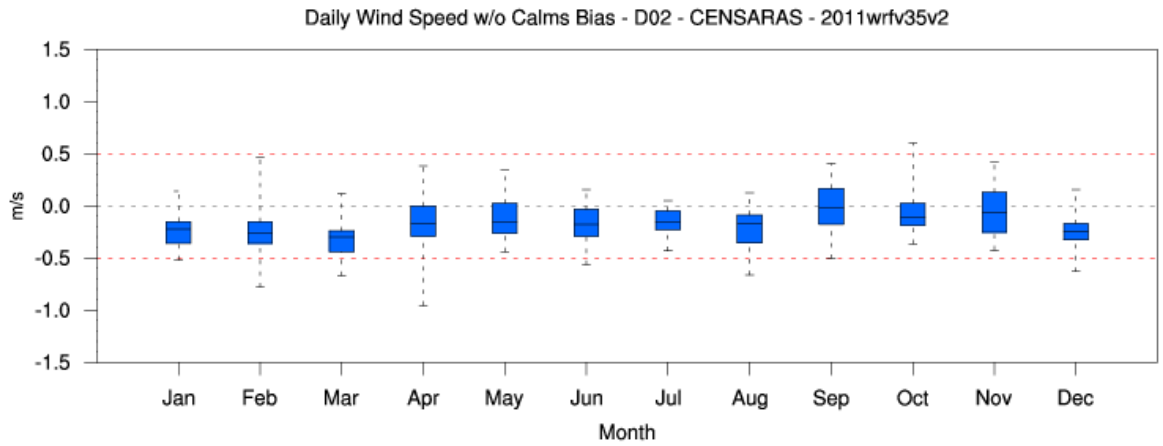

Figure B-16. Monthly boxplots of daily bias for 10-m wind speed (w/o calms included) for the nested domain for the CENSARAS region.

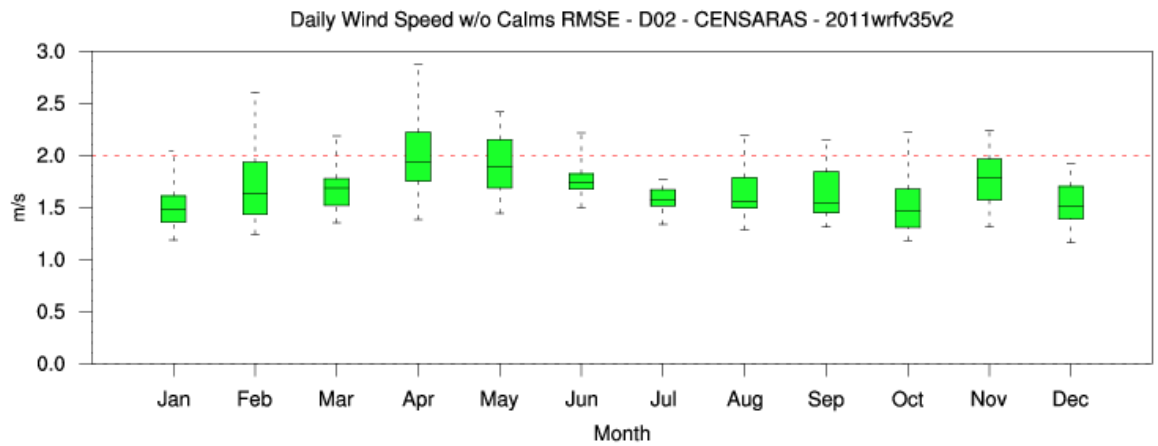

Figure B-17. Monthly boxplots of daily root mean square error for 10-m wind speed (w/o calms included) for the nested domain for the CENSARAS region.

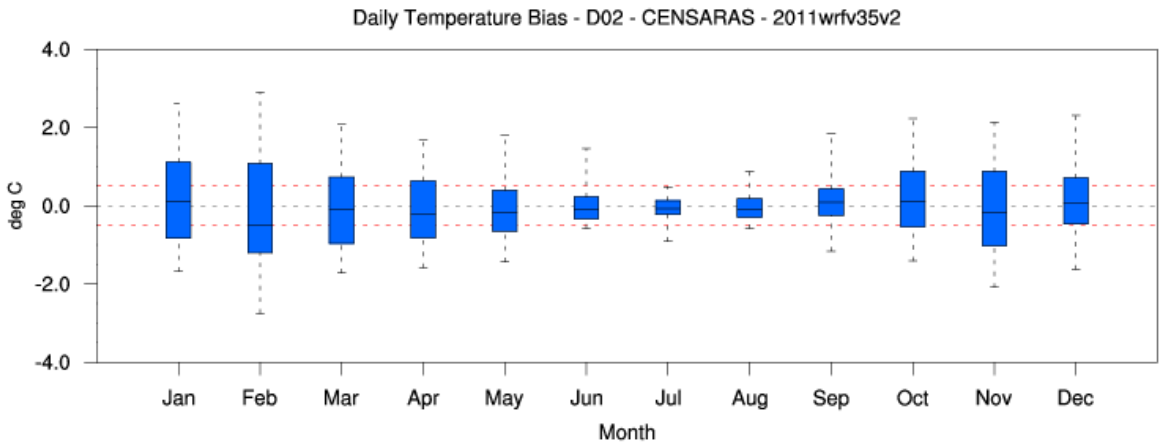

Figure B-18. Monthly boxplots of daily bias for 2-m temperature for the nested domain for the CENSARAS region.

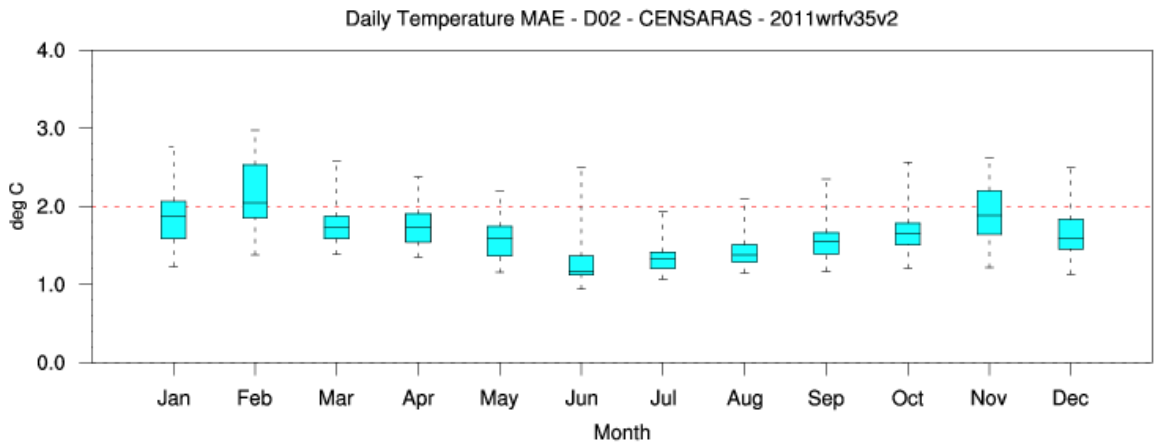

Figure B-19. Monthly boxplots of daily mean absolute error for 2-m temperature for the nested domain for the CENSARAS region.

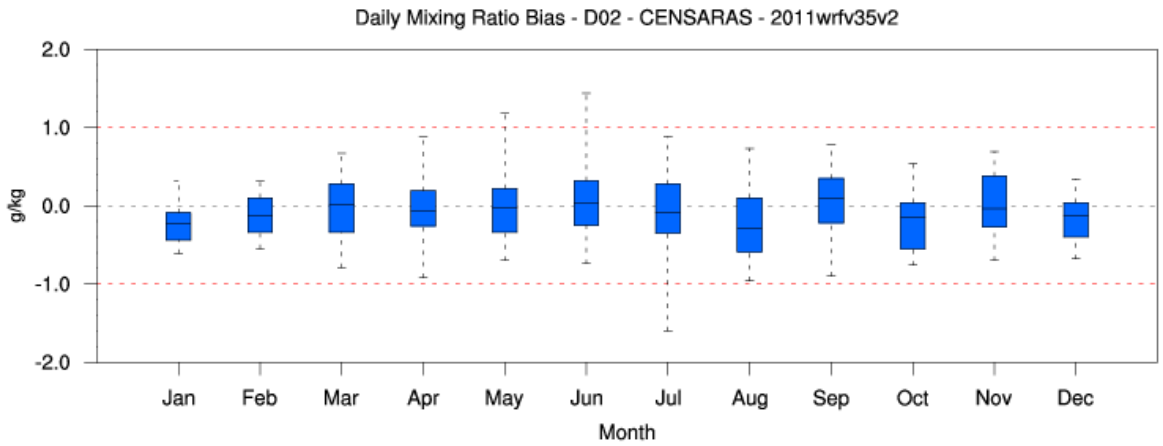

Figure B-20. Monthly boxplots of daily bias for 2-m mixing ratio for the nested domain for the CENSARAS region.

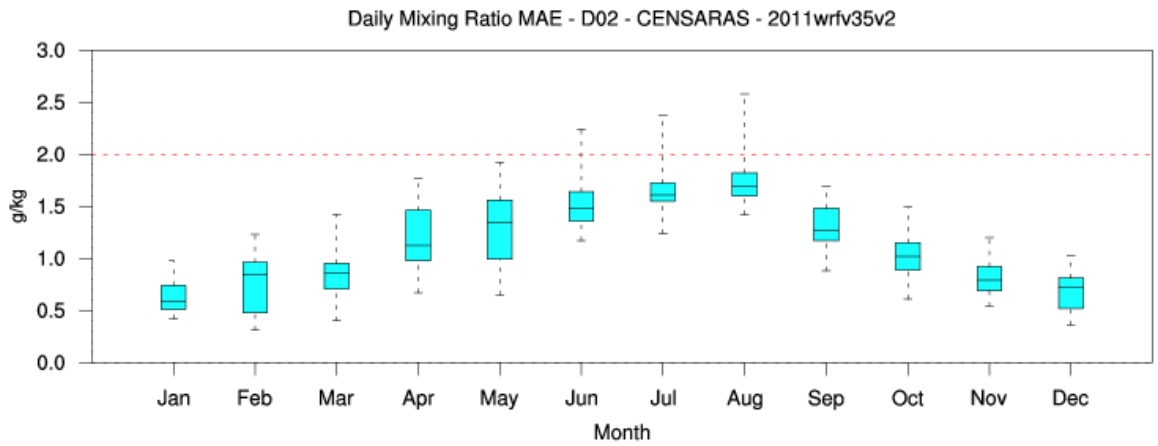

Figure B-21. Monthly boxplots of daily mean absolute error for 2-m mixing ratio for the nested domain for the CENSARAS region.

Daily Boxplots – LADCO

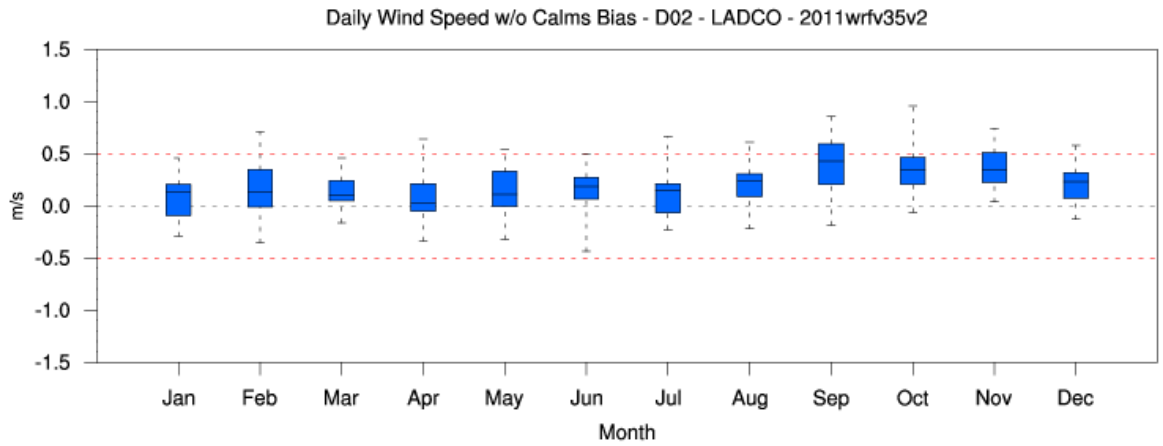

Figure B-22. Monthly boxplots of daily bias for 10-m wind speed (w/o calms included) for the nested domain for the LADCO region.

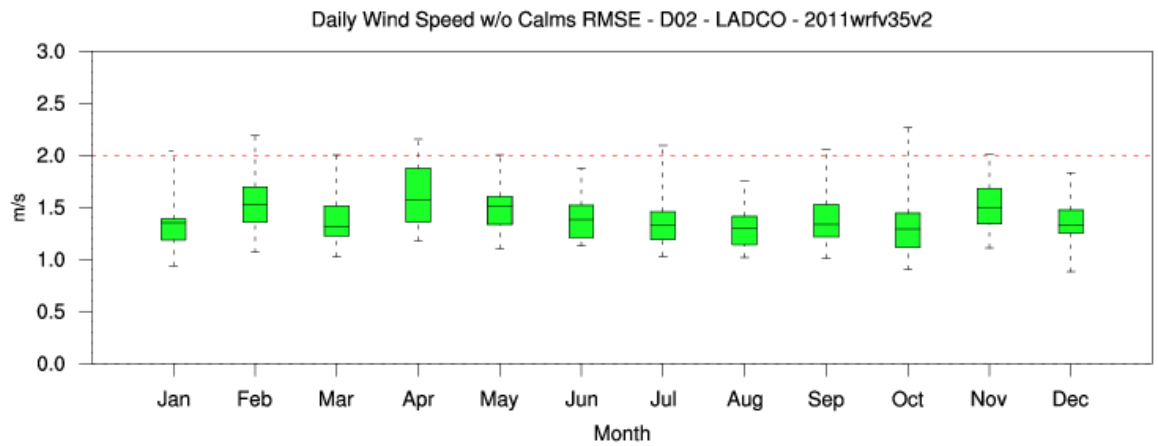

Figure B-23. Monthly boxplots of daily root mean square error for 10-m wind speed (w/o calms included) for the nested domain for the LADCO region.

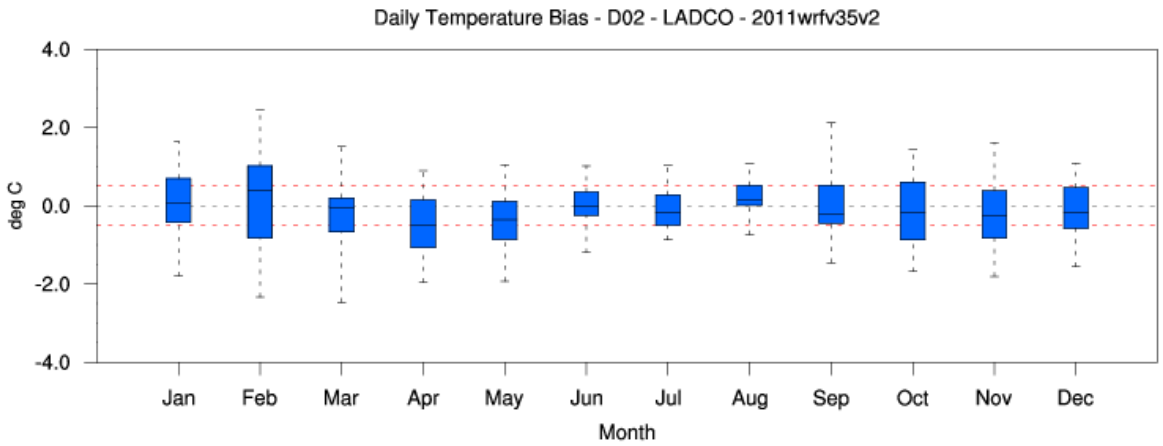

Figure B-24. Monthly boxplots of daily bias for 2-m temperature for the nested domain for the LADCO region.

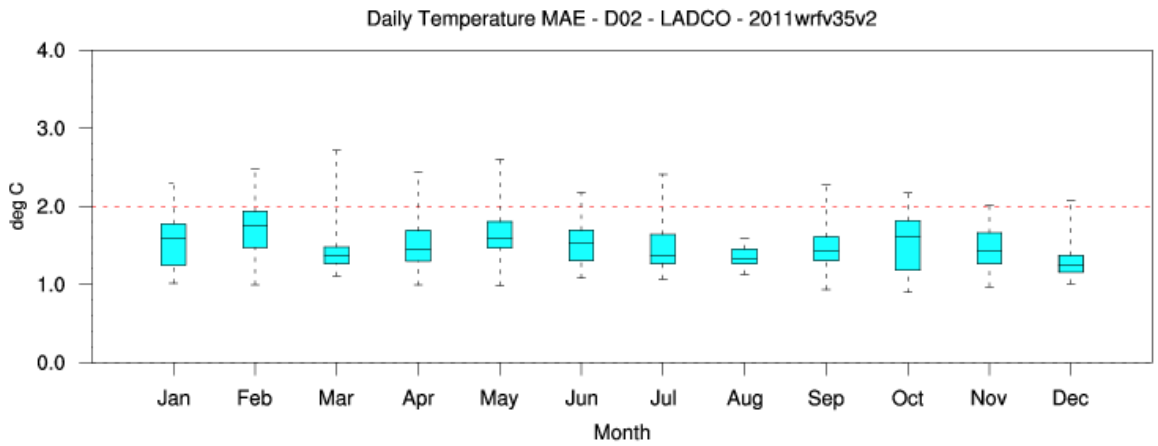

Figure B-25. Monthly boxplots of daily mean absolute error for 2-m temperature for the nested domain for the LADCO region.

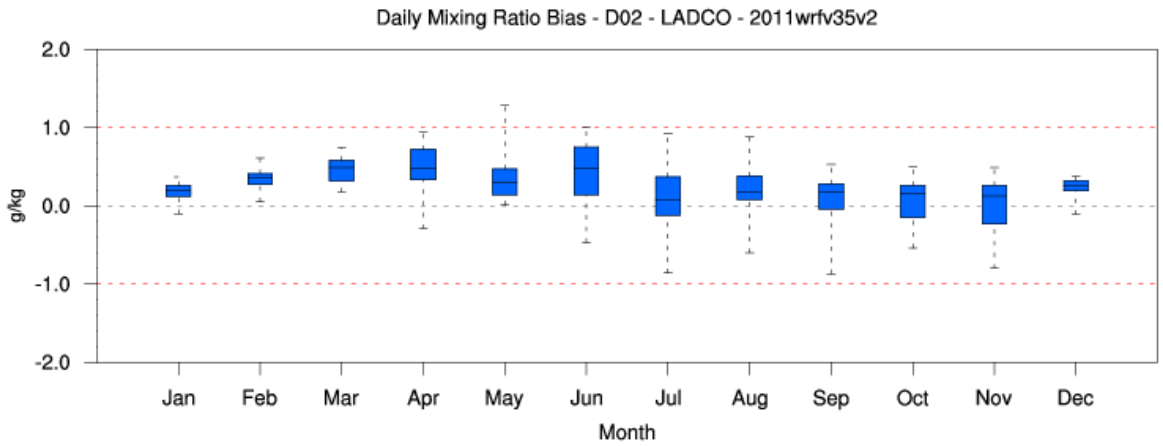

Figure B-26. Monthly boxplots of daily bias for 2-m mixing ratio for the nested domain for the LADCO region.

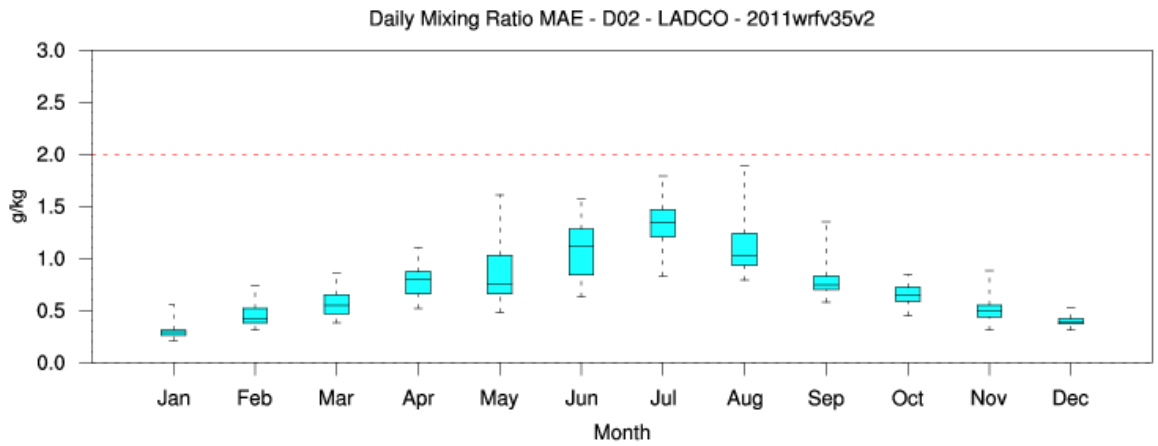

Figure B-27. Monthly boxplots of daily mean absolute error for 2-m temperature for the nested domain for the LADCO region.

Bakergrams – CENSARAN

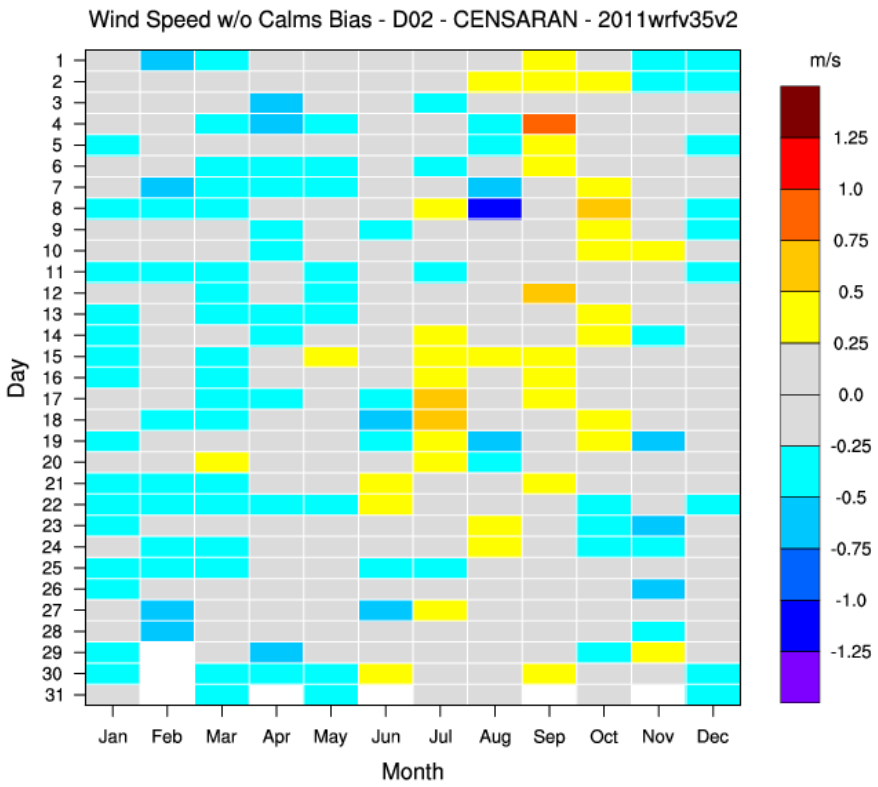

Figure B-28. Bakergram showing daily bias for 10-m wind speed (w/o calm winds included) for the nested domain for the CENSARAN region.

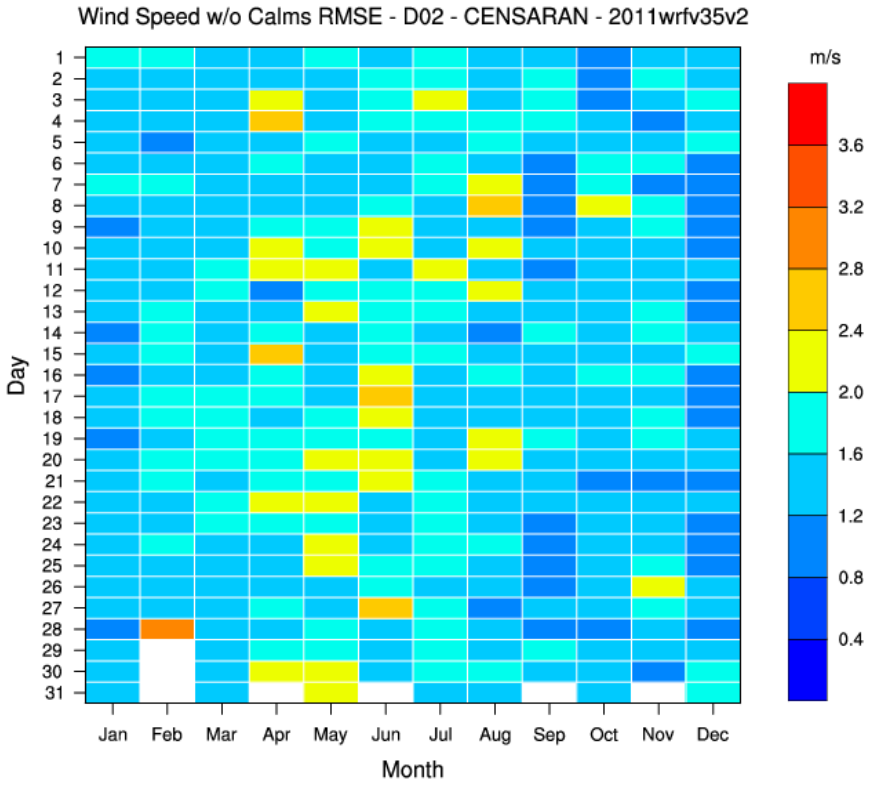

Figure B-29. Bakergram showing daily root mean square error for 10-m wind speed (w/o calm winds included) for the nested domain for the CENSARAN region.

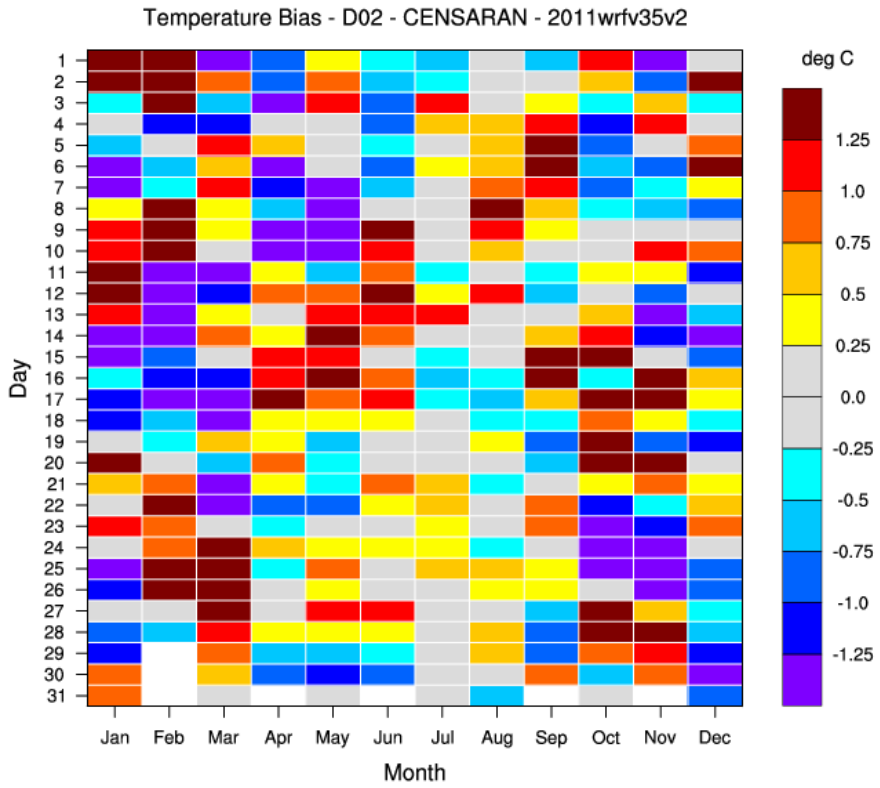

Figure B-30. Bakergram showing daily bias for 2-m temperature for the nested domain for the CENSARAN region.

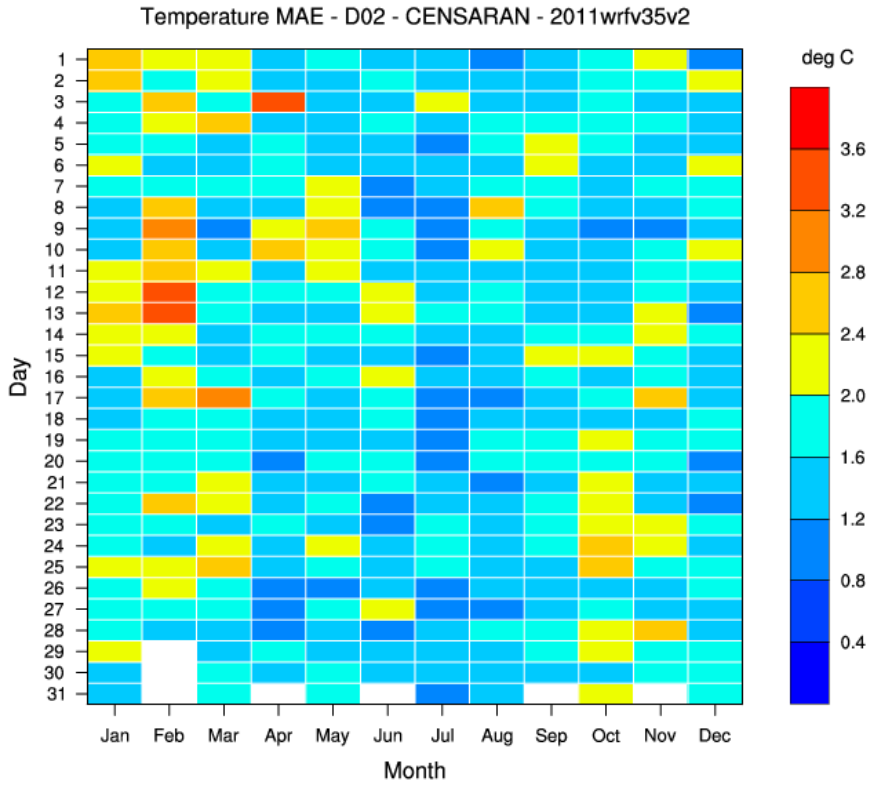

Figure B-31. Bakergram showing daily mean absolute error for 2-m temperature for the nested domain for the CENSARAN region.

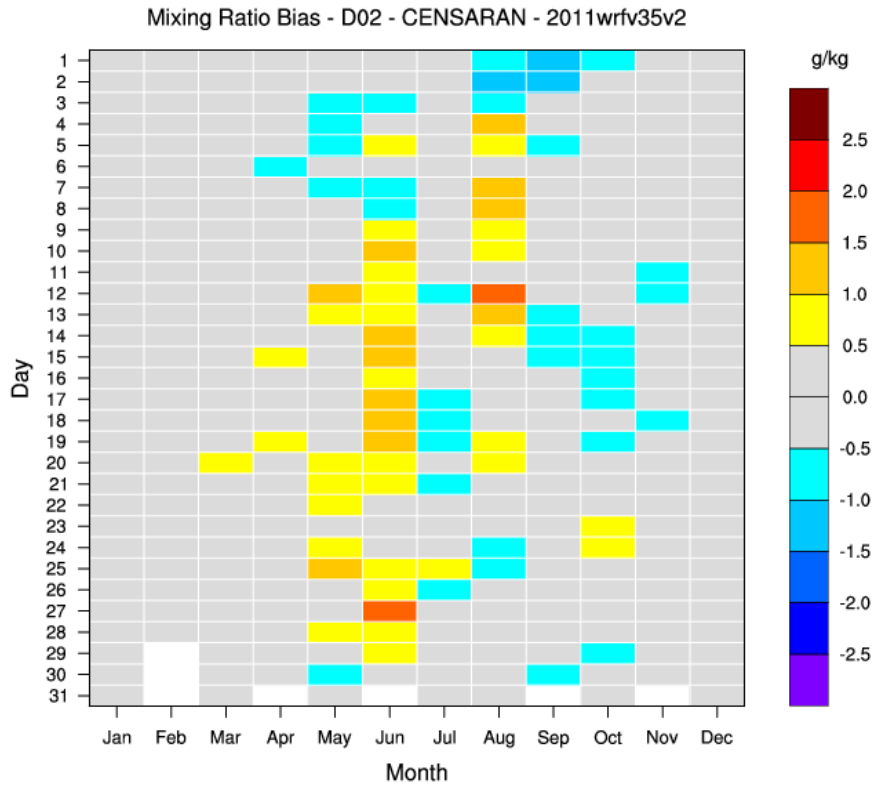

Figure B-32. Bakergram showing daily bias for 2-m mixing ratio for the nested domain for the CENSARAN region.

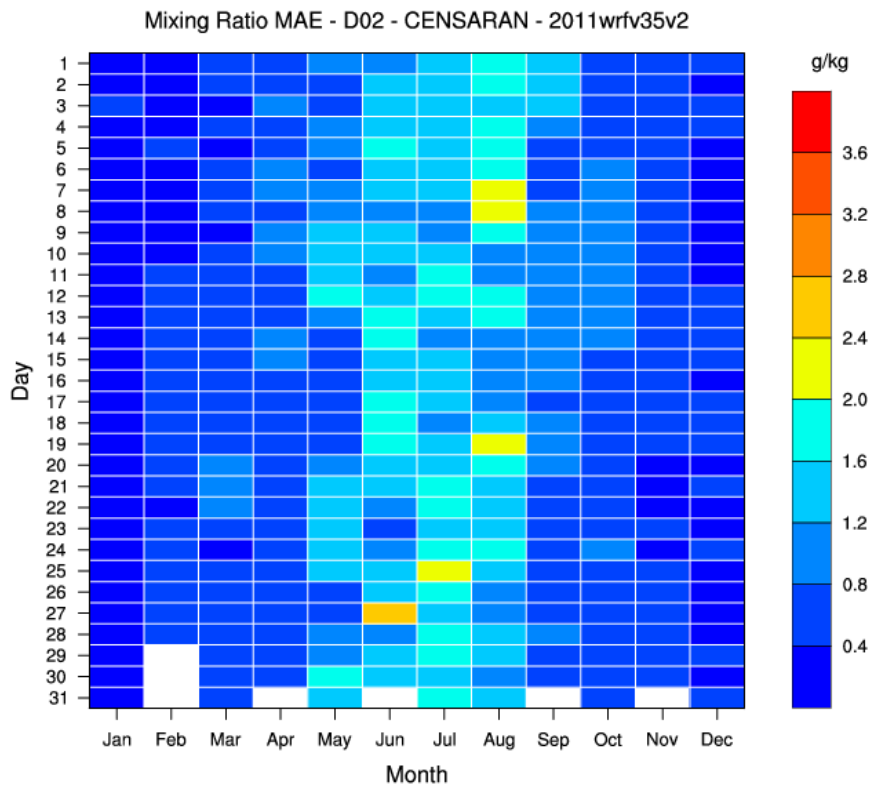

Figure B-33. Bakergram showing daily mean absolute error for 2-m mixing ratio for the nested domain for the CENSARAN region.

Bakergrams – CENSARAS

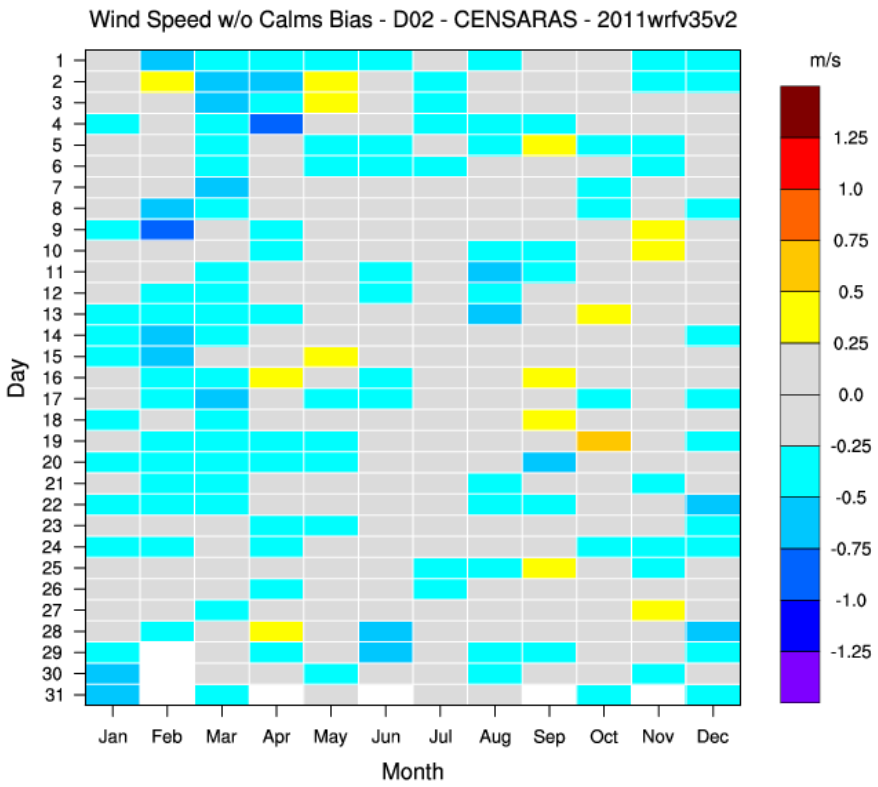

Figure B-34. Bakergram showing daily bias of 10-m wind speed (w/o calm winds included) for the nested domain for the CENSARAS region.

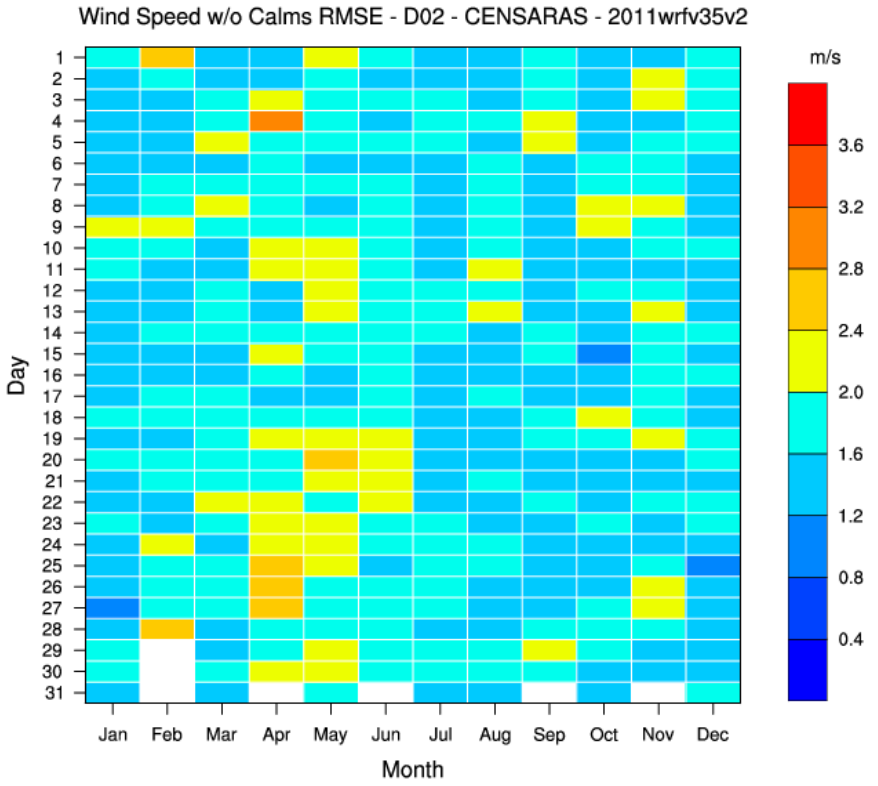

Figure B-35. Bakergram showing daily root mean square error of 10-m wind speed (w/o calm winds included) for the nested domain for the CENSARAS region.

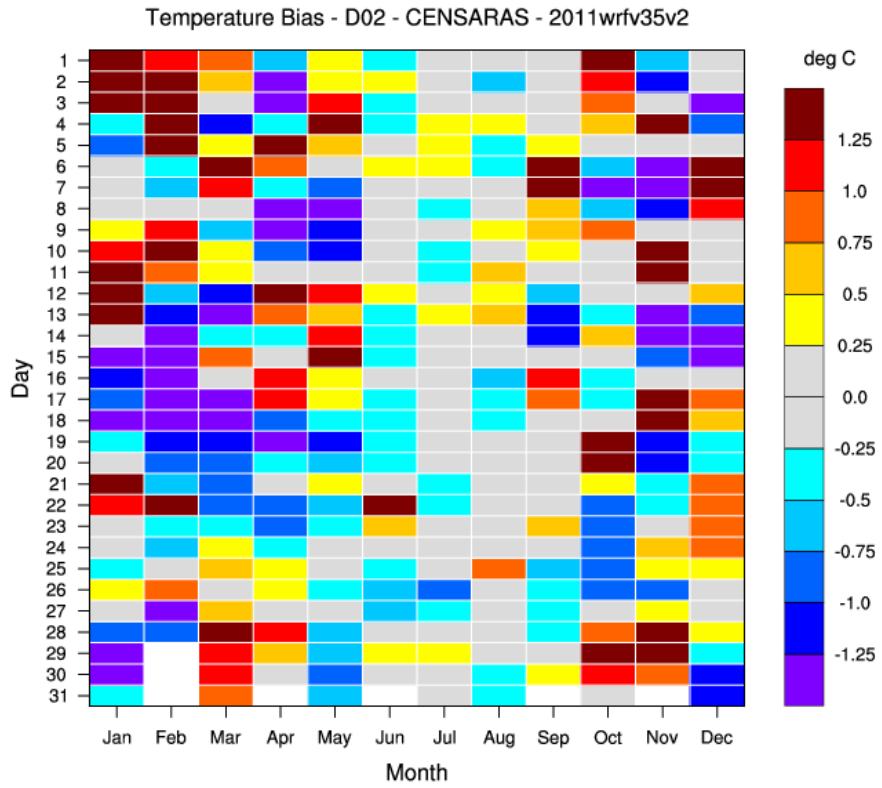

Figure B-36. Bakergram showing daily bias for 2-m temperature for the nested domain for the CENSARAS region.

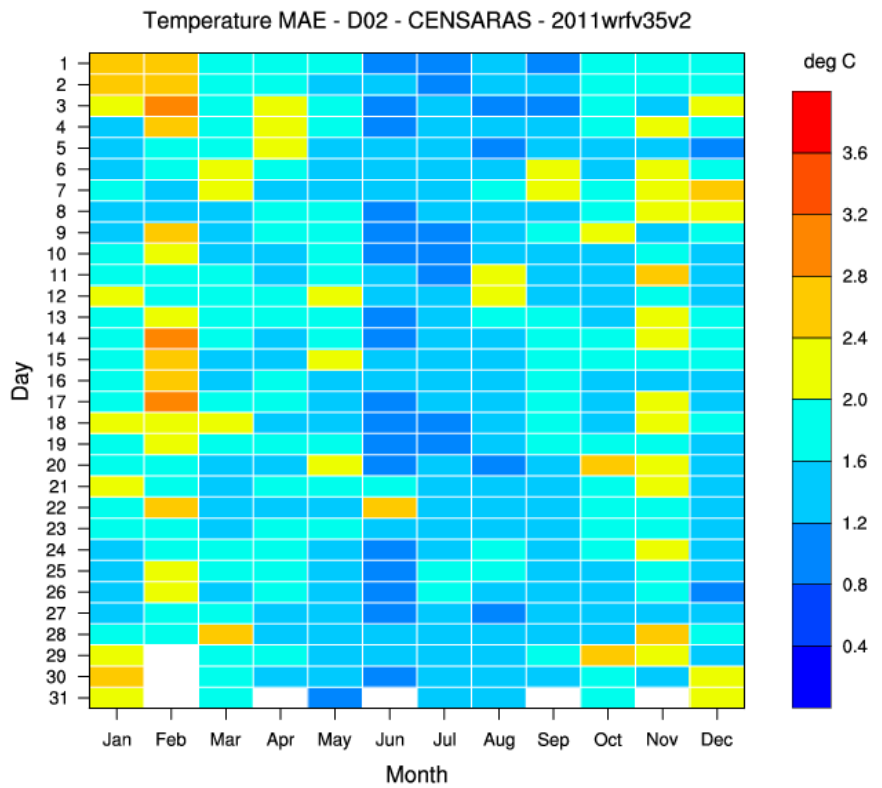

Figure B-37. Bakergram showing daily mean absolute error for 2-m temperature for the nested domain for the CENSARAS region.

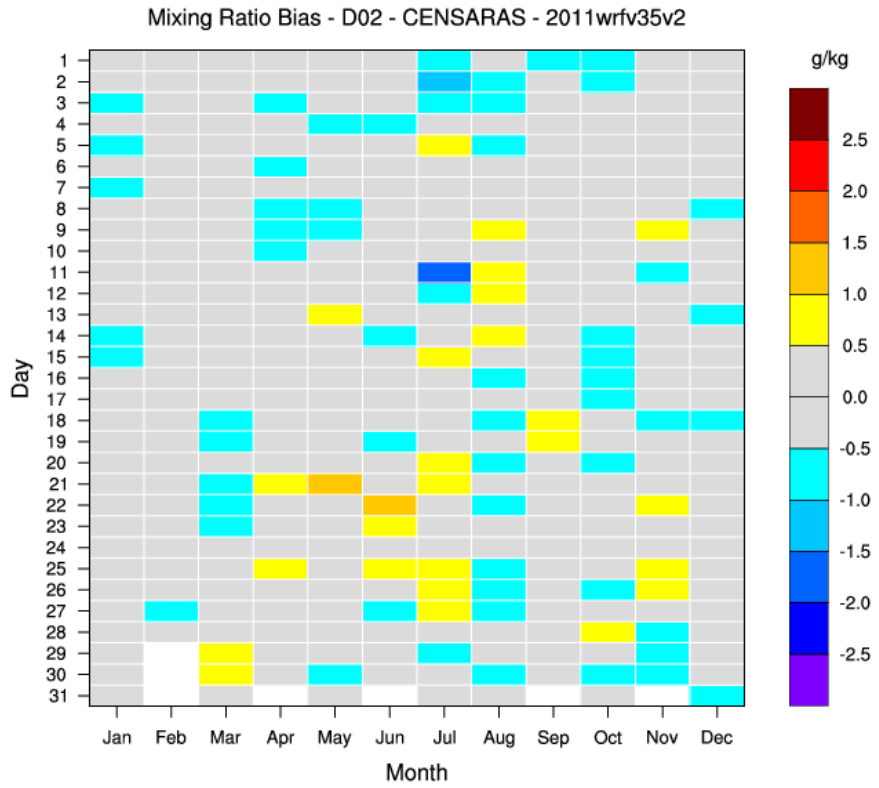

Figure B-38. Bakergram showing daily bias for 2-m mixing ratio for the nested domain for the CENSARAS region.

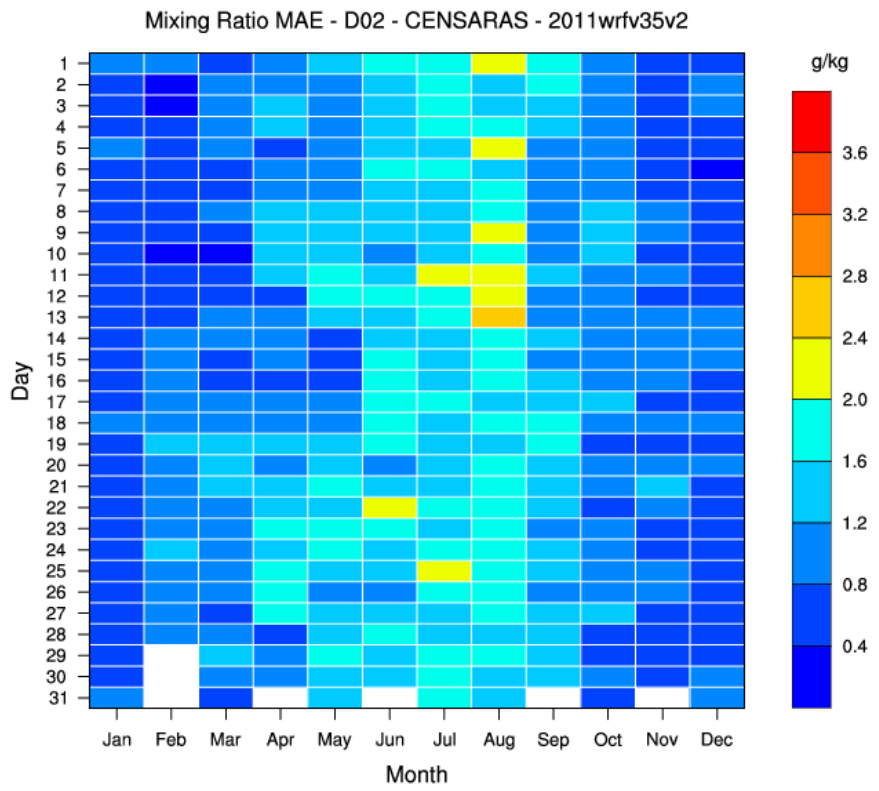

Figure B-39. Bakergram showing daily mean absolute error for 2-m mixing ratio for the nested domain for the CENSARAS region.

Bakergrams – LADCO

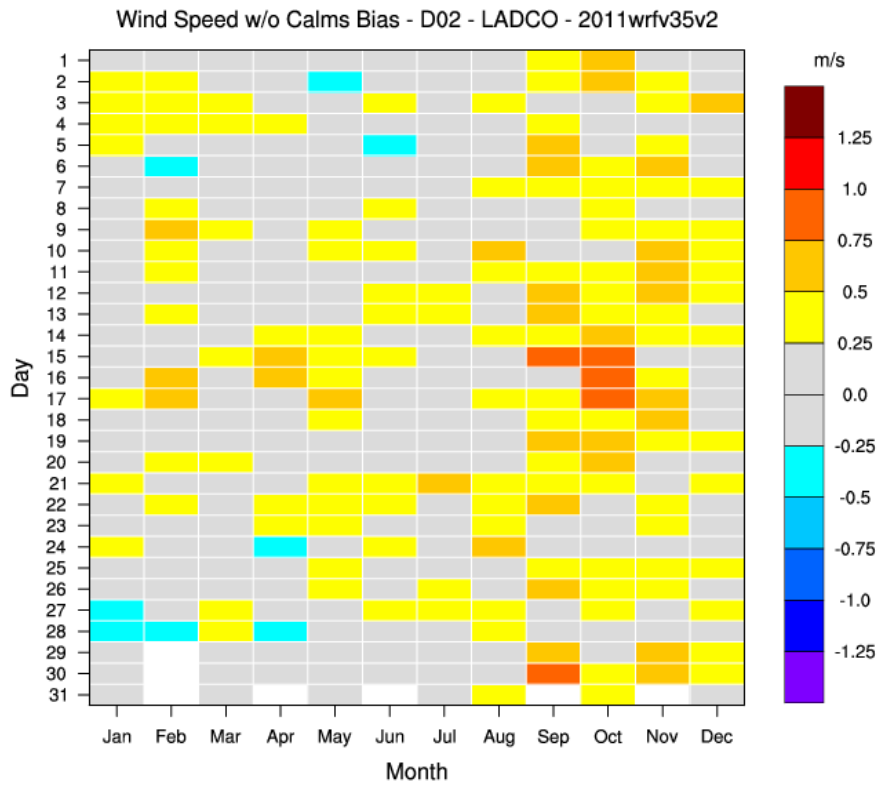

Figure B-40. Bakergram showing daily bias of 10-m wind speed (w/o calm winds included) for the nested domain for the LADCO region.

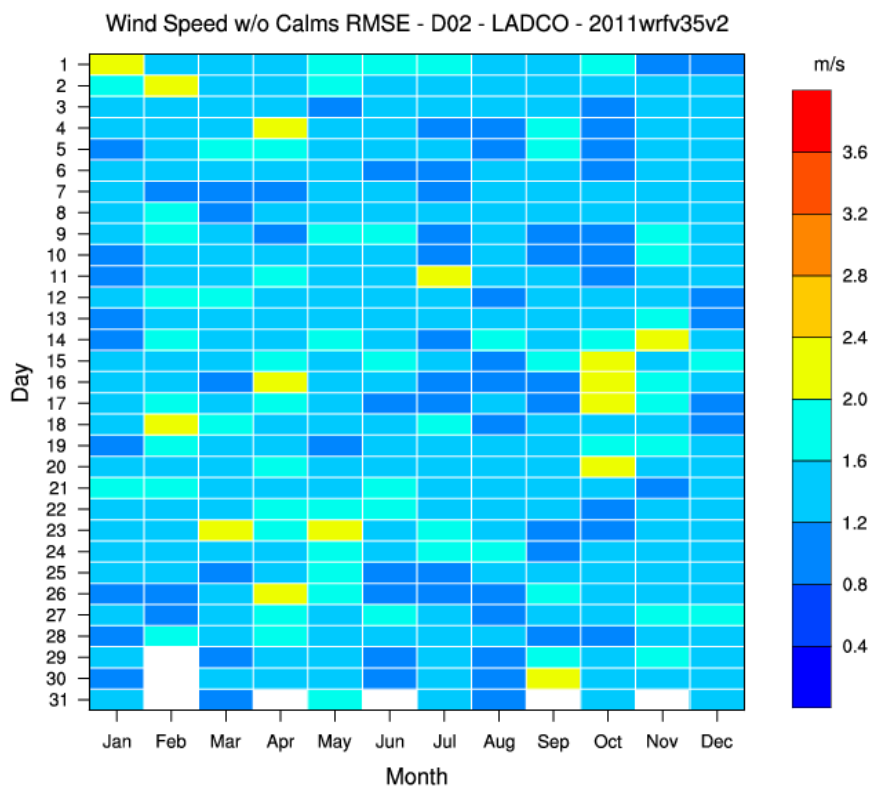

Figure B-41. Bakergram showing daily root mean square error of 10-m wind speed (w/o calm winds included) for the nested domain for the LADCO region.

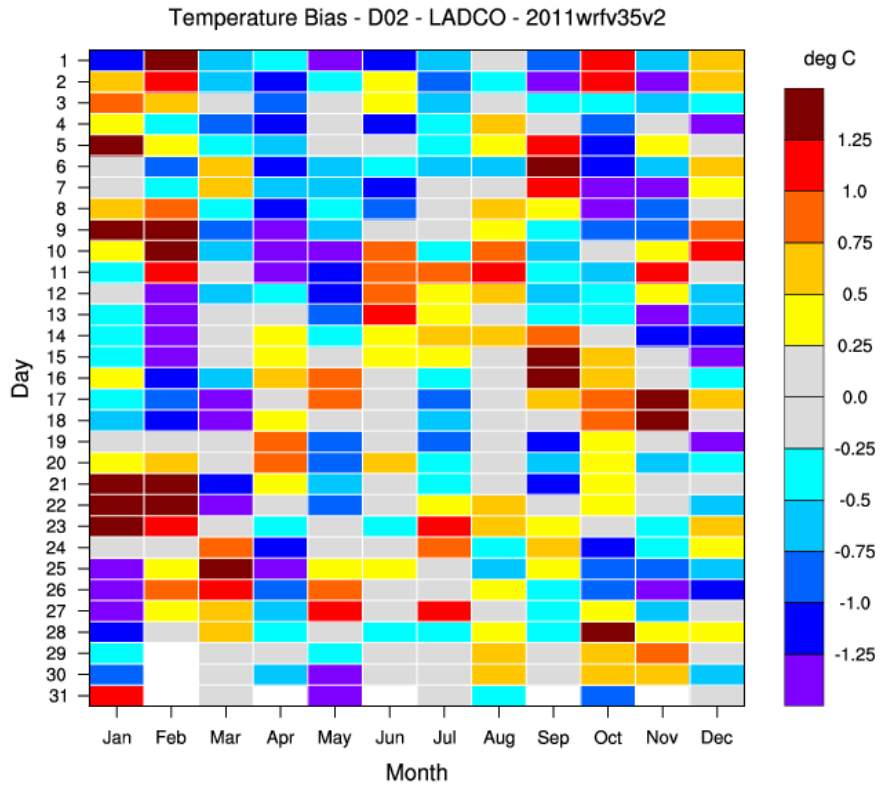

Figure B-42. Bakergram showing daily bias of 2-m temperature for the nested domain for the LADCO region.

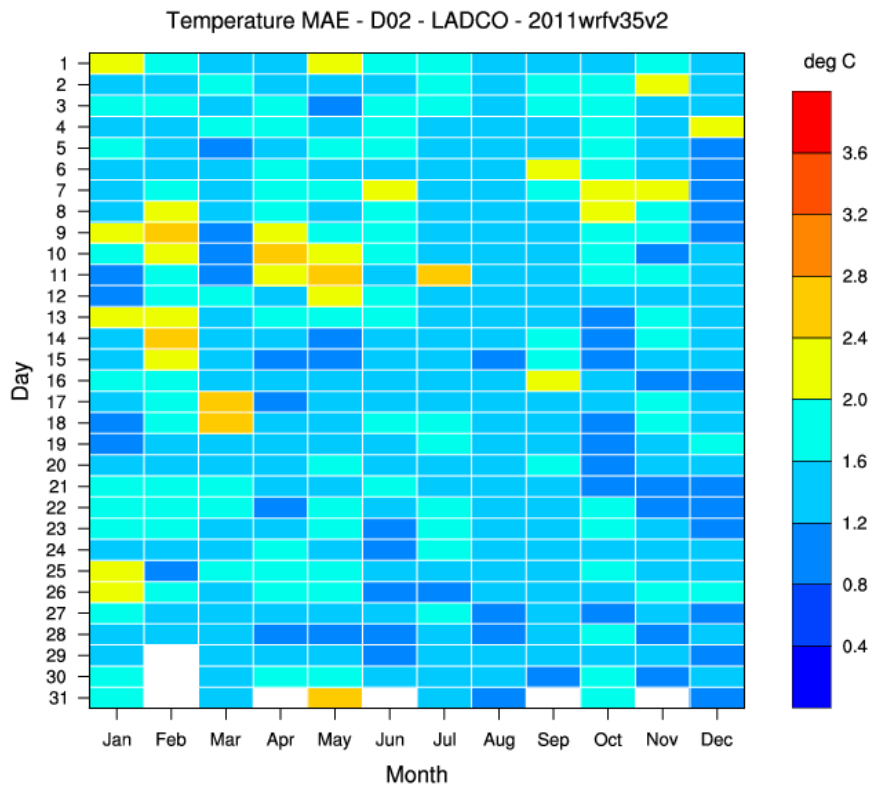

Figure B-43. Bakergram showing daily mean absolute error of 2-m temperature for the nested domain for the LADCO region.

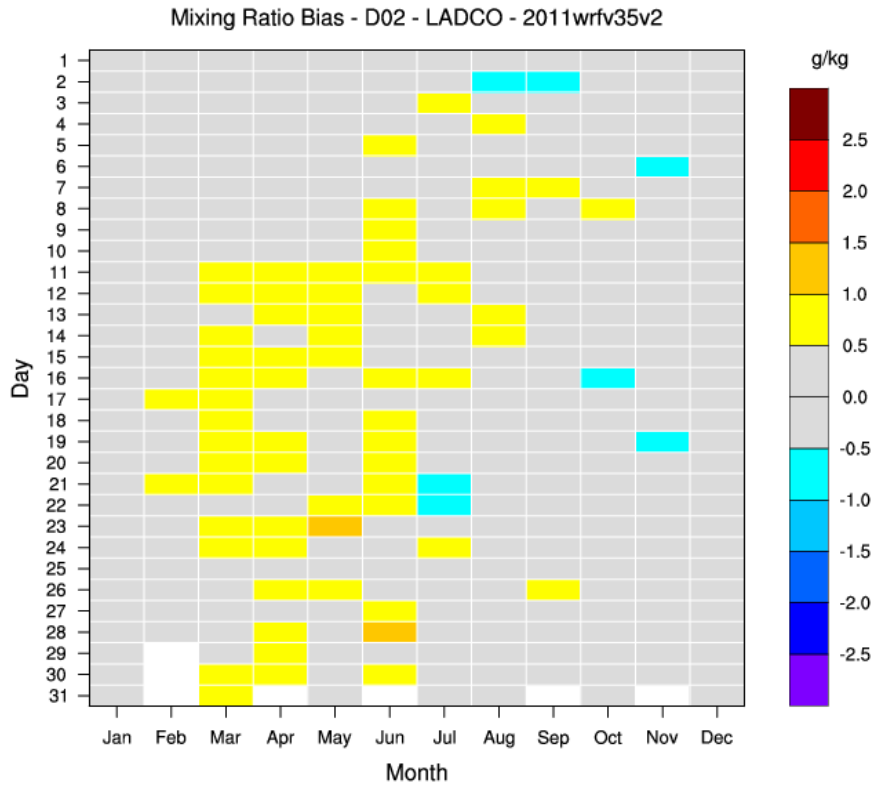

Figure B-44. Bakergram showing daily bias of 2-m mixing ratio for the nested domain for the LADCO region.

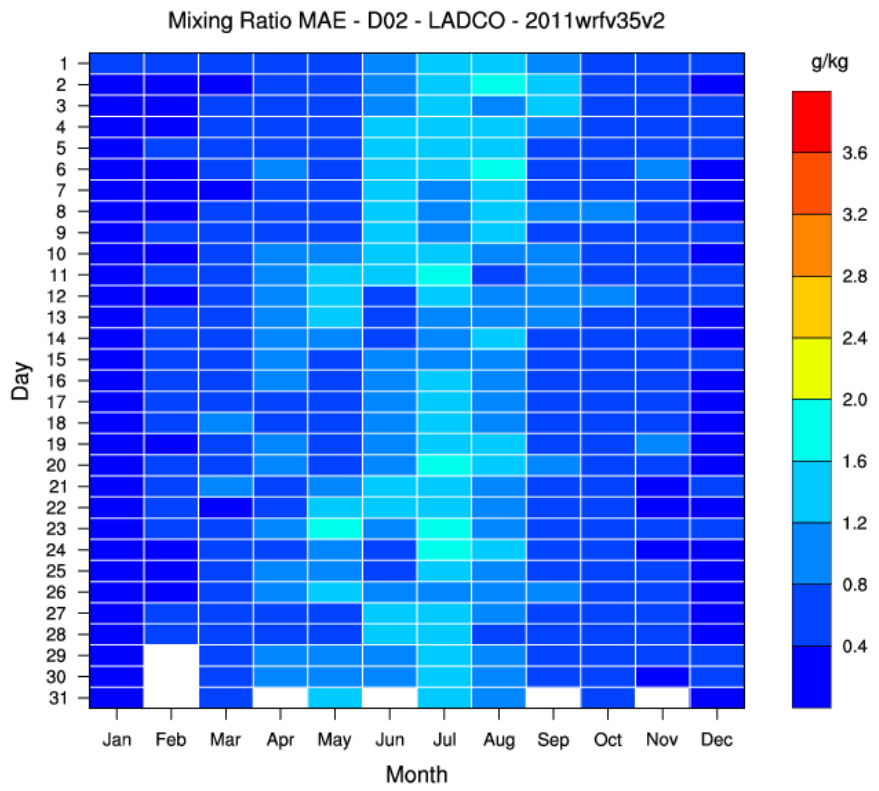

Figure B-45. Bakergram showing daily mean absolute error of 2-m mixing ratio for the nested domain for the LADCO region.

Hourly Timeseries – CENSARAN

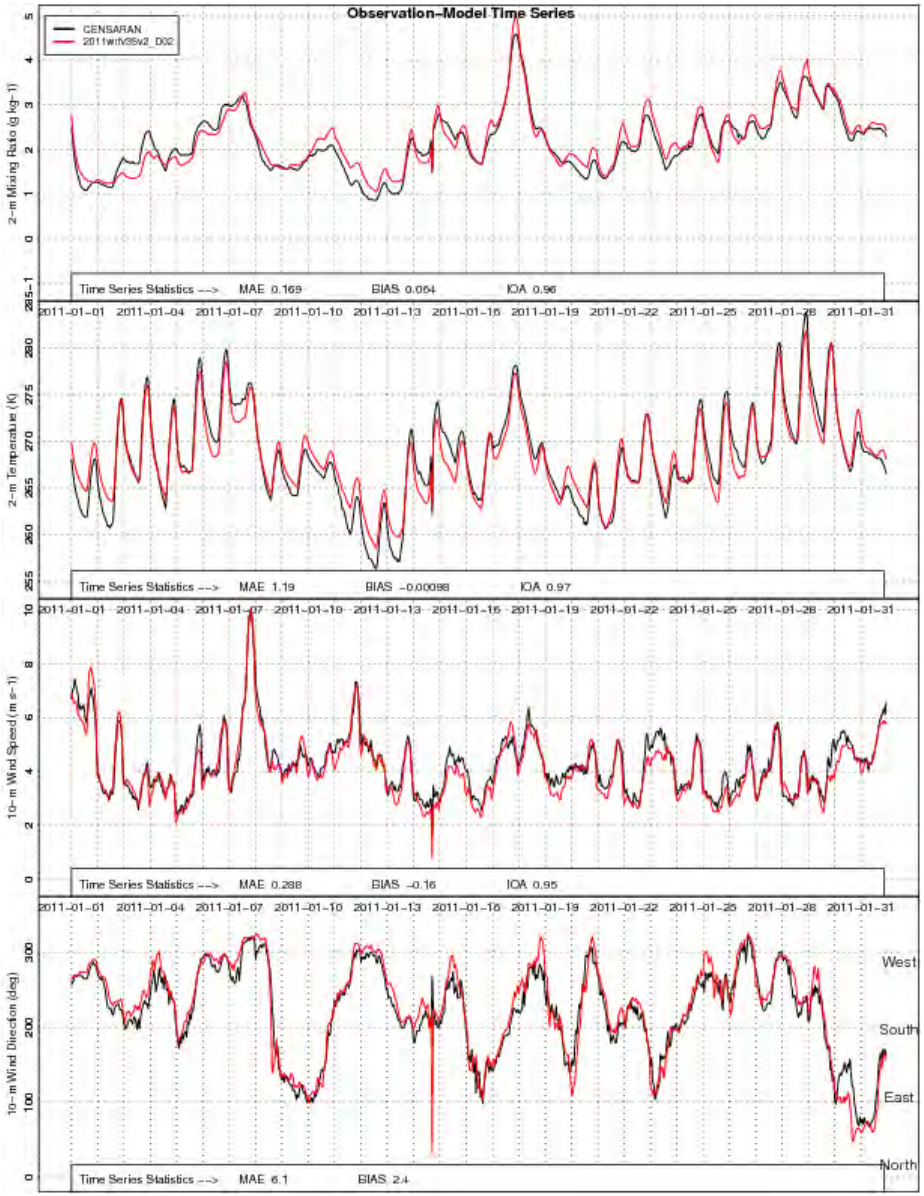

Figure B-46. Hourly timeseries for mean observed and modeled 2-m mixing ratio, 2-m temperature, and 10-m wind speed and direction during January 2011 for the CENSARAN region.

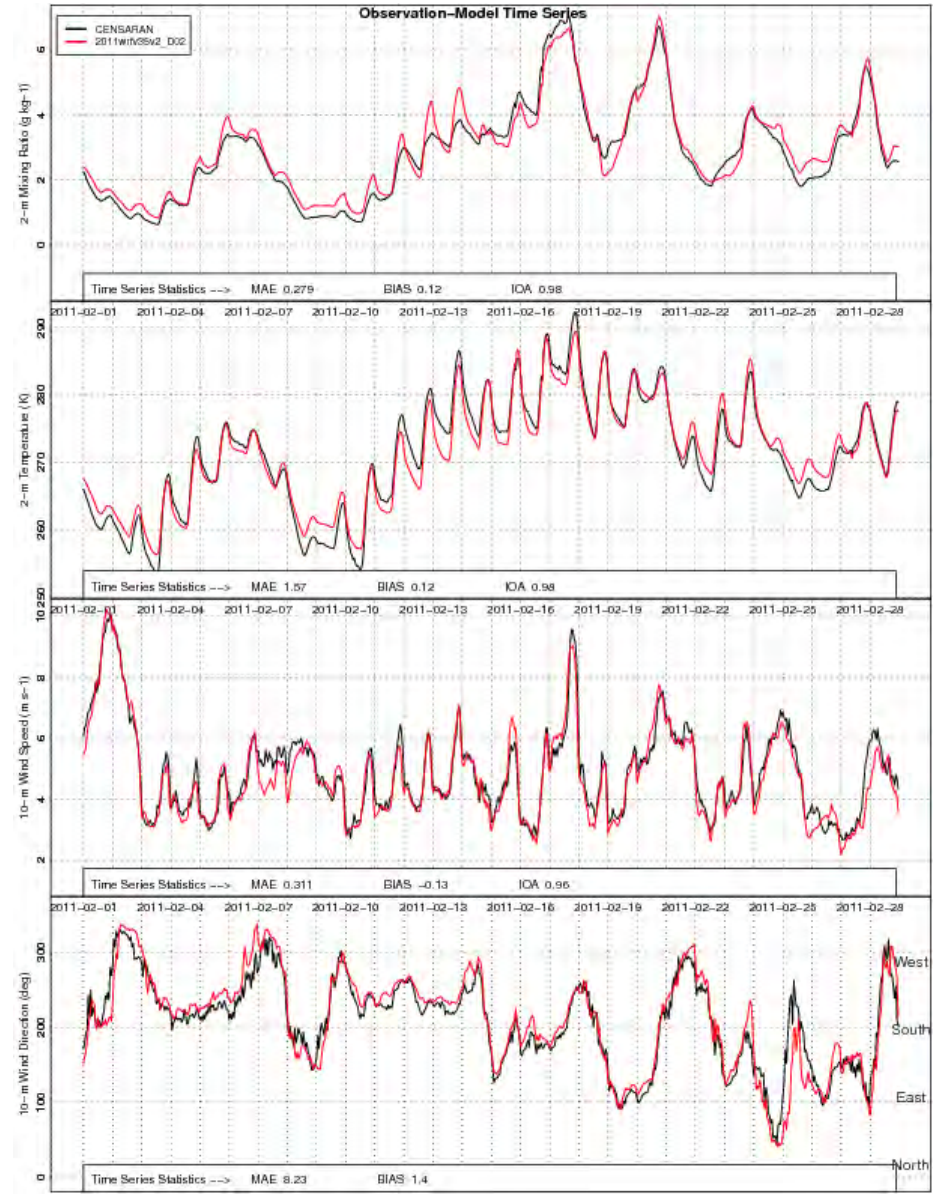

Figure B-47. Hourly timeseries for mean observed and modeled 2-m mixing ratio, 2-m temperature, and 10-m wind speed and direction during February 2011 for the CENSARAN region.

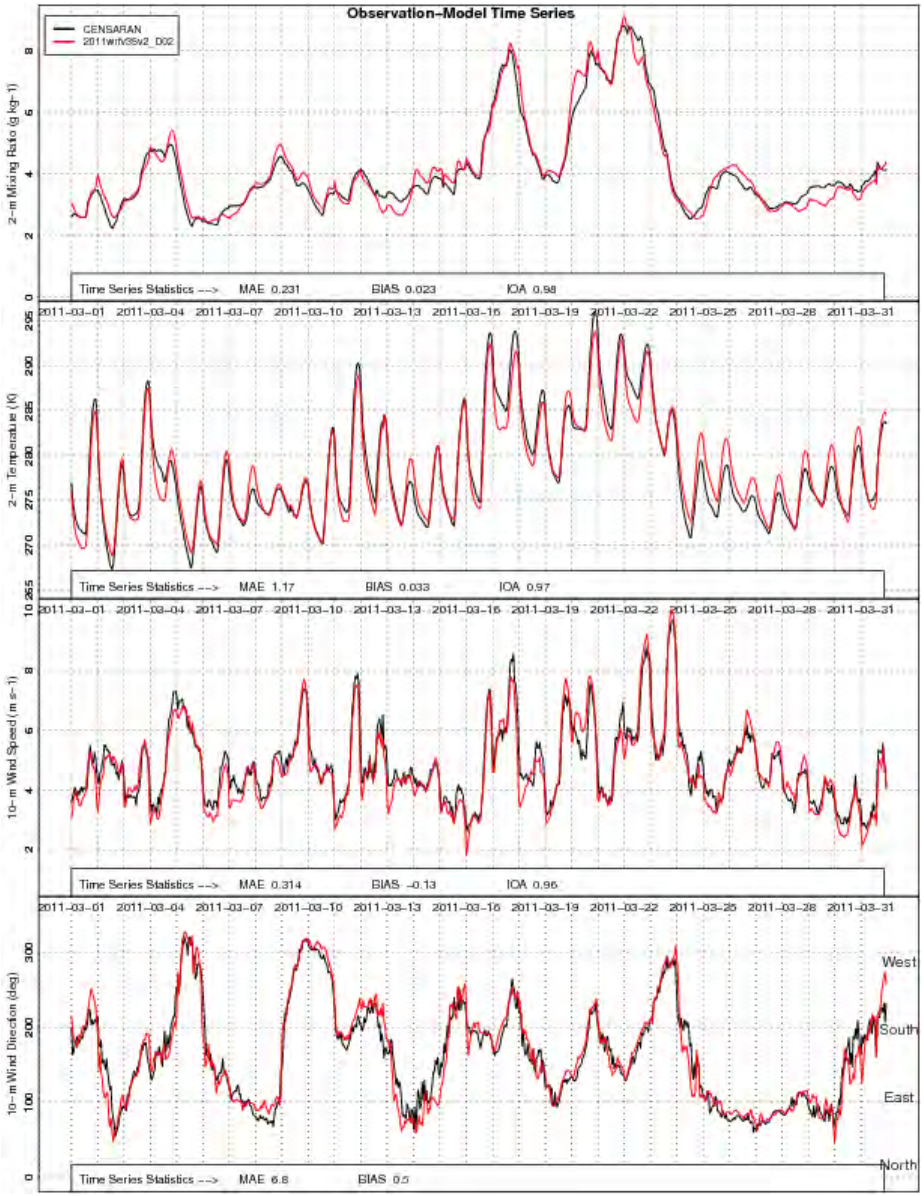

Figure B-48. Hourly timeseries for mean observed and modeled 2-m mixing ratio, 2-m temperature, and 10-m wind speed and direction during March 2011 for the CENSARAN region.

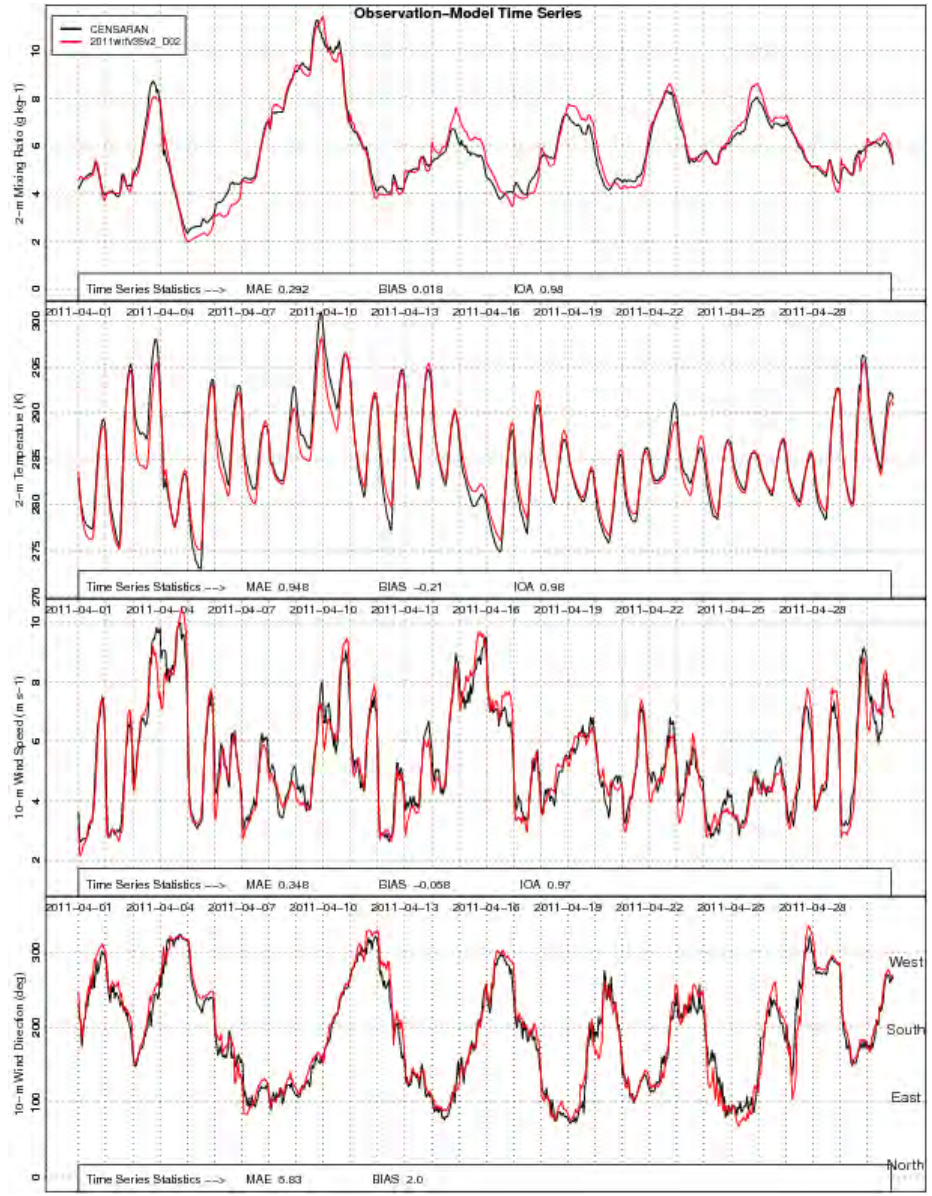

Figure B-49. Hourly timeseries for mean observed and modeled 2-m mixing ratio, 2-m temperature, and 10-m wind speed and direction during April 2011 for the CENSARAN region.

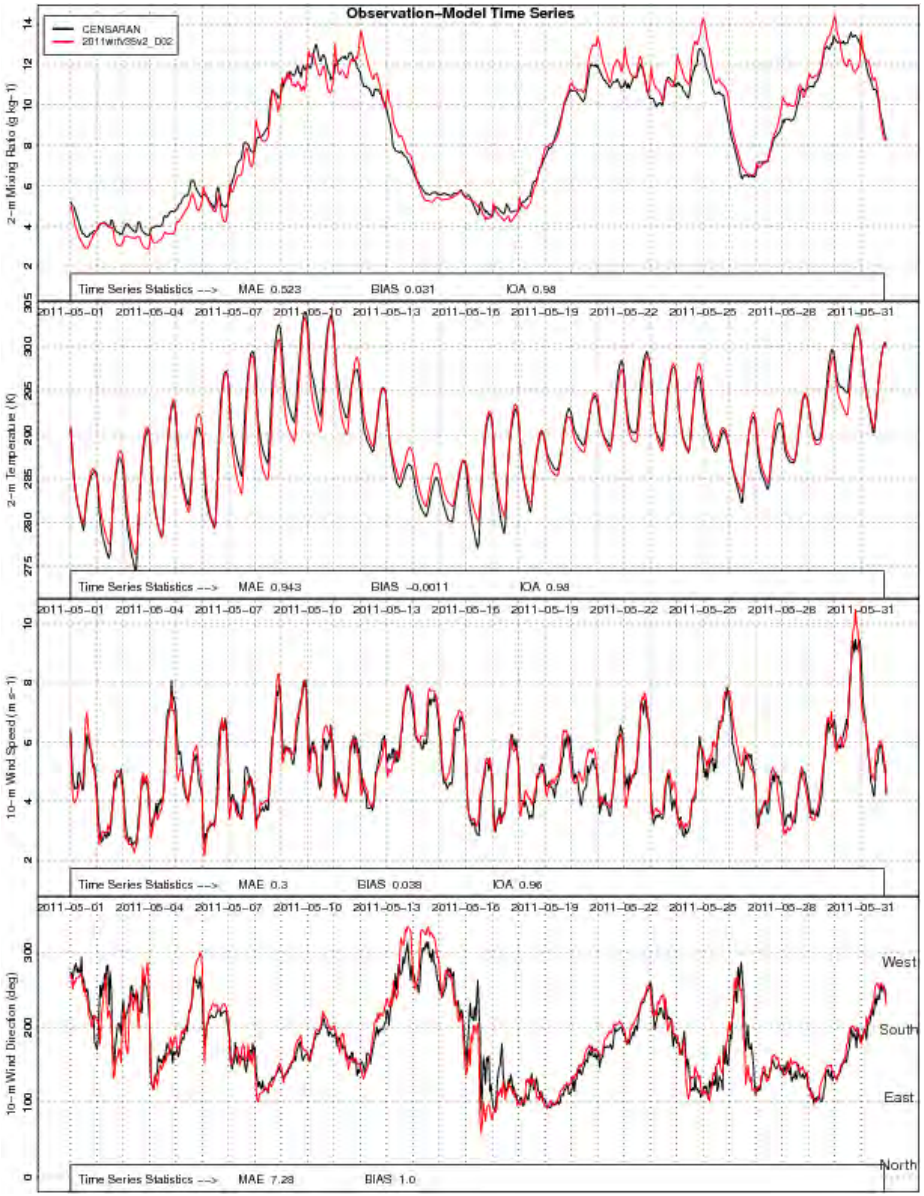

Figure B-50. Hourly timeseries for mean observed and modeled 2-m mixing ratio, 2-m temperature, and 10-m wind speed and direction during May 2011 for the CENSARAN region.

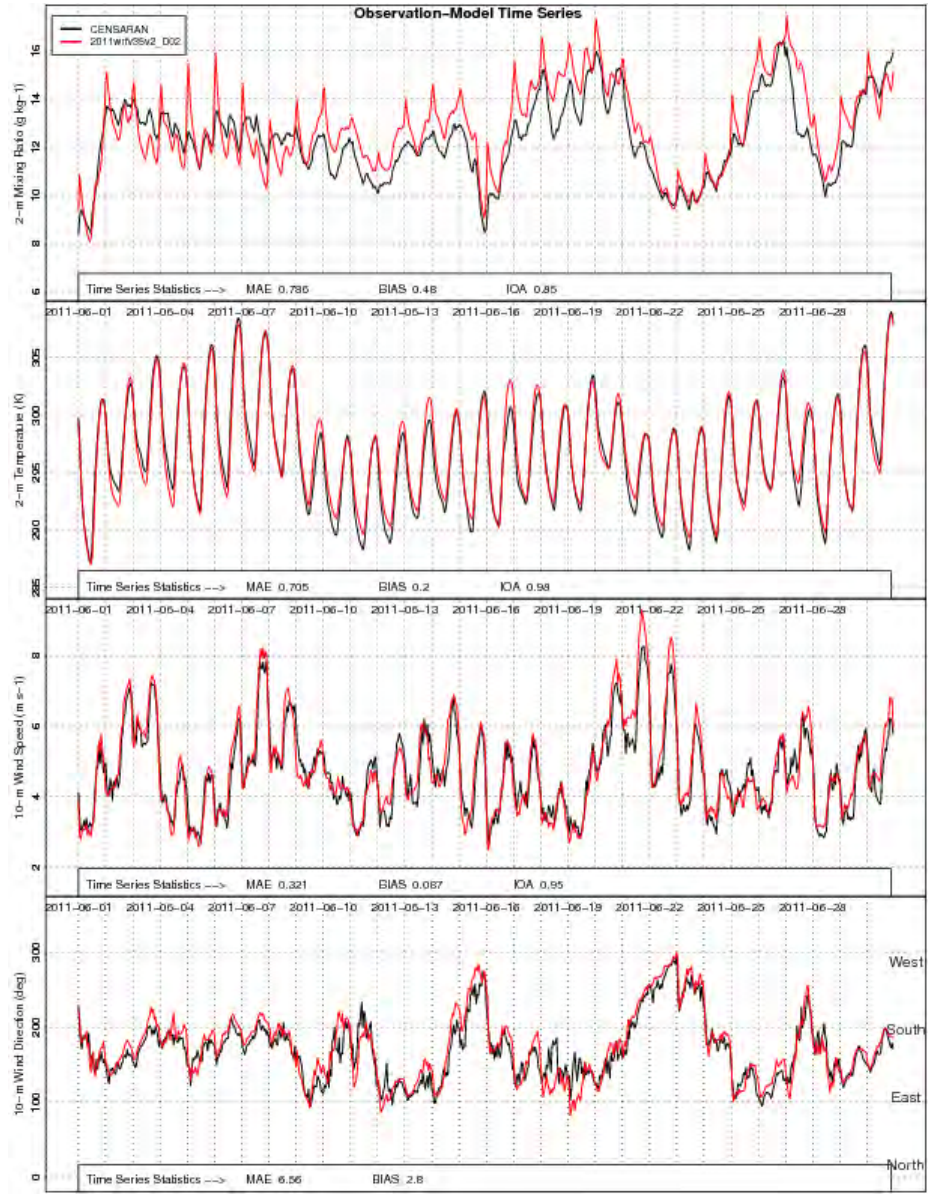

Figure B-51. Hourly timeseries for mean observed and modeled 2-m mixing ratio, 2-m temperature, and 10-m wind speed and direction during June 2011 for the CENSARAN region.

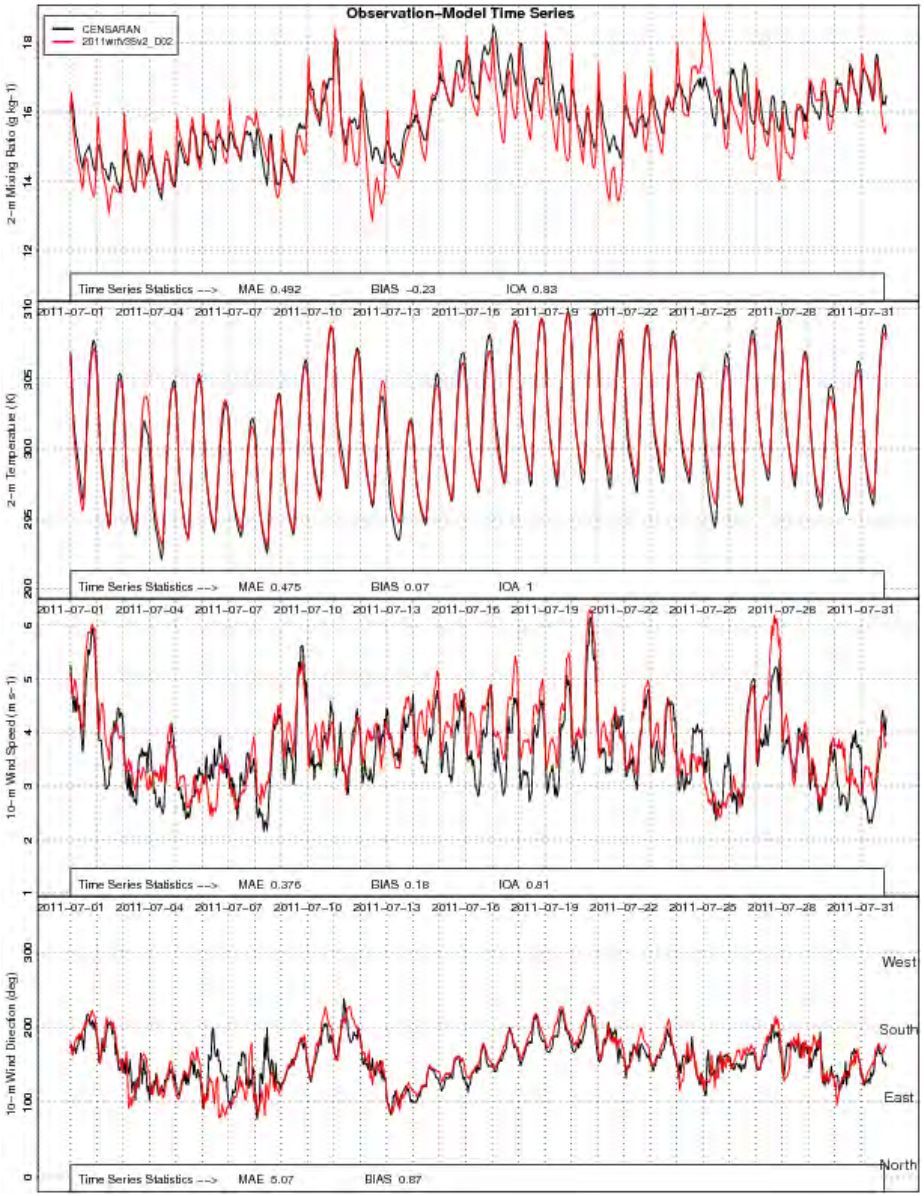

Figure B-52. Hourly timeseries for mean observed and modeled 2-m mixing ratio, 2-m temperature, and 10-m wind speed and direction during July 2011 for the CENSARAN region.

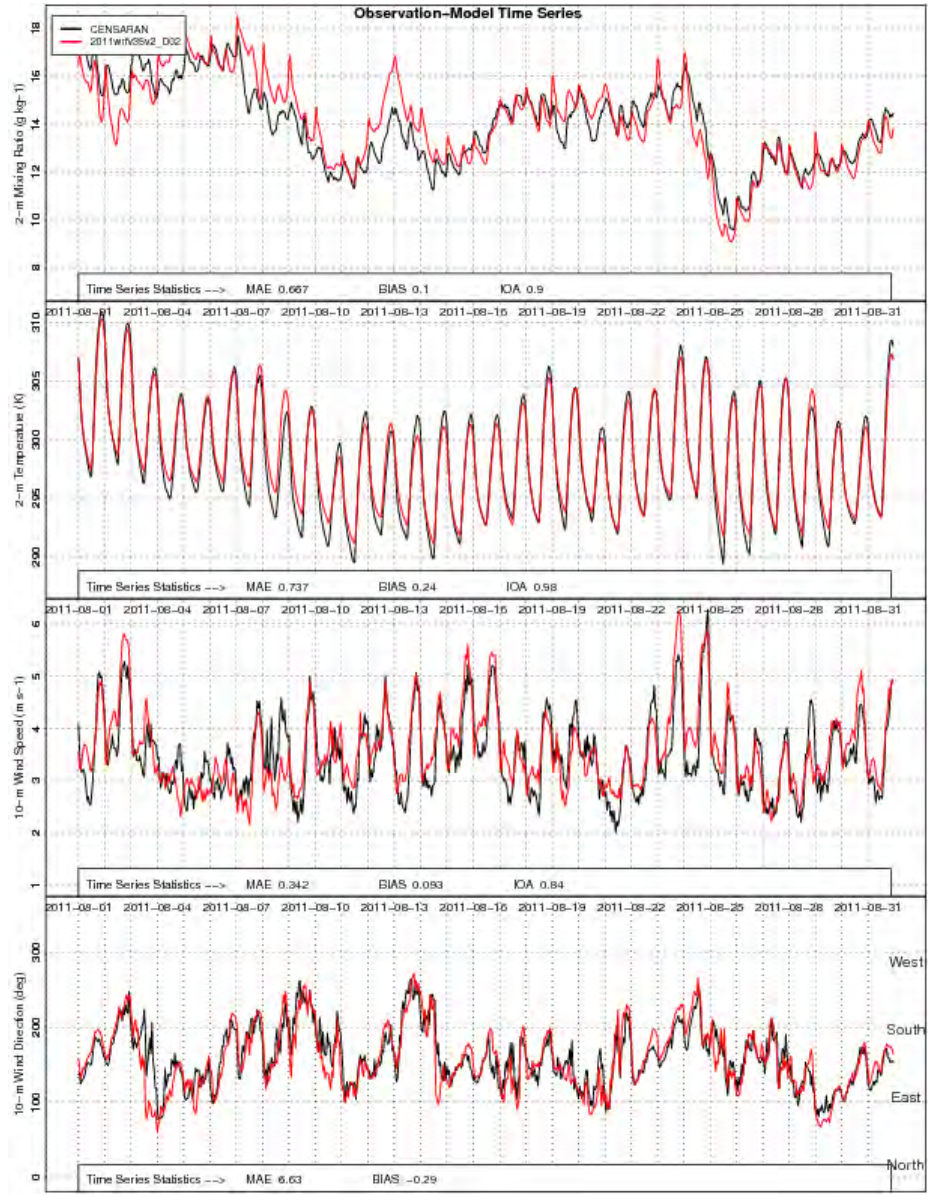

Figure B-53. Hourly timeseries for mean observed and modeled 2-m mixing ratio, 2-m temperature, and 10-m wind speed and direction during August 2011 for the CENSARAN region.

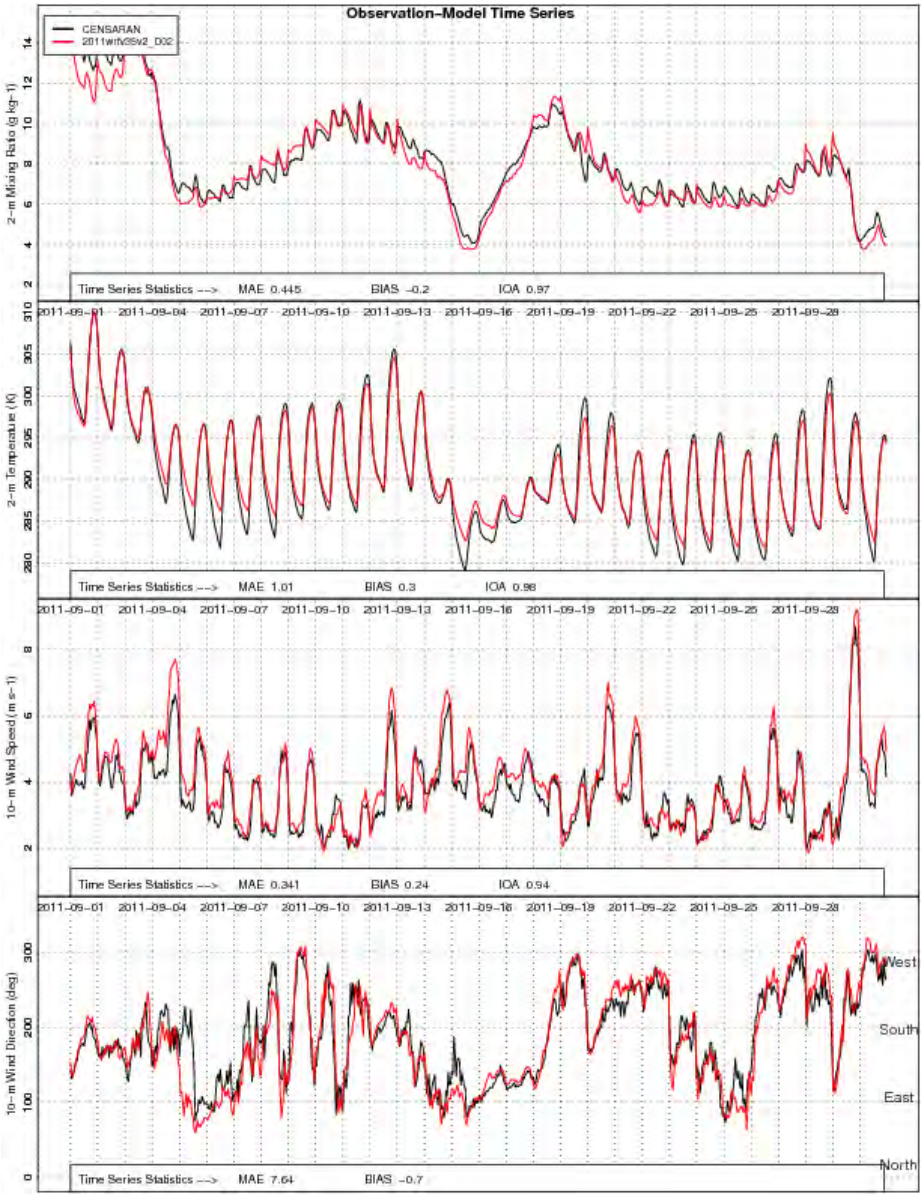

Figure B-54. Hourly timeseries for mean observed and modeled 2-m mixing ratio, 2-m temperature, and 10-m wind speed and direction during September 2011 for the CENSARAN region.

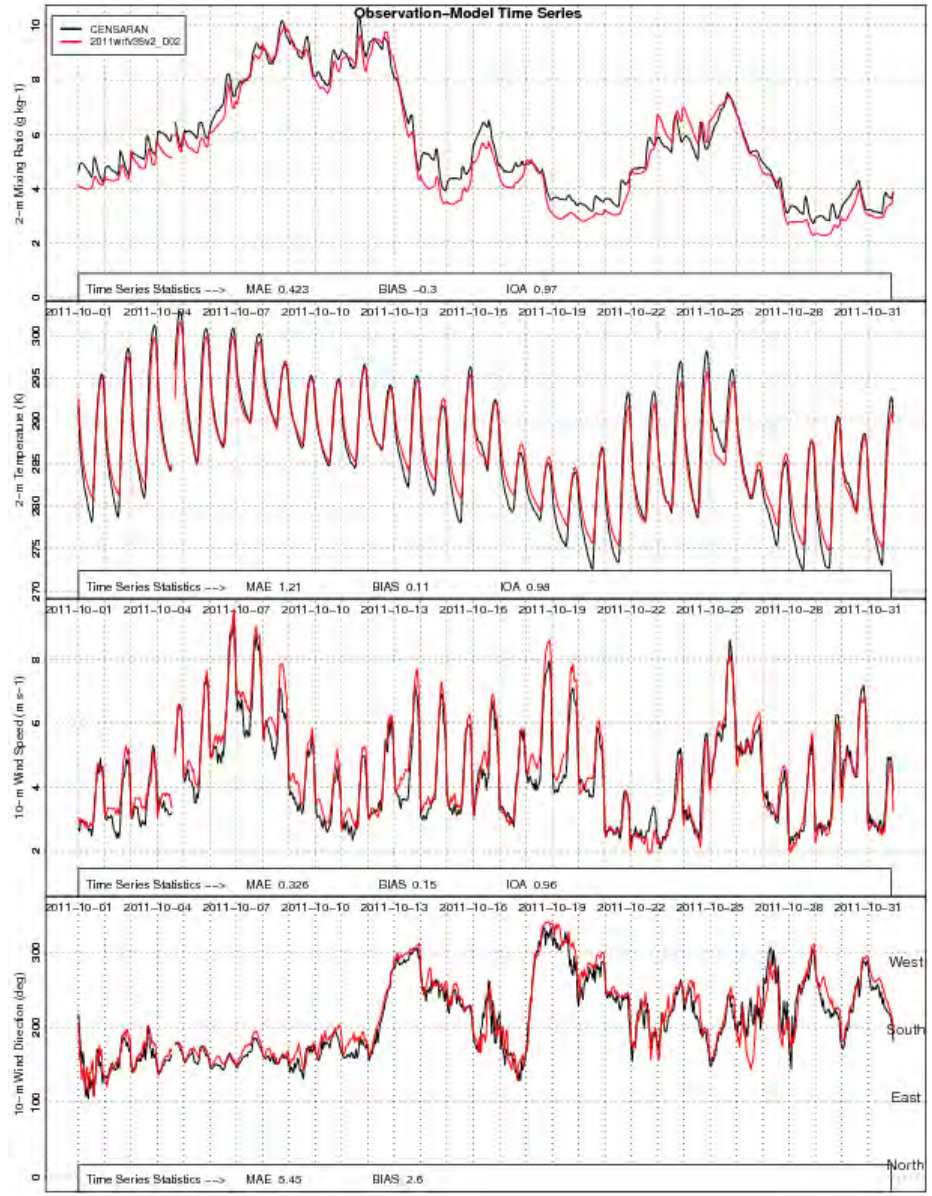

Figure B-55. Hourly timeseries for mean observed and modeled 2-m mixing ratio, 2-m temperature, and 10-m wind speed and direction during October 2011 for the CENSARAN region.

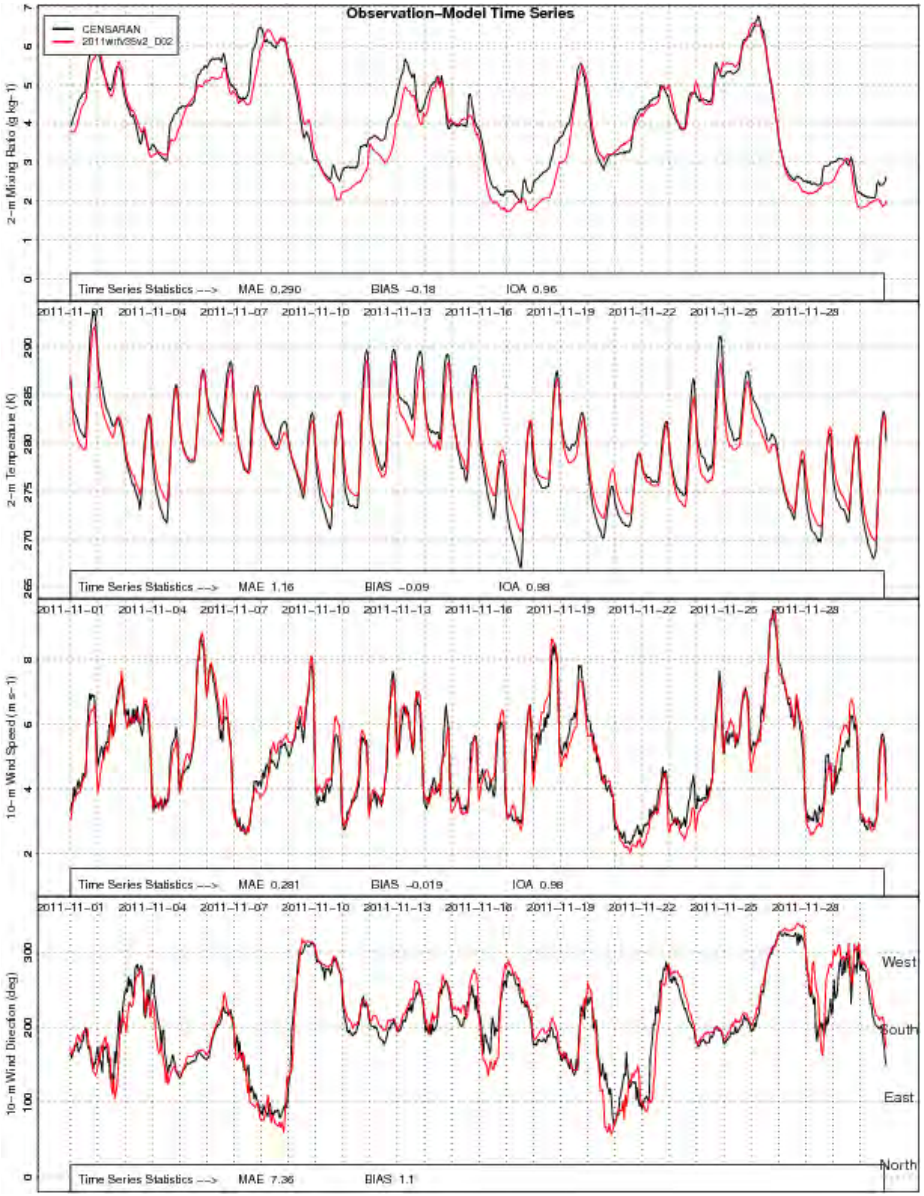

Figure B-56. Hourly timeseries for mean observed and modeled 2-m mixing ratio, 2-m temperature, and 10-m wind speed and direction during November 2011 for the CENSARAN region.

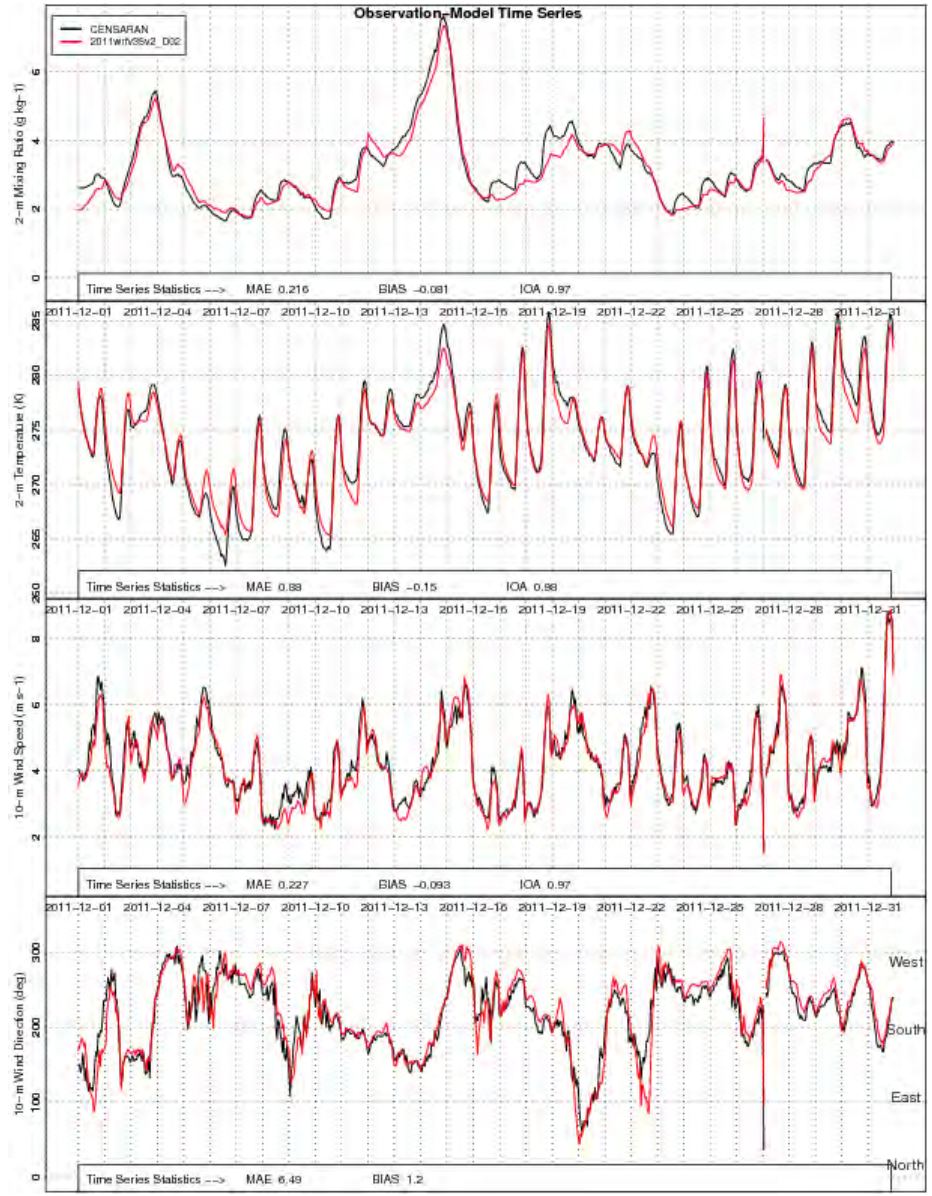

Figure B-57. Hourly timeseries for mean observed and modeled 2-m mixing ratio, 2-m temperature, and 10-m wind speed and direction during December 2011 for the CENSARAN region.

Hourly Timeseries – CENSARAS

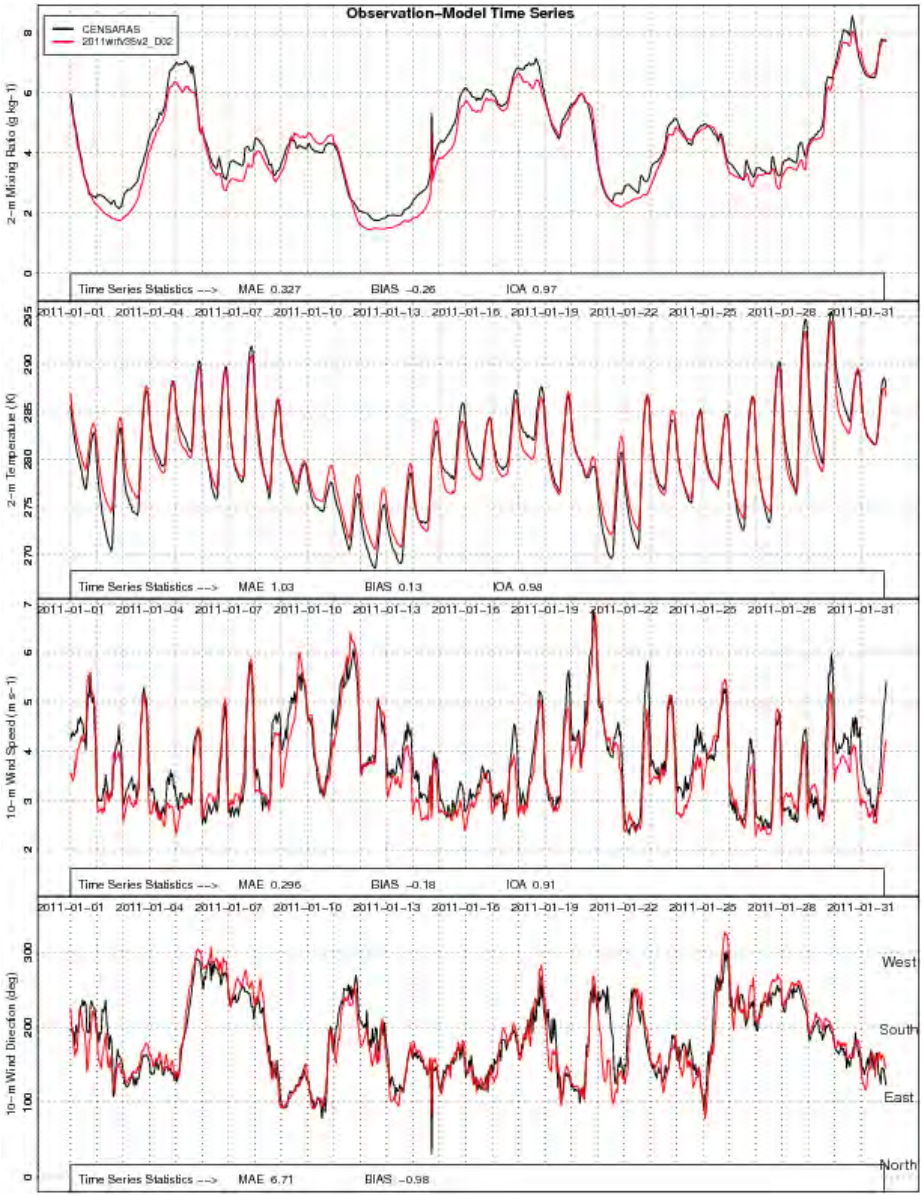

Figure B-58. Hourly timeseries for mean observed and modeled 2-m mixing ratio, 2-m temperature, and 10-m wind speed and direction during January 2011 for the CENSARAS region.

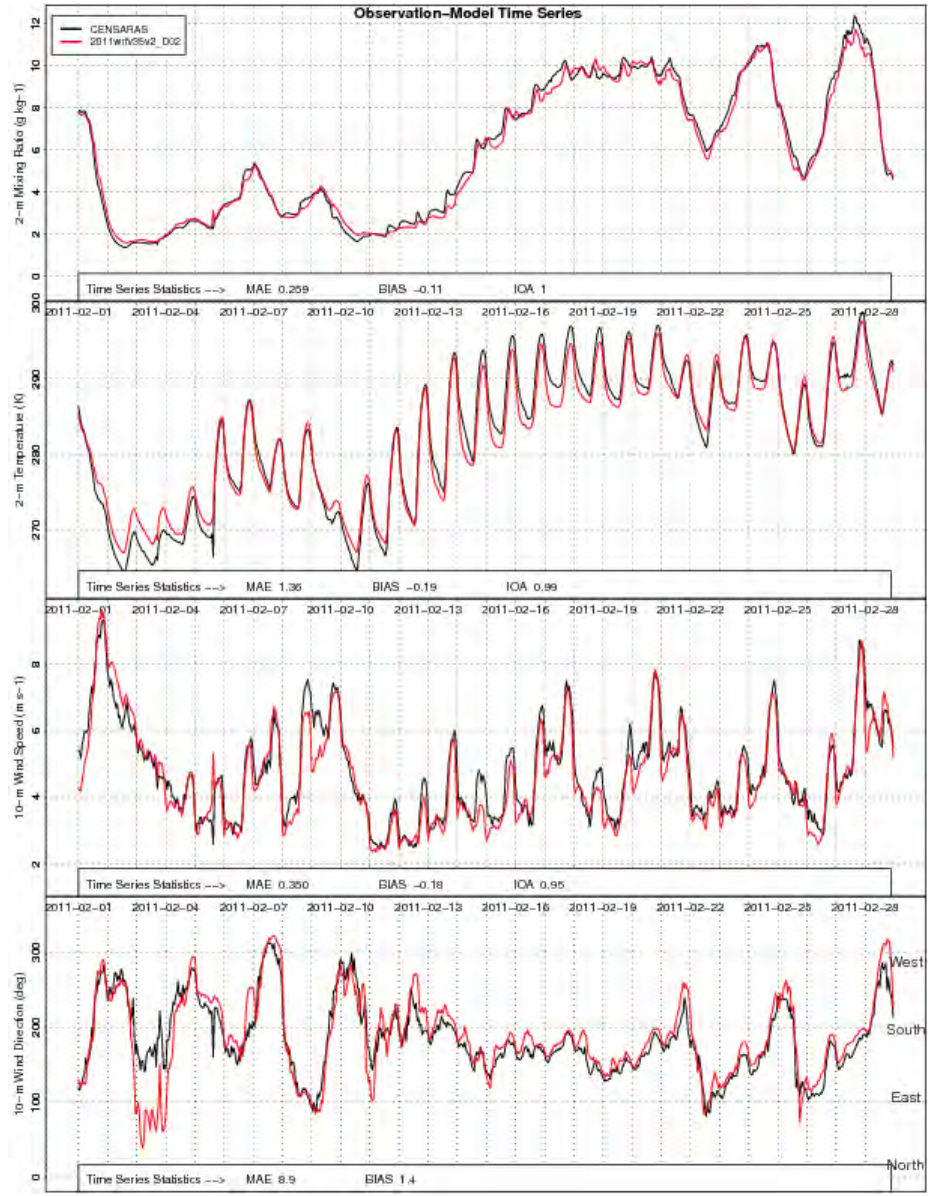

Figure B-59. Hourly timeseries for mean observed and modeled 2-m mixing ratio, 2-m temperature, and 10-m wind speed and direction during February 2011 for the CENSARAS region.

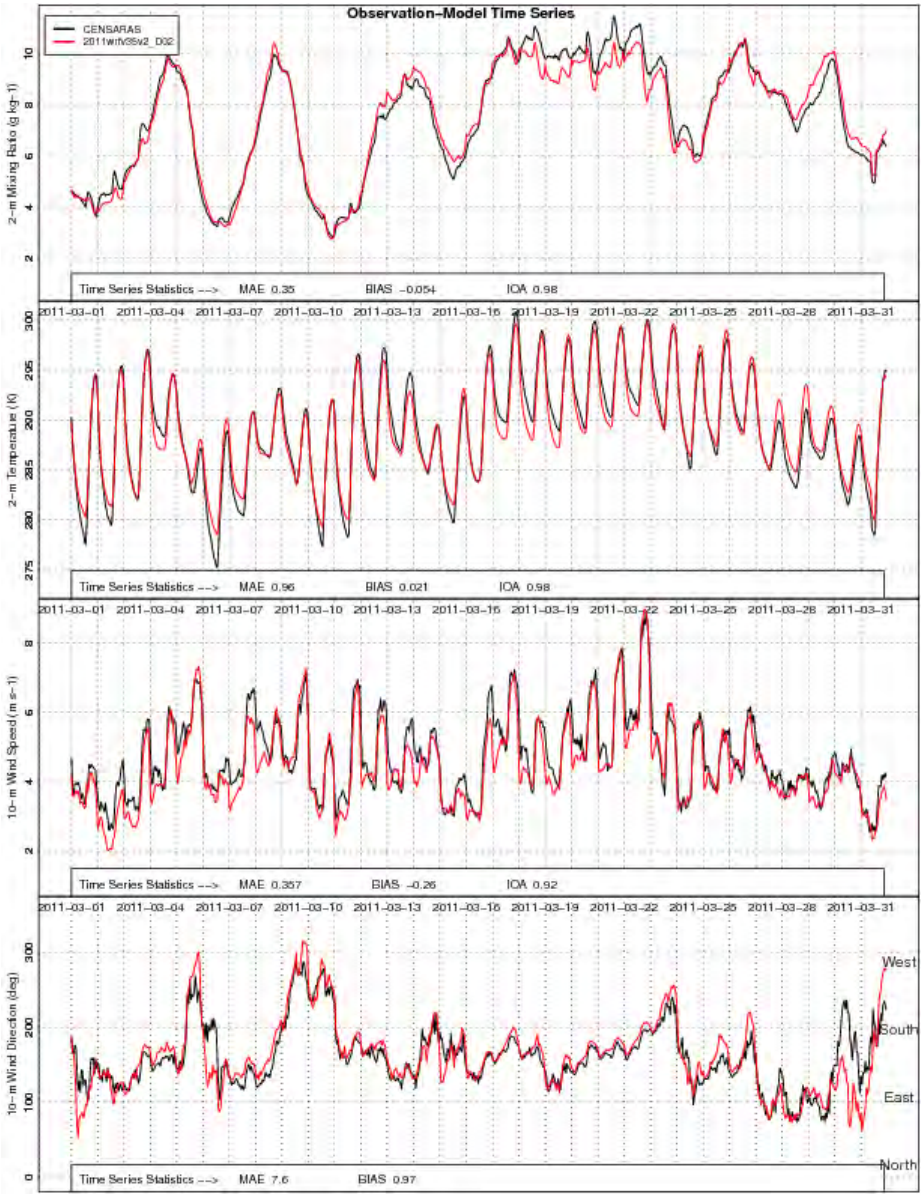

Figure B-60. Hourly timeseries for mean observed and modeled 2-m mixing ratio, 2-m temperature, and 10-m wind speed and direction during March 2011 for the CENSARAS region.

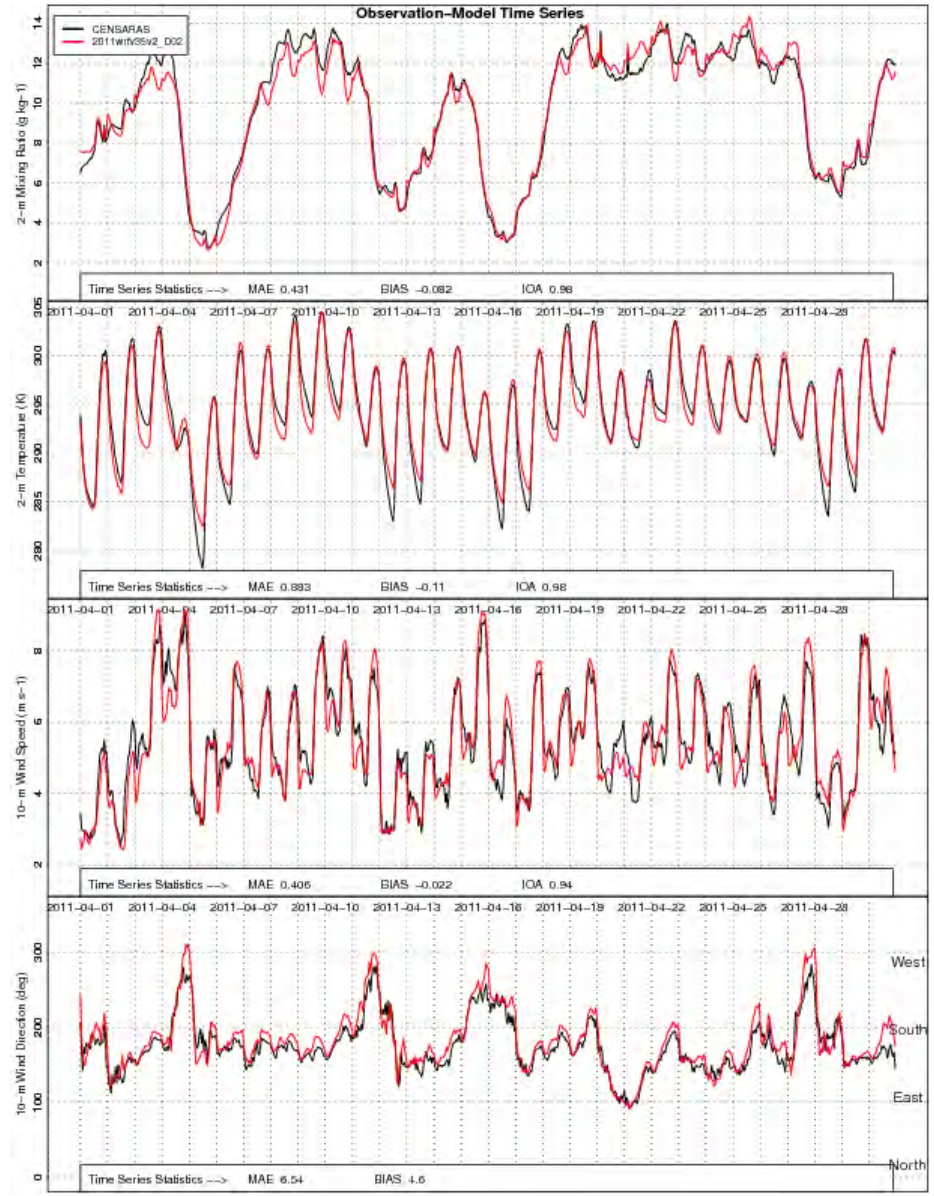

Figure B-61. Hourly timeseries for mean observed and modeled 2-m mixing ratio, 2-m temperature, and 10-m wind speed and direction during April 2011 for the CENSARAS region.

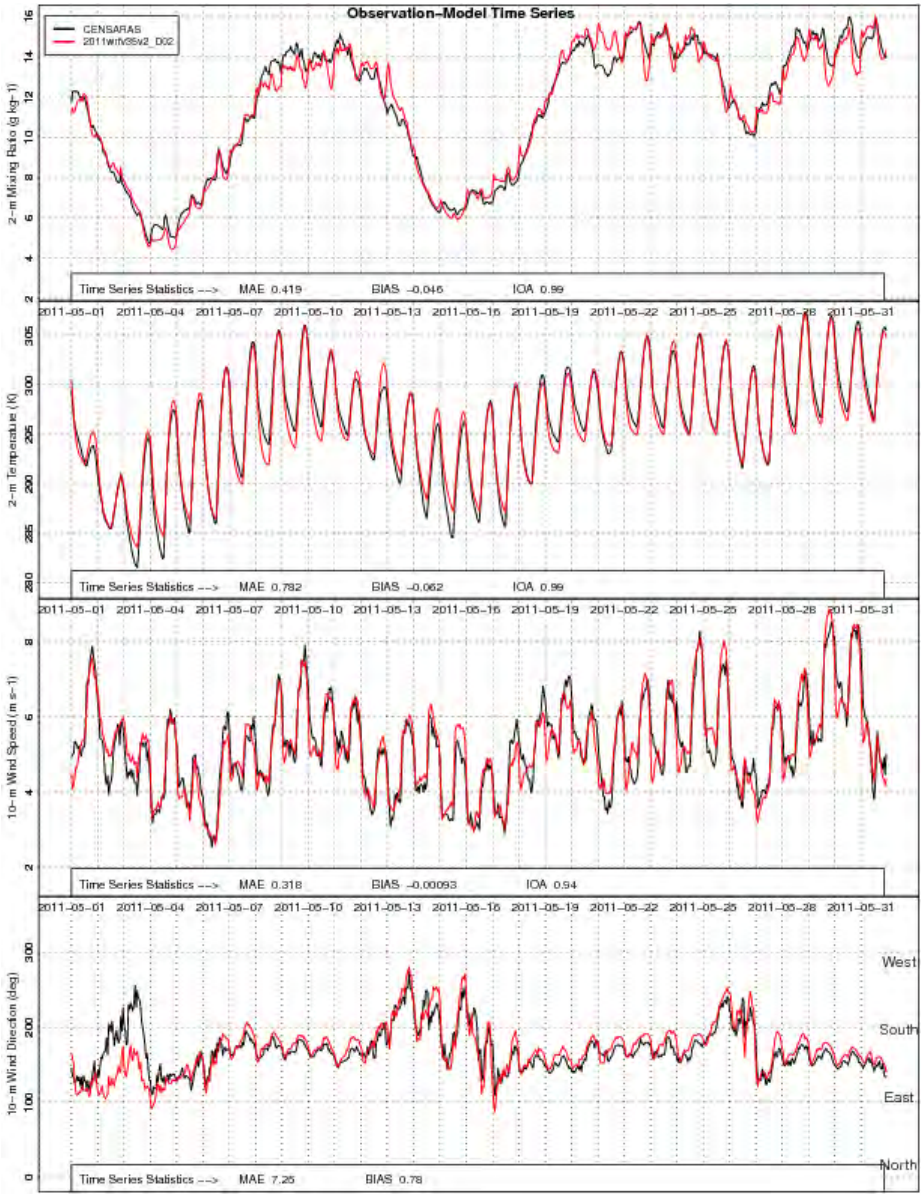

Figure B-62. Hourly timeseries for mean observed and modeled 2-m mixing ratio, 2-m temperature, and 10-m wind speed and direction during May 2011 for the CENSARAS region.

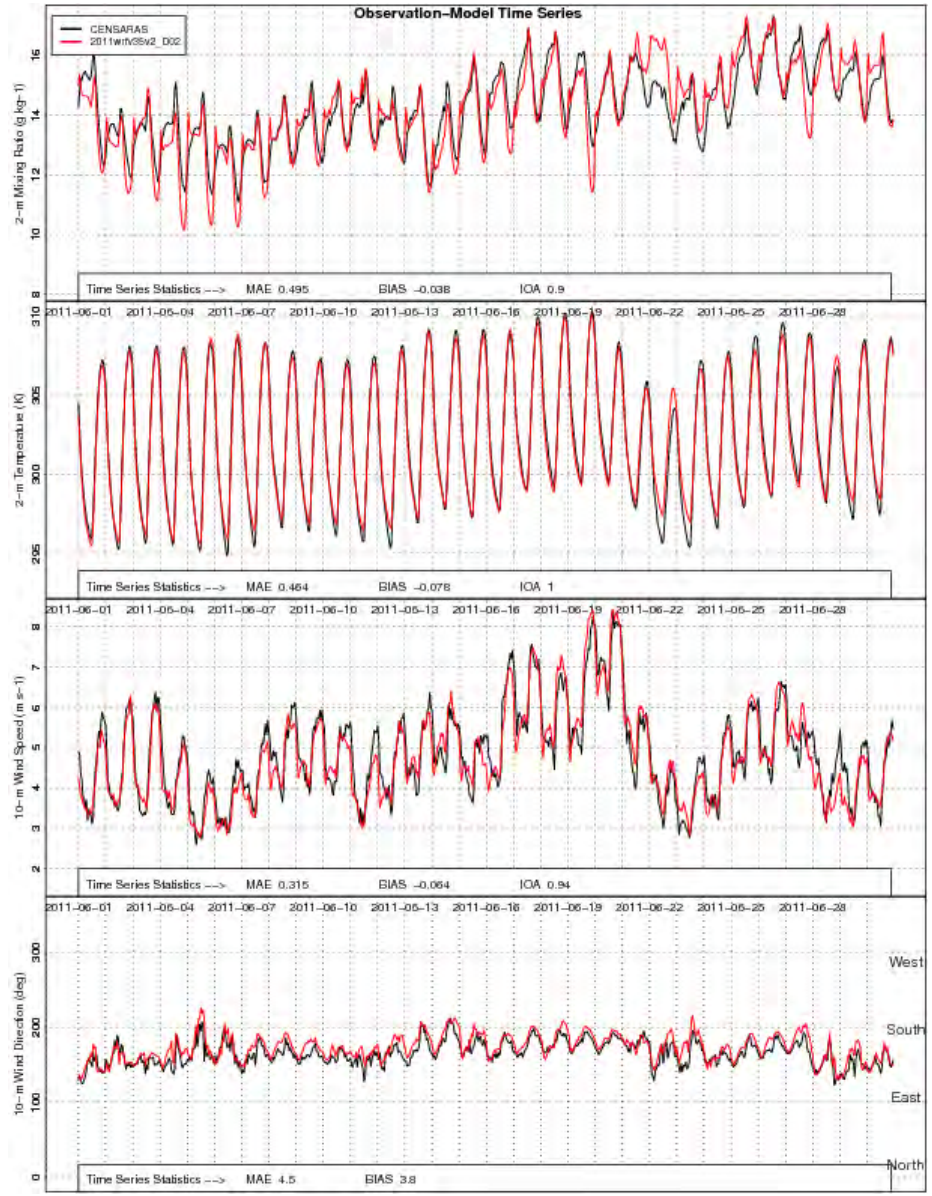

Figure B-63. Hourly timeseries for mean observed and modeled 2-m mixing ratio, 2-m temperature, and 10-m wind speed and direction during June 2011 for the CENSARAS region.

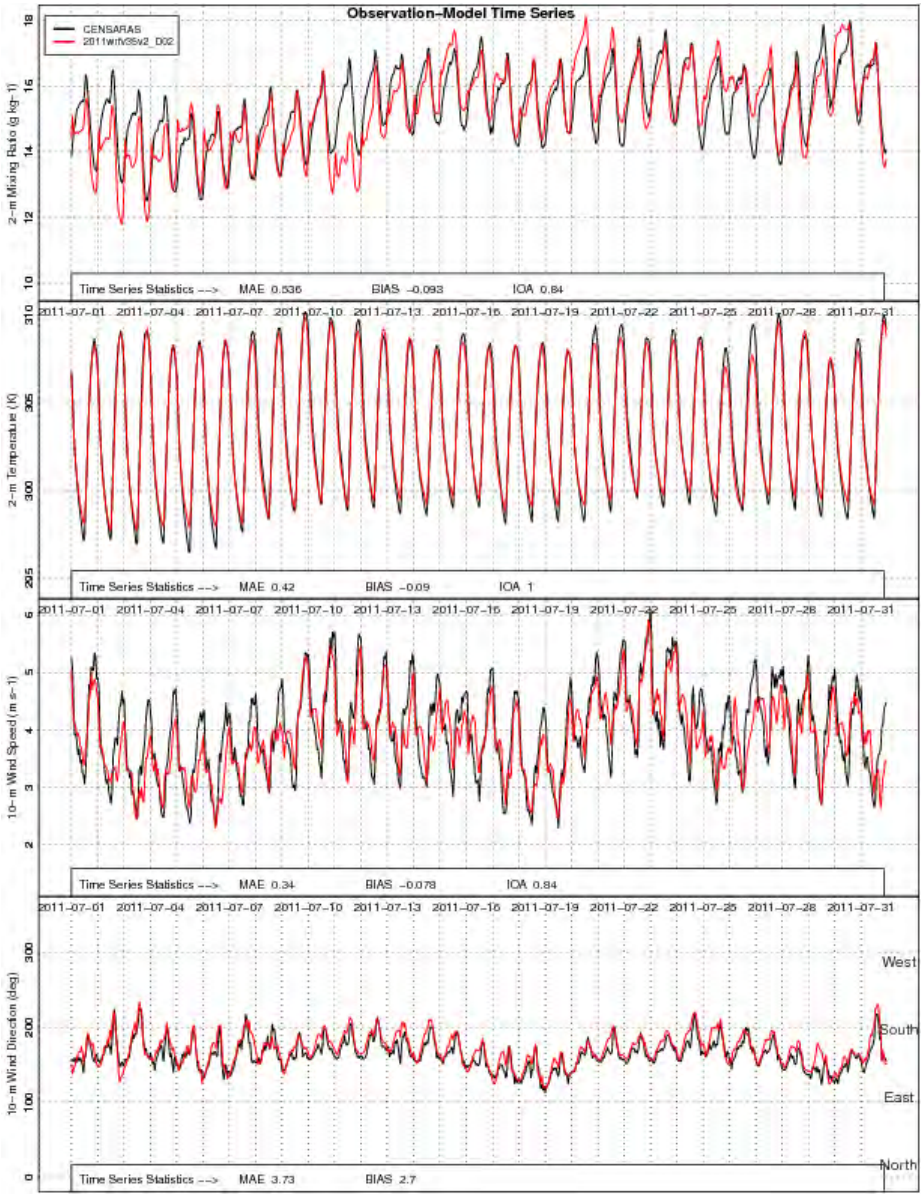

Figure B-64. Hourly timeseries for mean observed and modeled 2-m mixing ratio, 2-m temperature, and 10-m wind speed and direction during July 2011 for the CENSARAS region.

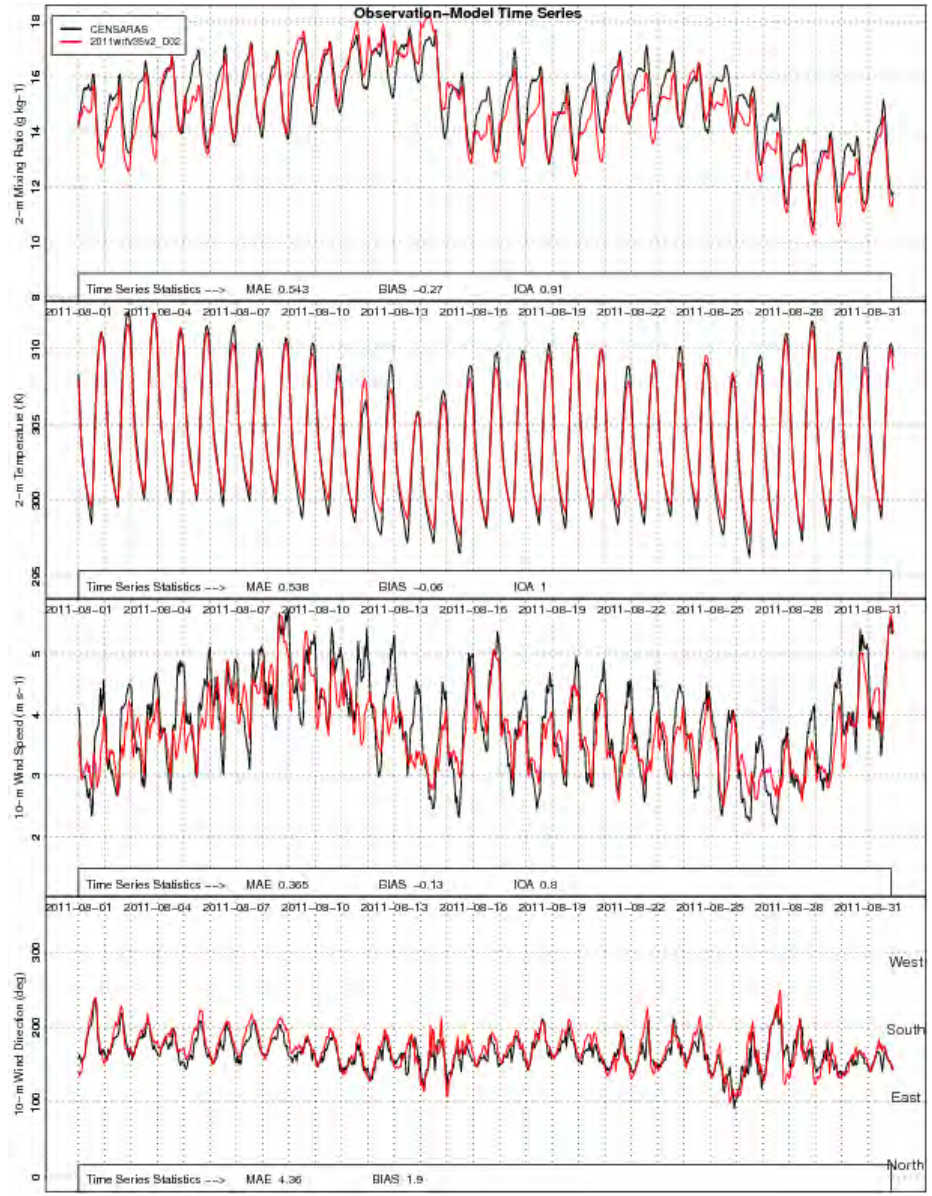

Figure B-65. Hourly timeseries for mean observed and modeled 2-m mixing ratio, 2-m temperature, and 10-m wind speed and direction during August 2011 for the CENSARAS region.

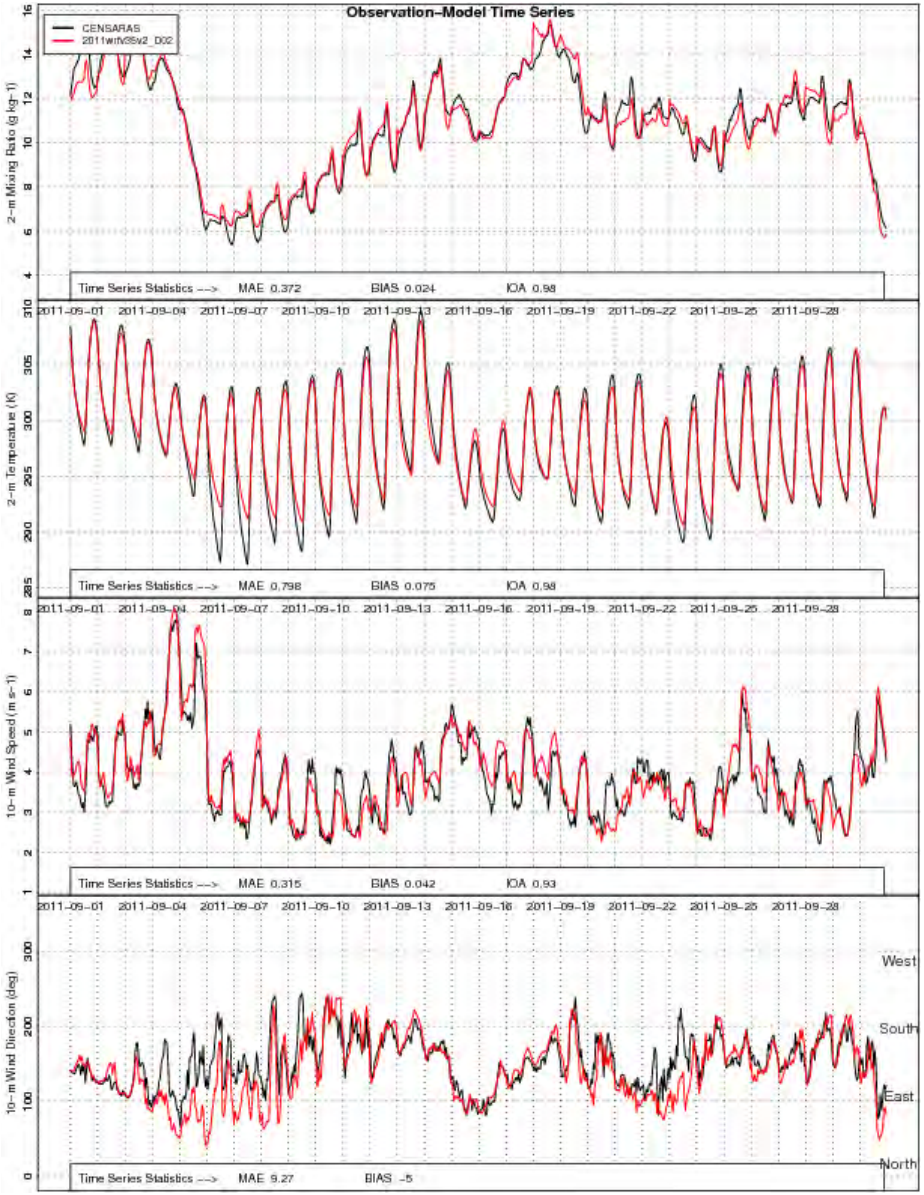

Figure B-66. Hourly timeseries for mean observed and modeled 2-m mixing ratio, 2-m temperature, and 10-m wind speed and direction during September 2011 for the CENSARAS region.

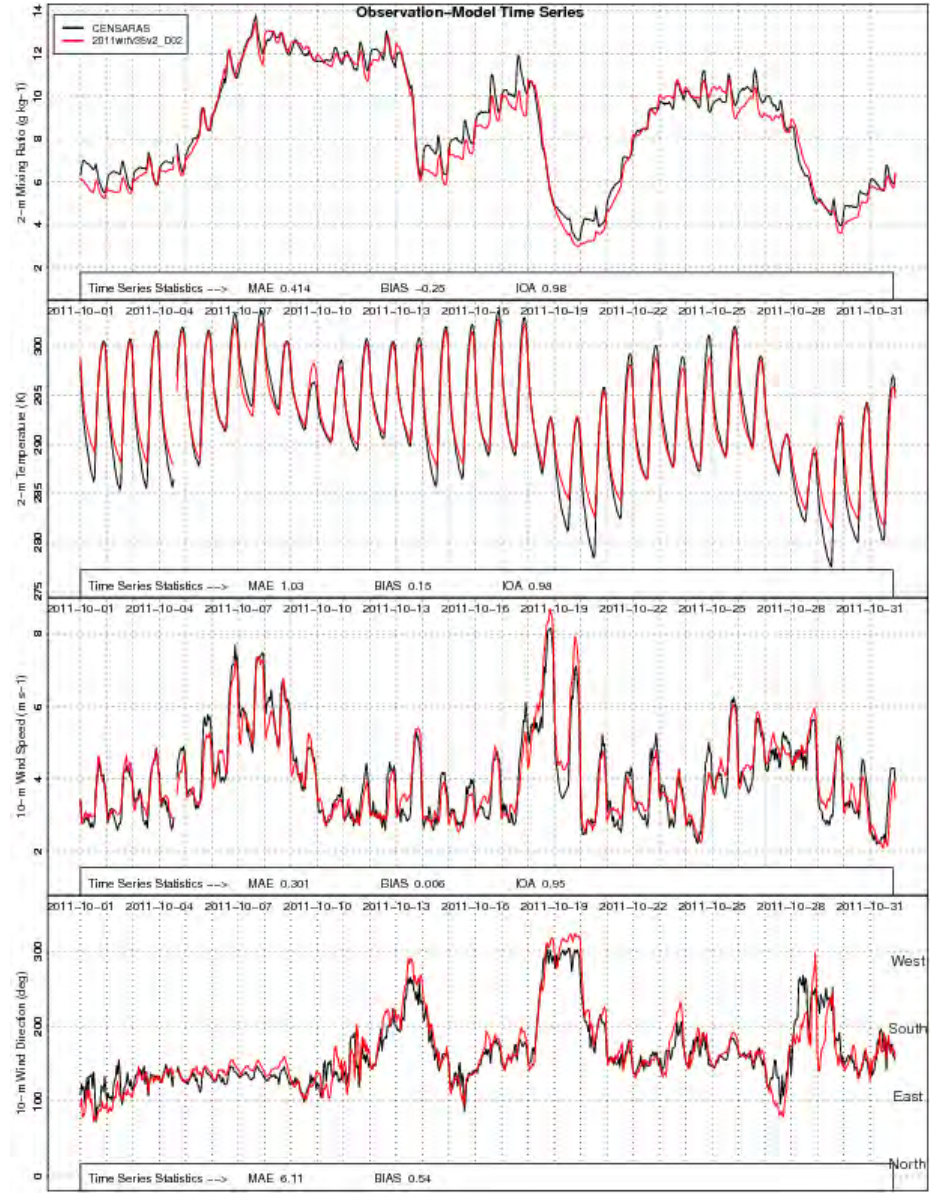

Figure B-67. Hourly timeseries for mean observed and modeled 2-m mixing ratio, 2-m temperature, and 10-m wind speed and direction during October 2011 for the CENSARAS region.

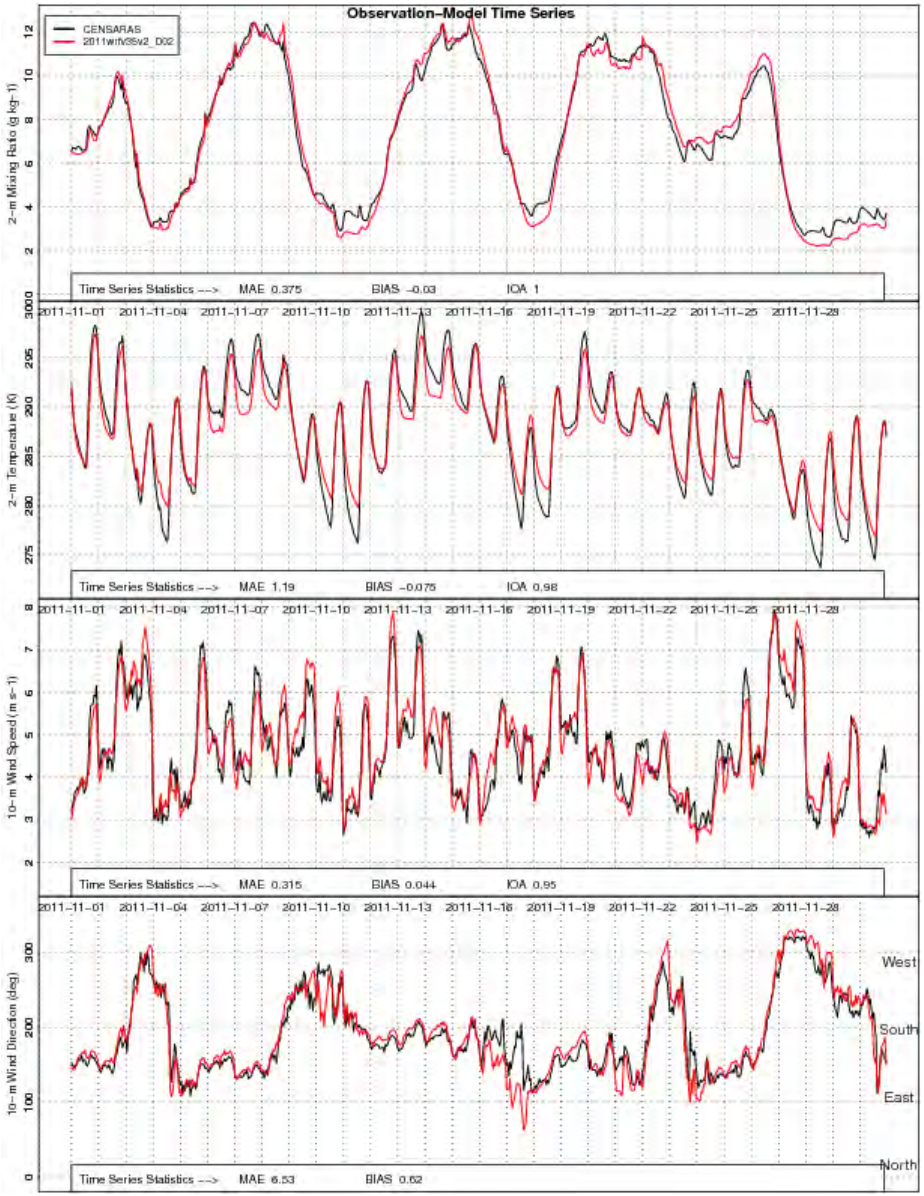

Figure B-68. Hourly timeseries for mean observed and modeled 2-m mixing ratio, 2-m temperature, and 10-m wind speed and direction during November 2011 for the CENSARAS region.

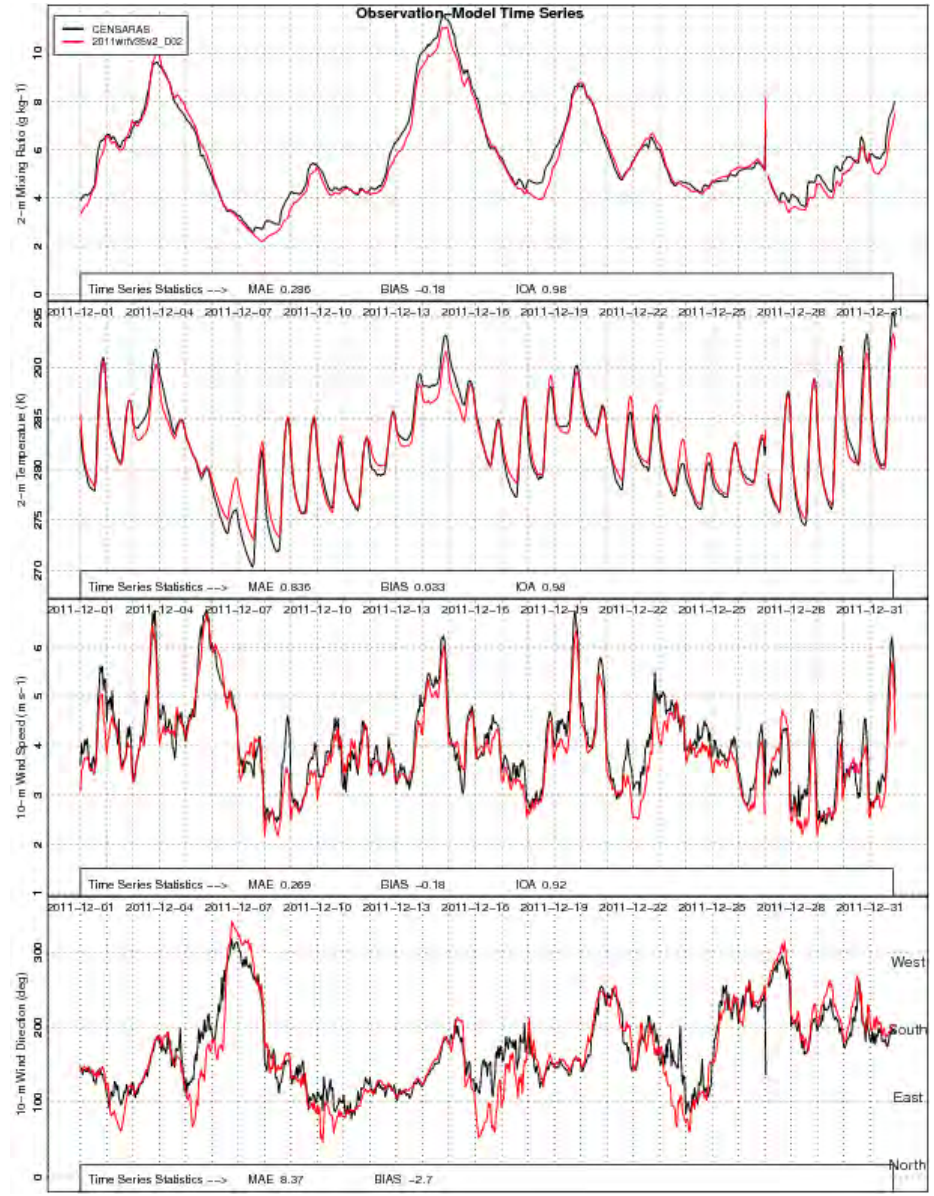

Figure B-69. Hourly timeseries for mean observed and modeled 2-m mixing ratio, 2-m temperature, and 10-m wind speed and direction during December 2011 for the CENSARAS region.

Hourly Timeseries – LADCO

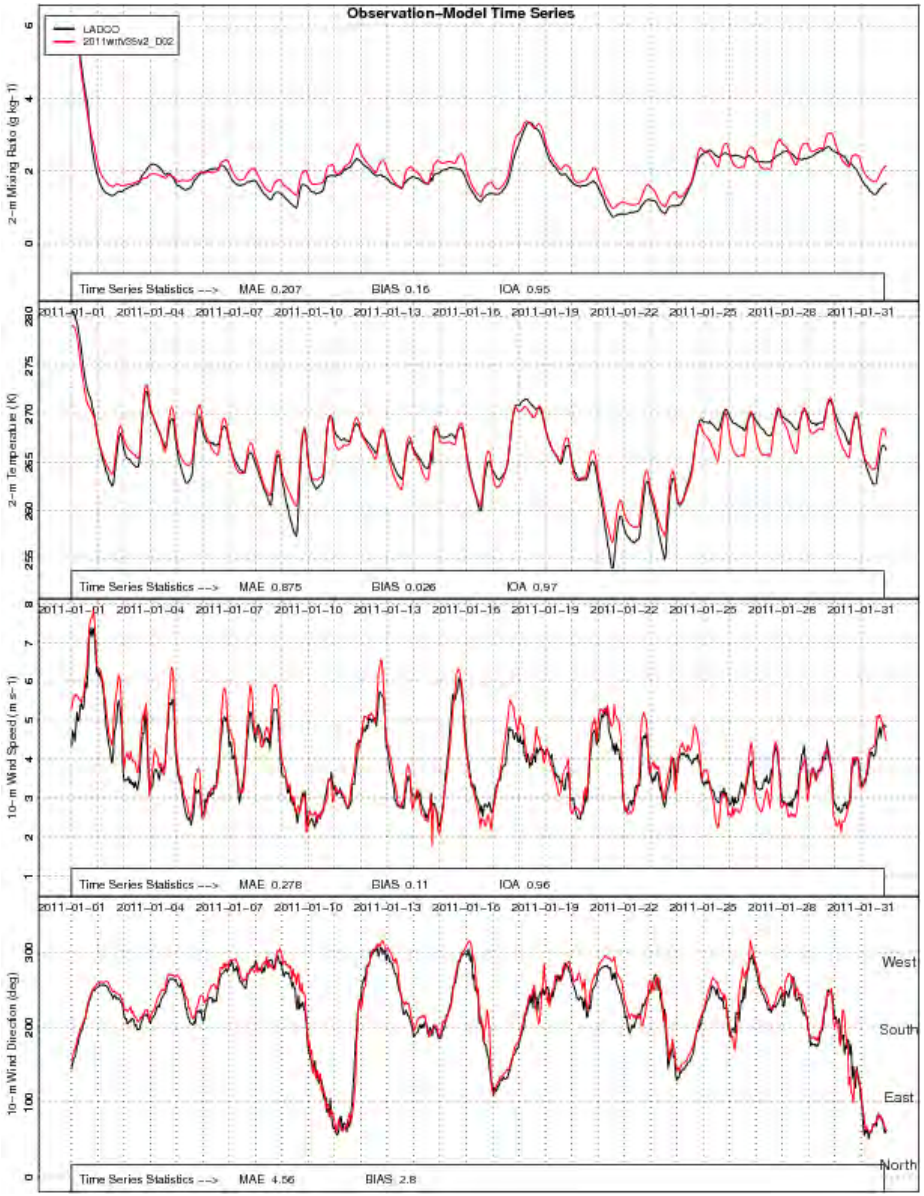

Figure B-70. Hourly timeseries for mean observed and modeled 2-m mixing ratio, 2-m temperature, and 10-m wind speed and direction during January 2011 for the LADCO region.

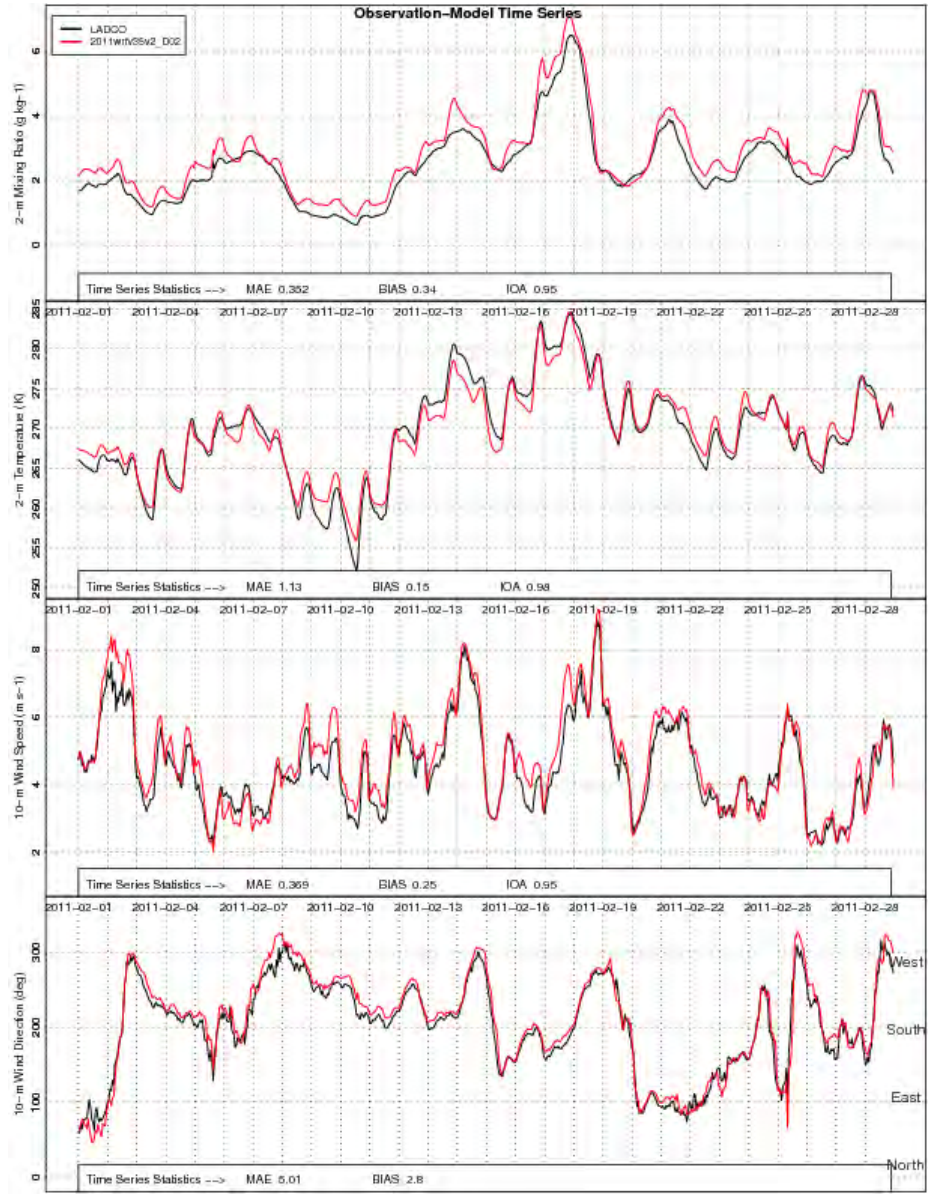

Figure B-71. Hourly timeseries for mean observed and modeled 2-m mixing ratio, 2-m temperature, and 10-m wind speed and direction during February 2011 for the LADCO region.

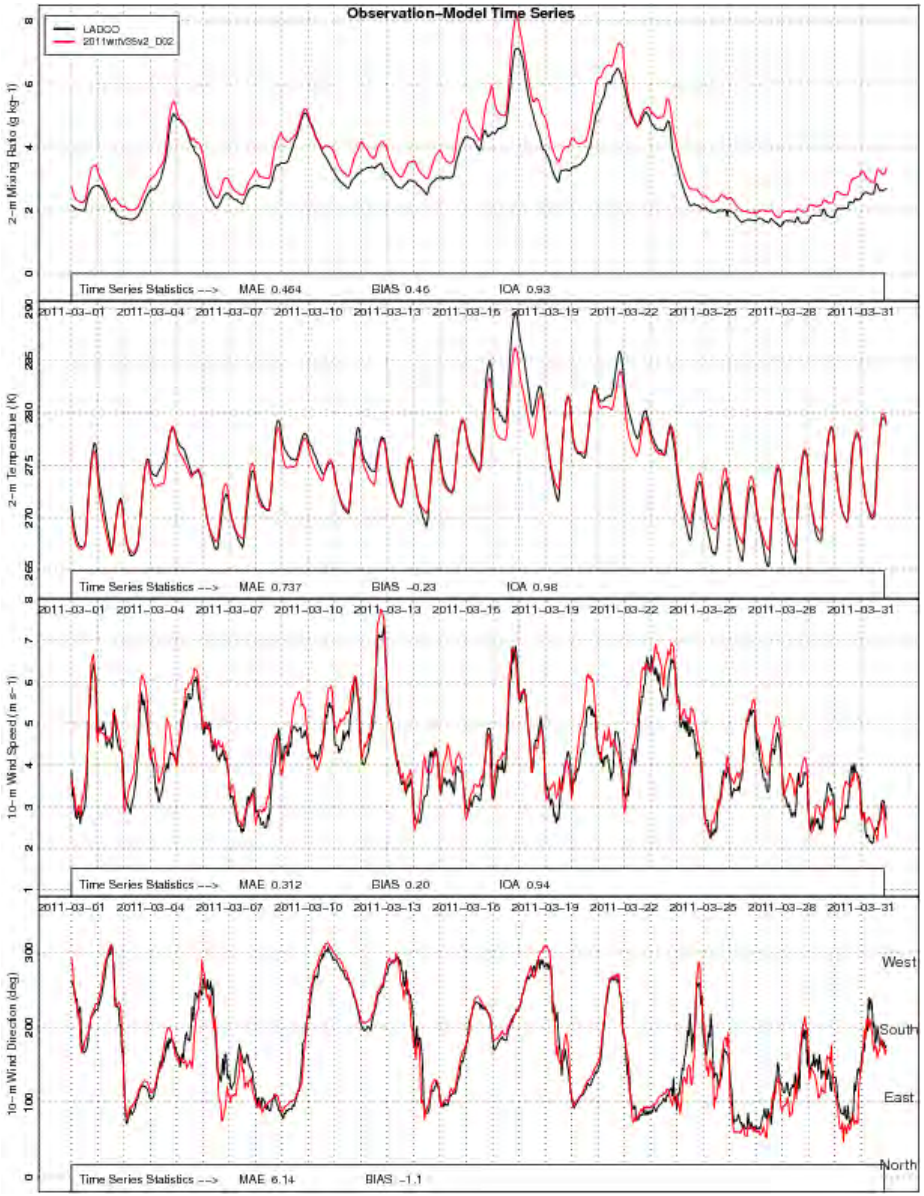

Figure B-72. Hourly timeseries for mean observed and modeled 2-m mixing ratio, 2-m temperature, and 10-m wind speed and direction during March 2011 for the LADCO region.

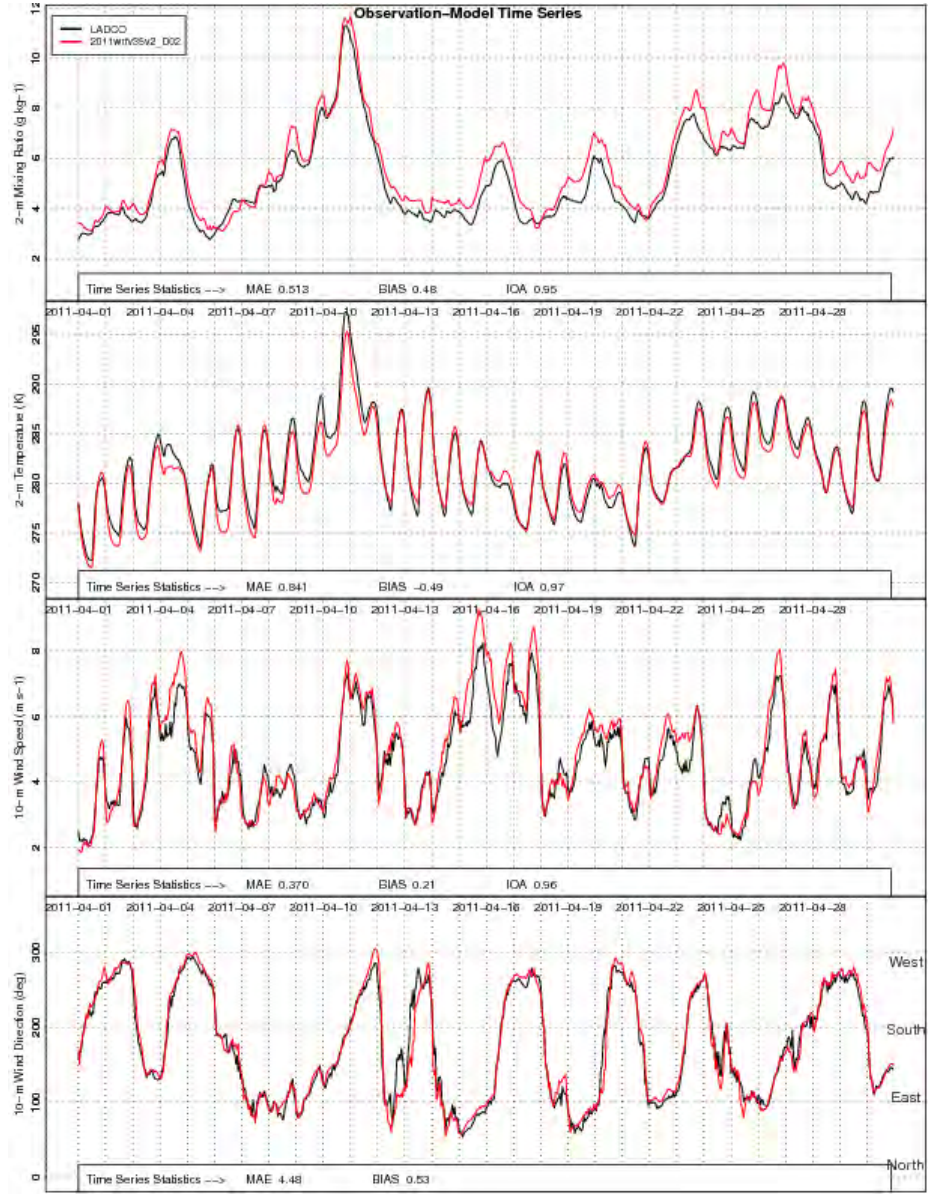

Figure B-73. Hourly timeseries for mean observed and modeled 2-m mixing ratio, 2-m temperature, and 10-m wind speed and direction during April 2011 for the LADCO region.

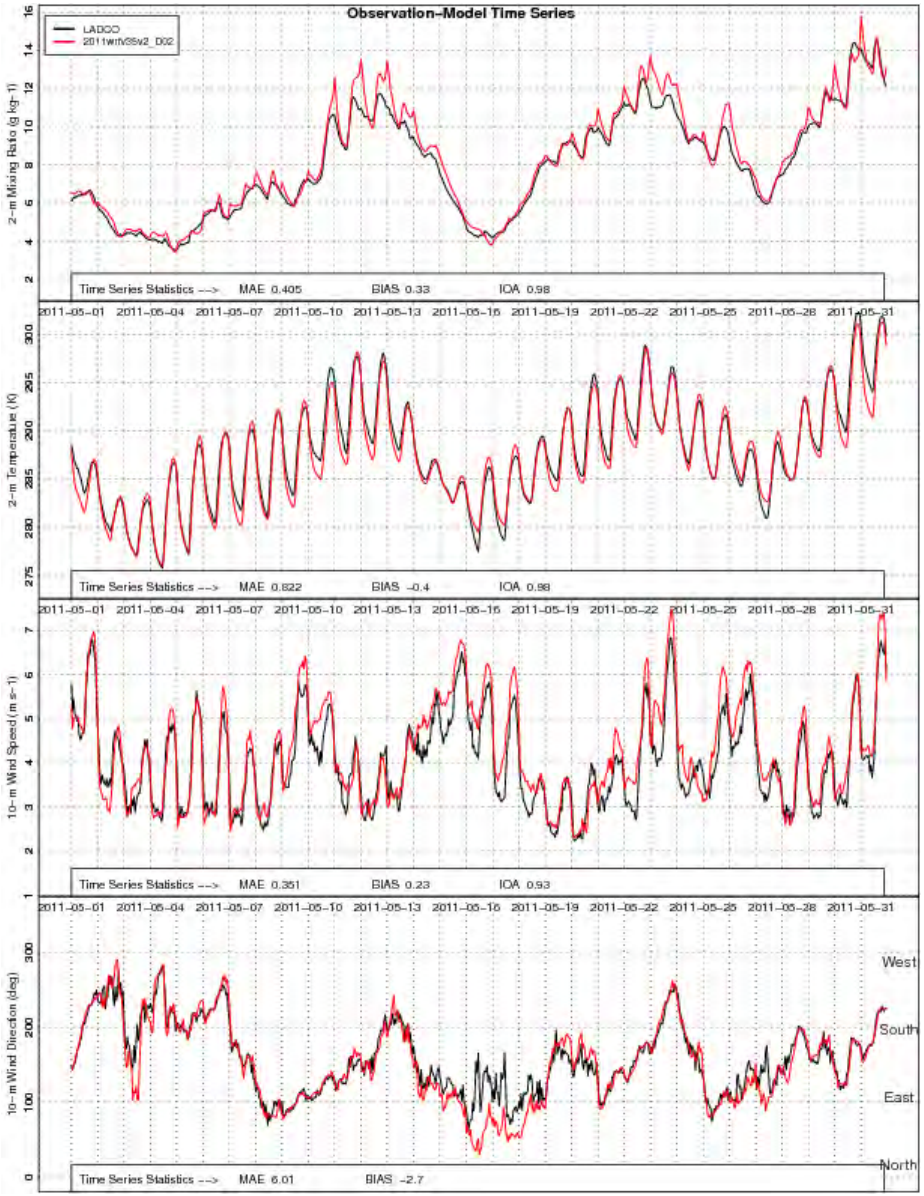

Figure B-74. Hourly timeseries for mean observed and modeled 2-m mixing ratio, 2-m temperature, and 10-m wind speed and direction during May 2011 for the LADCO region.

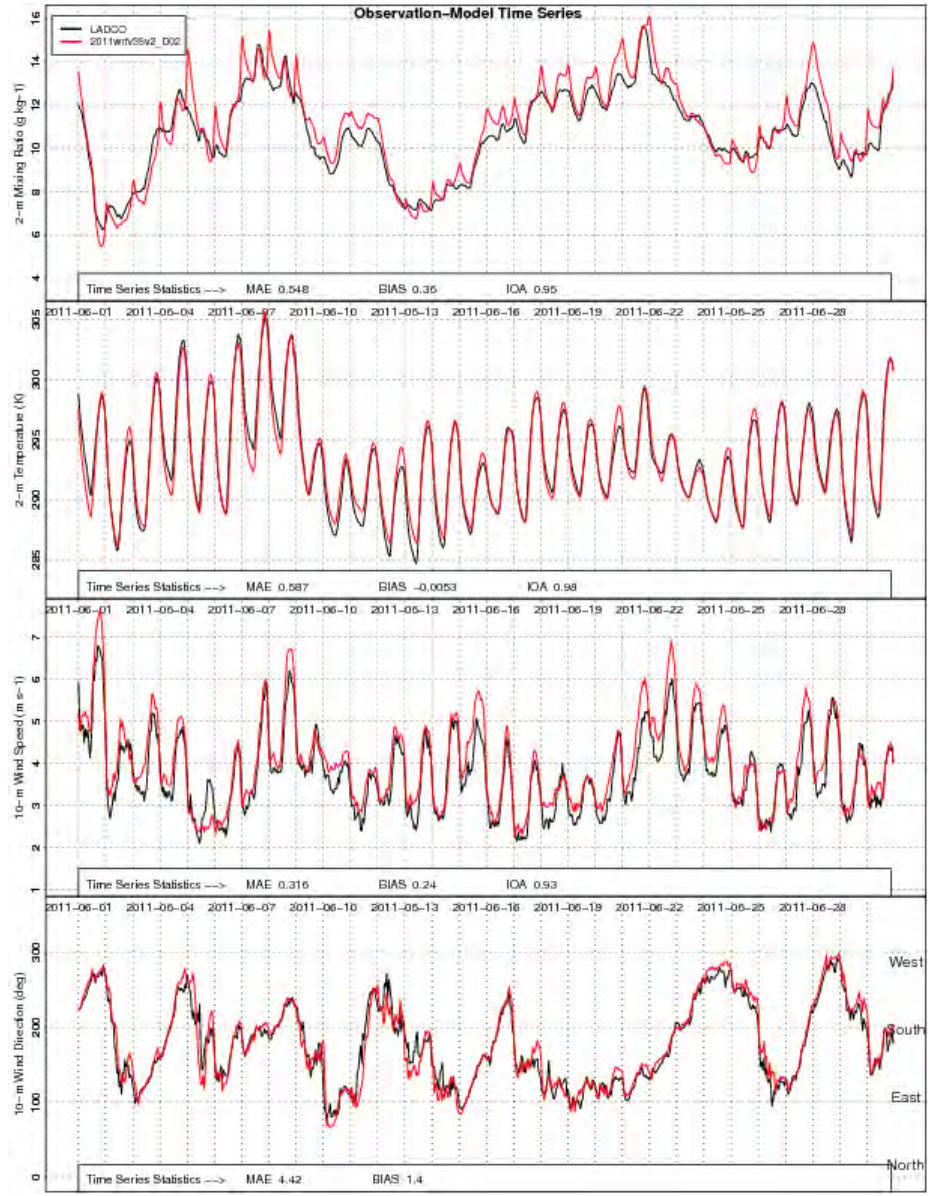

Figure B-75. Hourly timeseries for mean observed and modeled 2-m mixing ratio, 2-m temperature, and 10-m wind speed and direction during June 2011 for the LADCO region.

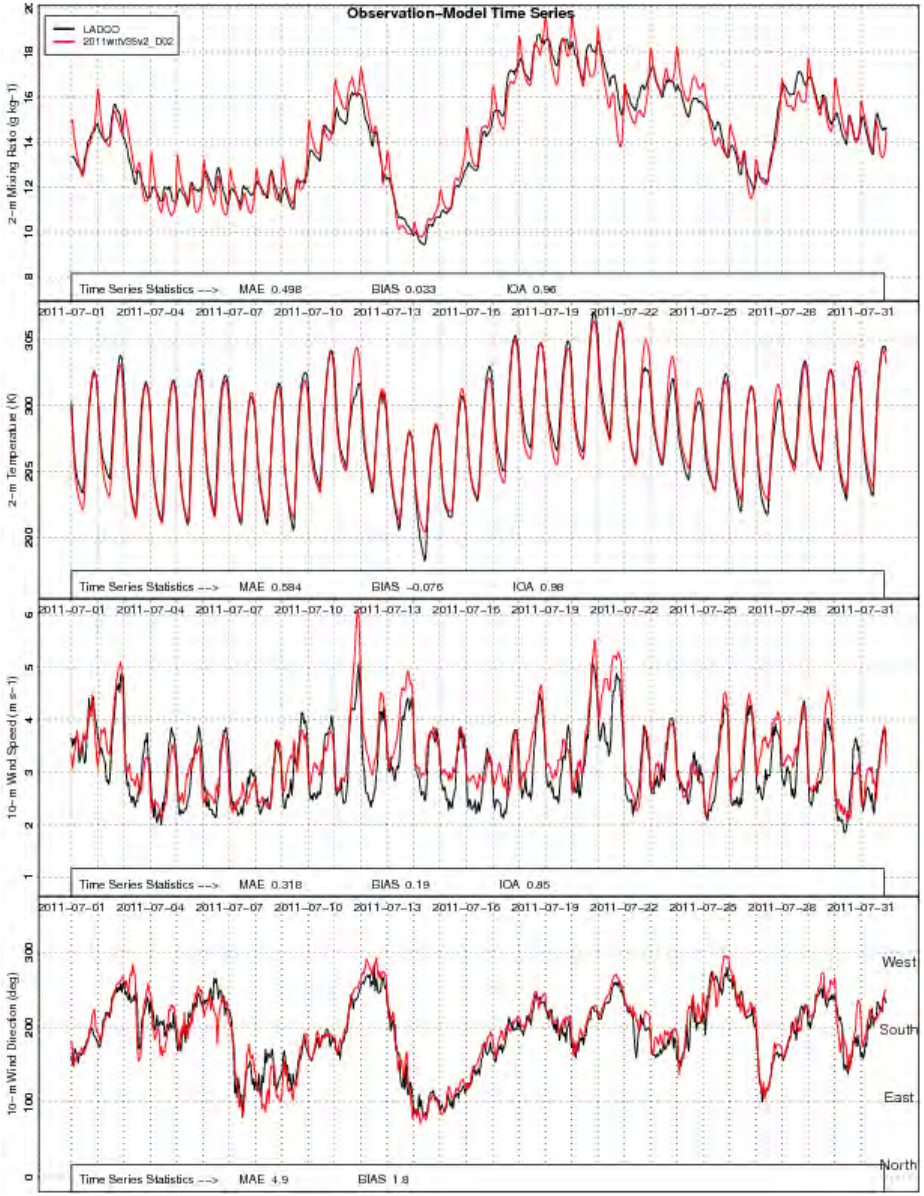

Figure B-76. Hourly timeseries for mean observed and modeled 2-m mixing ratio, 2-m temperature, and 10-m wind speed and direction during July 2011 for the LADCO region.

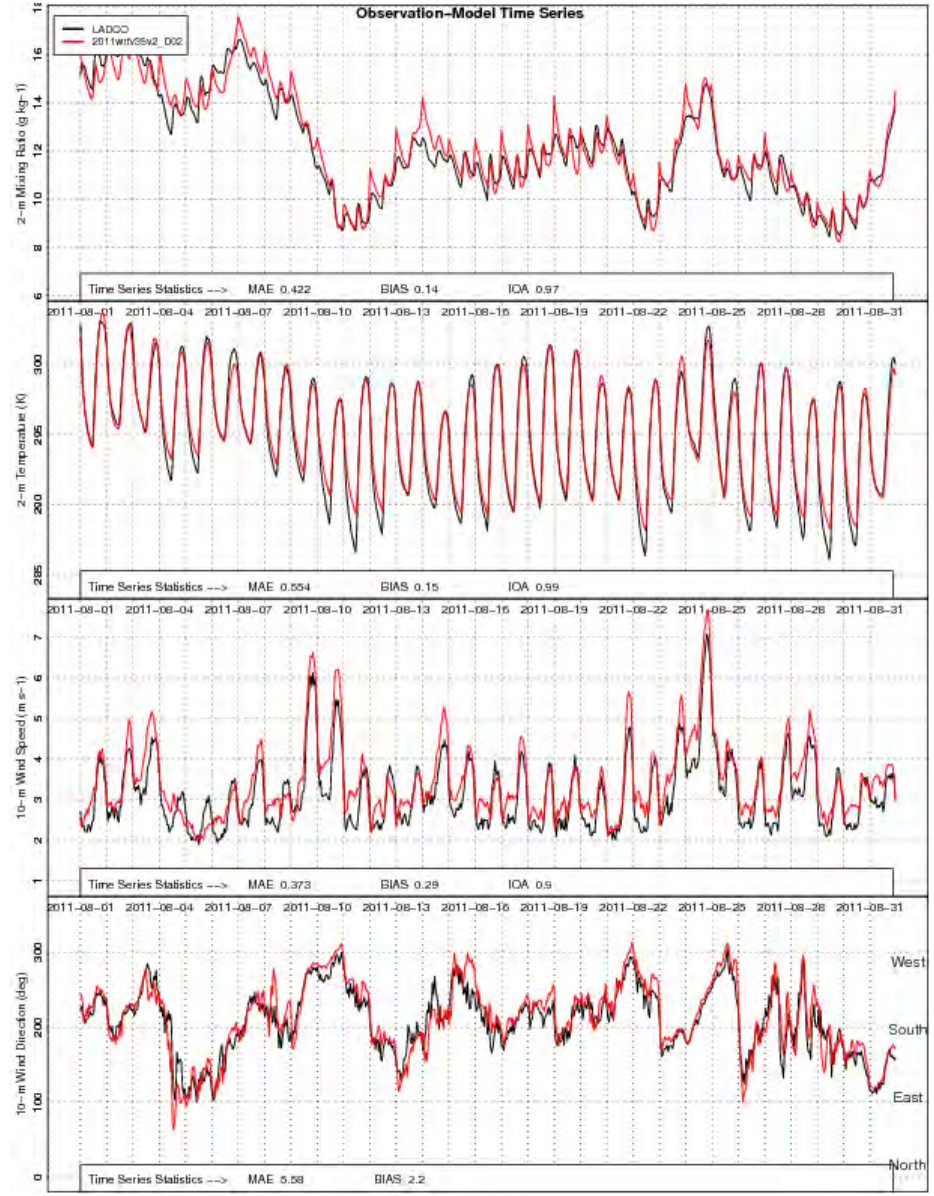

Figure B-77. Hourly timeseries for mean observed and modeled 2-m mixing ratio, 2-m temperature, and 10-m wind speed and direction during August 2011 for the LADCO region.

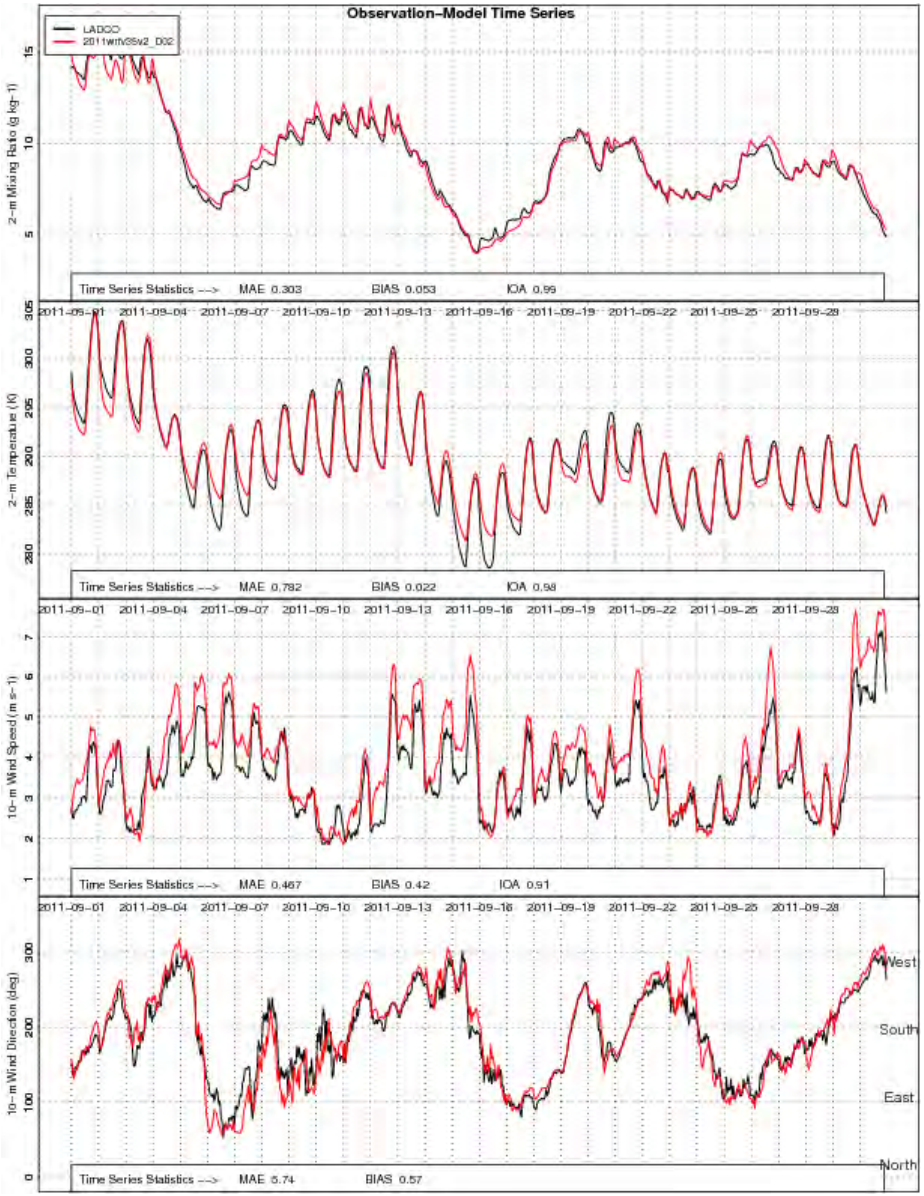

Figure B-78. Hourly timeseries for mean observed and modeled 2-m mixing ratio, 2-m temperature, and 10-m wind speed and direction during September 2011 for the LADCO region.

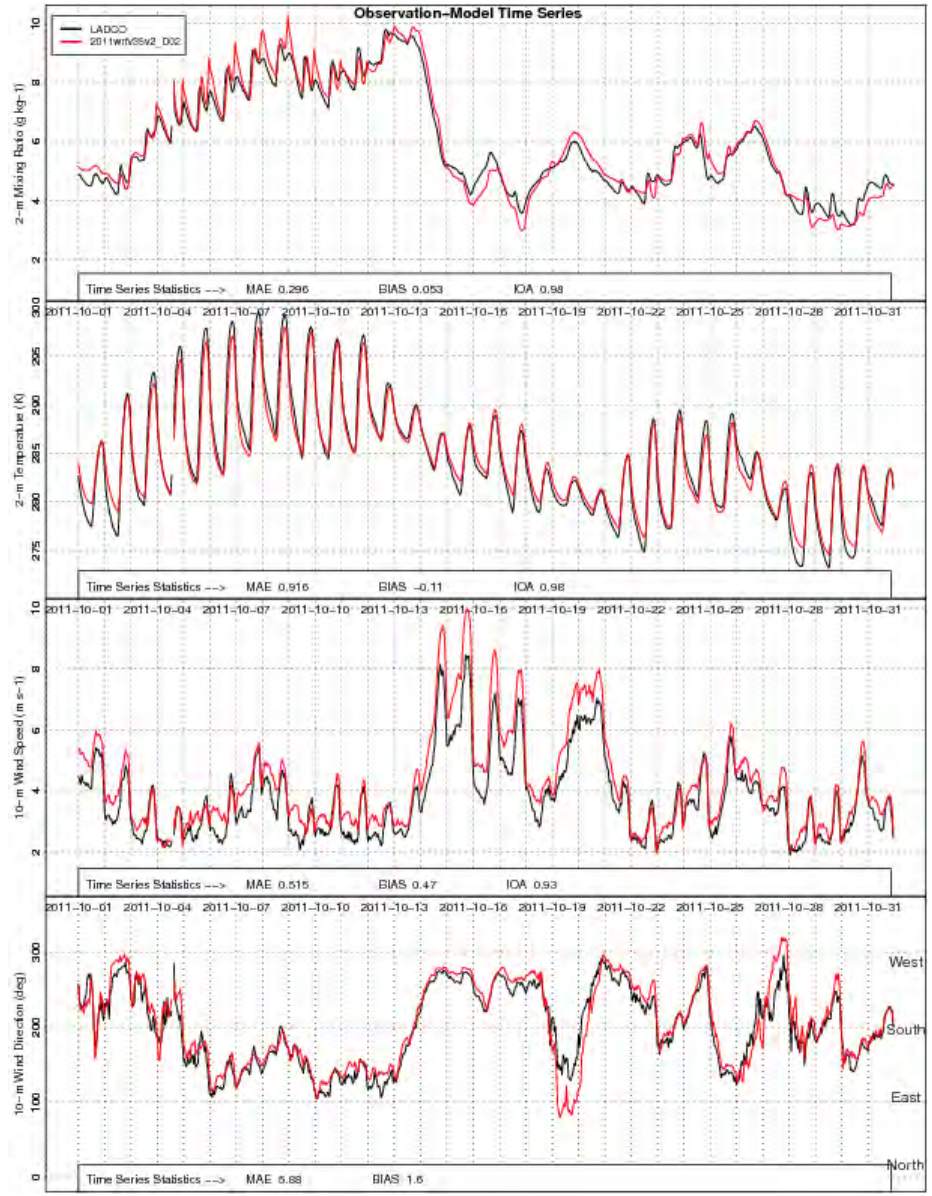

Figure B-79. Hourly timeseries for mean observed and modeled 2-m mixing ratio, 2-m temperature, and 10-m wind speed and direction during October 2011 for the LADCO region.

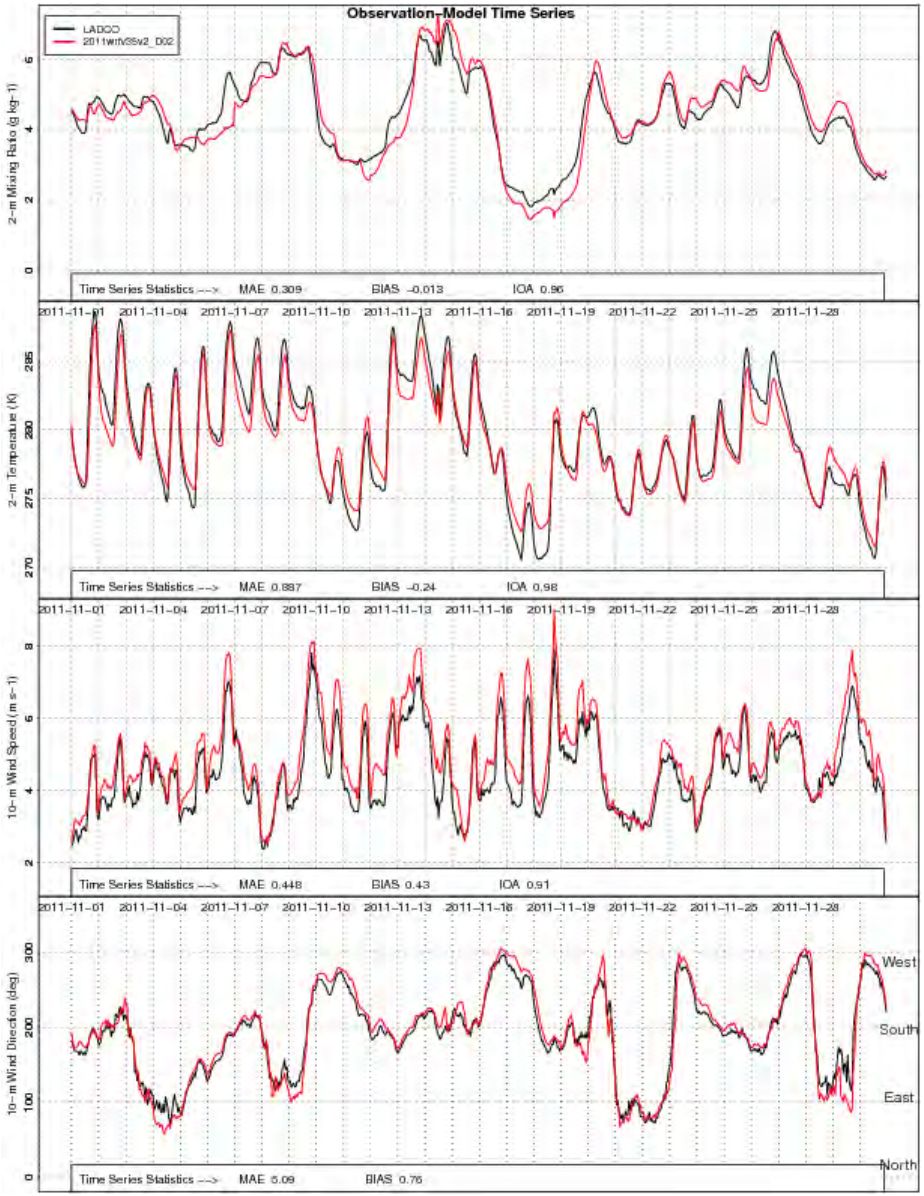

Figure B-80. Hourly timeseries for mean observed and modeled 2-m mixing ratio, 2-m temperature, and 10-m wind speed and direction during November 2011 for the LADCO region.

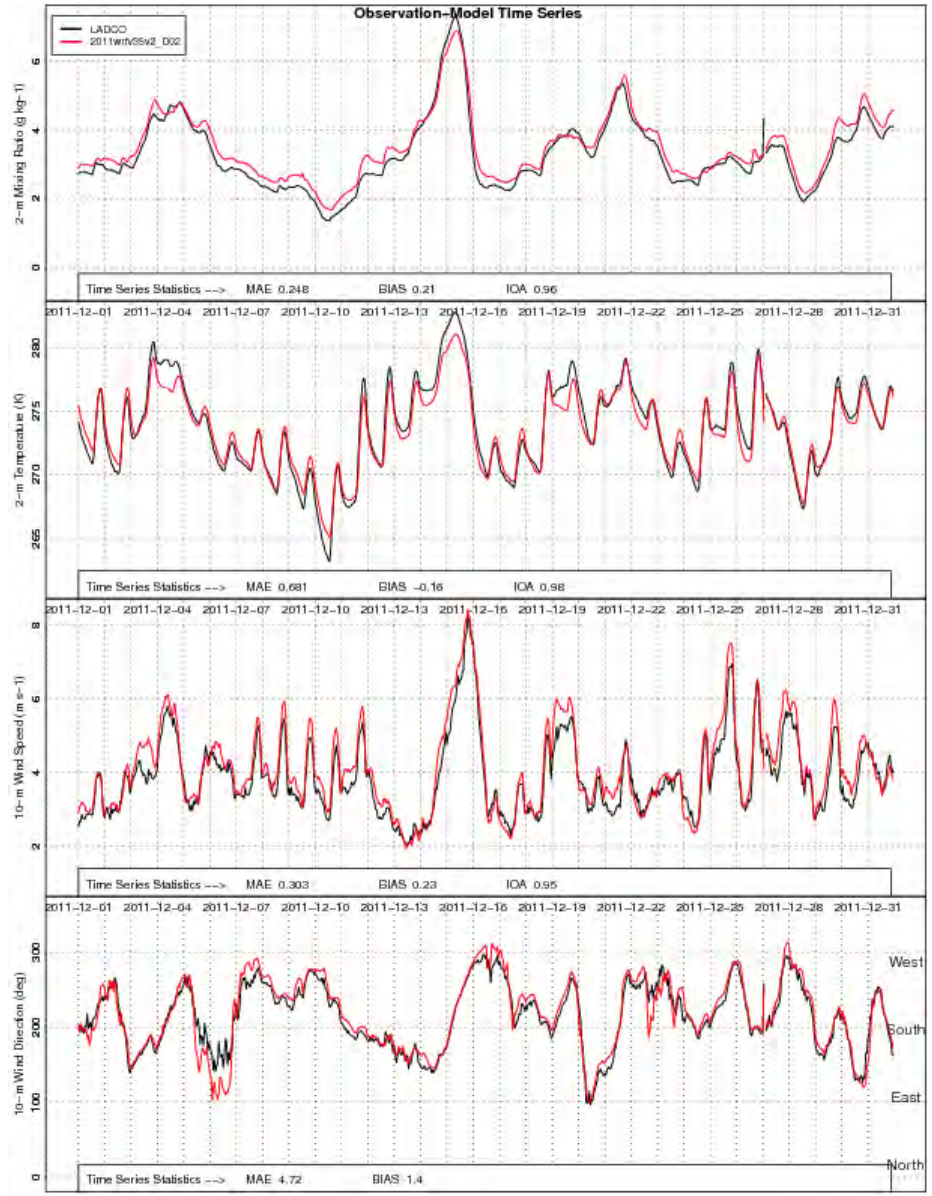

Figure B-81. Hourly timeseries for mean observed and modeled 2-m mixing ratio, 2-m temperature, and 10-m wind speed and direction during December 2011 for the LADCO region.

APPENDIX C: UPPER AIR EVALUATION PLOTS

12 Z

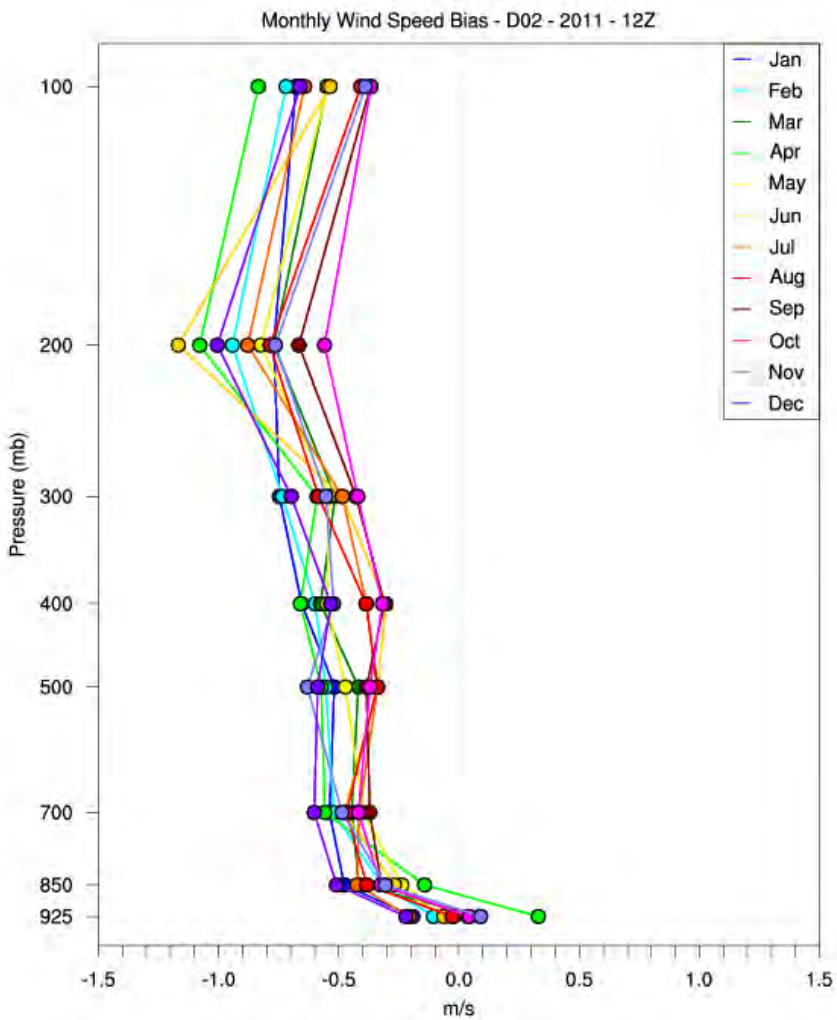

Figure C-1. Vertical profiles of monthly bias for wind speed at 12Z for all months of 2011 for the EASTUS region.

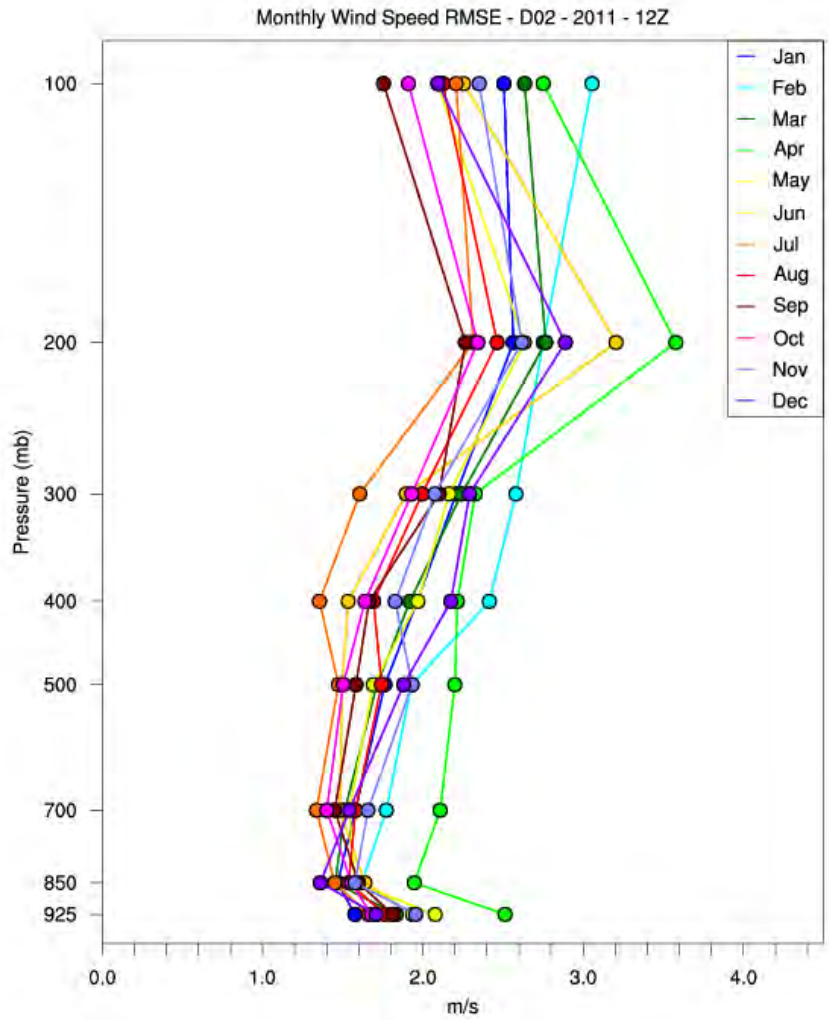

Figure C-2. Vertical profiles of monthly root mean square error for wind speed at 12Z for all months of 2011 for the EASTUS region.

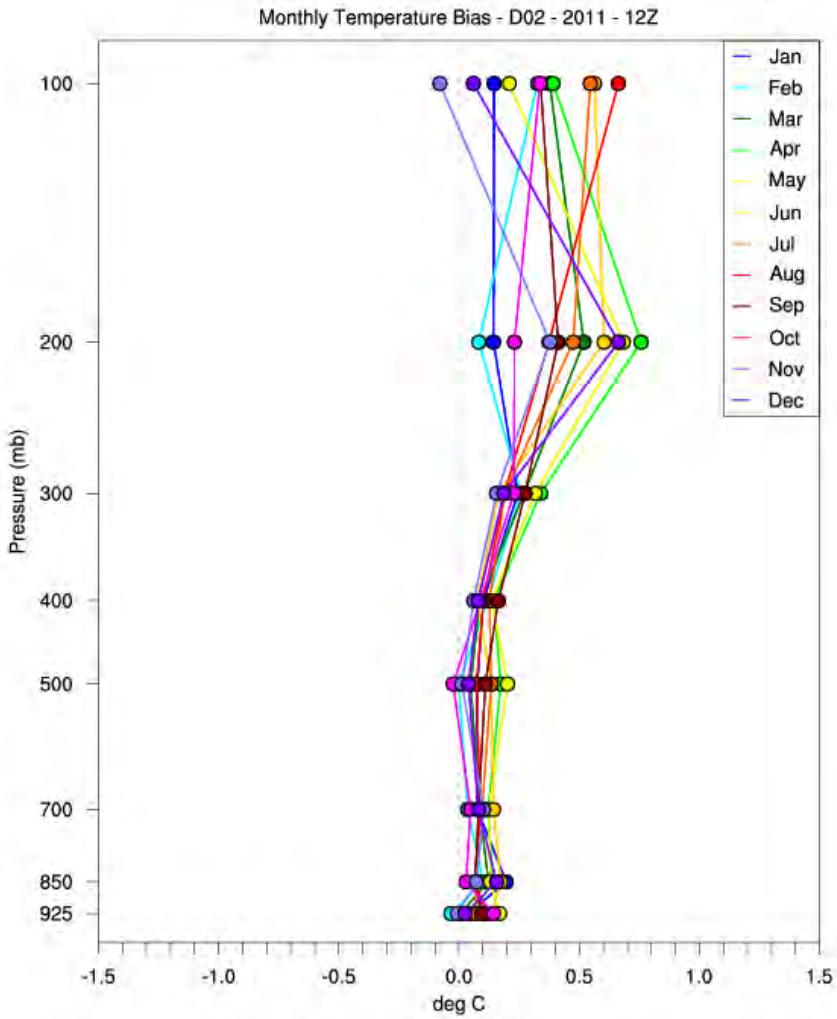

Figure C-3. Vertical profiles of monthly bias for temperature at 12Z for all months of 2011 for the EASTUS region.

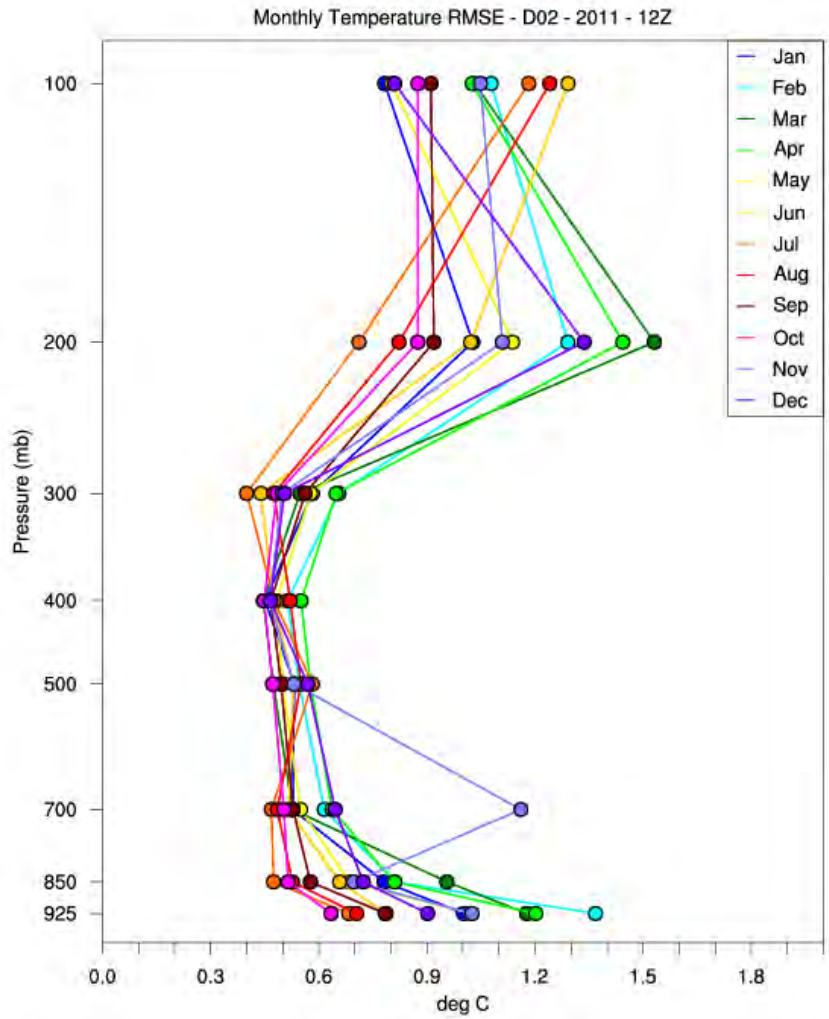

Figure C-4. Vertical profiles of monthly root mean square error for temperature at 12Z for all months of 2011 for the EASTUS region.

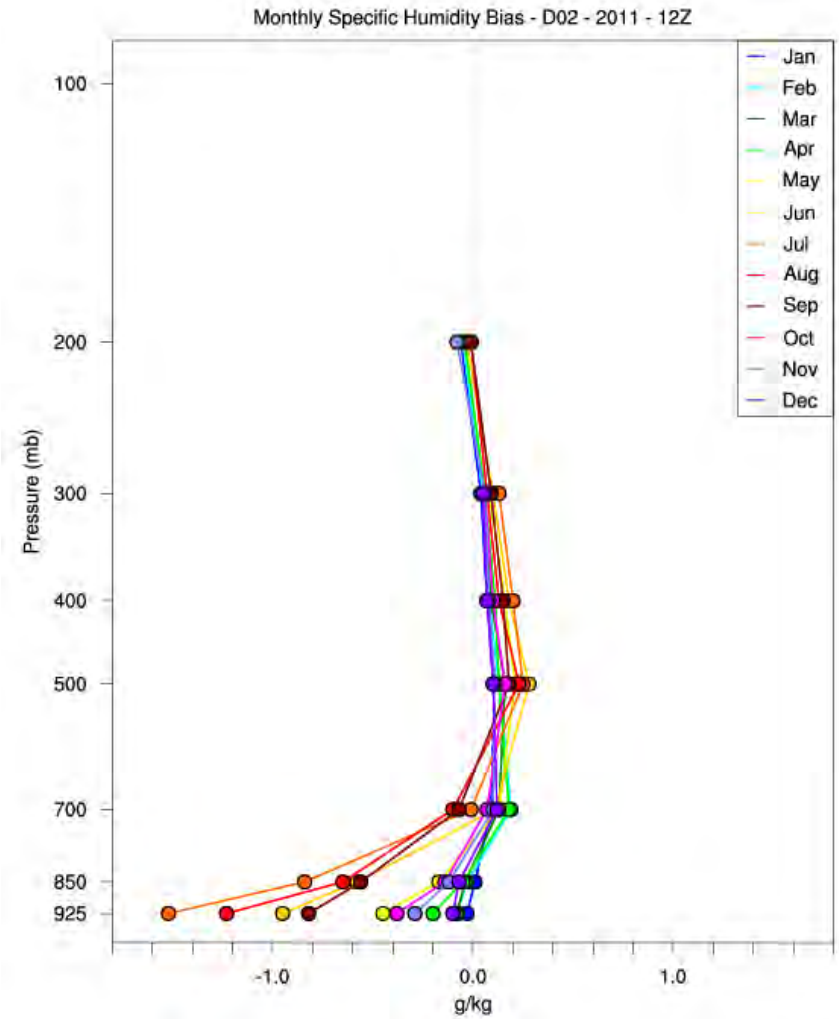

Figure C-5. Vertical profiles of monthly bias for specific humidity at 12Z for all months of 2011 for the EASTUS region.

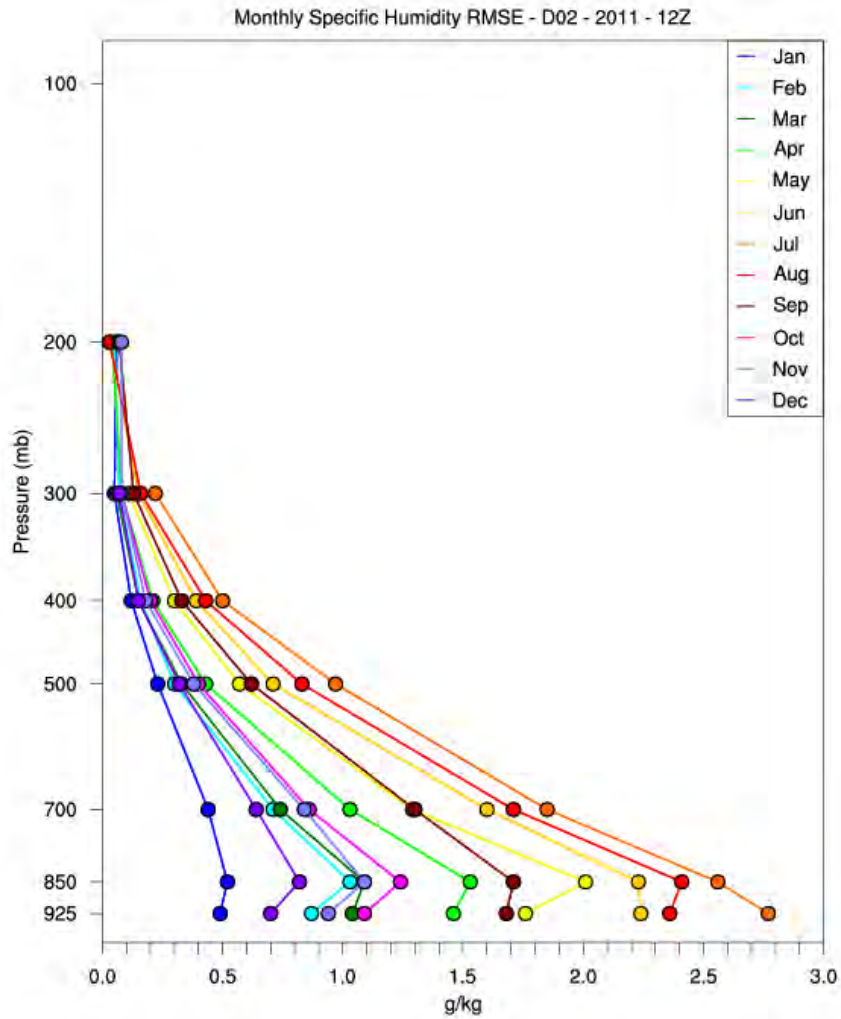

Figure C-6. Vertical profiles of monthly root mean square error for specific humidity at 12Z for all months of 2011 for the EASTUS region.

0 Z

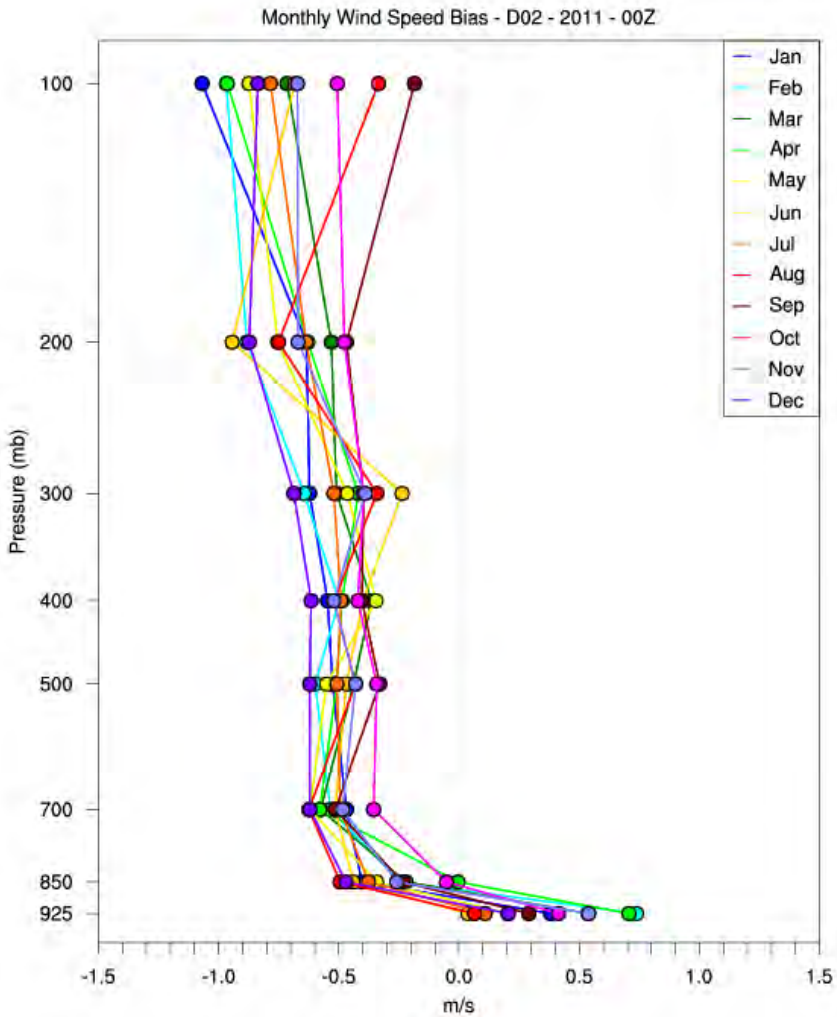

Figure C-7. Vertical profiles of monthly bias for wind speed at 00Z for all months of 2011 for the EASTUS region.

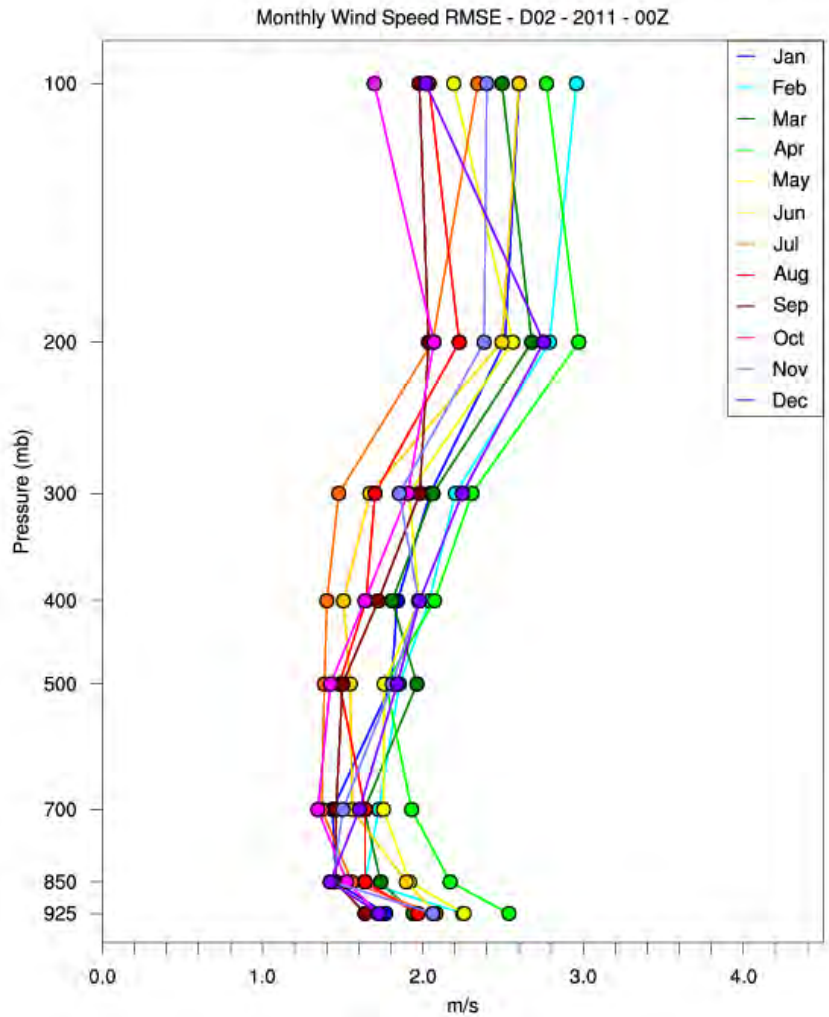

Figure C-8. Vertical profiles of monthly root mean square error for wind speed at 00Z for all months of 2011 for the EASTUS region.

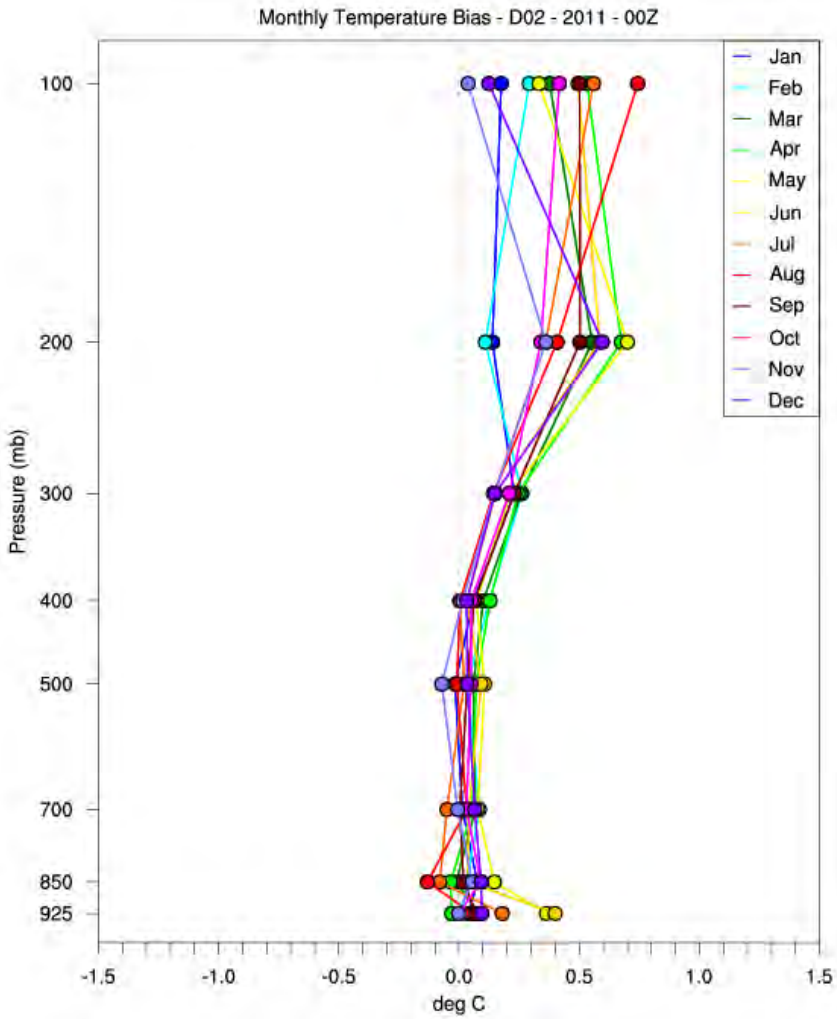

Figure C-9. Vertical profiles of monthly bias for temperature at 00Z for all months of 2011 for the EASTUS region.

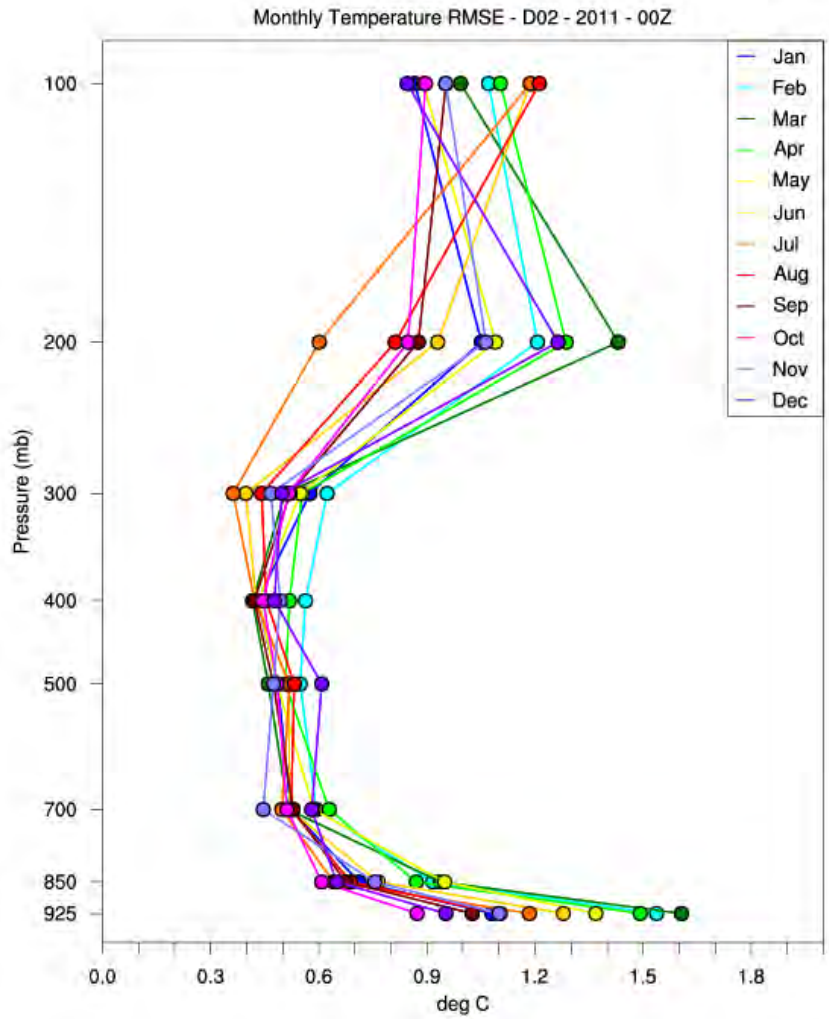

Figure C-10. Vertical profiles of monthly root mean square error for temperature at 00Z for all months of 2011 for the EASTUS region.

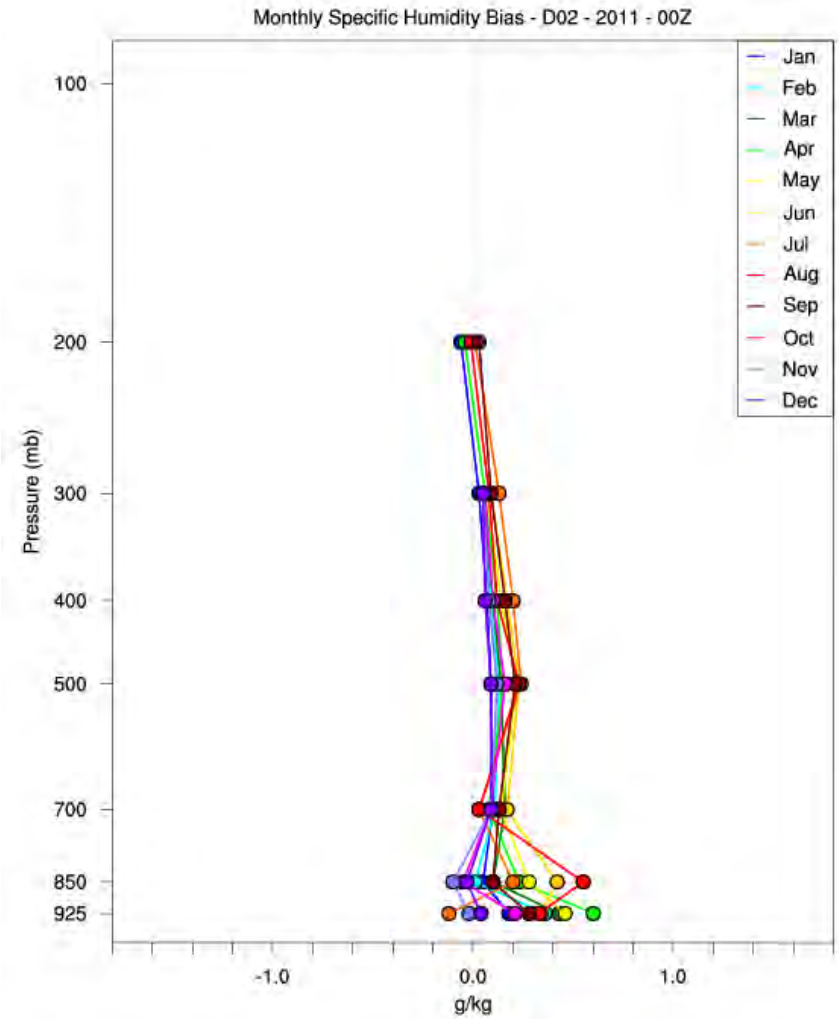

Figure C-11. Vertical profiles of monthly bias for specific humidity at 00Z for all months of 2011 for the EASTUS region.

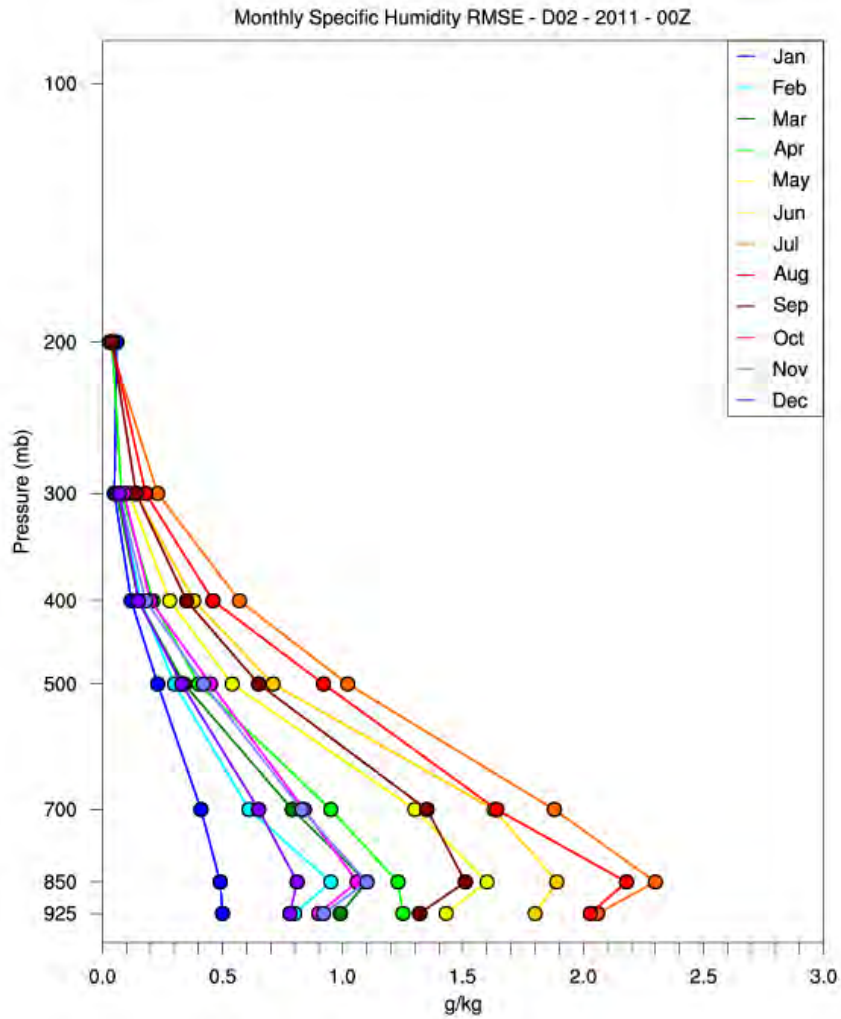

Figure C-12. Vertical profiles of monthly root mean square error for specific humidity at 00Z for all months of 2011 for the EASTUS region.

APPENDIX D: MONTHLY ACCUMULATED PRECIPITATION PLOTS

January

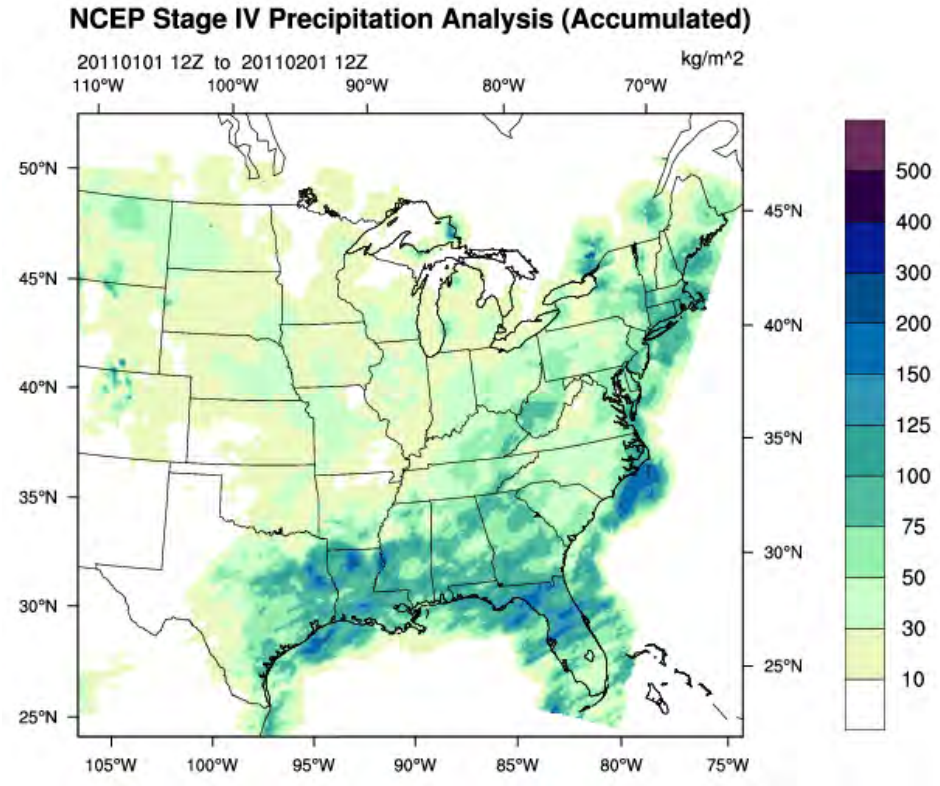

Figure D-1. Daily NCEP Stage IV precipitation data accumulated over the month of January 2011.

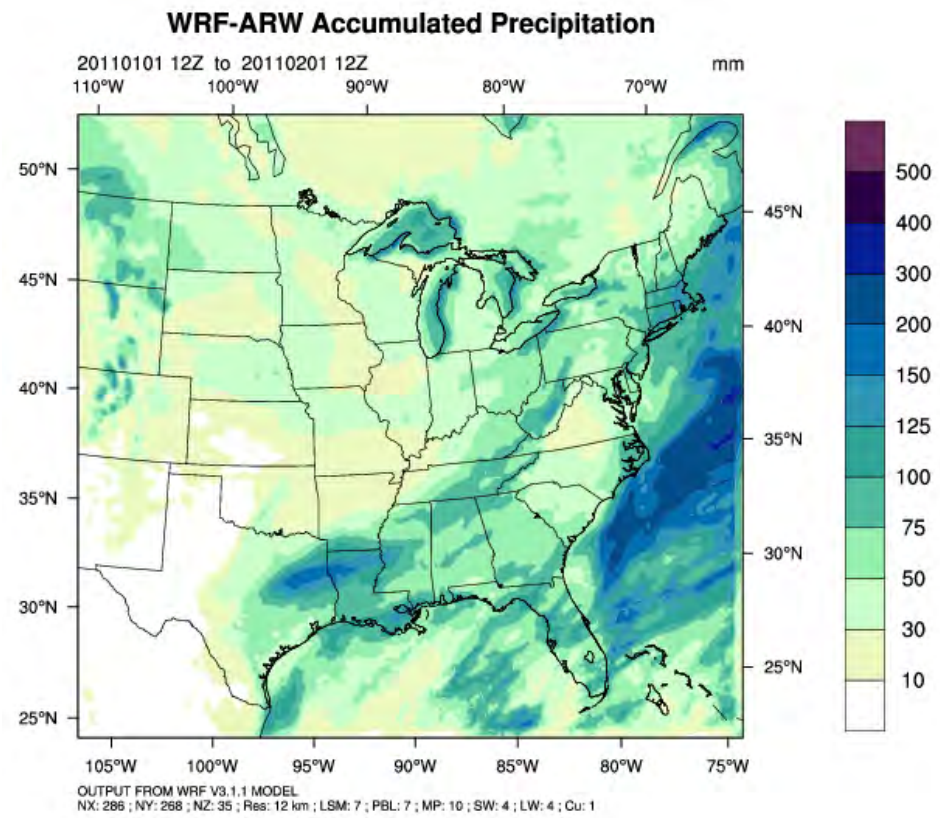

Figure D-2. WRF simulated precipitation accumulated over the month of January 2011.

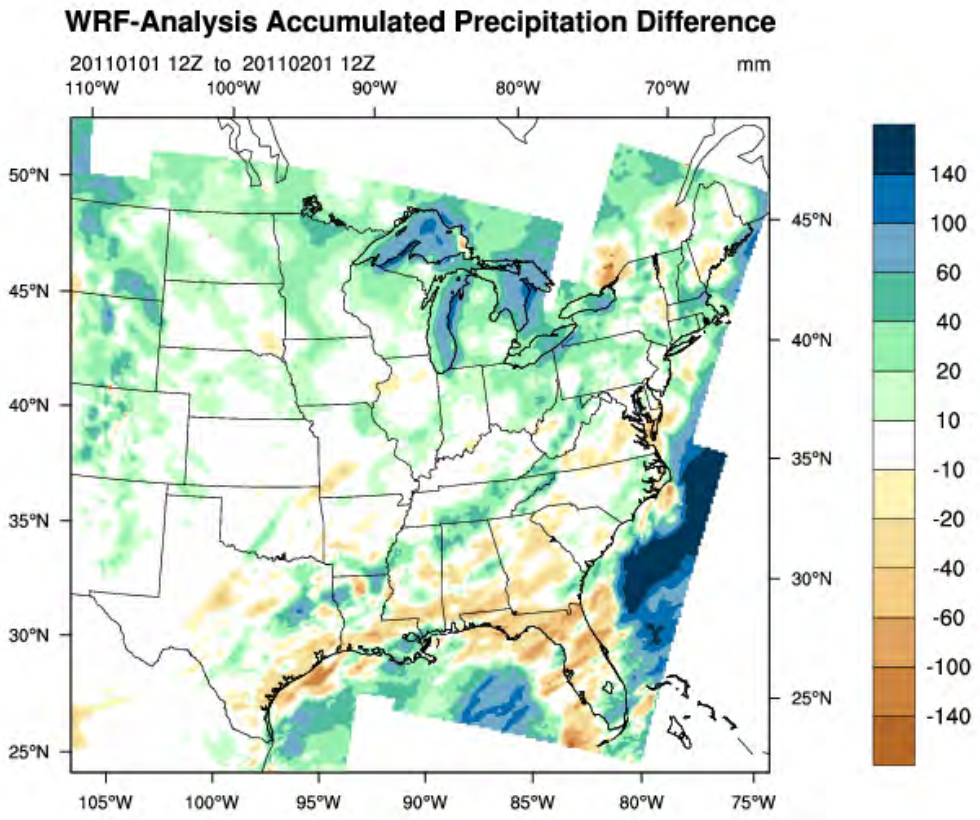

Figure D-3. Monthly accumulated observed and modeled precipitation difference for January 2011.

February

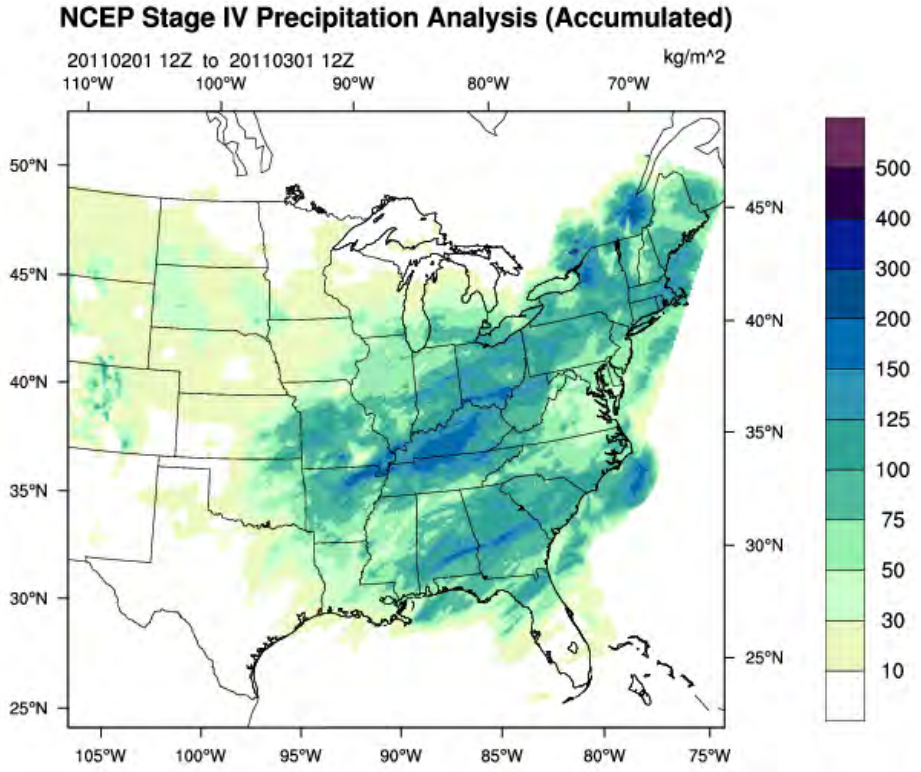

Figure D-4. Daily NCEP Stage IV precipitation data accumulated over the month of February 2011.

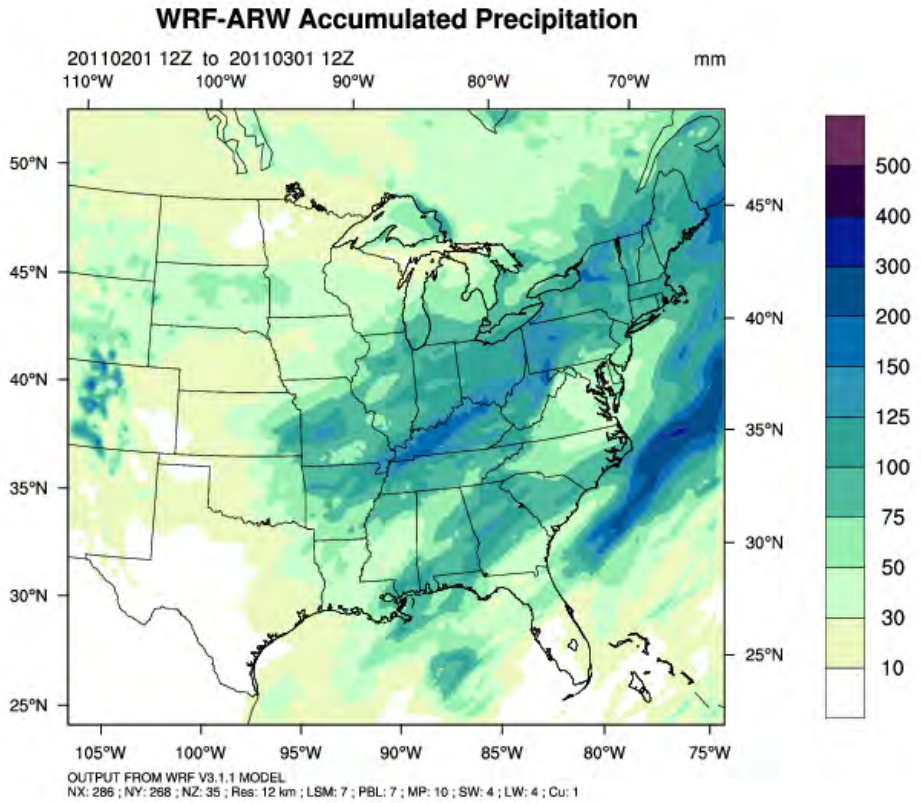

Figure D-5. WRF simulated precipitation accumulated over the month of February 2011.

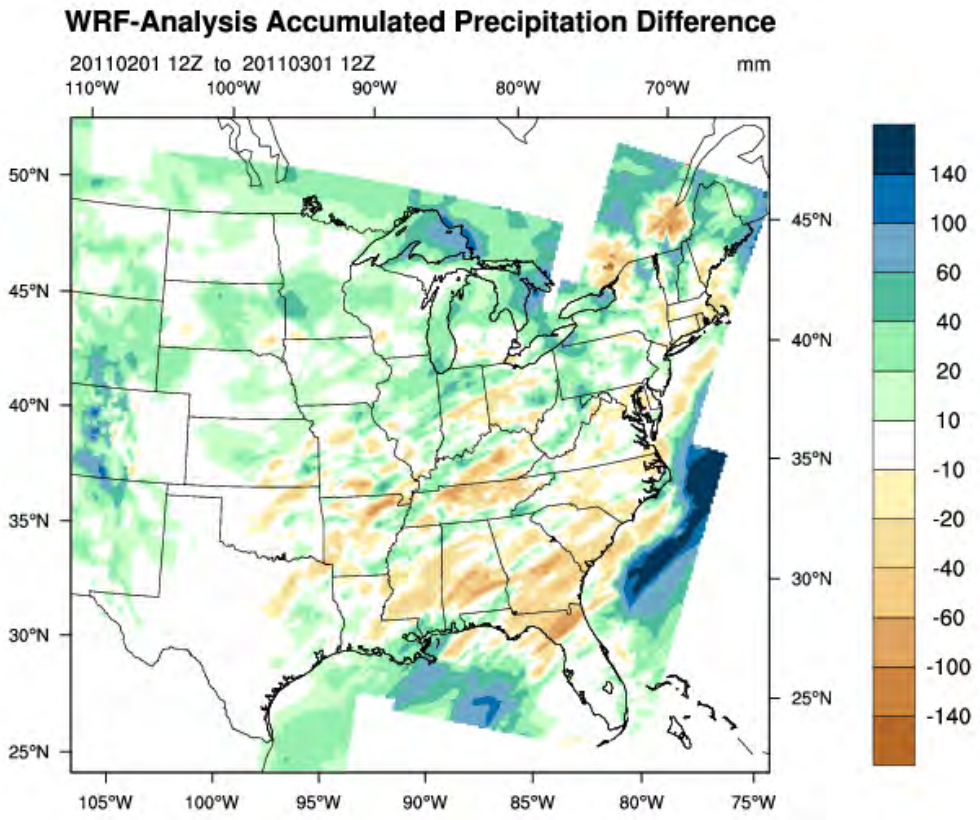

Figure D-6. Monthly accumulated observed and modeled precipitation difference for February 2011.

March

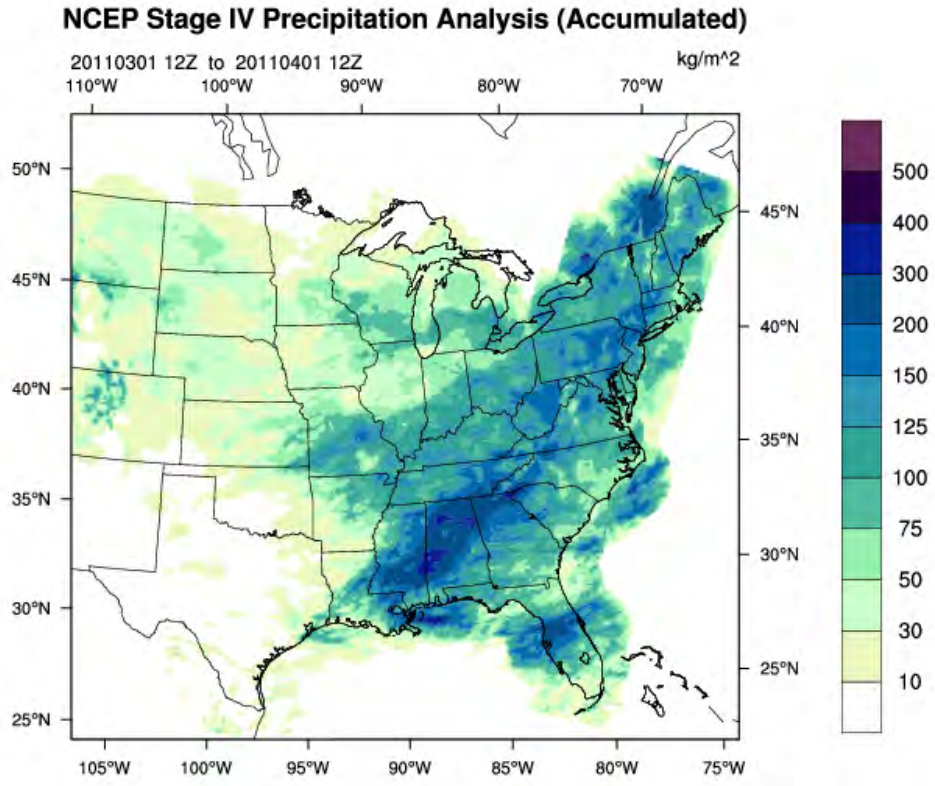

Figure D-7. Daily NCEP Stage IV precipitation data accumulated over the month of March 2011.

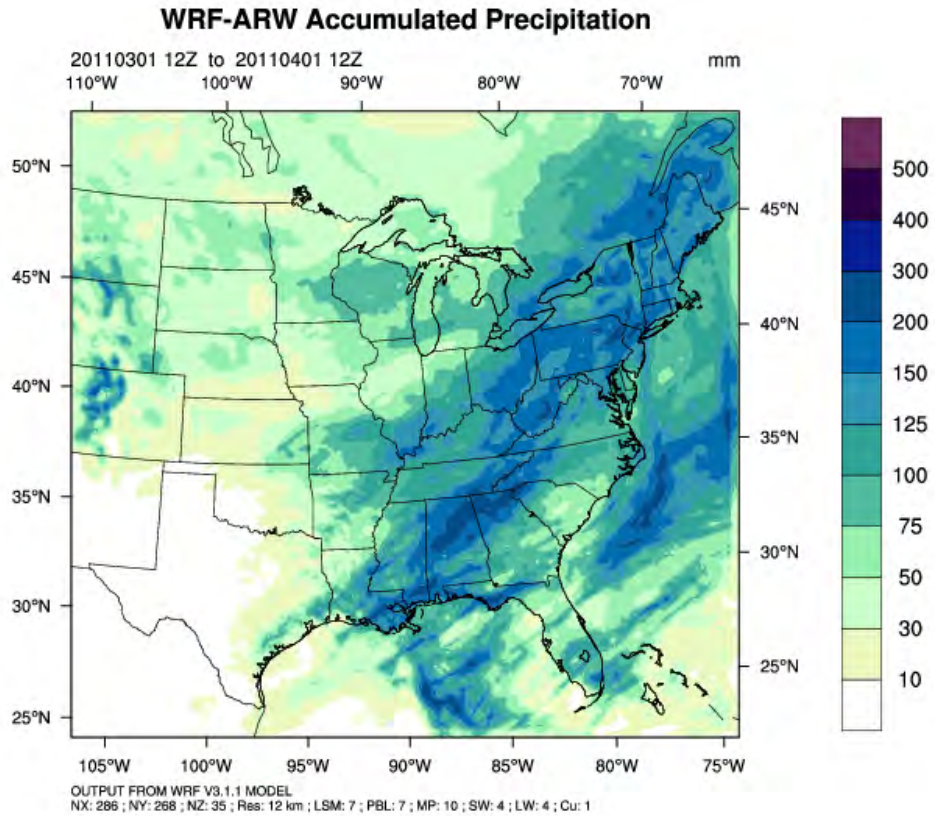

Figure D-8. WRF simulated precipitation accumulated over the month of March 2011.

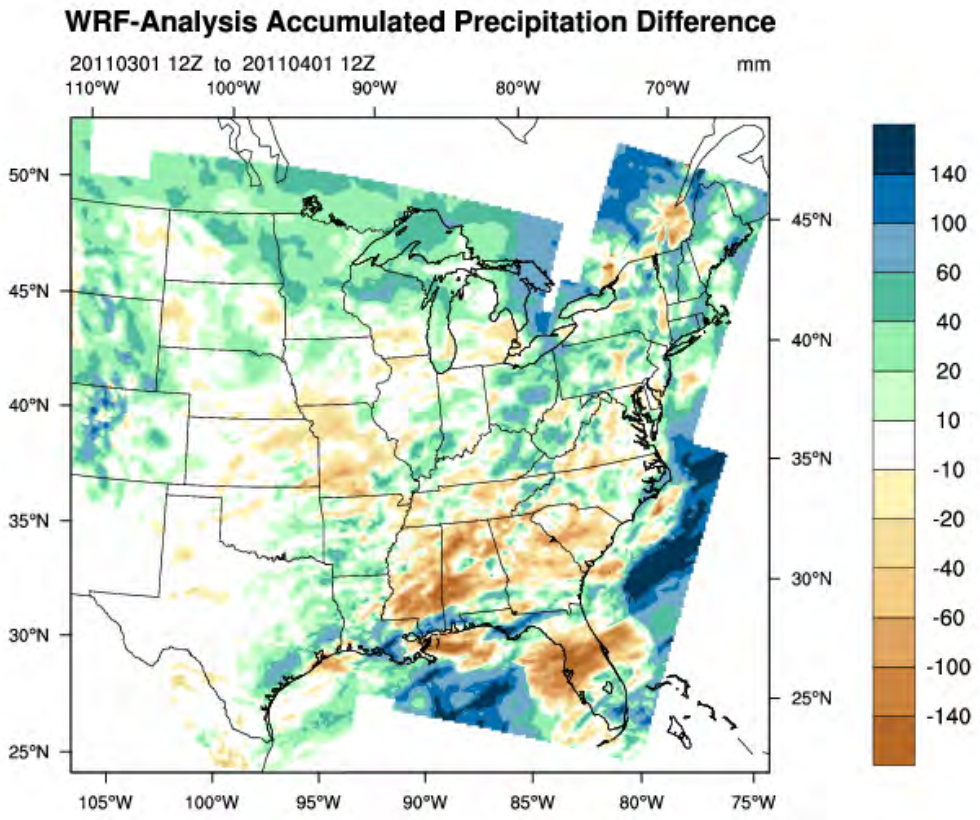

Figure D-9. Monthly accumulated observed and modeled precipitation difference for March 2011.

April

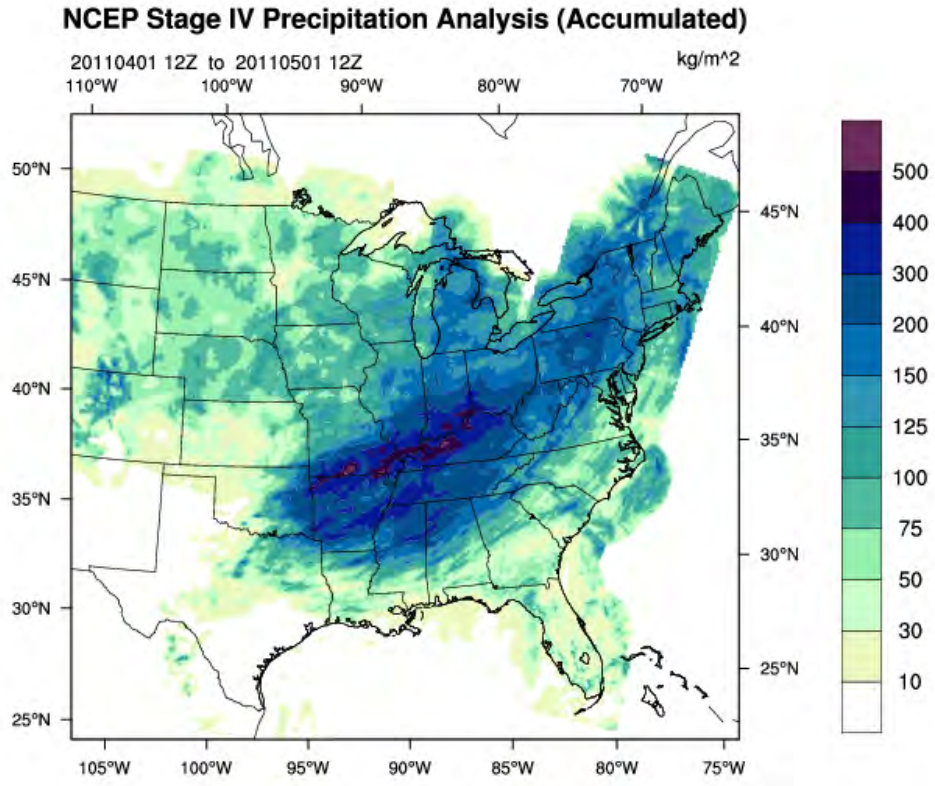

Figure D-10. Daily NCEP Stage IV precipitation data accumulated over the month of April 2011.

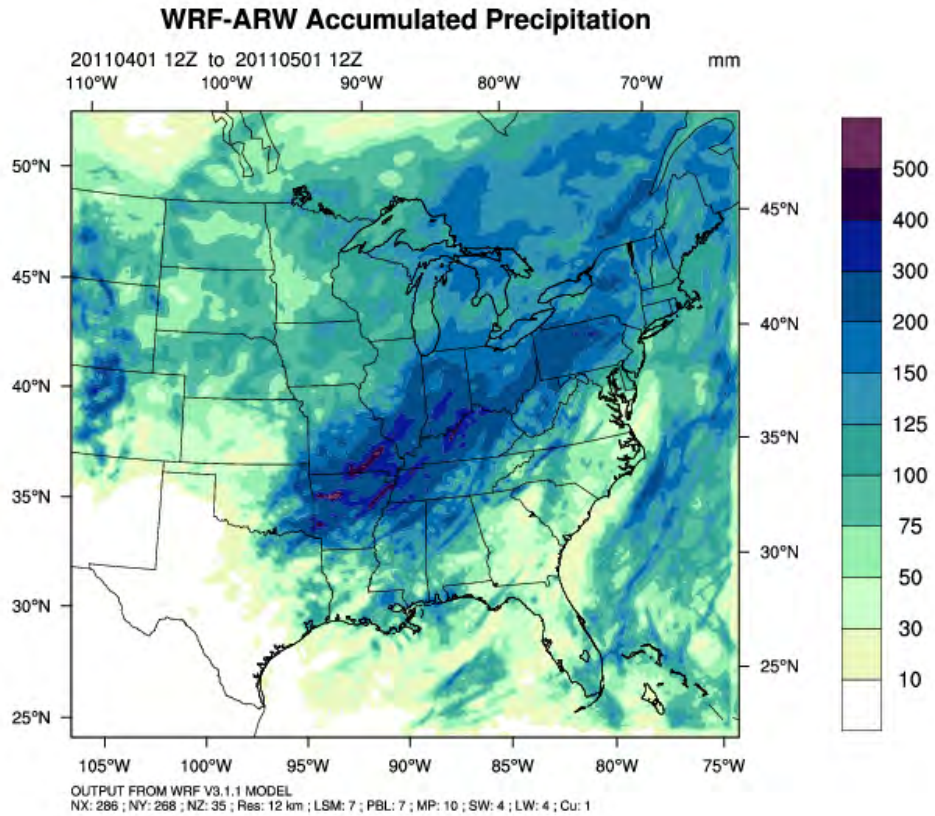

Figure D-11. WRF simulated precipitation accumulated over the month of April 2011.

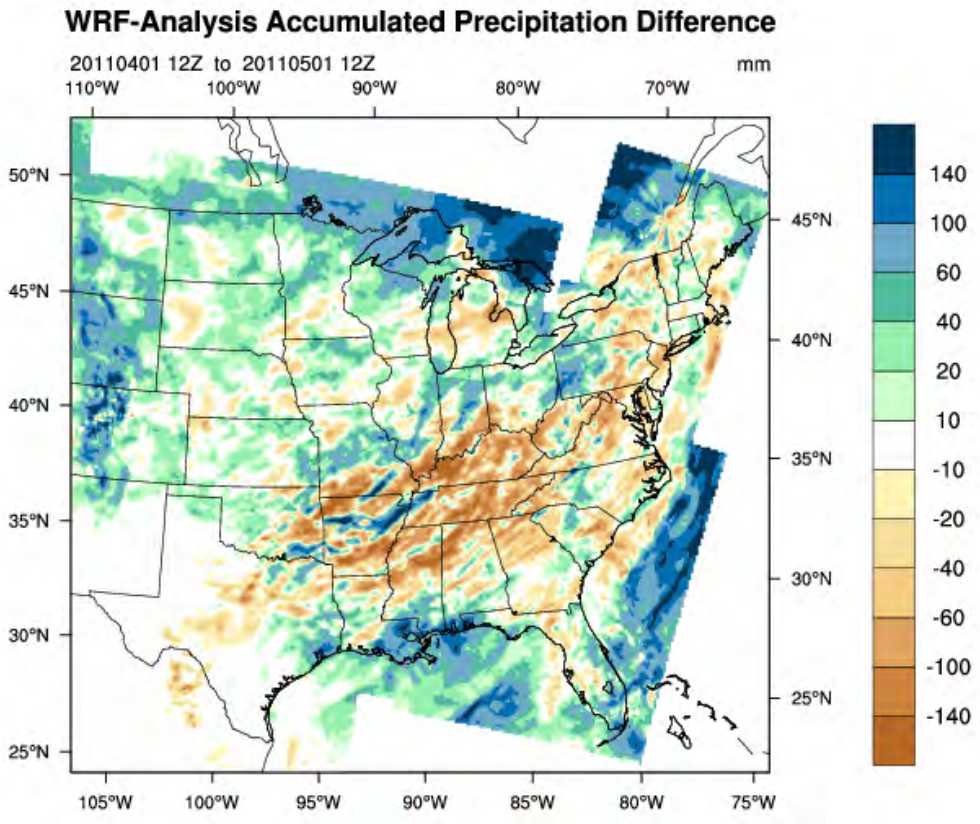

Figure D-12. Monthly accumulated observed and modeled precipitation difference for April 2011.

May

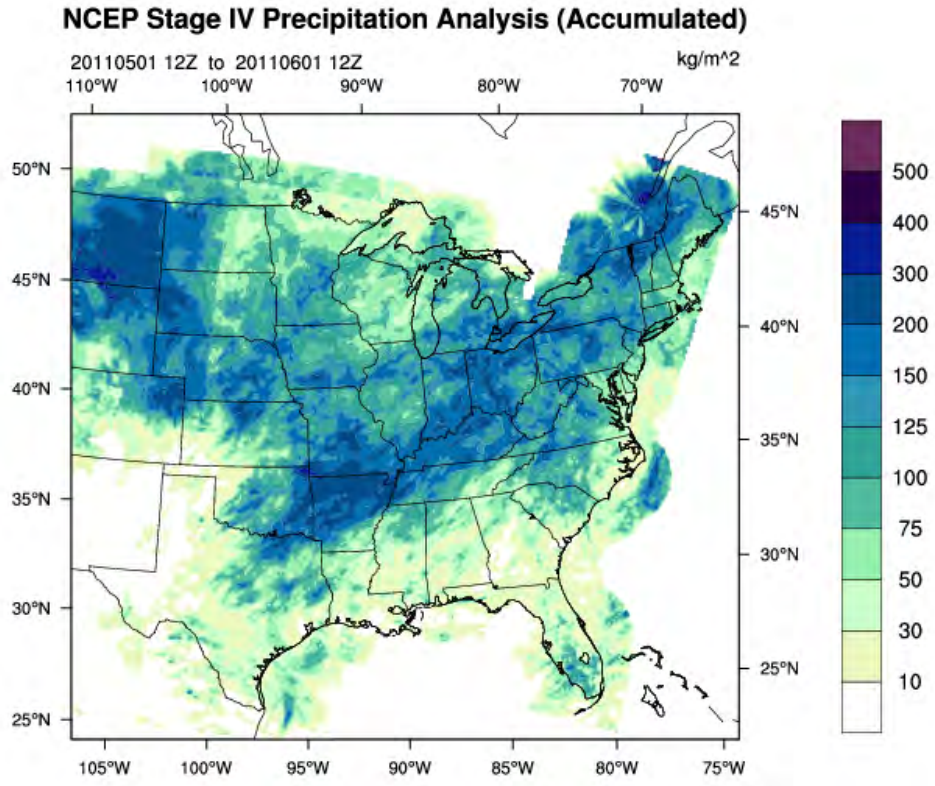

Figure D-13. Daily NCEP Stage IV precipitation data accumulated over the month of May 2011.

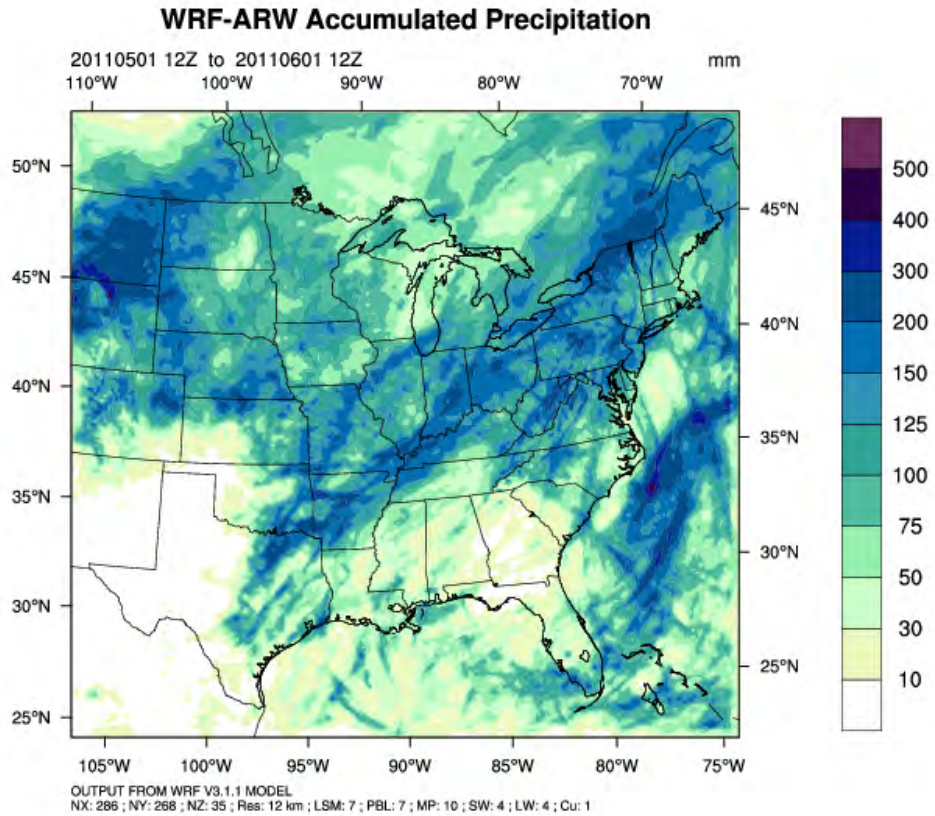

Figure D-14. WRF simulated precipitation accumulated over the month of May 2011.

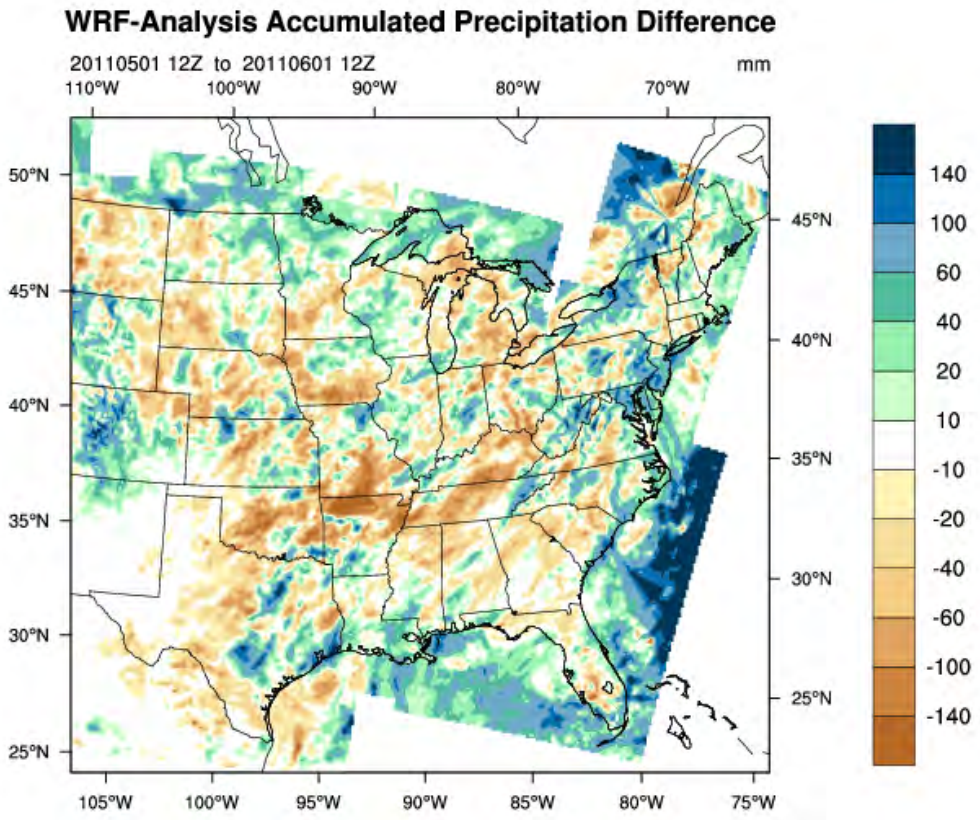

Figure D-15. Monthly accumulated observed and modeled precipitation difference for May 2011.

June

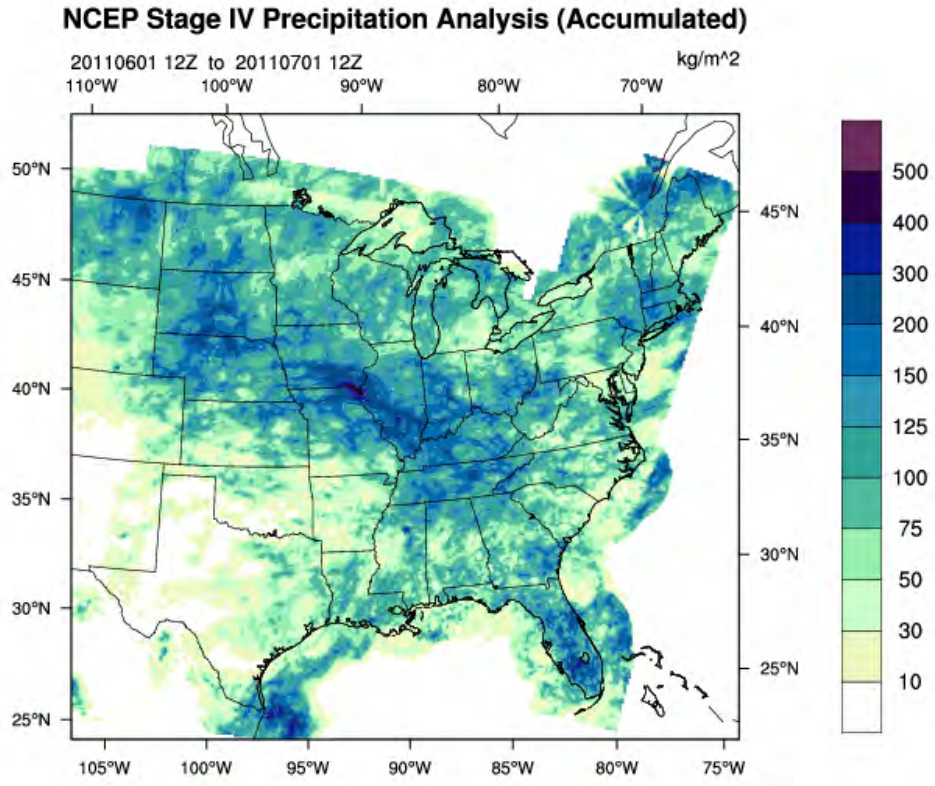

Figure D-16. Daily NCEP Stage IV precipitation data accumulated over the month of June 2011.

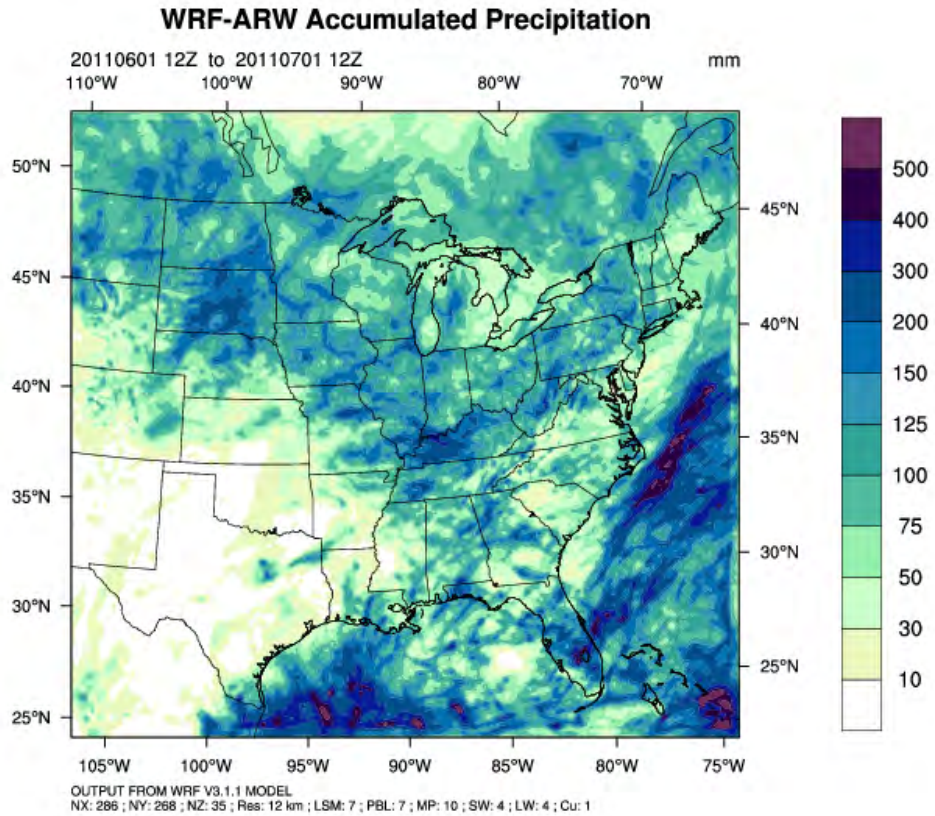

Figure D-17. WRF simulated precipitation accumulated over the month of June 2011.

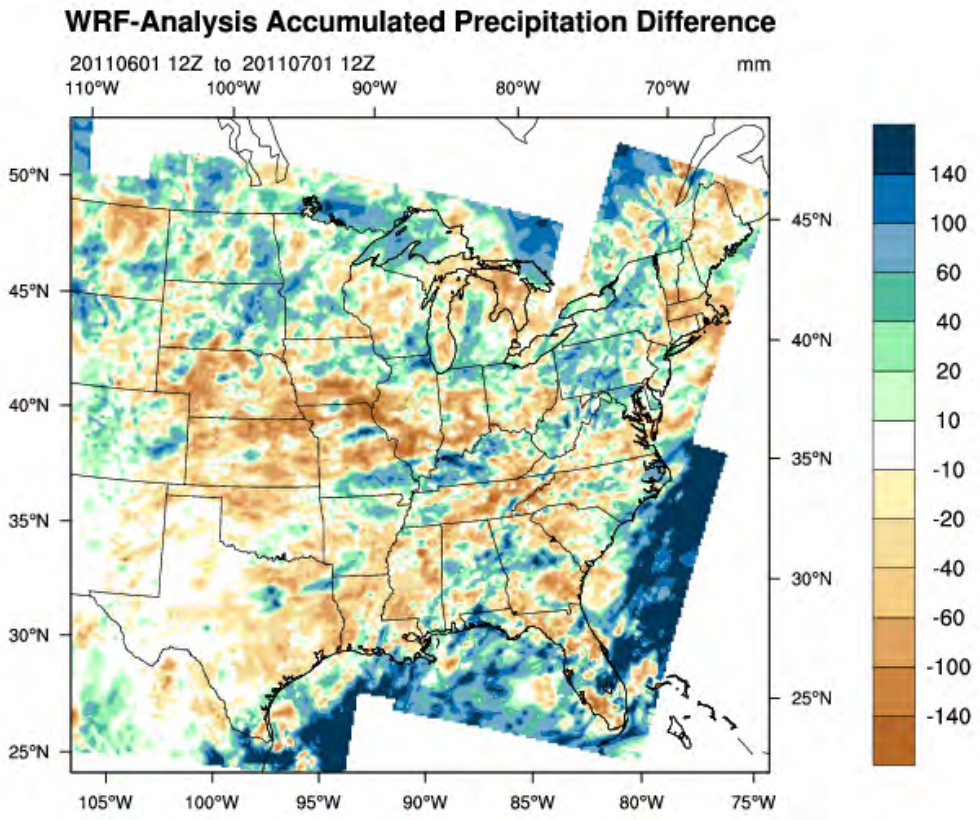

Figure D-18. Monthly accumulated observed and modeled precipitation difference for June 2011.

July

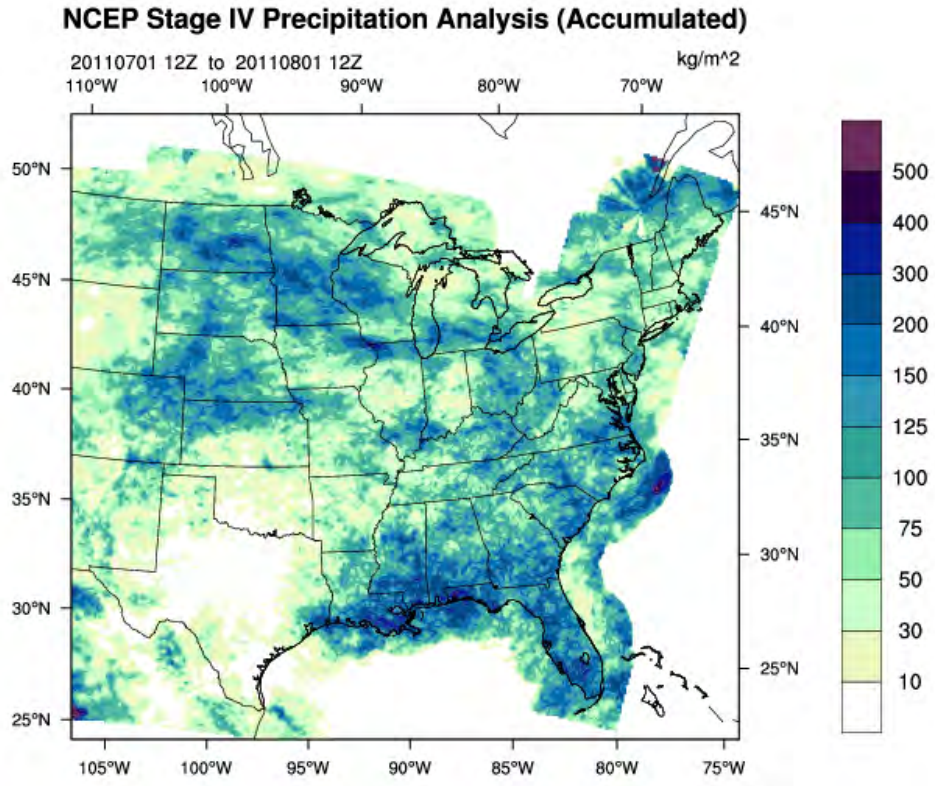

Figure D-19. Daily NCEP Stage IV precipitation data accumulated over the month of July 2011.

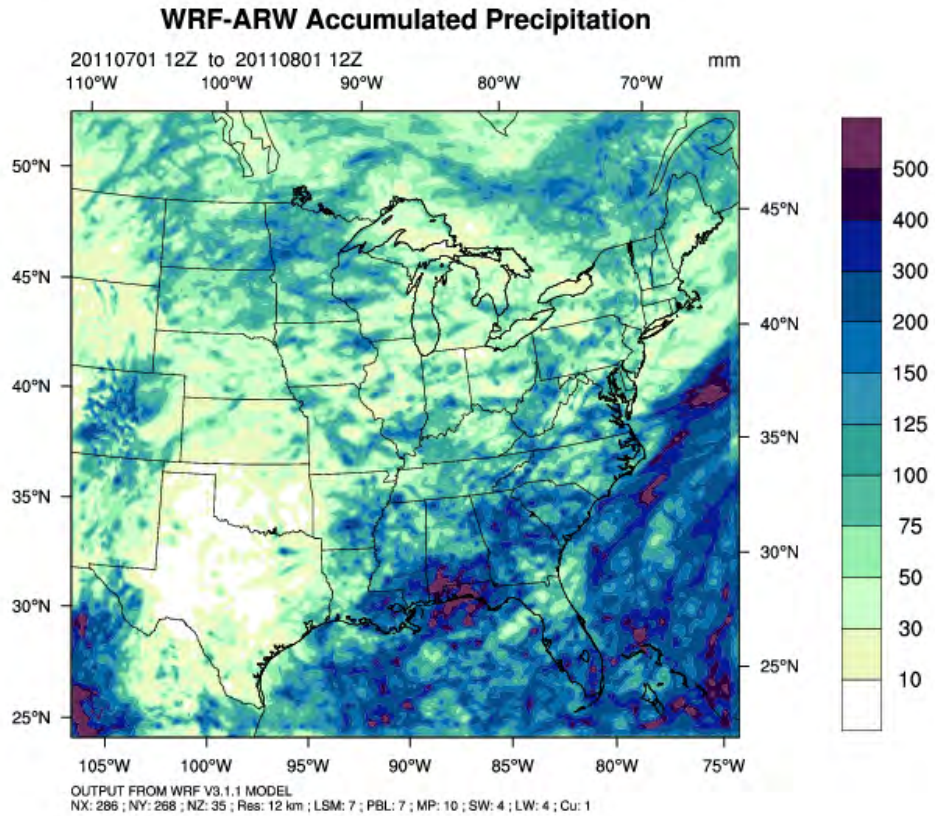

Figure D-20. WRF simulated precipitation accumulated over the month of July 2011.

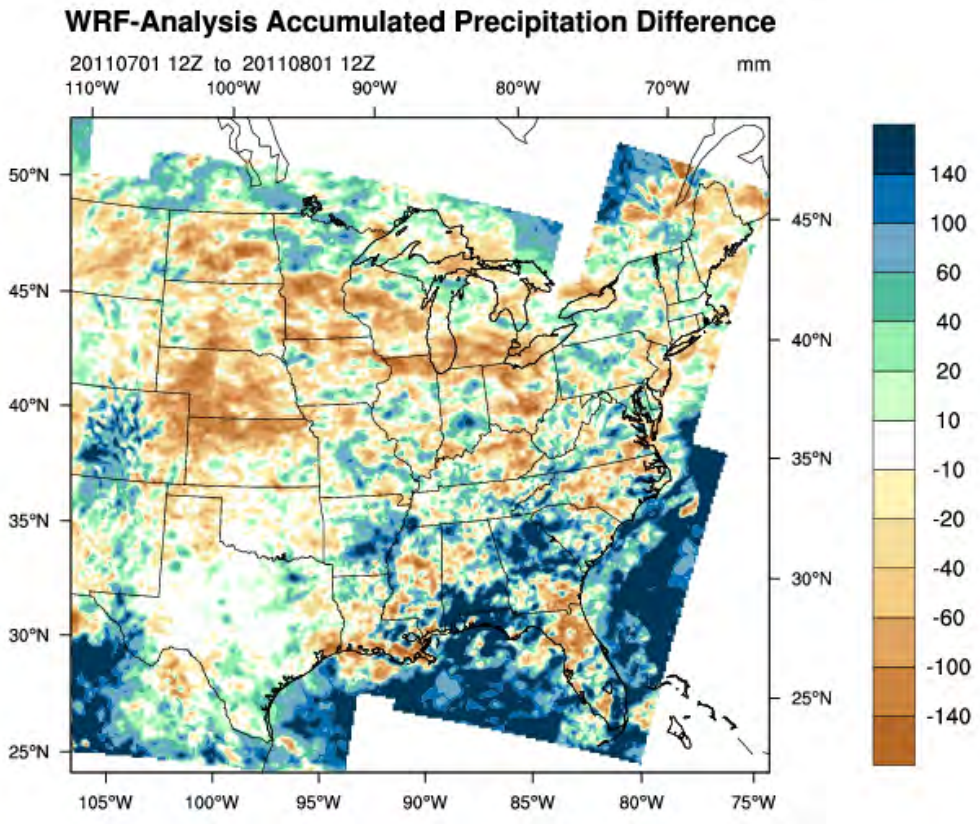

Figure D-21. Monthly accumulated observed and modeled precipitation difference for July 2011.

August

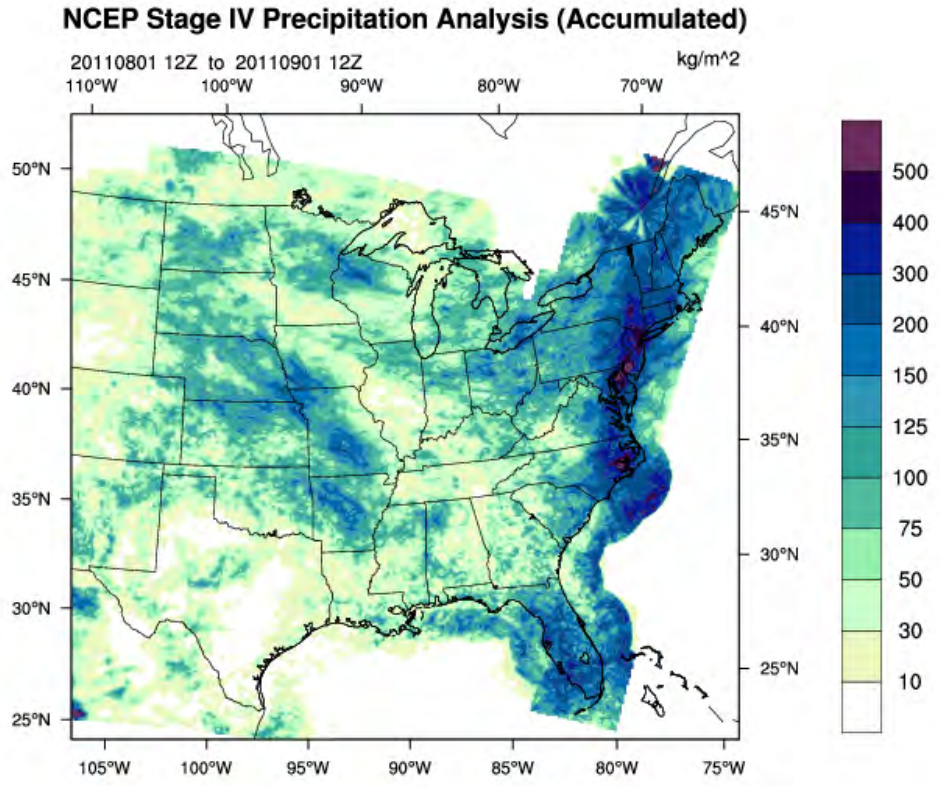

Figure D-22. Daily NCEP Stage IV precipitation data accumulated over the month of August 2011.

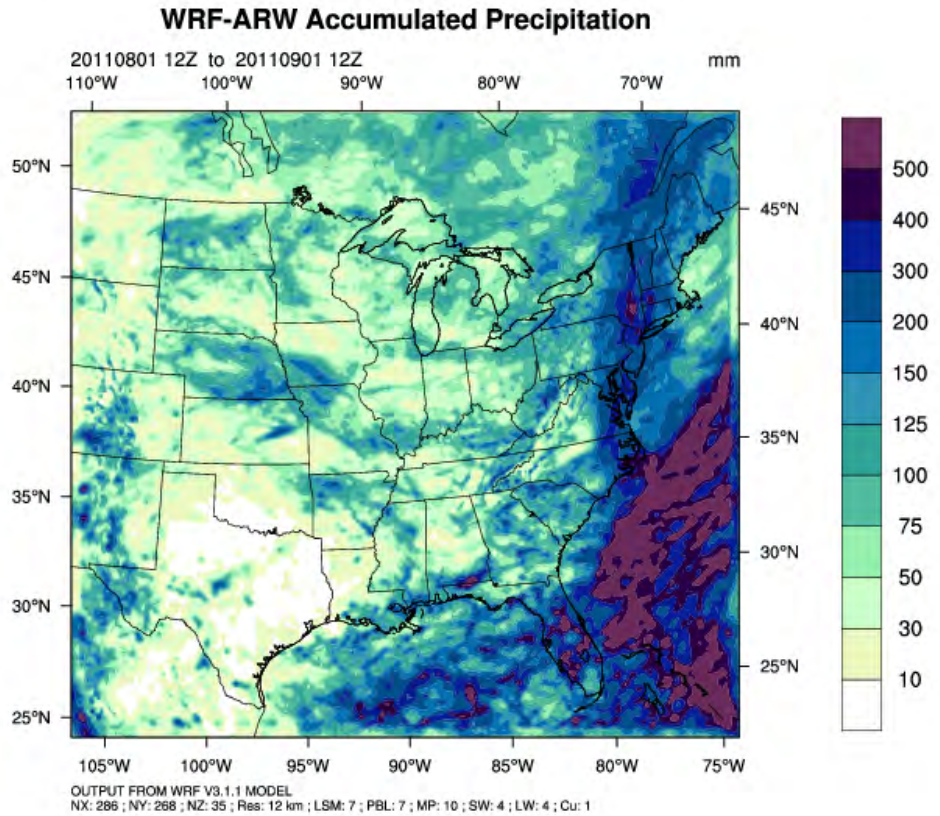

Figure D-23. WRF simulated precipitation accumulated over the month of August 2011.

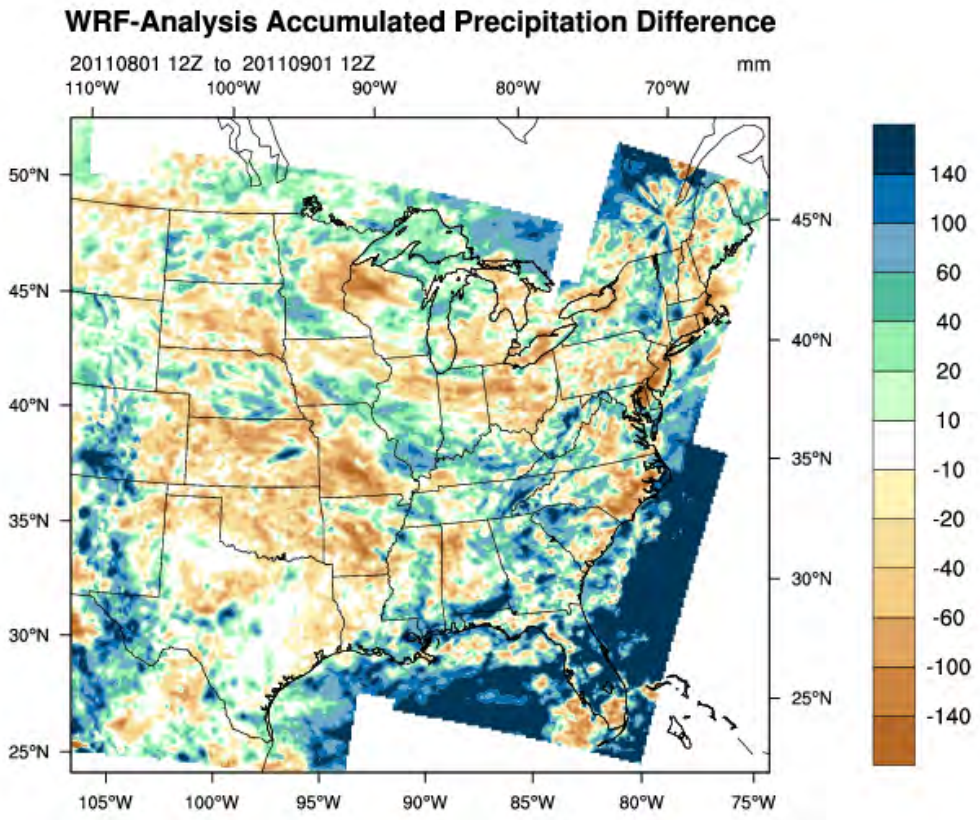

Figure D-24. Monthly accumulated observed and modeled precipitation difference for August 2011.

September

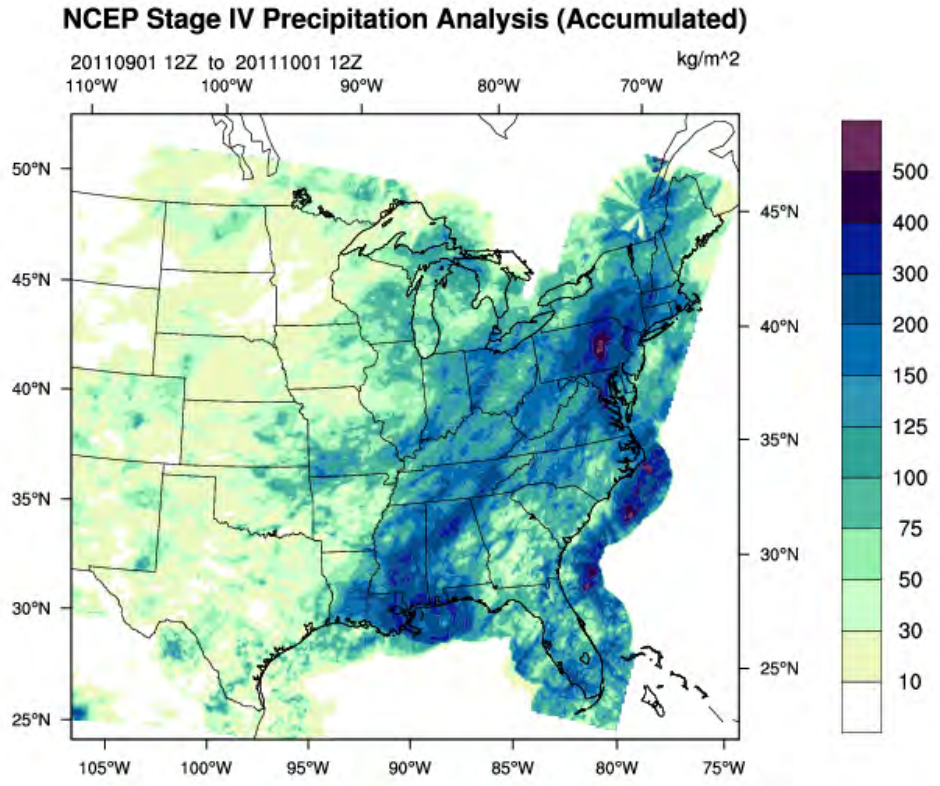

Figure D-25. Daily NCEP Stage IV precipitation data accumulated over the month of September 2011.

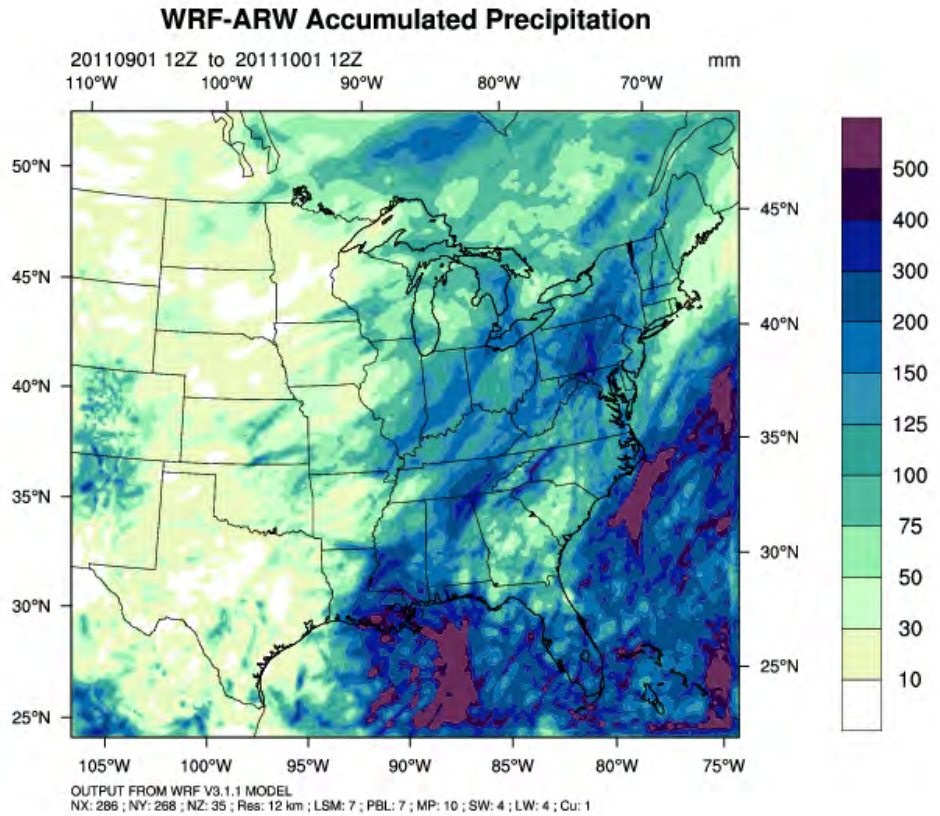

Figure D-26. WRF simulated precipitation accumulated over the month of September 2011.

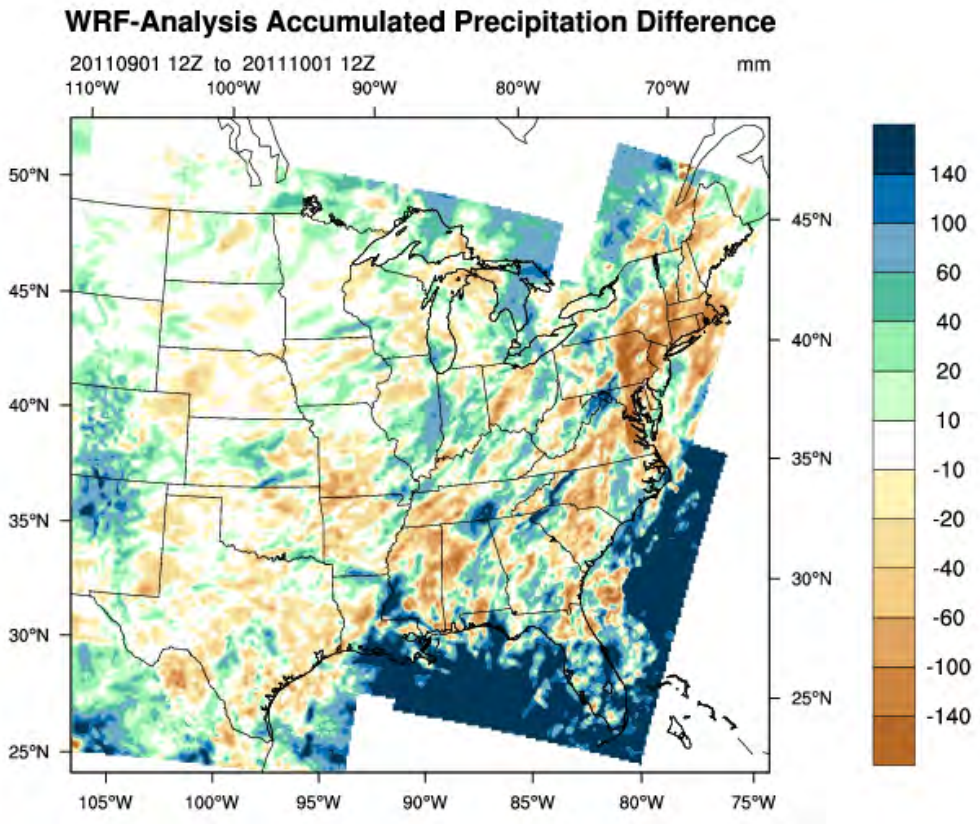

Figure D-27. Monthly accumulated observed and modeled precipitation difference for September 2011.

October

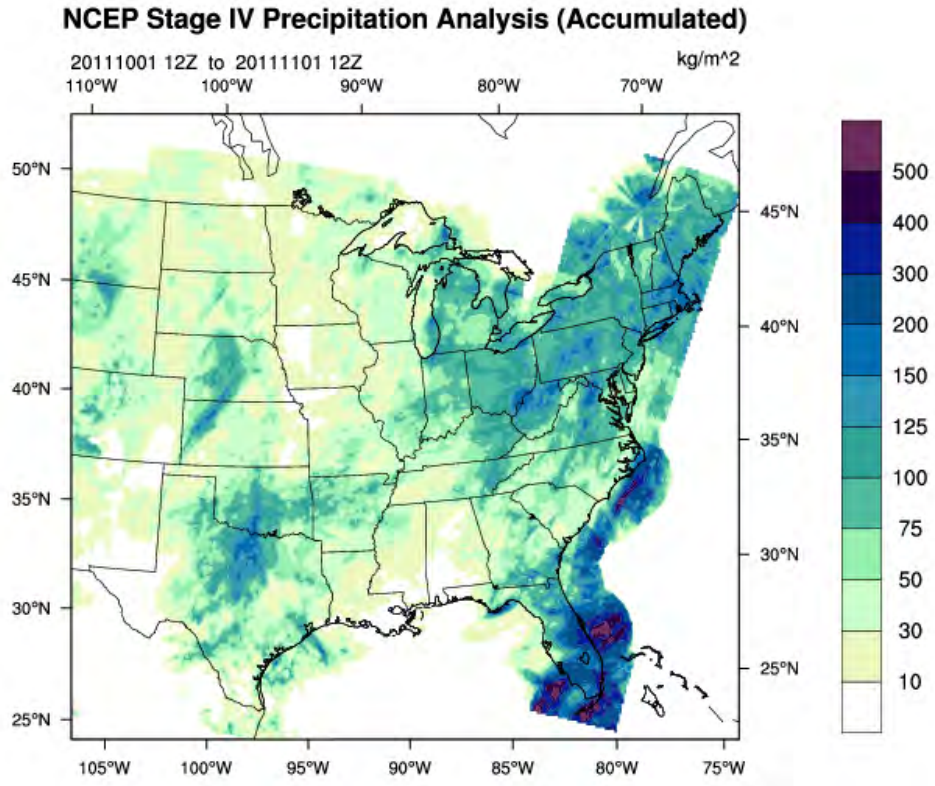

Figure D-28. Daily NCEP Stage IV precipitation data accumulated over the month of October 2011.

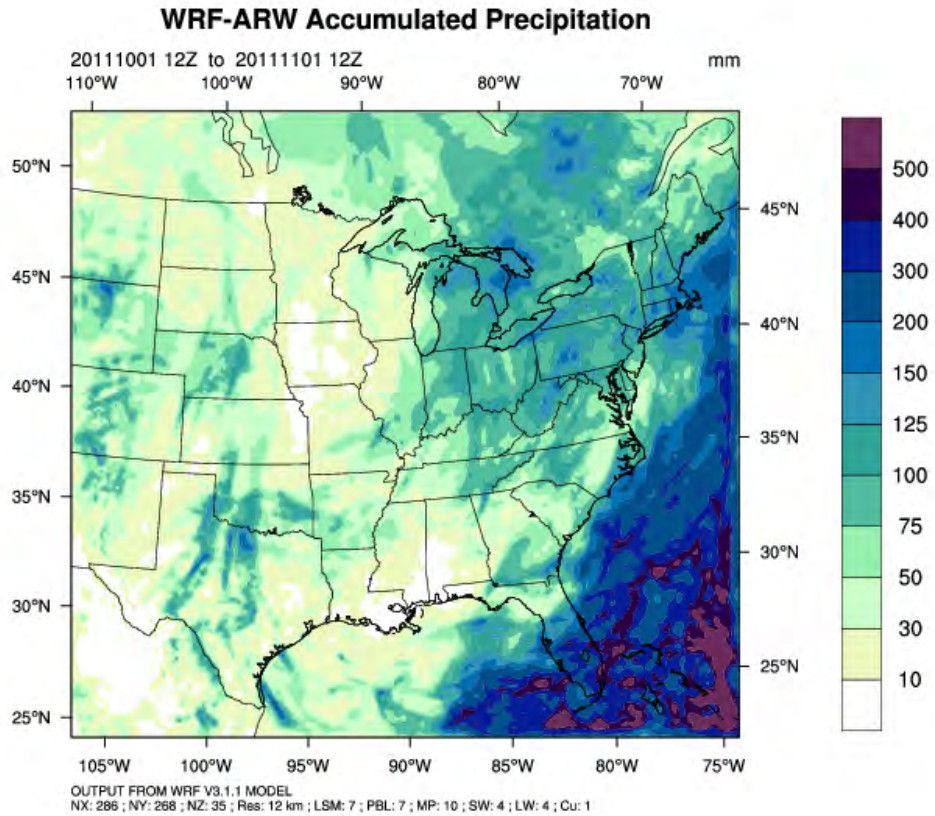

Figure D-29. WRF simulated precipitation accumulated over the month of October 2011.

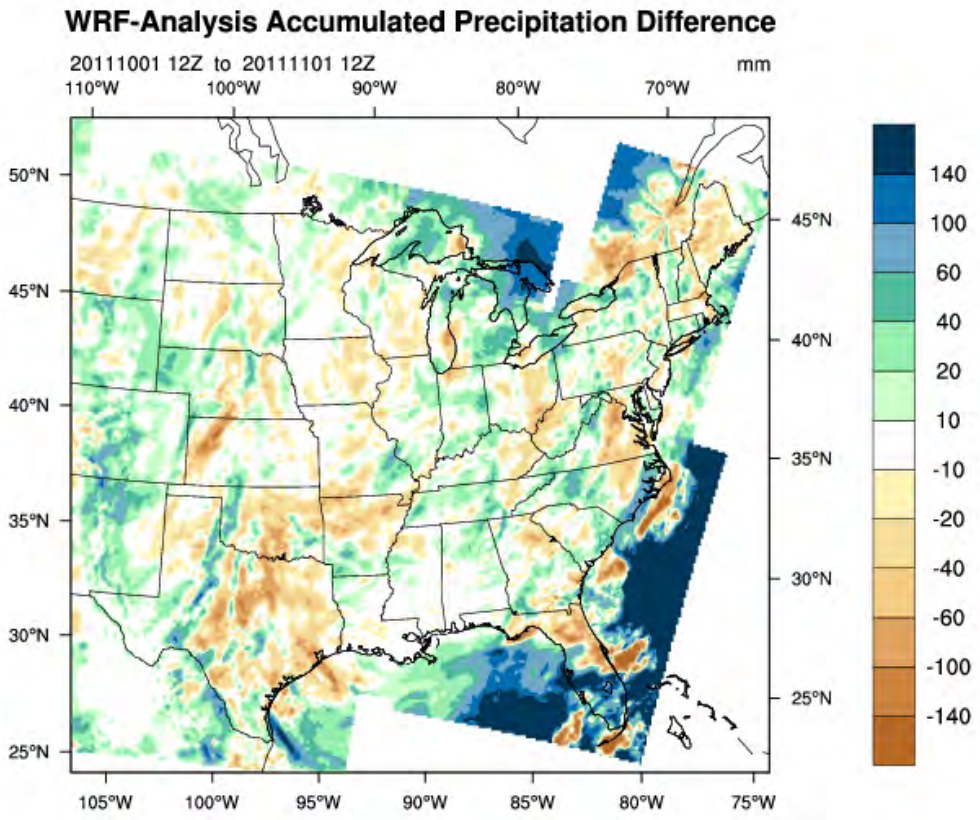

Figure D-30. Monthly accumulated observed and modeled precipitation difference for October 2011.

November

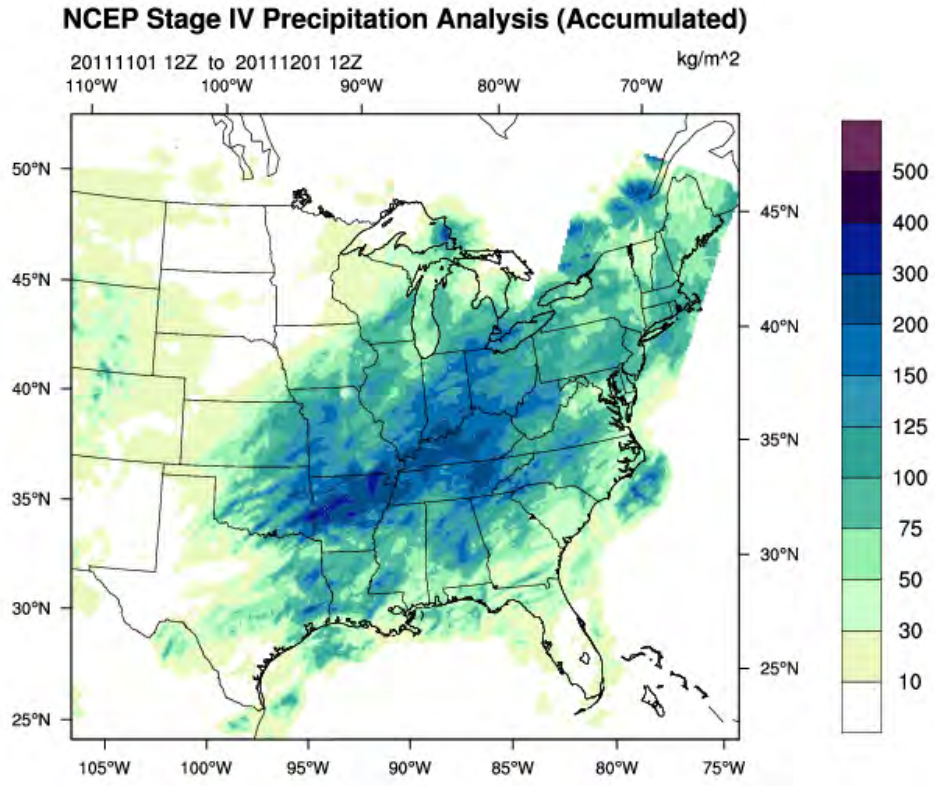

Figure D-31. Daily NCEP Stage IV precipitation data accumulated over the month of November 2011.

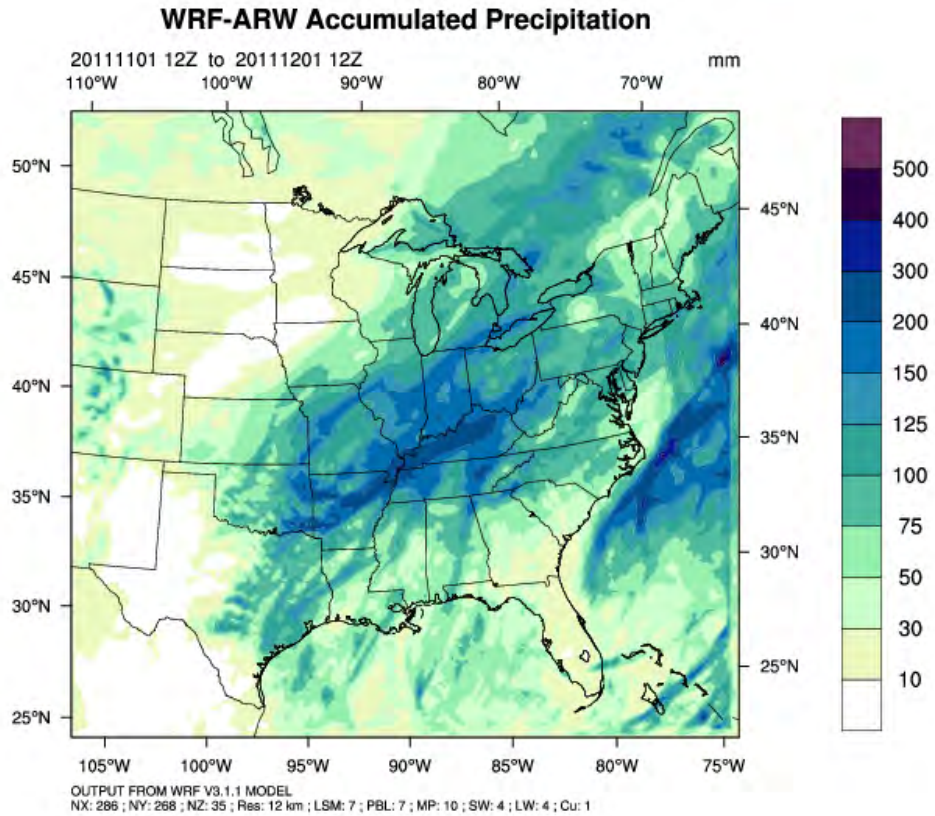

Figure D-32. WRF simulated precipitation accumulated over the month of November 2011.

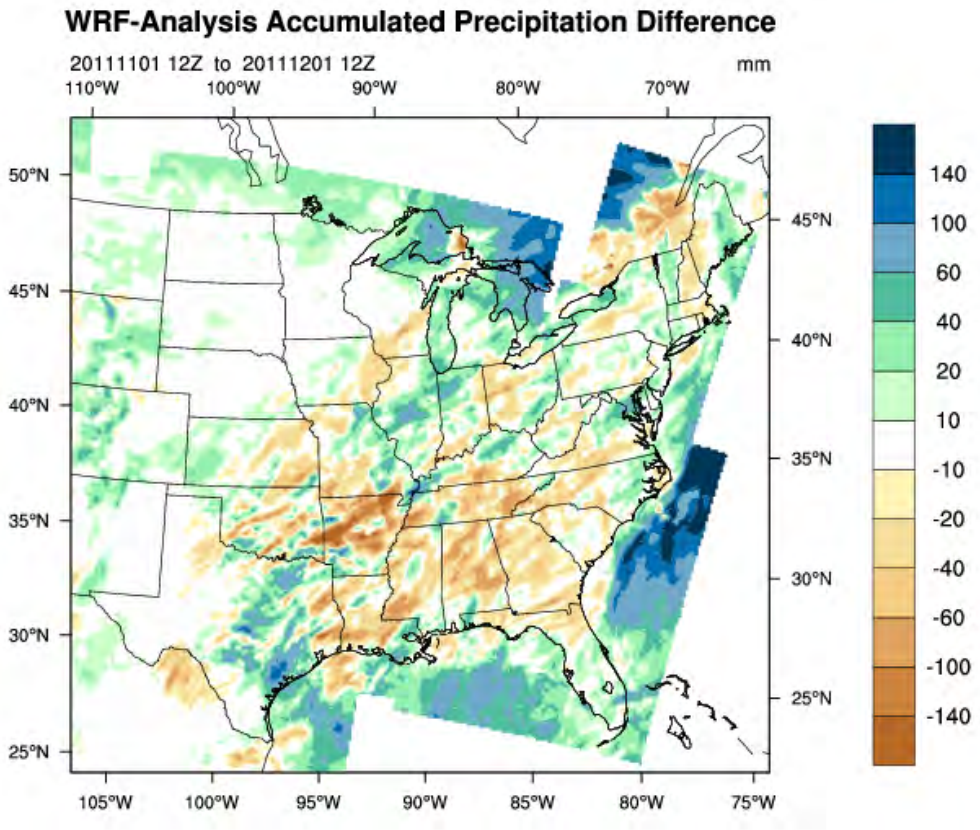

Figure D-33. Monthly accumulated observed and modeled precipitation difference for November 2011.

December

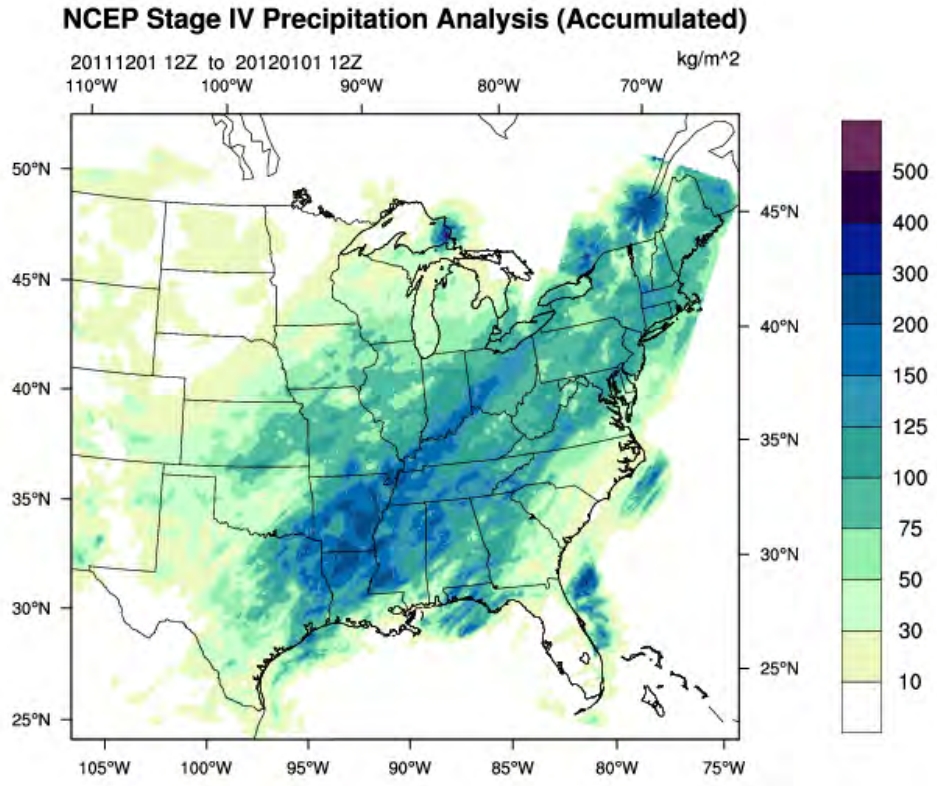

Figure D-34. Daily NCEP Stage IV precipitation data accumulated over the month of December 2011.

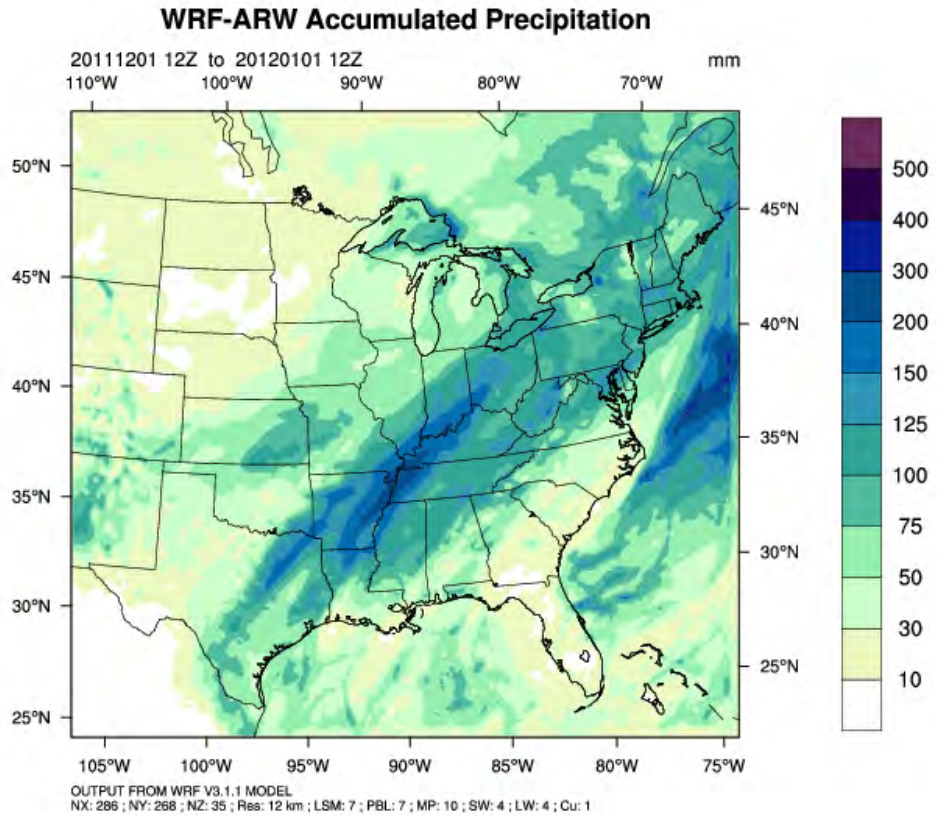

Figure D-35. WRF simulated precipitation accumulated over the month of December 2011.

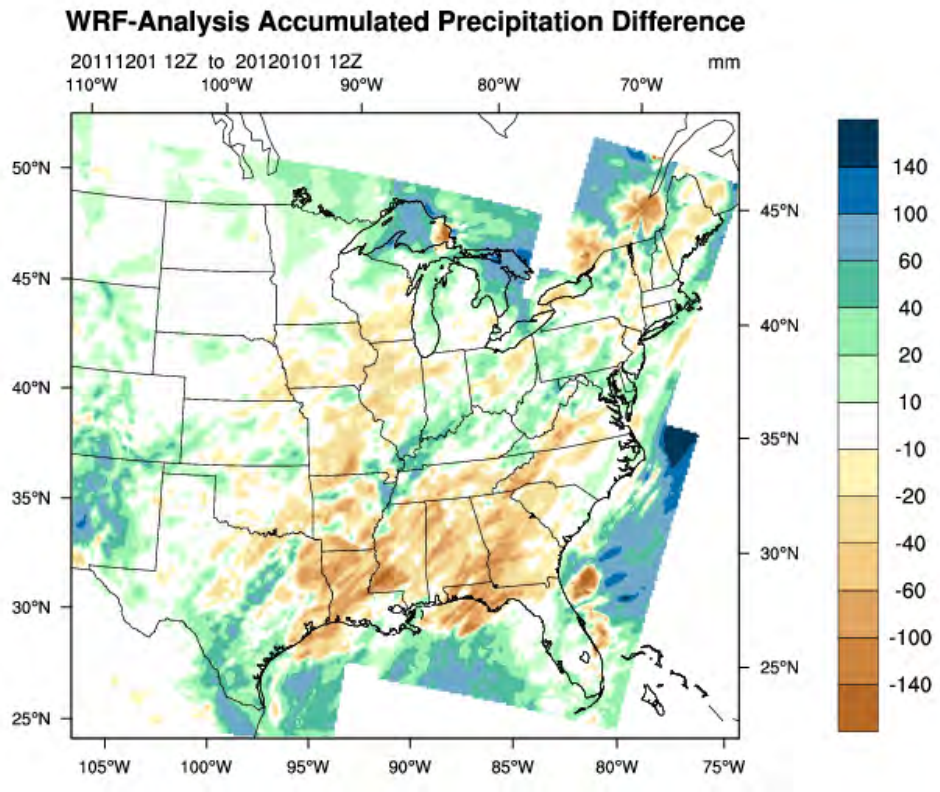

Figure D-36. Monthly accumulated observed and modeled precipitation difference for December 2011.